Modeling of Gaseous Ferritic Nitrocarburizing of Steels

by

Haoxing You

WORCESTER POLYTECHNIC INSTITUE

In partial fulfillment of the requirements for the

Degree of Doctor of Philosophy

in

Material Science and Engineering

February 2024

Professor Richard D. Sisson Jr. Advisor

Professor Emeritus of Mechanical and Materials Engineering

Abstract

Gaseous nitriding and ferritic nitrocarburizing (FNC) are typical thermochemical surface treatment methods to improve the wear and corrosion resistance, as well as fatigue endurance of steel parts such as shafts and gears[1, 2]. During the treatment, the atomic nitrogen and carbon are introduced into steel surface, a compound layer (also called white layer) composed of ε-Fe_{2-3}(C,N) and γ'-Fe_4N iron (carbon-)nitrides will form on the steel surface, and underneath the compound layer, there will be a diffusion zone with alloy (carbon-)nitrides dispersed [3-5]. The compound layer can improve the wear and corrosion resistance of the steel while the diffusion zone is in favor of the fatigue endurance. The modified mechanical properties of the steel parts mainly depend on the thickness, phase constitution of the compound layer as well as the depth of the diffusion zone, which are governed by several critical process parameters including temperature, nitriding potential, carburizing potential, and process duration [6-8]. The objectives of the current project are to develop a fundamental understanding of gaseous nitrocarburizing of steels and to establish a computational model for gaseous nitrocarburizing process.

Two series of gaseous FNC trials have been carried out, in the first FNC trial, three different materials were selected for investigations, AISI 4140, AISI 1018 and cast iron (ASTM A536 80-55-06). The samples were nitrocarburized at 579 °C with 4 $atm^{-1/2}$ nitriding potential. Three different carburizing potentials were applied and for each carburizing potential, there were four different process durations. The samples from both FNC trials were characterized with the same procedure. To obtain the total weight gain during the FNC process, the weight of each individual sample was recorded before and after the FNC treatment. The morphology of the compound layer was observed with optical microscope, SEM, and EDS mapping. The average compound layer thickness was measured from the micrographs and the compound layer growth kinetics were fitted with parabolic law. The compound layer phase constitution was analyzed with XRD and Rietveld refinement. The alloy specific potential diagrams were developed with Thermo-Calc, and the diffusion path was determined on the potential diagrams and isopleths to interpret the microstructural profiles in the compound layer. The microhardness profile was tested with line scans in the diffusion zone. The nitrogen and carbon concentration profiles were measured by OES with a layer-by-layer method. The effective nitrogen diffusion coefficient in specific steel was determined with a reversed method from the experimentally measured nitrogen concentration profiles and interpreted with the diffusion with trapping model [9-11].

1. Mittemeijer, E.J. and M.A. Somers, *Thermochemical surface engineering of steels*. 2014: Woodhead Publishing Cambridge.
2. Pye, D., *Practical nitriding and ferritic nitrocarburizing*. 2003: ASM international.
3. Yang, M., *Nitriding--Fundamentals, Modeling and Process Optimization*. 2012, Worcester Polytechnic Institute Massachusetts.
4. Dossett, J. and G. Totten, *Fundamentals of nitriding and nitrocarburizing.* ASM Handbook: Steel Heat Treating Fundamentals and Processes; ASM International: Materials Park, OH, USA, 2013: p. 619.
5. Slycke, J., L. Sproge, and J. Agren, *Nitrocarburizing and the Ternary Fe--N--C Phase Diagram.* Scand. J. Metall., 1988. **17**(3): p. 122-126.
6. Du, H. and J. Ågren. *Kinetics of Compound-Layer Growth during Nitrocarburizing*. in *Materials science forum*. 1992. Trans Tech Publ.
7. Woehrle, T., A. Leineweber, and E. Mittemeijer, *Microstructural and phase evolution of compound layers growing on α–iron during gaseous nitrocarburizing.* Metallurgical and Materials Transactions A, 2012. **43**(7): p. 2401-2413.
8. Du, H., M.A. Somers, and J. Agren, *Microstructural and compositional evolution of compound layers during gaseous nitrocarburizing.* Metallurgical and Materials Transactions A, 2000. **31**(1): p. 195-211.
9. Makhlouf, M.M., *Hydrogen uptake by AISI 4340 steel during cadmium electroplating.* 1990.
10. Oriani, R.A., *The diffusion and trapping of hydrogen in steel.* Acta metallurgica, 1970. **18**(1): p. 147-157.
11. McNabb, A. and P. Foster, *A new analysis of diffusion of hydrogen in iron and ferritic steels.* Transactions of the Metallurgical Society of AIME, 1963. **227**(3): p. 618-&.

Acknowledgement

First and foremost, I would like to express my deepest gratitude to my advisor, Prof. Richard D. Sisson, for providing me with this opportunity and for his continuous support and guidance. I miss the Thermodynamic lectures he delivered, always unravels the complex concepts simply but thoroughly.

I also want to extend my appreciation to Prof. Mei Yang, Prof. Yu Zhong, and Prof. Jianyu Liang for their support. Prof. Mei Yang's academic guidance and expertise in thermodynamic diagram development have been critically helpful to my research project. The mentorship from Prof. Mei Yang and Prof. Yu Zhong has always been a source of encouragement in daily life.

Special thanks to Dr. Boquan Li and Micheal Collins for their training and assistance with the lab instruments, enabling me to utilize the equipment proficiently and effectively for my research.

I would like to acknowledge the support and sponsor from all CHTE member companies. Special thanks to Olga Rowan from Caterpillar, her guidance for metallurgy sample preparation has saved me countless hours. Special thanks to Rodney Kennedy from Bodycote for his consistently strong support throughout all our experiments.

My gratitude also goes to my colleagues and friends at CHTE, including Haixuan Yu, Yishu Zhang, and Rick Smith. I've learned a lot from the collaborations and I'm grateful for the knowledge and experiences shared by each of them. Special thanks to Haixuan Yu, for providing me with valuable advice and guidance during the challenging times.

Last but not least, I owe the greatest debt of gratitude to my parents, Mei Wang and Yiqiang You. Your encouragement has always been the pillar of support in my life journey.

Table of Contents

Chapter 1: Introduction

Nitriding and ferritic nitrocarburizing are widely used surface thermochemical treatment methods to improve wear, corrosion resistance and fatigue endurance of steels in industry. During nitriding and nitrocarburizing process, atomic nitrogen and carbon are introduced into the surface of steel components, then, a compound layer with a diffusion zone beneath it will form at the surface of the component [1, 2]. The compound layer mainly consists of γ'-Fe_4N and ε-$Fe_{2-3}(C,N)$ phase can significantly improve the wear and corrosion resistant and the diffusion zone with dispersed alloy (carbon-)nitrides will improve the fatigue endurance [3-5]. There are several different approaches that can introduce atomic nitrogen and carbon into steels, such as gaseous, salt bath, and plasma methods [1].

Gaseous nitriding/nitrocarburizing method is widely used in industry since the process is easy to control by controlling the gas composition and gas flow. The gaseous nitriding method was firstly developed at the beginning of 20^{th} century by Adolph Machlet from American Gas Company [6]. During the early development of industrial application of gaseous nitriding process, the main challenge was its low performance reliability [7]. The mechanical properties of nitrided steels are determined by the thickness and microstructure of nitrided case which are controlled by the three process parameters which are temperature, nitriding potential/ammonia dissociation rate, and process time [8-10]. To improve the process reliability, researchers have investigated the influence of specific process parameters [11-14]. It is critical to fully understand the thermodynamics and kinetics during the gaseous nitriding process and model the process parameters. Models have been established based on these process parameters to predict gaseous nitriding process of pure irons and steels [9, 10, 12, 13, 15-20]. With these models, we are able to select certain parameters to meet specifications and achieve precise gaseous nitriding process control.

Compared with gaseous nitriding, nitrocarburizing process, in which atomic carbon is introduced into component at the same time usually requires much shorter process time to produce required nitrided case. There are four determinant process parameters for gaseous nitrocarburizing process, which are temperature, nitriding potential, carburizing potential, and time. Typical gaseous nitrocarburizing process is carried out at a temperature between 500 °C and 580 °C. For process media, besides ammonia or dissociated ammonia gas as nitrogen source, carbon dioxide, carbon monoxide, endogas, or some hydrocarbons such as methane or propane is added as carbon source [1].

The first challenge of industrial application of gaseous nitrocarburizing process is to measure and control the process parameter, carburizing potential especially [21]. By adding the carbon source atmosphere, there will be several different carburizing reactions occurring which makes the measurement and control of carburizing potential more complicated.

Another challenge is to understand the thermodynamics of kinetics of nitrocarburizing of alloy steels. Most of the investigations to date are based on pure irons. But for practical purpose, we need to further investigate how different parameters influence the nitrocarburizing process. Currently, industry mostly use try and error method to determine specific process parameters to meet specification, an effective model that can predict the properties such as compound layer thickness, case depth, and compound layer growth kinetics based on certain process parameters is needed. Besides, the influence of diffused carbon on diffusion of nitrogen needs to be investigated.

Therefore, the objective of the current project is to develop a fundamental understanding of gaseous nitrocarburizing of steels and develop a computational model to predict the compound layer composition and growth kinetics as well as case depth. The model will be verified experimentally and then utilized to determine process parameters to satisfy specifications.

Figure 1 summarizes the questions that need to be investigated to establish the computational model for gaseous ferritic nitrocarburizing process. The diagram shows the schematic nitrogen and carbon concentration profiles in compound layer and diffusion zone after gaseous nitrocarburizing process of steels. Based on theoretical analysis and experimental results, this project will answer the following critical questions to establish the gaseous nitrocarburizing model.

- Model the nitrogen and carbon flux at steel surface; the total flux of nitrogen and carbon can be determined by measuring the weight gain of the sample after nitrocarburizing process, then, combining measured nitrogen and carbon concentration profiles, the flux of nitrogen and carbon can be calculated respectively. The influence of different carburizing potential to flux will be investigated.
- Calculate the incubation time for compound layer formation; the incubation time can be estimated by measuring the compound layer thickness and applying parabolic law to fit the compound layer growth kinetics. To predict the incubation time, we need to define the maximum nitrogen and carbon solubility in the steel from the alloy specific isopleth diagrams for certain steel.

- Determine the growth kinetics of the compound layer. A series of experiments will be conducted to determine the time and temperature dependence of compound layer growth kinetics.
- Determine the sequence of phases in the compound layer (diffusion paths). Alloy specific Lehrer and Kunze diagrams as well as quasi-ternary isopleths will be developed. These diagrams will be used to create diffusion paths to determine the sequence of phases in compound layer and diffusion zone.
- The porosity development in the compound layer under a variety of nitrocarburizing conditions (T, t, KN and KC) will be investigated. The focus will be on stoichiometry changes in the ε-Fe_{2-3}N phase as a function of KN.
- Determine the diffusivities of nitrogen and carbon in the steel (diffusion with trapping), the nitrogen and carbon concentration profile in the diffusion zone can be measured by layer-by-layer OES tests. The diffusivities of nitrogen and carbon in the diffusion zone can be determined with an inverse method which will fit the experimentally measured concentration profile with a computational model. A diffusion with a chemical reaction or trapping model will be used.

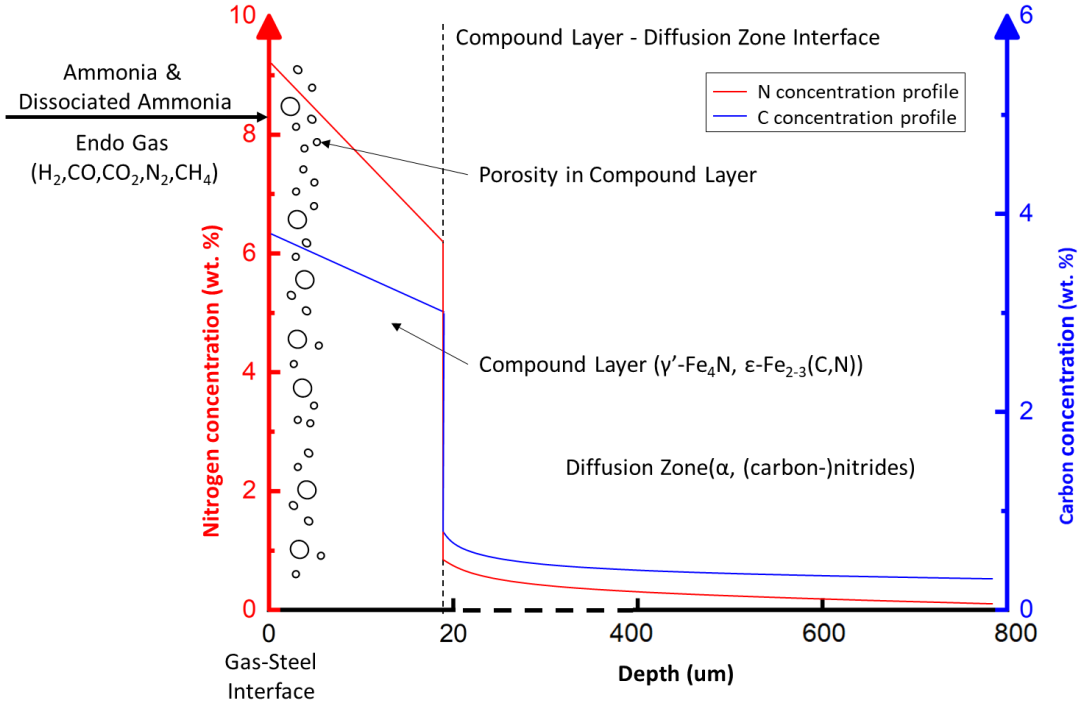

Figure 1 Schematic diagram of nitrogen and carbon concentration profiles in steel after gaseous FNC process

Reference

1. Mittemeijer, E.J. and M.A. Somers, *Thermochemical surface engineering of steels*. 2014: Woodhead Publishing Cambridge.
2. Pye, D., *Practical nitriding and ferritic nitrocarburizing*. 2003: ASM international.
3. Somers, M., P. Colijn, and E. Mittemeijer, *MICROSTRUCTURAL AND COMPOSITIONAL EVOLUTION OF IRON-CARBONITRIDE COMPOUND LAYERS DURING SALT BATH NITROCARBURIZING.* INTERNAL AND EXTERNAL NITRIDING AND NITROCARBURIZING OF IRON AND IRON-BASED ALLOYS, 1990: p. 237.
4. Somers, M.A., *Thermodynamics, kinetics and microstructural evolution of the compound layer; A comparison of the states of knowledge of nitriding and nitrocarburising.* HEAT TREATMENT OF METALS-BIRMINGHAM-, 2000. **27**(4): p. 92-101.
5. Du, H., M.A. Somers, and J. Agren, *Microstructural and compositional evolution of compound layers during gaseous nitrocarburizing.* Metallurgical and Materials Transactions A, 2000. **31**(1): p. 195-211.
6. Machlet, A., *Treatment of Steel, Iron, etc*, in *U. S. Patent*. 1913.
7. Zinchenko, V. and V.Y. Syropyatov, *New possibilities of gas nitriding as a method for anticorrosion treatment of machine parts.* Metal science and heat treatment, 1998. **40**(7): p. 261-265.
8. Somers, M.A. *Nitriding and nitrocarburizing: Status and future challenges*. in *Proceedings of heat treat & surface engineering conference & expo, Chennai, India*. 2013.
9. Yang, M., *Nitriding--Fundamentals, Modeling and Process Optimization*. 2012, Worcester Polytechnic Institute Massachusetts.
10. Yang, M. and R. Sisson Jr, *Modeling the nitriding process of steels.* Advanced Materials & Processes, 2012. **170**(7): p. 33-37.
11. Malinova, T., S. Malinov, and N. Pantev, *Simulation of microhardness profiles for nitrocarburized surface layers by artificial neural network.* Surface and Coatings Technology, 2001. **135**(2-3): p. 258-267.
12. Tijani, Y.A., *Modeling and Simulation of Thermochemical Heat Treatment Processes: A Phase Field Calculation of Nitriding in Steel*. 2008, Universität Bremen.
13. Du, H. and J. Ågren. *Kinetics of Compound-Layer Growth during Nitrocarburizing*. in *Materials science forum*. 1992. Trans Tech Publ.
14. Göhring, H., et al., *Thermodynamics of the Fe-N and Fe-NC systems: The Fe-N and Fe-NC phase diagrams revisited.* Metallurgical and Materials Transactions A, 2016. **47**(12): p. 6173-6186.

15. H.-J., S., B. Reinhold, and K. Wilsdorf, *Gas nitriding–process control and nitriding non-ferrous alloys.* Surface engineering, 2001. **17**(1): p. 41-54.
16. Yang, M., et al., *Modeling the gas nitriding process of low alloy steels.* Journal of Materials Engineering and Performance, 2013. **22**(7): p. 1892-1898.
17. Woehrle, T., A. Leineweber, and E. Mittemeijer, *Microstructural and phase evolution of compound layers growing on α–iron during gaseous nitrocarburizing.* Metallurgical and Materials Transactions A, 2012. **43**(7): p. 2401-2413.
18. Mittemeijer, E.J. and M.A. Somers, *Thermodynamics, kinetics, and process control of nitriding.* Surface Engineering, 1997. **13**(6): p. 483-497.
19. Yang, M., et al., *Simulation of the ferritic nitriding process.* International Heat Treatment and Surface Engineering, 2011. **5**(3): p. 122-126.
20. Slycke, J., L. Sproge, and J. Agren, *Nitrocarburizing and the Ternary Fe--N--C Phase Diagram.* Scand. J. Metall., 1988. **17**(3): p. 122-126.
21. Leineweber, A., T. Gressmann, and E. Mittemeijer, *Simultaneous control of the nitrogen and carbon activities during nitrocarburising of iron.* Surface and Coatings Technology, 2012. **206**(11-12): p. 2780-2791.

Chapter 2: Literature review

Fundamental of nitriding and nitrocarburizing

As an important thermochemical surface treatment, gaseous nitriding/nitrocarburizing will introduce atomic nitrogen/nitrogen and carbon into the surface, which will form a compound layer consists of γ'-Fe_4N phase and ε-Fe_{2-3}(C,N) and a diffusion zone beneath the compound layer [1]. The compound layer, usually up to 20 um, with improved hardness can significantly improve the wear resistance and atmosphere corrosion resistance [2-4]. In case of nitrocarburizing of steels, alloy elements such as aluminum and chromium will form alloy (carbon-)nitrides which will precipitate in the diffusion zone and enhance the fatigue endurance [5-8].

Typical nitriding/nitrocarburizing process temperature is between 500 °C and 580 °C which is below A_{C1} in the ferrite region in the iron-nitrogen phase diagrams [5]. The process dose not increase the strength of the core of the component since there is no phase transformation in the core. Steels are usually quenched and tempered to harden the core part before nitriding/nitrocarburizing process.

Compared with traditional gaseous nitriding process, gaseous nitrocarburizing process involves the gas atmosphere supplying atomic carbon, such as carbon monoxide, carbon dioxide, hydrocarbons (methane, propane), or endogas [5]. There will be several different carburizing reactions which make it more difficult to measure and control the carburizing potential. For example, if we add carbon dioxide as carbon source atmosphere, firstly, carbon dioxide will be reduced by hydrogen:

$$CO_2 + H_2 \rightarrow CO + H_2O$$

then, we will have heterogeneous water gas reaction:

$$2CO + H_2 \rightarrow [C] + H_2O$$

and also, the Boudouard reaction:

$$2CO \rightarrow [C] + CO_2$$

The carbon monoxide and hydrogen may also form methane:

$$CO + 3H_2 \rightarrow CH_4 + H_2O$$

then, we will also have:

$$CH_4 \rightarrow [C] + 2H_2$$

For nitriding potential, we usually have:

$$2NH_3 \rightarrow 2[N] + 3H_2$$

the nitriding potential is thus defined as:

$$K_N = \frac{p_{NH_3}}{{p_{H_2}}^{3/2}}$$

However, with different carburizing reactions, we will have three different carburizing potentials simultaneously:

from the heterogeneous water gas reaction, we have:

$$K_{CW} = \frac{p_{CO} * p_{H_2}}{p_{H_2O}}$$

and with the Boudouard reaction, we have:

$$K_{CB} = \frac{{p_{CO}}^2}{p_{CO_2}}$$

and for methane reaction, we also have:

$$K_C = \frac{P_{CH_4}}{{p_{H_2}}^2}$$

The nitriding potential is calculated by measuring the hydrogen in the exhaust gas with a hydrogen probe. But determination of carburizing potential also requires comparison of kinetics of different carburizing reactions.

There are several different nitrocarburizing approaches as the variants of process media and treated materials.

Gaseous ferritic nitrocarburizing

In gaseous nitrocarburizing process, components are heated up in a furnace with controlled atmosphere. Typical nitrogen source media is ammonia gas. Carbon dioxide, carbon monoxide, endogas, or carbon hydrogen gas such as methane and propane can be used as

carbon source atmosphere [5]. During the gaseous nitrocarburizing process, nitrogen and carbon chemical potential is usually measured and controlled by controlling the atmosphere composition and the gas flow rate.

Plasma ferritic nitrocarburizing

Plasma (ion) nitrocarburizing process uses glow discharge technology to introduce atomic nitrogen and carbon into the material. Compared with gaseous nitrocarburizing process, the atomic nitrogen and carbon are created by the ionization of gas, typically nitrogen and methane. It is reported that, compared with gaseous nitrocarburizing process, plasma nitrocarburizing process is usually more efficient and creates more uniform compound layer and diffusion zone [9]. However, plasma nitrocarburizing process is typically conducted in a vacuum furnace which will increase the equipment cost and energy consumption for industrial application [10].

Salt bath nitrocarburizing

Salt bath nitrocarburizing, also known as liquid nitrocarburizing process, is usually carried out at temperature range between 500 °C and 630 °C in molten alkali cyanate salt with pre-heated steel components [3]. With a certain catalyst, the salt will react with the component surface and provide atomic nitrogen and carbon. Due to direct contact of component surface with molten salt, the process has shorter process time. However, it is hard to measure the chemical potential and to maintain performance reliability [11].

Thermodynamics and Fe-C-N phase diagram

To establish a computational model for gaseous ferritic nitrocarburizing process, it is imperative to fully understand the thermodynamics and kinetics of the whole process. The most basic way to investigate the phase transformation and phase stability during nitrocarburizing process is through the phase diagrams. In the current project, the iron-nitrogen binary phase diagram, iron-nitrogen-carbon ternary phase diagram, Lehrer diagram, and potential diagram for pure iron are investigated. Certain diagrams for specific alloy steel (AISI 4140) which is used in our experiments are developed with the computational thermodynamic calculation software Thermo-Calc.

Fe-N system and Fe-C-N system

Figure 2 shows the iron-nitrogen binary phase diagram [12]. The typical nitrocarburizing temperature is below the A_{C1} temperature (592 °C), in this temperature range, the nitrogen solubility in ferrite is almost up to 6 wt. %, with higher nitrogen content, we will firstly have γ'-Fe_4N phase and then ε-$Fe_{2\text{-}3}(C,N)$ with even higher nitrogen content. This explains

the double layered compound layer structure observed in the nitriding trial of pure iron [13]. As shown in

Figure 3, the compound layer has a ε-Fe_{2-3}(C,N) top layer and a γ'-Fe_4N phase layer underneath.

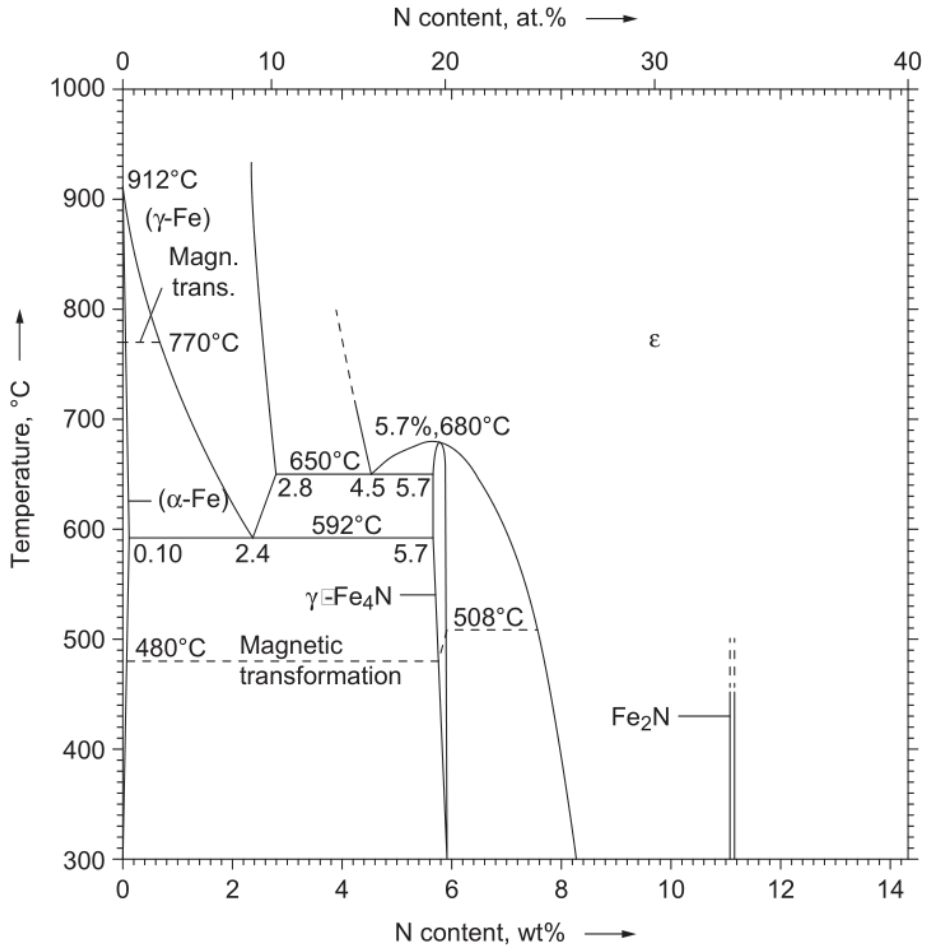

Figure 2 Iron-Nitrogen phase diagram [12]

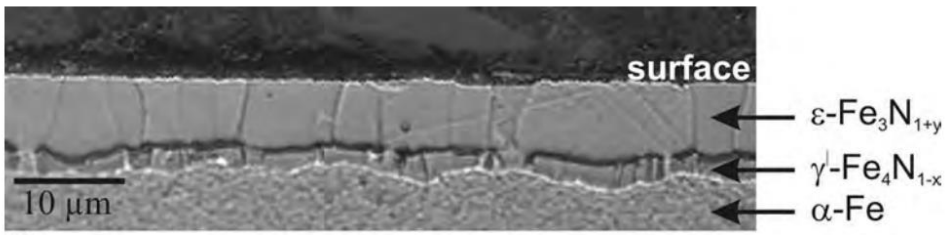

Figure 3 Cross section of nitrided pure iron with double layered compound layer [13]

For the purpose of nitriding of carbon steels, or nitrocarburizing, the iron-carbon-nitrogen phase diagram need to be studied. Figure 4 shows the Fe-C-N phase diagram plotted at 580 °C with (a) developed by Slycke et al. [14] and (b) developed with Thermo-Calc TCFE-9 database. By adding carbon, at certain carbon content, the ε-Fe_{2-3}(C,N) phase will form with the increase of nitrogen content before the γ'-Fe_4N phase. Besides, the γ'-Fe_4N phase can only exist at low carbon content region. This represents that the existence of carbon can stable the ε-Fe_{2-3}(C,N) phase [15].

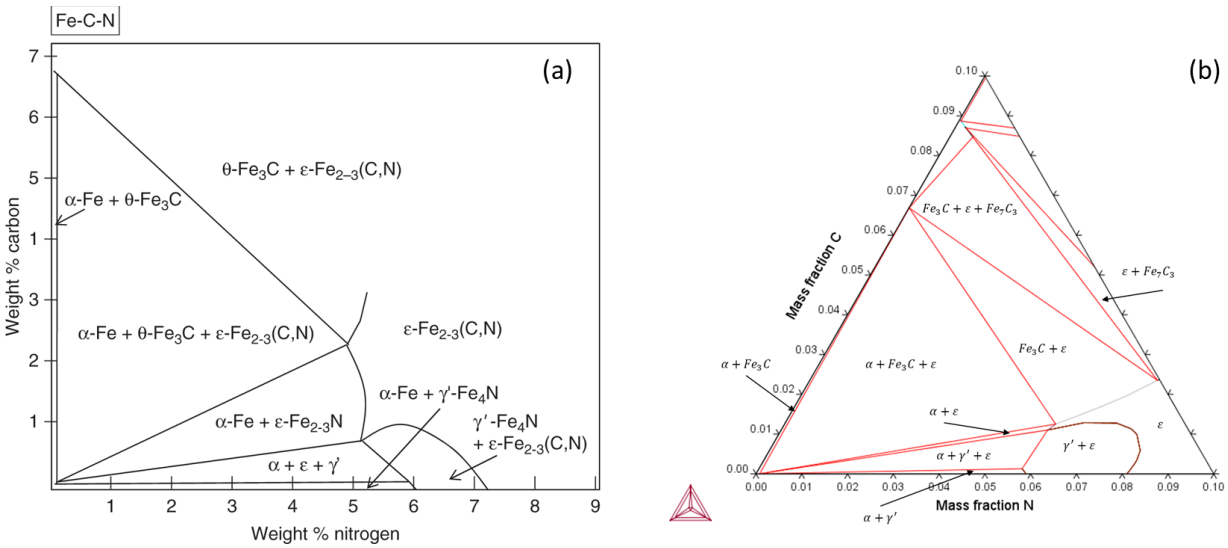

Figure 4 Fe-C-N ternary phase diagram at 580 °C (a) developed by Slycke et al. [14] and (b) developed with Thermo-Calc

Lehrer diagram and potential diagram

The Lehrer diagram, as shown in Figure 5, was firstly presented by Lehrer [16]. It shows the phase stability of iron-nitrogen system at different temperature and nitriding potential. For practical purpose, steels are usually nitrided instead of pure iron. Thus, the 'Lehrer diagram' for specific alloys (AISI 4140 alloy) were developed with computational thermodynamics method by Mei, Yang [17]. The diagram was developed by Themo-Calc software, and it turned out the alloy specific Lehrer diagram differs significantly from the pure iron one as shown in Figure 6.

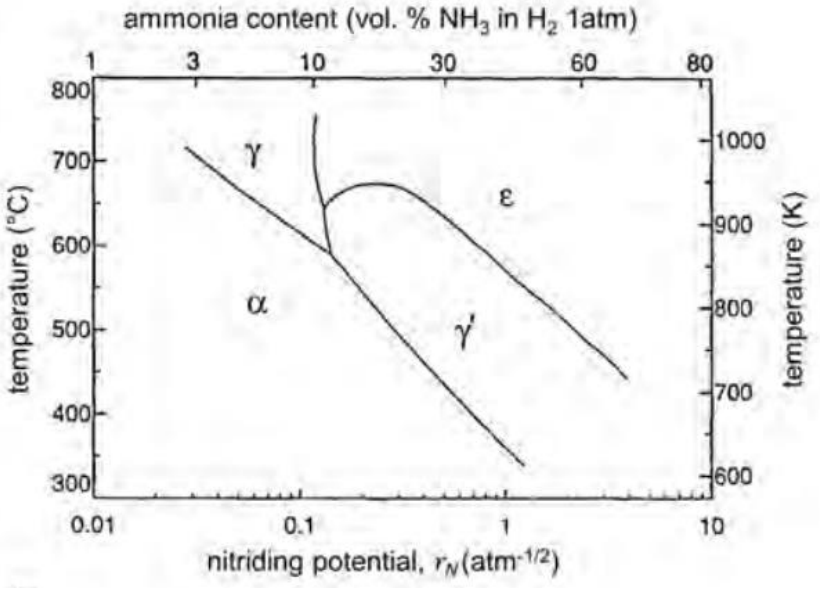

Figure 5 Lehrer diagram of iron-nitrogen system [16]

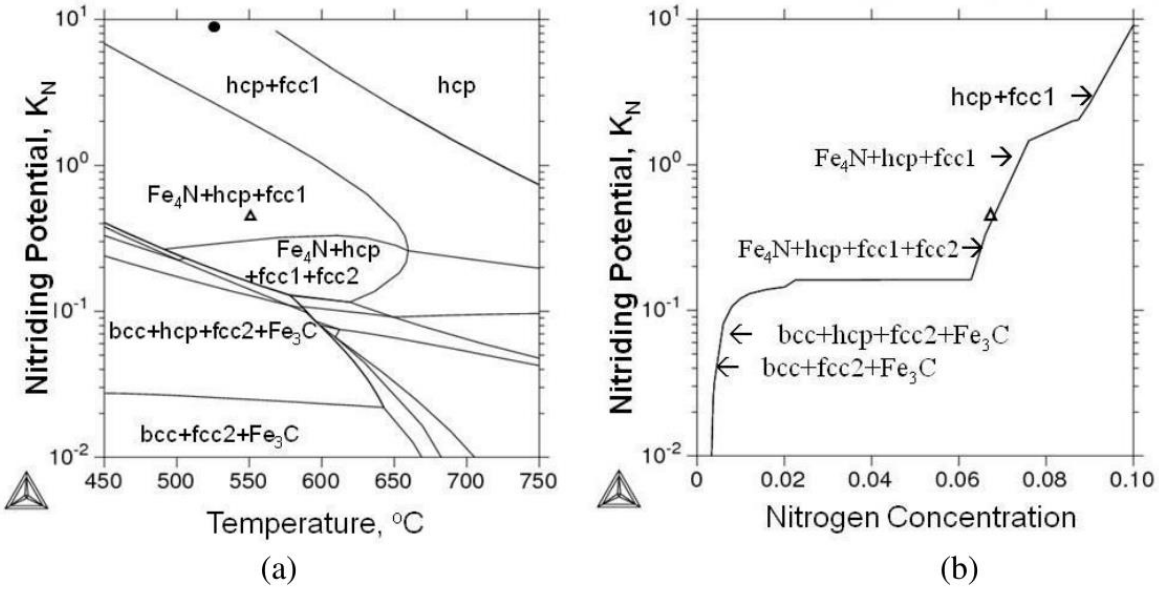

Figure 6 (a) Alloy specific Lehrer diagram for AISI 4140, and (b) nitriding potential evolution with nitrogen concentration plotted at 548 °C [17]

After Lehrer's investigation of iron-nitrogen system, lots of following up efforts have been carried out. Out of all these efforts, the influence of carbon to Fe-N system has been revealed. The Fe-N phase diagram at different carbon activity was plotted as shown in Figure 7 [18]. As we can see, with higher carbon activity, the ε phase region is much larger, which means ε phase is stabilized and carbon is favorable for the formation of ε phase at

the surface of nitrided pure iron. A ‘potential diagram’ which is able to show phase stability with nitriding potential versus carburizing potential was also plotted as shown in Figure 8.

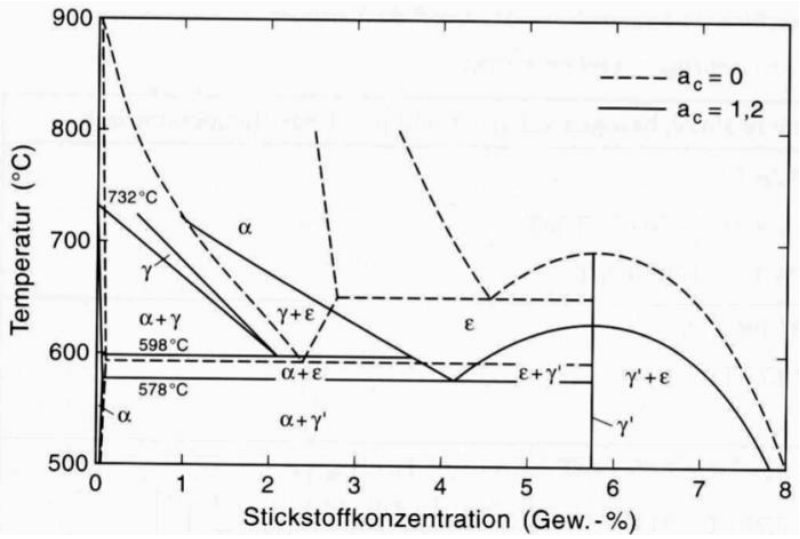

Figure 7 Pseudo binary phase diagram in Fe-C-N system with different carbon activity [18]

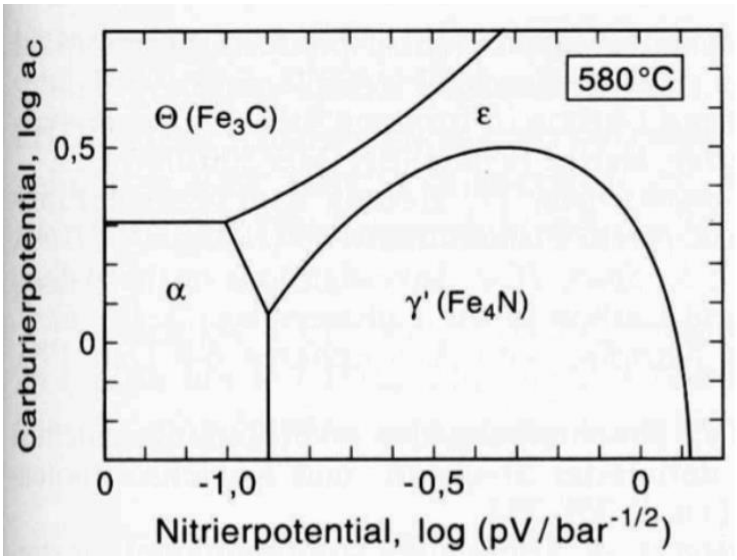

Figure 8 Nitriding potential vs. carburizing potential diagram for pure iron at 580 °C

Compound layer development

Microstructure evolution of the compound layer during nitriding and nitrocarburizing

During nitriding of pure iron, as mentioned above and exhibited in

Figure 3, a double layered (ε+γ') compound layer will form at the surface. This process, as investigated by several researchers [13, 19-21], can be illustrate as the following steps. At the beginning of the process, atomic nitrogen is introduced in the ferrite matrix after the gas solid reaction at the surface. With the nitrogen accumulation in the ferrite, the nitrogen content will exceed the solubility limit and the γ' phase will nucleate. Due to the nitrogen diffusion in the ferrite is much faster than it in the nitrides [22], the γ' nitrides will grow larger with the nitrogen supply from the adjacent ferrite matrix and form a closed layer after some time. then, if the applied nitriding potential is high enough, the ε nitrides will nucleate at the top of γ' nitrides layer and grow to a closed layer at the top surface.

For nitrocarburizing process of pure iron, the phase evolution in the compound layer will be more complicated due to the simultaneously diffusion of nitrogen and carbon. Limited papers have presented a systematic study of microstructure evolution during the nitrocarburizing process. Based on the observation of compound layer phase constitution of the samples processed for different durations, a diffusion path was determined in the Fe-C-N phase diagram as shown in Figure 10 [23]. With the diffusion path, the basic phase evolution during nitrocarburizing process can be summarized as the following steps. At the beginning of nitrocarburizing α-iron, since the carburizing reaction is always much faster than nitriding reactions [23], and the solubility of carbon is lower than nitrogen in ferrite, a single layer of cementite (θ) will form at the surface as shown in Figure 9 (a). The ε carbonitrides will form then at the interface between cementite and the substrate, and it will form a θ/ε double layer as shown in Figure 9 (b). Then the ε phase will grow towards both sides (grow further into substrate and the transform the cementite layer into carbonitrides) as shown in Figure 9 (c). The growth of ε carbonitrides phase will stop when there is only a single layer of ε phase as shown in Figure 9 (d). Then, the γ' nitrides will nucleate at the interface between ε phase layer and substrate (Figure 9 (e)) and the γ' phase will grow until there is a layer of γ' phase formed between the ε phase layer and the substrate as shown in Figure 9 (f).

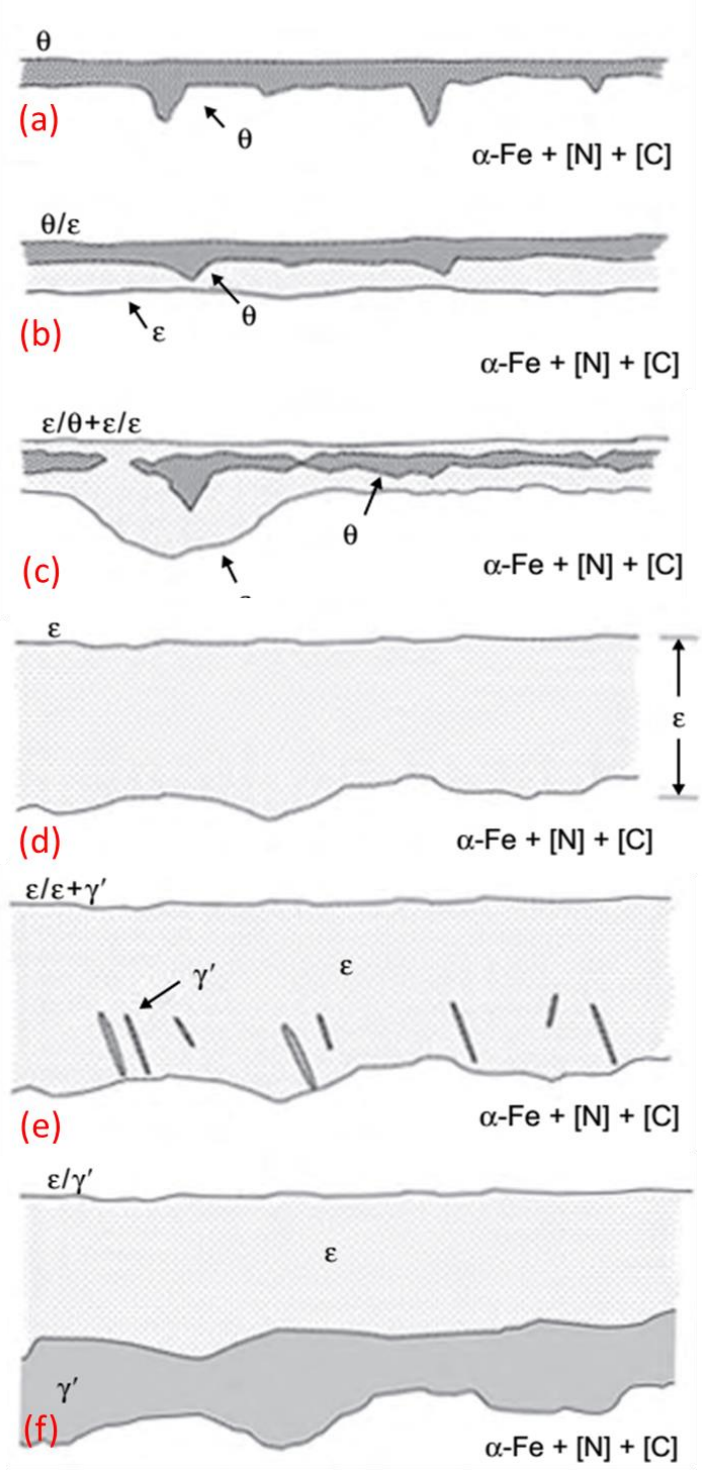

Figure 9 Microstructure development of nitrocarburizing of α-iron [23]

Alloy effects during compound layer development

As common nitrocarburized material, the compound layer microstructure evolution of steels is studied. Compared with pure iron, the occurrence of different alloy elements will influence the microstructure development of compound layer. Based on the interaction with nitrogen, the alloy elements in common steel are classified as 'strong group' (Ti, V, Cr), and 'weak group' (Al, Mo, Si) [24]. This classification is based on the thermodynamic calculation of Gibbs energy and precipitation misfit energy [6, 7, 25]. With strong interaction element, the alloy nitrides MN_x will form and precipitate rapidly as the nitrocarburizing process starts. As a consequence, the iron nitrides will not only form as a compound layer, but also form along the grain boundaries in the diffusion zone [25] as shown in Figure 11 (Fe-4at. % V specimen nitrided at 580 °C) . For the weak interaction alloy elements, the formation of alloy nitrides will be slow, and part of the alloy element will dissolve in the nucleated γ' nitrides, which results more nitrogen diffusing deeper and the γ' nitrides layer will be penetrating into the depth [8] as shown in Figure 12 (Fe-4.7 at. % Al specimen nitrided at 580 °C).

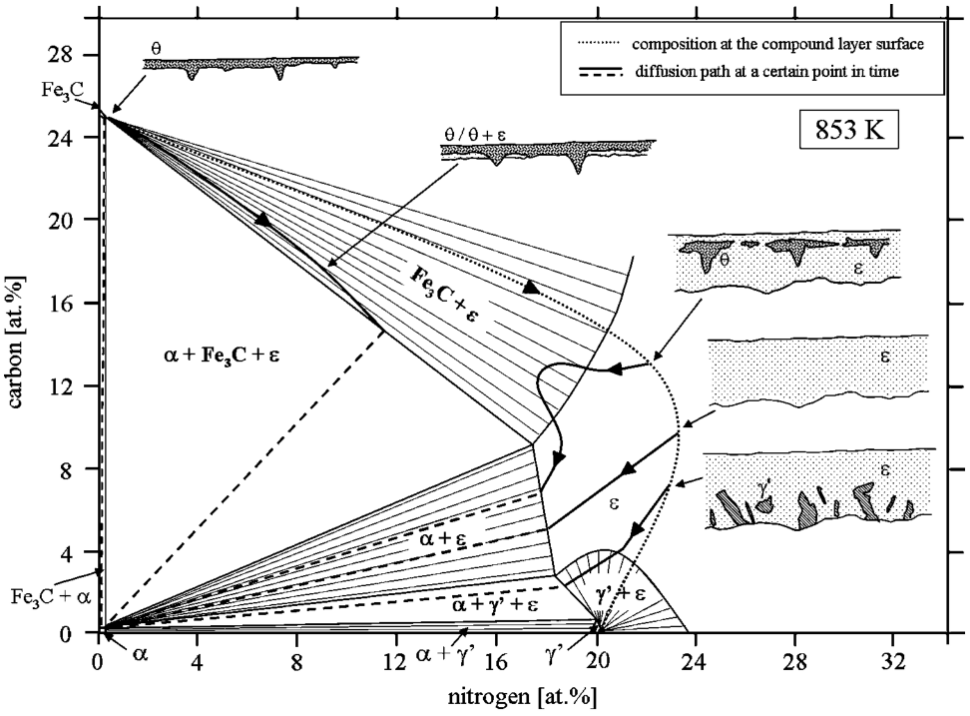

Figure 10 Diffusion path in the isothermal section of Fe-C-N phase diagram at 580 °C together with the microstructure evolution of the compound layer [23]

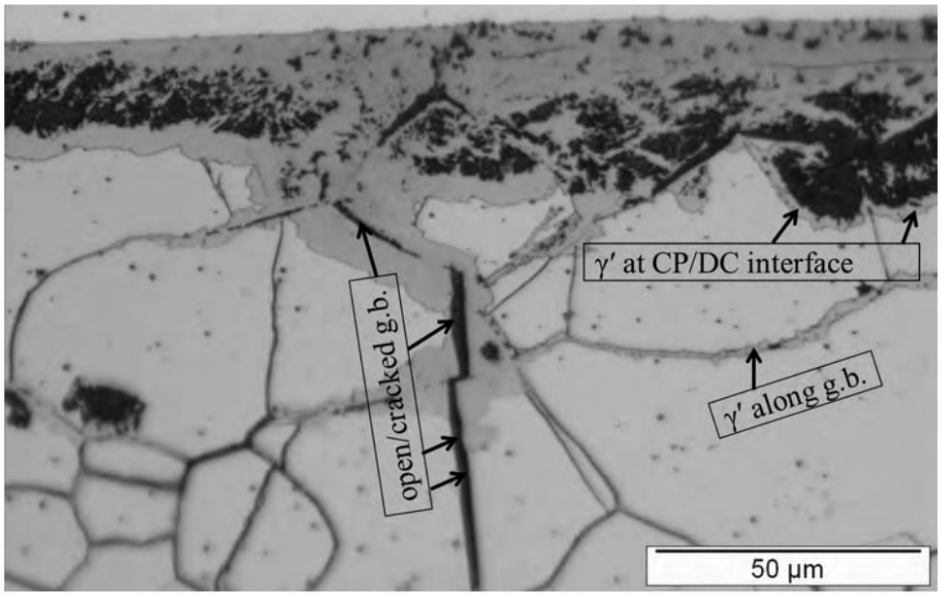

Figure 11 Cross section of Fe-4 at. %V specimen nitrided at 580 °C [25]

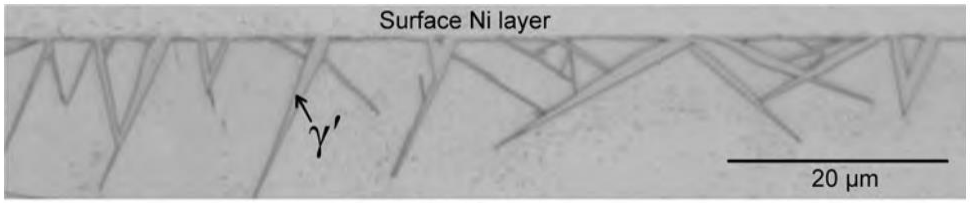

Figure 12 Cross section of Fe-4.7 at. % Al specimen nitrided at 580 °C [8]

State-of-art in modeling of nitriding and nitrocarburizing process

With more and more advances in understanding of diffusion, phase transformation, thermodynamics in Fe-C-N system, there are different models established for the gas nitriding and nitrocarburizing process. The formation of the compound layer is a result of atomic nitrogen and carbon diffusing into the steel matrix, reacting with the iron and alloy elements to form stable compounds, such as γ'-Fe_4N, ε-$Fe_{2-3}(C,N)$, and other alloy (carbon-)nitrides. Modeling the gas nitriding/nitrocarburizing process requires understanding the kinetics of diffusion and reaction, as well as the thermodynamics of the compound layer formation, which is typically controlled by the process parameters like temperature, gas composition (nitriding and carburizing potential), and process durations.

Double-layer diffusion model

During the nitriding and nitrocarburizing of pure iron process, the compound layer is typically composed of an ε layer and a γ' layer as shown in Figure 3. Mittemeijie and Somers established a model for compound layer growth kinetics based on the flux balance and local equilibrium at the surface and interface. The principle of the model is based on flux balance and local equilibrium at the ε/γ' and γ'/α interface as shown in Figure 13 [26].

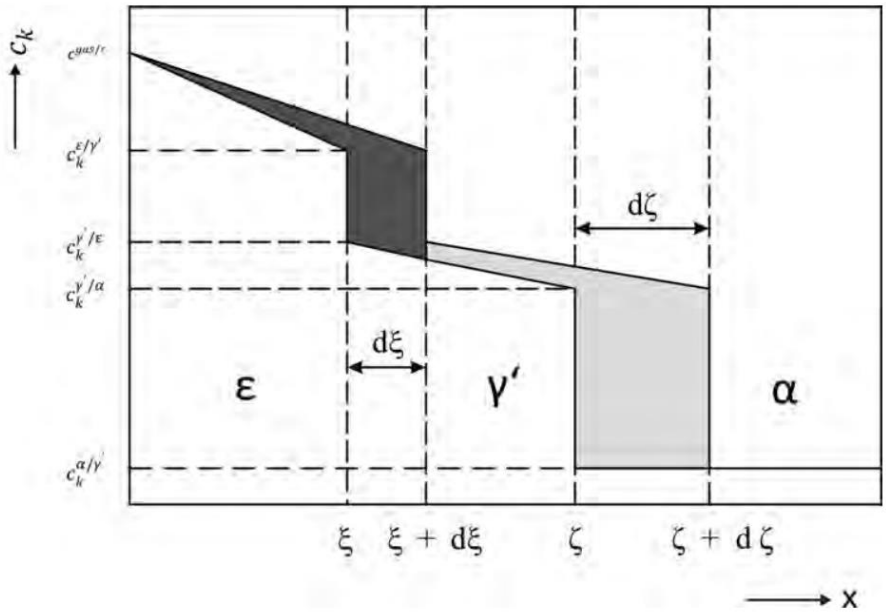

Figure 13 Schematic of concentration-depth profile in the double-layer diffusion model [26]

If we consider a β phase growing in phase α. There must be diffusion between two phases. We will have flux balance equation at the phase interface as [27] :

$$\frac{v^{\beta/\alpha}}{V^{\beta}}\left(u^{\beta/\alpha}-u^{\beta/\alpha}\right)=J^{\beta}-J^{\alpha}\ \ldots\ldots(1)$$

in which, $v^{\beta/\alpha}$ is migration rate of β/α phase interface, V^{β} is partial volume per mole of substitutional atom in β phase. $u^{\beta/\alpha}$ and $u^{\beta/\alpha}$ are the content of substitutional atom on the α and β side of the interface. Typically, we can assume local equilibrium is established at the interface of two phases, then the content value $u^{\beta/\alpha}$ and $u^{\beta/\alpha}$ can be obtained from the phase diagram directly and the flux can be calculated with Fick's first law. With $v\beta/\alpha V^{\beta}\left(u^{\beta/\alpha}-u^{\beta/\alpha}\right)=J^{\beta}-J^{\alpha}$ ... ...(1, the growth rate of the phase interface can be calculated.

The flux balance equation can be solved both in analytical method and in numerical method. If we consider the diffusivity as concentration-dependent, the equation can only be solved by numerical method [27].

In the case of nitrocarburizing of iron, we can have two flux balance equations for both C and N at ε/γ' interface and γ'/α interfaces as [27]:

at ε/γ' interface:

$$\frac{v^{\varepsilon/\gamma'}}{V^{\beta}}\left(u_k^{\varepsilon/\gamma'} - u_k^{\gamma'/\varepsilon}\right) = J_k^{\varepsilon} - J_k^{\gamma'} \ldots\ldots(2)$$

at γ'/α interface, we also have:

$$\frac{v^{\gamma'/\alpha}}{V^{\beta}}\left(u_k^{\gamma'/\alpha} - u_k^{\alpha/\gamma'}\right) = J_k^{\gamma'} - J_k^{\alpha} \ldots\ldots(3)$$

where k can be substituted by C and N. To calculate the carbon and nitrogen flux in different phases, we can simplify the C (or nitrogen) concentration profile in different phase as error function liked. For example, for carbon concentration in ε phase [27]:

$$u_C^{\varepsilon} = a_0 + a_1\, erf\left(\frac{x}{\sqrt{4Dt}}\right) \ldots\ldots(4)$$

In which the diffusivity D is customized based on the coupling of C and N, given by four components D_{CC}, D_{NN}, D_{CN}, and D_{NC}, referring the effective nitrogen/ carbon diffusivity influenced by local nitrogen and carbon concentration. These coefficients also including a_0 and a_1 can be calculated by DICTRA program [1]. With the concentration profile and customized diffusivity, the flux can be calculated with Fick's first law and then we can calculate the growth rate of the phase interface.

Compound layer growth model

However, in the case of nitriding and nitrocarburizing of steels, the situation is more complicated due to the high carbon content and existence of alloy elements. No clear interface can be observed between the ε and γ' phase layer. Based on the results of the current project, the two phases are mostly mixed with each other. Thus, Yang and Sisson established the compound layer growth model following Somer's model[17, 28, 29].

In the compound layer growth model, the whole compound layer was considered as a single layer with mixed nitrides. Firstly, the incubation time for compound layer formation was determined by comparing the numerically solved surface nitrogen content with the maximum nitrogen solubility in the steel. The growth of the compound layer was fitted with as function of process duration based on the experimental results. To establish the

nitrogen concentration-depth profile, Yang developed alloy specific Lehrer diagrams [30] and derived isopleth for specific alloys as shown in Figure 14, with which the local nitrogen content at the interface of compound layer could be determined. The nitrogen concentration in the diffusion zone was also modeled with experimentally fitted effective nitrogen diffusivity in the specific alloy [30].

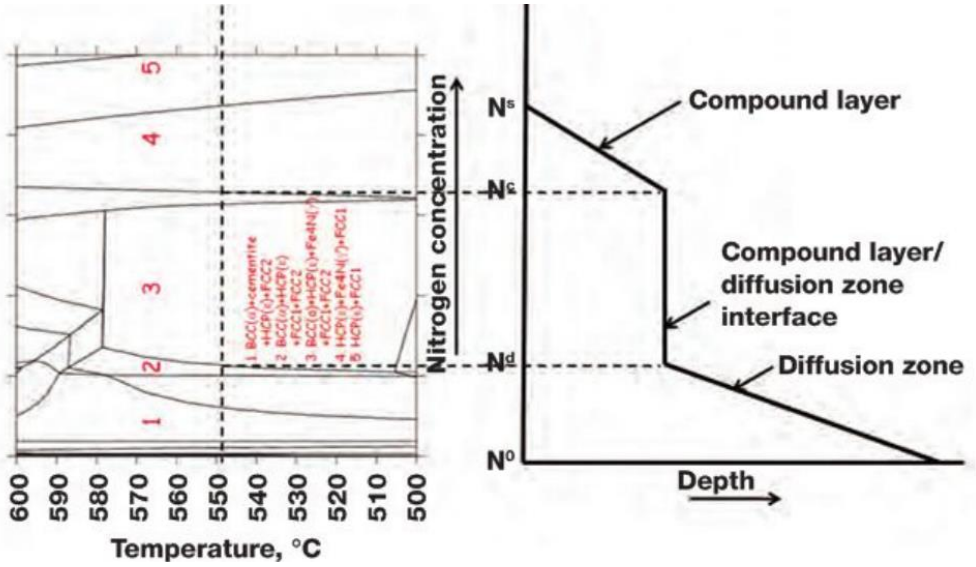

Figure 14 Relationship between the isopleth (left) and the interface nitrogen content in the compound layer growth model for nitrided AISI 4140 steel

Other models

Apart from the models above, there has been other ongoing efforts on modeling the gas nitriding and nitrocarburizing process. Tijani presented the application of phase field method to model steel nitriding [31]. This model uses a special parameter to describe nitriding layers on steel. The parameter is only non-zero on specific parts of the steel surface. A partial differential equation controls how this parameter changes over time. This method treats the entire steel surface at once. The interface is identified by the phase field parameter's value, which changes with time and space. The model includes equations for concentration and phase fields, which are solved using finite element method. This approach was used to simulate nitriding in low-carbon steel and the formation of compound layers. The numerical results match well with experimental data.

Other novel methods such as artificial neural network was also applied to predict the nitrocarburizing process. Malinova utilized the artificial neural network to predict the microhardness profile in the steel after the nitrocarburizing process [32]. The input data for the network includes the process parameters and the steel composition. The training data for the neural network were from published literature and authors experiments. The

microhardness profiles after nitrocarburizing were predicted with trained network and compared with the experimental measurement.

Overall, the nitriding and nitrocarburizing performance on pure iron has been thoroughly investigated and well understood. The compound layer growth and phase evolution can be predicted based on certain process parameters. Regarding nitriding and nitrocarburizing of steels, the thermodynamic data for Fe-C-N system is outdated and incomplete {Somers, 2013 #36}. The phase evolution of the compound layer and the compound layer growth kinetics still have many open questions. Besides, the effective diffusivity of nitrogen in different steels still requires to be investigated to establish a systematic computational model for gas nitriding and nitrocarburizing process.

Reference

1. Du, H., M.A. Somers, and J. Agren, *Microstructural and compositional evolution of compound layers during gaseous nitrocarburizing.* Metallurgical and Materials Transactions A, 2000. **31**(1): p. 195-211.
2. Pye, D., *Practical nitriding and ferritic nitrocarburizing*. 2003: ASM international.
3. Qiang, Y., S. Ge, and Q. Xue, *Study on the structure and wear resistance of two-step salt bath nitrocarburized steel.* Wear, 1998. **218**(2): p. 232-236.
4. Winter, K.-M., *Gaseous nitriding: in theory and in real life.* Technical Paper of United Process Controls, Process-Electronic GmbH, Heiningen, Germany, 2009.
5. Mittemeijer, E.J. and M.A. Somers, *Thermochemical surface engineering of steels*. 2014: Woodhead Publishing Cambridge.
6. Hosmani, S.S., R.E. Schacherl, and E.J. Mittemeijer, *Microstructure of the "white layer" formed on nitrided Fe-7 wt.% Cr alloys.* International journal of materials research, 2006. **97**(11): p. 1545-1549.
7. Hosmani, S.S., R.E. Schacherl, and E.J. Mittemeijer, *Morphology and constitution of the compound layer formed on nitrided Fe–4wt.% V alloy.* Journal of materials science, 2009. **44**(2): p. 520-527.
8. Meka, S.R., et al., *Unusual nucleation and growth of γ' iron nitride upon nitriding Fe–4.75 at.% Al alloy.* Philosophical Magazine, 2012. **92**(9): p. 1083-1105.
9. Mirjani, M., A. Shafyei, and F. Ashrafizadeh, *Plasma and gaseous nitrocarburizing of C60W steel for tribological applications.* Vacuum, 2009. **83**(7): p. 1043-1048.
10. Spies, H., et al., *Active screen plasma nitriding and nitrocarburizing of steels: An overview.* Int. Heat Treat. Surf. Eng, 2014. **8**: p. 94-106.
11. Somers, M., P. Colijn, and E. Mittemeijer, *MICROSTRUCTURAL AND COMPOSITIONAL EVOLUTION OF IRON-CARBONITRIDE COMPOUND*

LAYERS DURING SALT BATH NITROCARBURIZING. INTERNAL AND EXTERNAL NITRIDING AND NITROCARBURIZING OF IRON AND IRON-BASED ALLOYS, 1990: p. 237.
12. Massalski, T., *Phase diagrams in materials science.* Metallurgical Transactions A, 1989. **20**(8): p. 1295-1323.
13. Somers, M. and E. Mittemeijer, *Verbindungsschichtbildung während des Gasnitrierens und des Gasund Salzbadnitrocarburierens.* HTM Journal of Heat Treatment and Materials, 1992. **47**(1): p. 5-13.
14. Slycke, J., L. Sproge, and J. Agren, *Nitrocarburizing and the Ternary Fe--N--C Phase Diagram.* Scand. J. Metall., 1988. **17**(3): p. 122-126.
15. Göhring, H., et al., *Thermodynamics of the Fe-N and Fe-NC systems: The Fe-N and Fe-NC phase diagrams revisited.* Metallurgical and Materials Transactions A, 2016. **47**(12): p. 6173-6186.
16. Lehrer, E., *Über das Eisen-Wasserstoff-Ammoniak-Gleichgewicht.* Zeitschrift für Elektrochemie und angewandte physikalische Chemie, 1930. **36**(6): p. 383-392.
17. Yang, M., et al., *Simulation of the ferritic nitriding process.* International Heat Treatment and Surface Engineering, 2011. **5**(3): p. 122-126.
18. Kunze, J., *Thermodynamische Gleichgewichte im System Eisen-Stickstoff-Kohlenstoff.* HTM Journal of Heat Treatment and Materials, 1996. **51**(6): p. 348-354.
19. Winter, K.-M. *Gaseous nitriding: in theory and in real life*. in *Proc. 25th Conf., IN, Sept*. 2009.
20. Mittemeijer, E.J. and M.A. Somers, *Thermodynamics, kinetics, and process control of nitriding.* Surface Engineering, 1997. **13**(6): p. 483-497.
21. Hosmani, S., R. Schacherl, and E. Mittemeijer, *Compound layer formation on iron-based alloys upon nitriding; phase constitution and pore formation.* HTM Journal of Heat Treatment and Materials, 2008. **63**(3): p. 139-146.
22. Somers, M., et al., *Dependence of the lattice parameter of γ' iron nitride, Fe4N1− x, on nitrogen content; Accuracy of the nitrogen absorption datairon nitride, Fe4N1− x, on nitrogen content; Accuracy of the nitrogen absorption data.* Metallurgical Transactions A, 1989. **20**(8): p. 1533-1539.
23. Woehrle, T., A. Leineweber, and E. Mittemeijer, *Microstructural and phase evolution of compound layers growing on α–iron during gaseous nitrocarburizing.* Metallurgical and Materials Transactions A, 2012. **43**(7): p. 2401-2413.
24. Somers, M., R. Lankreijer, and E. Mittemeijer, *Excess nitrogen in the ferrite matrix of nitrided binary iron-based alloys.* Philosophical Magazine A, 1989. **59**(2): p. 353-378.
25. Meka, S.R. and E.J. Mittemeijer, *Abnormal nitride morphologies upon nitriding iron-based substrates.* JOM, 2013. **65**(6): p. 769-775.

26. Dossett, J. and G. Totten, *Fundamentals of nitriding and nitrocarburizing.* ASM Handbook: Steel Heat Treating Fundamentals and Processes; ASM International: Materials Park, OH, USA, 2013: p. 619.
27. Du, H. and J. Ågren. *Kinetics of Compound-Layer Growth during Nitrocarburizing*. in *Materials science forum*. 1992. Trans Tech Publ.
28. Yang, M. and R. Sisson Jr, *Modeling the nitriding process of steels.* Advanced Materials & Processes, 2012. **170**(7): p. 33-37.
29. Yang, M., *Nitriding--Fundamentals, Modeling and Process Optimization*. 2012, Worcester Polytechnic Institute Massachusetts.
30. Yang, M. and R. Sisson, *Gaseous nitriding process control: application of customised lehrer diagrams.* International Heat Treatment and Surface Engineering, 2013. **7**(4): p. 164-171.
31. Tijani, Y.A., *Modeling and Simulation of Thermochemical Heat Treatment Processes: A Phase Field Calculation of Nitriding in Steel*. 2008, Universität Bremen.
32. Malinova, T., S. Malinov, and N. Pantev, *Simulation of microhardness profiles for nitrocarburized surface layers by artificial neural network.* Surface and Coatings Technology, 2001. **135**(2-3): p. 258-267.

Chapter 3: Nitriding and ferritic nitrocarburizing of low alloy steels

Haoxing You, Richard D. Sisson Jr.
Center for Heat Treating Excellence (CHTE)
Worcester Polytechnic Institute; 100 Institute Rd; Worcester, MA 01609, USA

Abstract

As an important thermochemical surface treatment, ferritic nitrocarburizing has been widely utilized in steel industry to improve the wear and corrosion resistance, as well as fatigue endurance of steel parts. In the current project, nitrocarburizing trials with different carburizing potentials and durations were conducted for AISI 4140, AISI 1018, and ductile cast iron (ASTM A536 80-55-06). The compound layer morphology was observed with optical and scanning electron microscopy and compared for different alloys. The compound layer growth kinetics was compared for different alloys and different carburizing potentials. The phase constitution in the compound layer was analyzed with X-ray diffraction. The phase evolution of the compound layer was analyzed, and the diffusion path was discussed. The microhardness profile and C & N concentration profiles in the diffusion zone were measured and compared for the samples of different materials and various process conditions.

Introduction

Nitriding and ferritic nitrocarburizing are key surface thermochemical treatments in industry, aimed at enhancing the wear, corrosion resistance, and fatigue life of steel. During these processes, atomic nitrogen and carbon are introduced into the steel surface, resulting in a compound layer and a diffusion zone underneath. The compound layer, typically composed of γ'-Fe_4N and ε-$Fe_{2-3}(C,N)$, significantly enhances wear and corrosion resistance, while the diffusion zone, with alloy (carbon-)nitrides disperse, improve fatigue endurance[1-3].

There are several methods to introduce nitrogen and carbon into steels, including gaseous, salt bath, and plasma processes. The gaseous method is mostly utilized in industry for its controllability by controlling gas composition and flow rate. Adolph Machlet of the American Gas Company firstly developed gaseous nitriding method in the early 20th

century [4]. For the purpose of gaseous nitriding process control, thorough investigations have been carried out to study the influence of different process parameters and different models have been established to predict the process results [5-13]. Compared to nitriding, nitrocarburizing (which introduces carbon together with nitrogen) typically requires shorter processing times to produce the desired nitrided case [14]. The main parameters influencing the gaseous nitrocarburizing process are temperature, nitriding potential, carburizing potential, and duration. Besides nitrogen source gas, carbon dioxide, carbon monoxide, endo gas, or hydrocarbons (e.g., methane or propane) are typically applied as carbon sources[3].

Challenges in modeling gaseous nitrocarburizing include accurately measuring and controlling the carburizing potentials due to the complex carburizing reactions [15]. Additionally, there's a need to understand the thermodynamics and kinetics of nitrocarburizing in alloy steels, since most up to date research focuses on pure irons [1, 16-19]. Industry often relies on trial-and-error method to determine process parameters for nitrocarburizing of alloy steels.

In the present work, nitrocarburizing trials with various carburizing potentials and process durations were carried out for different material samples. The compound layer morphology and phase constitution on these samples were characterized and compared. The microhardness profile and N & C concentration profiles in the diffusion zone were measured and compared.

Experiments

AISI 4140, AISI 1018, and cast iron (ASTM A536 80-55-06) were selected for nitrocarburizing trials. All the nitrocarburizing trials were conducted at the same process temperature 579 ℃ and the same nitriding potential 4 $atm^{-1/2}$. Three different carburizing potentials were applied for each material, and for each carburizing potential, there were four different process durations selected. All samples were pre-oxidized in air at 360 ℃ for 1 hour and post-oxidized in air at 496 ℃ for 1 hour. The detailed process parameters for each trial are presented in *Table 1*.

Table 1 Experimental plan for the 1st FNC trial

Material	Ferritic Nitrocarburizing			
	Nitriding potential ($atm^{-1/2}$)	**Temperature (°C)**	**Carburizing potential**	**Time (hrs)**
AISI 4140 **AISI 1018** **Cast iron (ASTM A536 80-55-06)**	4	579 °C	0	1
				2
				4
				8
			9	1
				2
				4
				8
			12	1
				2
				4
				8
The pre-oxidation is performed at 680°F, 60 minutes with 90-100 CFH of air. The post-oxidation is performed at 925°F, 60 minutes with 90-100 CFH of air.				

The materials were heat treated at Bodycote before the FNC trials, the AISI 4140 steel rods were quenched and tempered at 565 °C for 2 hours, AISI 1018 steel rods were annealed, the cast iron samples were normalized. After pre-FNC heat treatment, AISI 4140 and AISI 1018 steel rods were machined into disks with 1.2" diameter and 0.5" thickness. The cast iron samples were 0.75" in square with 0.3" thickness since there were cut off from parts with complex shape as shown in *Figure 15*. A unique sample ID was engraved on each sample. Following machining and engraving, the samples were ultrasonically cleaned with ethanol. After cleaning, the weight of each individual sample was recorded to obtain the weight gain after the FNC trials.

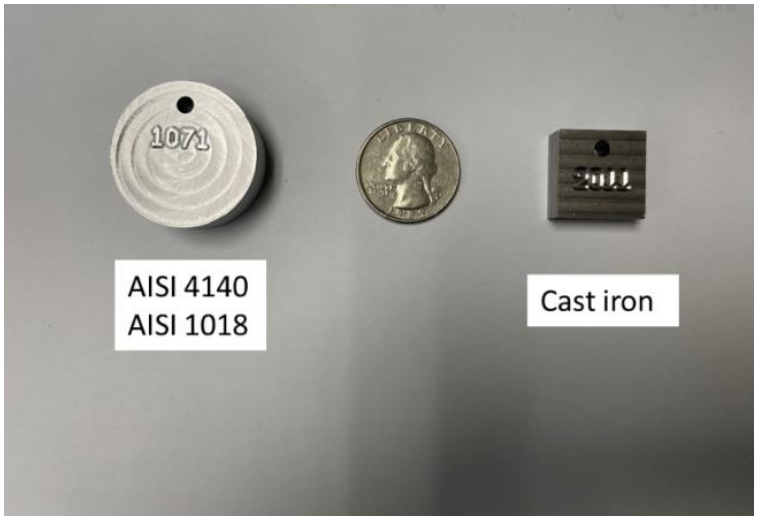

Figure 15 Machined sample disks of different materials

The chemical composition of AISI 1018, AISI 4140, and cast iron (ASTM A536 80-55-06) were measured with OES and compared with specification as shown in

Table 2.

Table 2 Chemical composition measurement with OES

AISI 1018								
	C	Mn	S	P	Fe			
OES measurement (wt. %)	0.18	0.84	0.006	0.0045	Balance			
Specification (wt. %)	0.15-0.20	0.6-0.9	<0.05	<0.04	Balance			
AISI 4140								
	C	Cr	Mn	Si	Mo	S	P	Fe
OES measurement (wt. %)	0.405	0.9	0.88	0.28	0.16	0.007	0.01	Balance
Specification (wt. %)	0.38-0.43	0.80-1.10	0.75-1.0	0.15-0.30	0.15-0.25	<0.04	<0.035	Balance
Cast iron (ASTM A536 80-55-06)								
	C	Si	Mn	Cr	Ni	Cu	Mg	Fe
OES measurement (wt. %)	5.16	4.37	0.15	0.054	0.32	0.52	0.04	Balance
Specification (wt. %)	3.4-3.8	2.35-2.75	<0.4	<0.08	<0.5	<0.6	0.025-0.055	Balance

The Rockwell hardness of pre-FNC heat treated samples were measured and shown in Table 3. The microhardness line scan results of these samples were also shown in Figure 16.

Table 3 Rockwell hardness of pre-FNC heat treated materials

	AISI 4140	**AISI 1018**	**Cast iron**
Mean	36.2 HRC	70.1 HRB	15.1 HRC
STDV	0.42	0.91	0.27

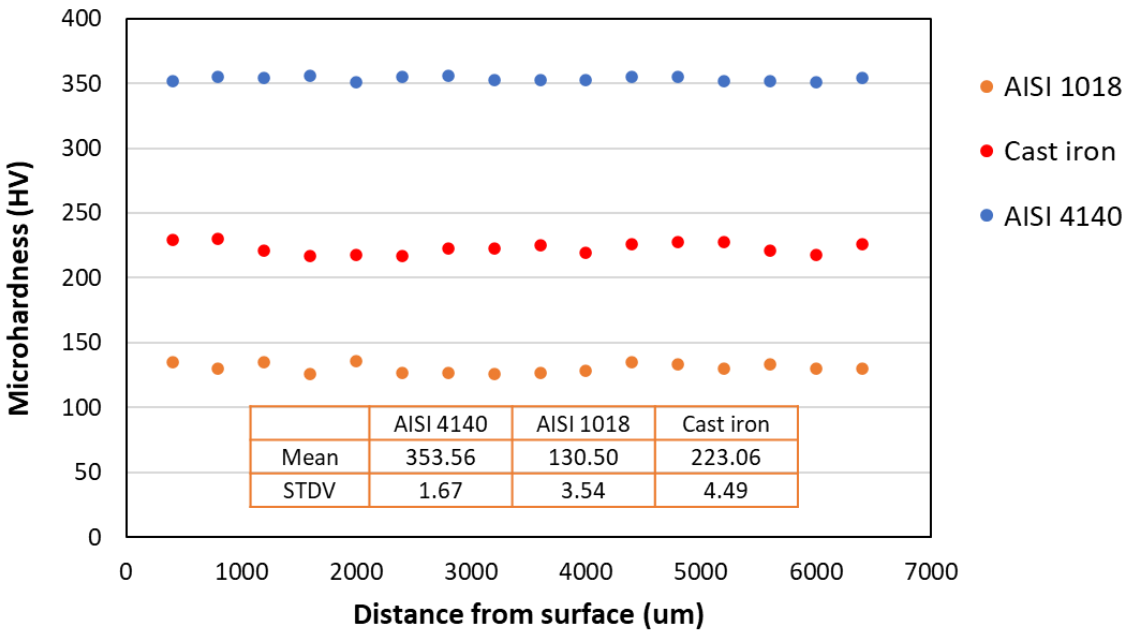

Figure 16 Microhardness line scan of pre-FNC heat treated materials

The microstructure of each material was characterized after the pre-FNC heat treatment as shown in *Figure 17*. AISI 4140 has tempered martensite after quenching and tempering, AISI 1018 has mix of ferrite and pearlite after annealing, and the cast iron sample has graphite nodules in ferrite matrix.

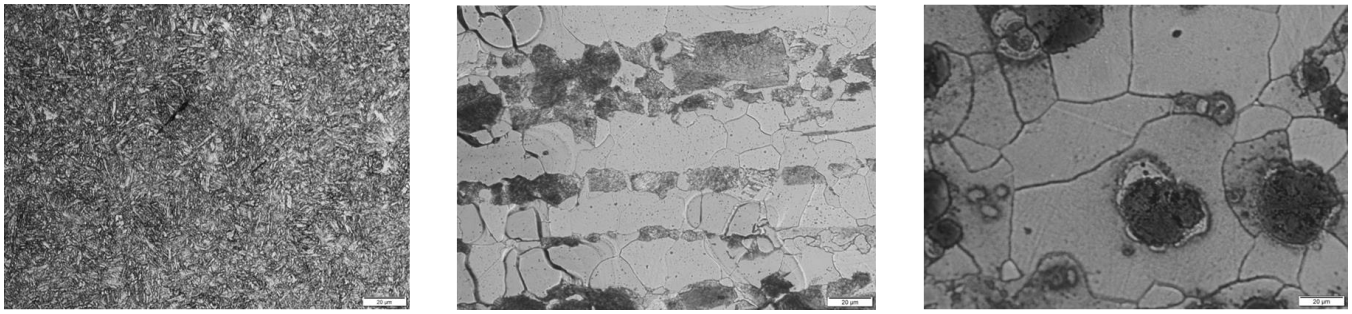

Figure 17 Microstructure after pre-FNC heat treatment (left: AISI 4140, middle: AISI 1018, right: cast iron)

After FNC trials, the samples from each different trial group were characterized. The total weight gain and average flux was measured by recording the weight of each sample before and after the FNC process. Morphology of the compound layer was observed with Nikon EPIPHOT optical microscopy, JEOL JSM-7000F SEM, and EDS. The compound layer phase constitution was analyzed with PANalytical x-ray diffractometer using Cr-Kα radiation at 30 kV voltage and 55 mA current. The microhardness profiles in the diffusion

zone were measured with Wilson VH 3300 Hardness Tester with 0.5 kgf. The nitrogen and carbon concentration profiles were measured with SPECTROLSB arc spark OES.

Results and Discussion

Weight gain and average flux measurement

The weight of each individual sample was recorded before and after the FNC process to obtain the total weight gain during the process. The average flux was calculated for each trial group with different carburizing potentials and process durations. The total weight gain and average flux for AISI 4140 and AISI 1018 samples with various carburizing potentials and different process durations (average value of 5 samples in each trial group) are summarized in *Table 4*.

Table 4 Total weight gain and average flux data comparison for AISI 4140 and AISI 1018 samples

KC	Trial ID	Toal weight gain (g)		Average flux (g/m^2*hr)	
		AISI 4140	AISI 1018	AISI 4140	AISI 1018
KC=0	Trial 1 (t=1)	0.0192	0.0150	7.1642	5.6119
	Trial 2 (t=2)	0.0300	0.0221	5.6007	4.1231
	Trial 3 (t=4)	0.0574	0.0412	5.3507	3.8470
	Trial 4 (t=8)	0.0793	0.0573	3.6978	2.6707
KC=9	Trial 6 (t=1)	0.0168	0.0184	6.2761	6.8657
	Trial 7 (t=2)	0.0398	0.0288	7.4216	5.3657
	Trial 8 (t=4)	0.0629	0.0517	5.8657	4.8246
	Trial 9 (t=8)	0.0831	0.0633	3.8741	2.9506
KC=12	Trial 11 (t=1)	0.0293	0.0287	10.9179	10.6940

	Trial 12 (t=2)	0.0446	0.0390	8.3284	7.2687
	Trial 13 (t=4)	0.0658	0.0519	6.1343	4.8414
	Trial 14 (t=8)	0.0792	0.0854	3.6931	3.9832

Figure 18 shows the total weight gain of the samples with various carburizing potentials. Typically, for both AISI 4140 and AISI 1018 samples, higher carburizing potential resulted in higher weight gain for the samples processed with the same durations.

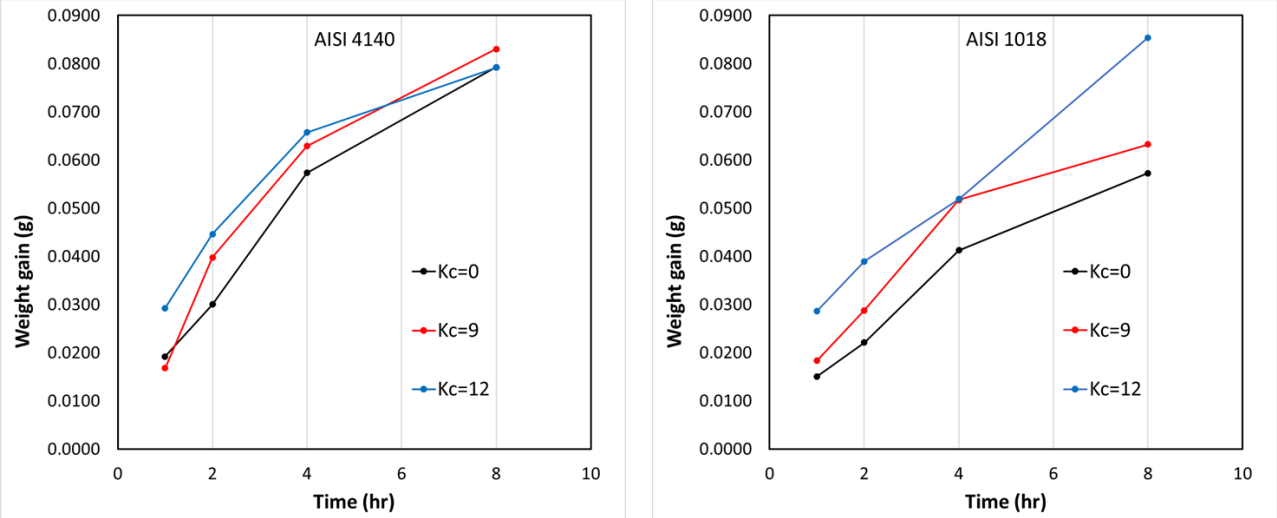

Figure 18 Total weight gain for the samples with various carburizing potentials after different process durations

The average flux during the FNC process was calculated as:

$$J = \frac{\Delta m}{A \times t} \quad (1)$$

In which,

J is the average flux during the process (g/m^2*hr),

Δm is the total weight gain during the process (g),

A is the surface area of the sample (m^2),

t is the process duration (hour)

The calculated average flux for both AISI 4140 and AISI 1018 samples with various carburizing potentials after different process durations are plotted in *Figure 19*. Basically, with higher carburizing potential, the average flux is higher for both AISI 4140 and AISI 1018 samples. The average flux difference due to the different carburizing potentials became smaller with longer process duration. Also, after the same process duration, AISI 4140 sample usually has higher weight gain and average flux than AISI 1018 sample, which should be contributed by higher alloy contents in AISI 4140 sample.

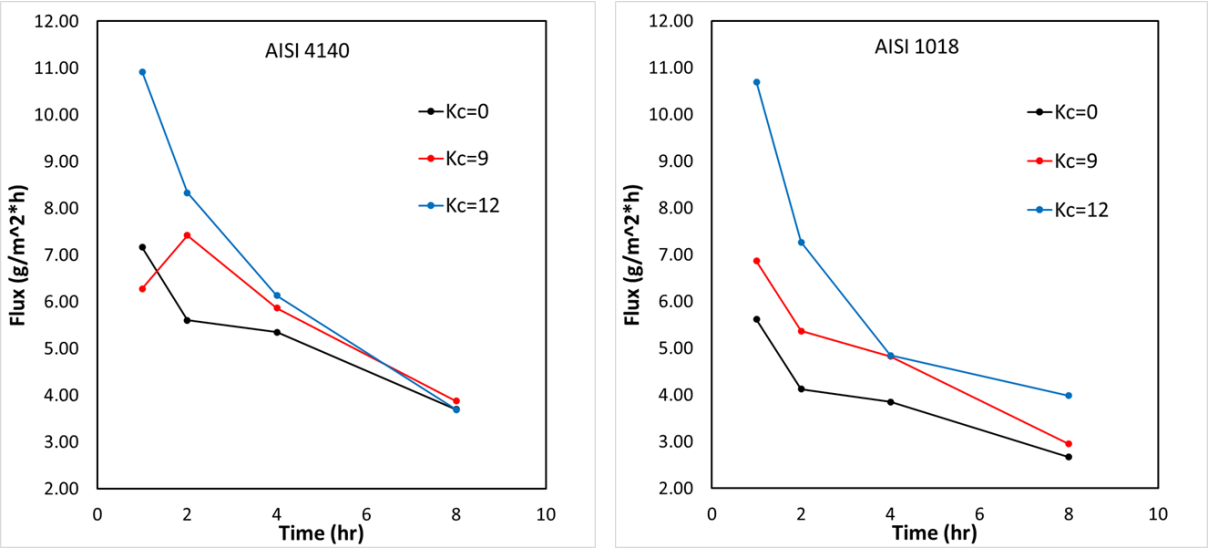

Figure 19 Average flux for the samples with various carburizing potentials after different process durations

Compound layer growth and phase constitution

After FNC trials, the compound layer was formed on both AISI 4140 and AISI 1018 samples. The morphology of the compound layer was observed with optical and scanning electron microscopy. The phase constitution of the compound layer was analyzed with X-ray diffraction and Rietveld refinement.

Figure 20 shows the compound layer formed on AISI 4140 samples processed with highest carburizing potential (Kc=12) for different durations (from left to right: 1 hour to 8 hours). *Figure 21* shows the compound layer formed on AISI 1018 samples processed with medium carburizing potential (Kc=9) for different durations. For all cast iron (ASTM A536 80-55-06) samples, there was no compound layer formed after FNC trials, only a thin oxide layer was observed on the surface. *Figure 22* shows the near surface microstructure of the cast iron samples processed with Kc=12 for different process durations (left to right: 1 hour to 8

hours). As shown in micrographs, the typical compound layer on AISI 4140 samples and AISI 1018 samples is composed of an oxide layer at the top, a porous layer, and a dense layer. With increased process duration, the compound layer is getting thicker. The micrographs of all other trial group samples could be found in Appendix 1: Compound layer morphology of FNC samples.

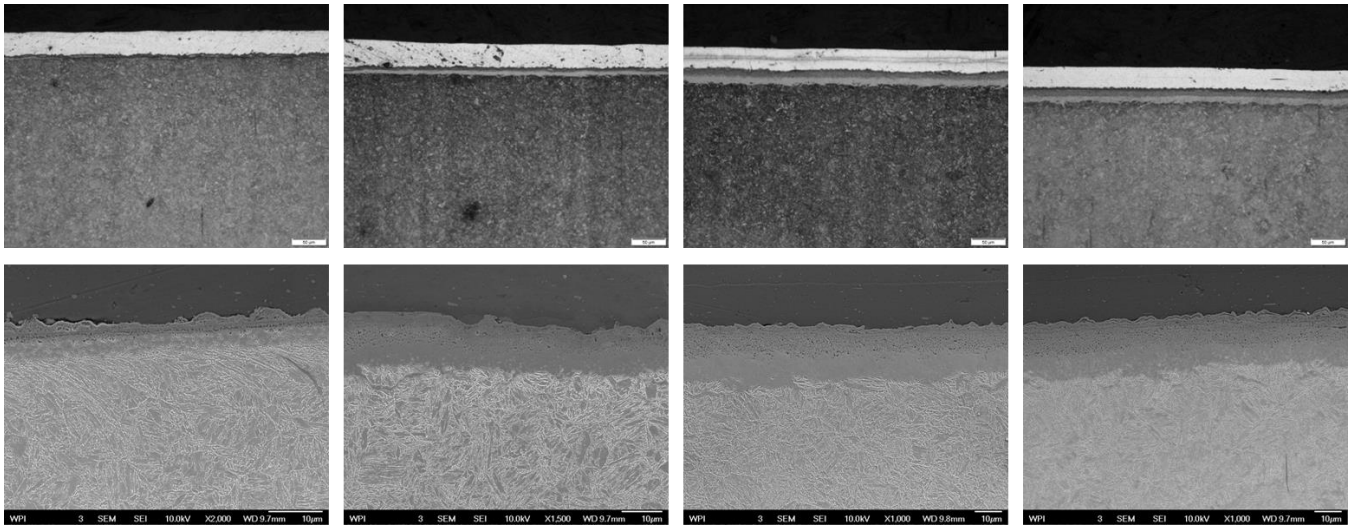

Figure 20 Compound layer of AISI 4140 samples processed with Kc=12 for different process durations (left to right: 1 hour, 2 hours, 4 hours, 8 hours)

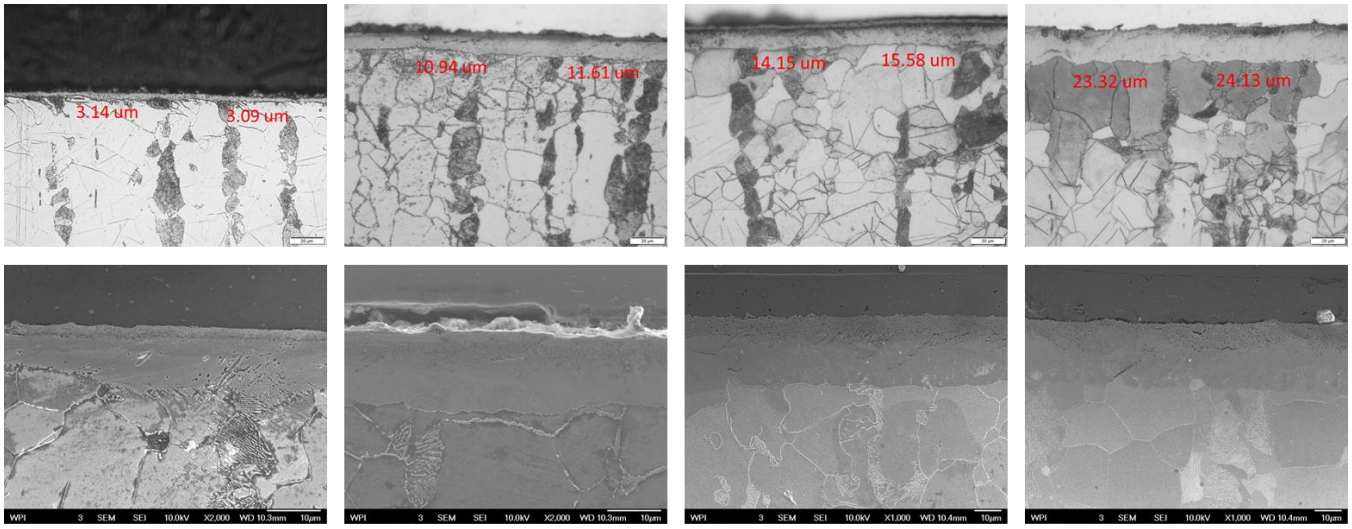

Figure 21 Compound layer of AISI 1018 samples processed with Kc=9 for different process durations (left to right: 1 hour, 2 hours, 4 hours, 8 hours)

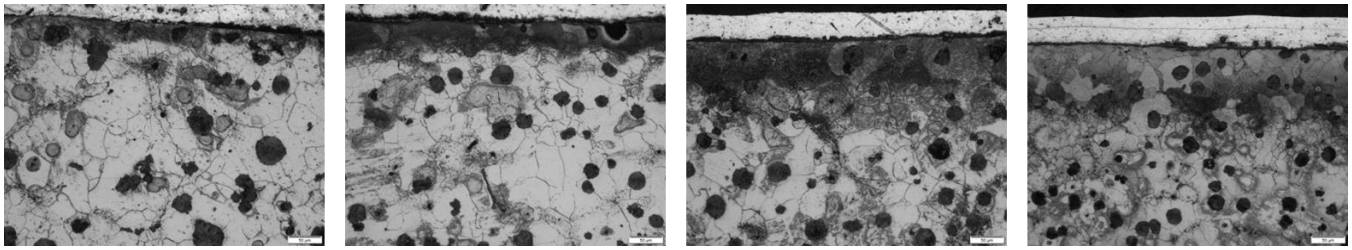

Figure 22 Near surface microstructure of cast iron samples processed with Kc=12 for different durations (left to right: 1 hour, 2 hours, 4 hours, 8 hours)

The average compound layer thickness for each trial group (with different carburizing potential and process duration) was measured from the micrographs. The data was summarized and compared in *Table 5* for both AISI 4140 and AISI 1018 samples.

Table 5 Average compound layer thickness of AISI 4140 and AISI 1018 samples from different trial groups

Process time (hr)	**Compound layer thickness (um)**					
	Kc=0		**Kc=9**		**Kc=12**	
	AISI 4140	AISI 1018	AISI 4140	AISI 1018	AISI 4140	AISI 1018
1	4.14	3.11	4.07	3.12	6.19	10.16
2	11.11	5.66	10.93	11.28	11.69	16.83
4	16.86	20.51	20.41	14.87	20.47	23.39
8	23.85	24.26	24.18	23.63	23.93	24.47

The phase constitution of the compound layer was analyzed by applying X-ray diffraction on the original sample surface after FNC trials. The penetration depth of XRD is approximately 10 μm, thus, the XRD pattern and refinement results provided the phase constitution information for around 10 μm depth from the surface. *Figure 23* and *Figure 24* shows the XRD pattern and refinement results of AISI 4140 and AISI 1018 samples respectively. For both AISI 4140 and AISI 1018 samples, the compound layer was identified as ε – $Fe_{2-3}(C,N)$ and γ' – Fe_4N nitrides, the oxide layer was identified as Fe_3O_4. For the cast iron samples, the oxide layer was also identified on the surface, and a small amount of iron nitrides was identified in the near surface region.

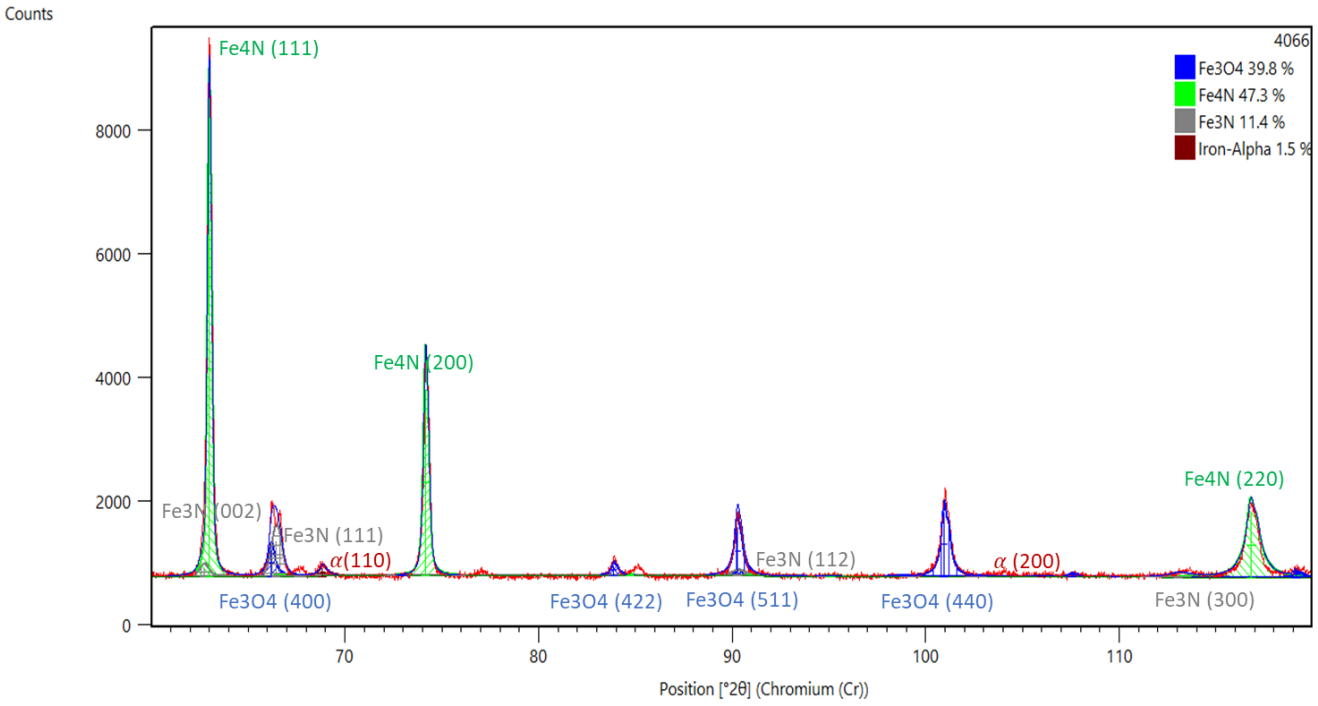

Figure 23 XRD pattern and refinement results of AISI 4140 samples processed with Kc=12 for 8 hours

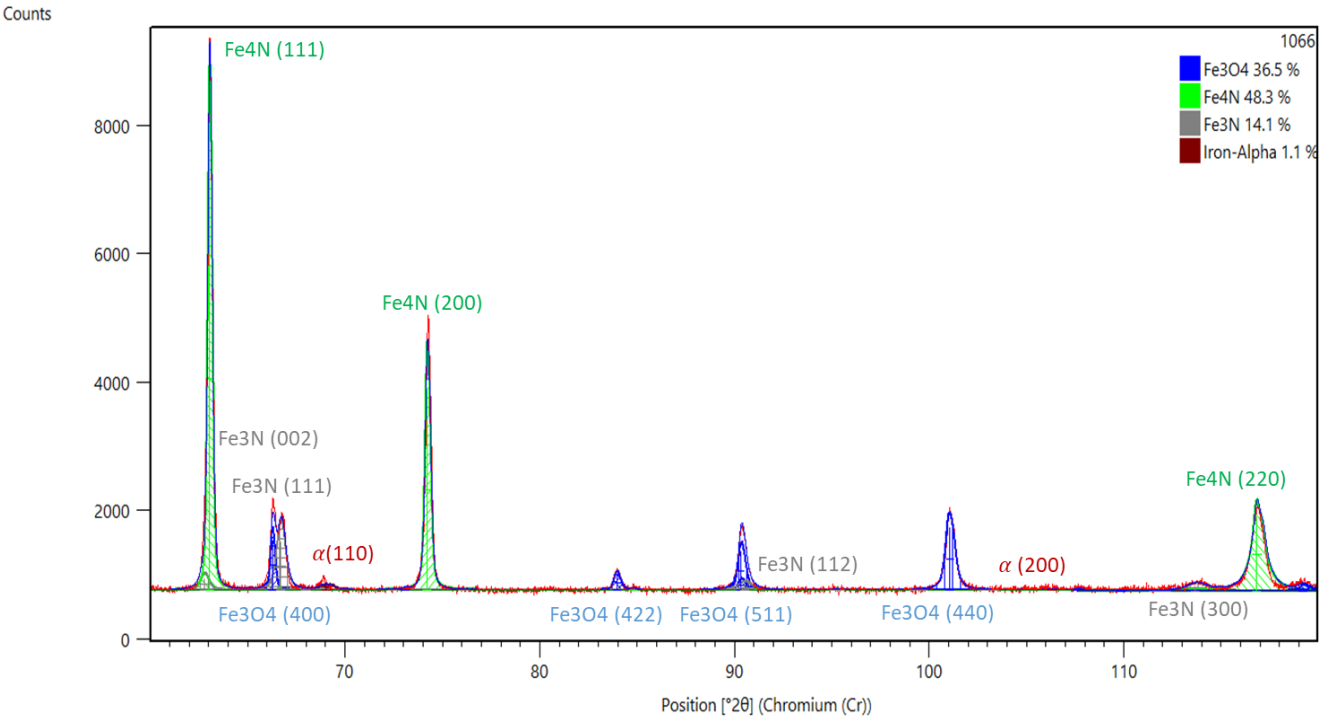

Figure 24 XRD pattern and refinement results of AISI 1018 samples processed with Kc=12 for 8 hours

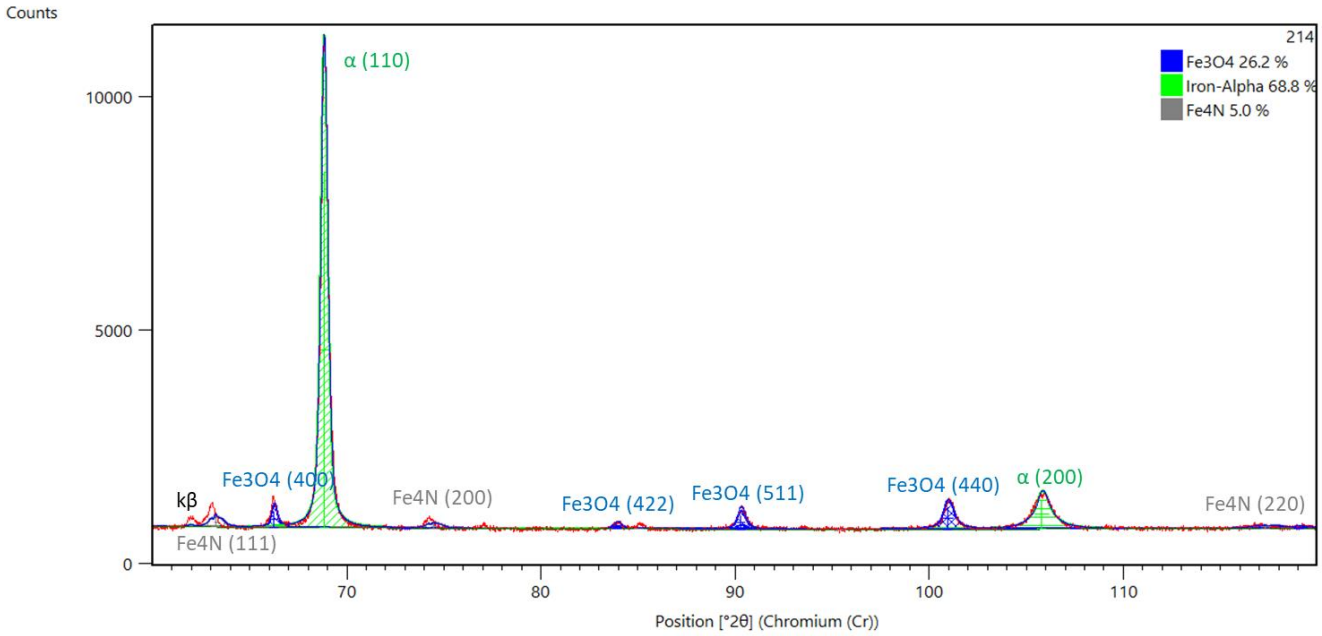

Figure 25 XRD pattern and refinement results of cast iron samples processed with Kc=12 for 8 hours

Diffusion zone microhardness profile and N & C concentration profile

After FNC trials, the microhardness profile for each trial group sample was tested and compared. Three line scans were conducted for each sample and the average value was obtained. *Figure 26*, *Figure 27*, and *Figure 28* shows the microhardness profiles for AISI 4140, AISI 1018, and cast iron samples processed with Kc=9 for various durations respectively. For all three material samples, the local hardness gets higher, and the case depth also increases with longer process duration. For the samples with the same process duration, the AISI 4140 sample usually has higher local hardness while the AISI 1018 sample has higher case depth, which can be explained by higher nitrogen diffusivity in AISI 1018 steel. For cast iron samples, even there was no compound layer formed on the surface, there is a hardened case in the near surface region, after 8 hours process time, the hardened case could reach to 200 μm. The samples processed with different carburizing potentials have the similar tendency as described above.

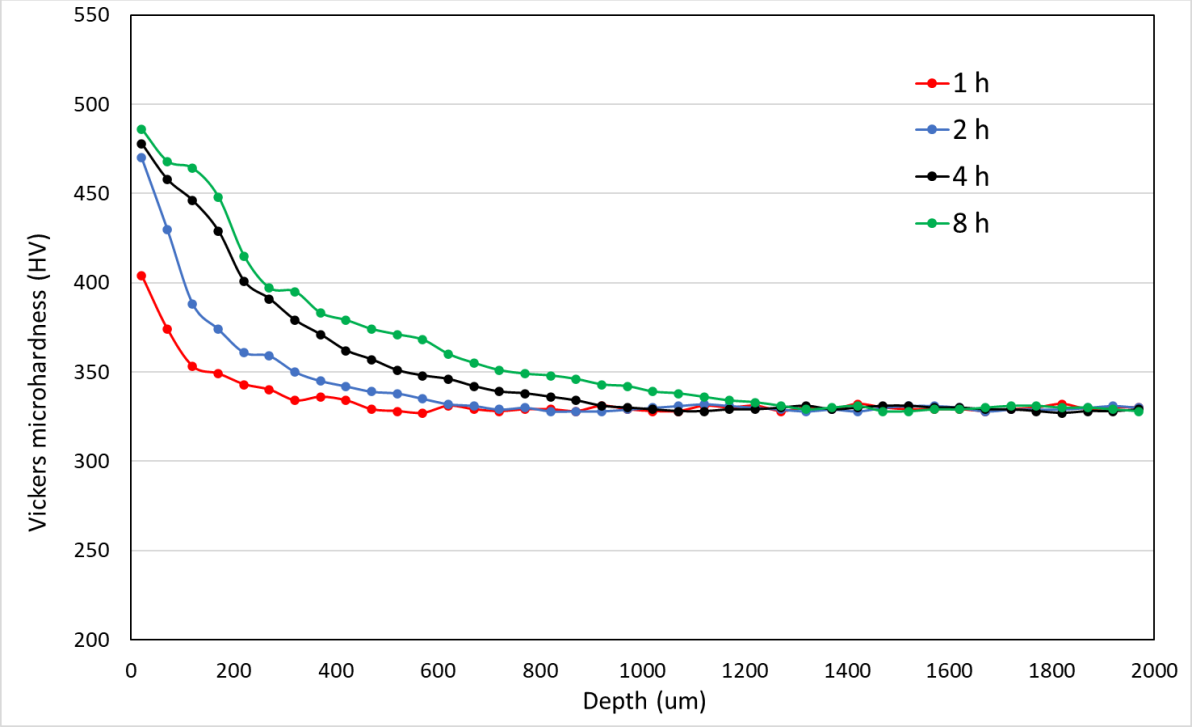

Figure 26 Microhardness profiles in the diffusion zone of AISI 4140 samples processed with Kc=9 for various process durations

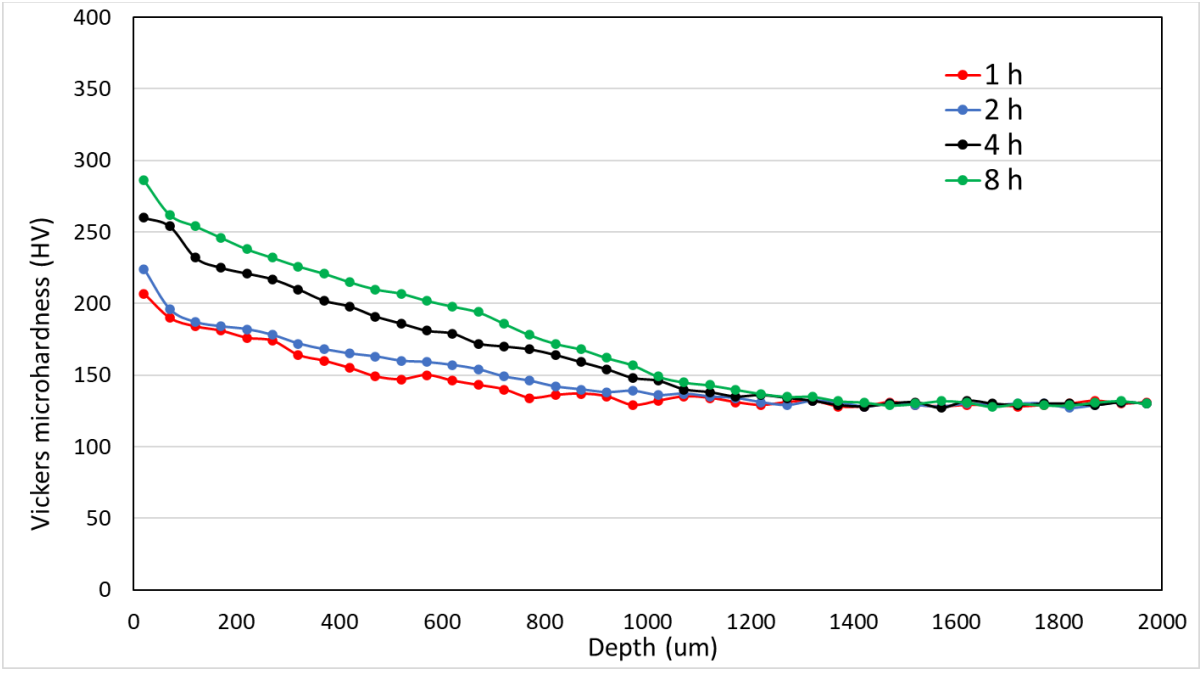

Figure 27 Microhardness profiles in the diffusion zone of AISI 1018 samples processed with Kc=9 for various process durations

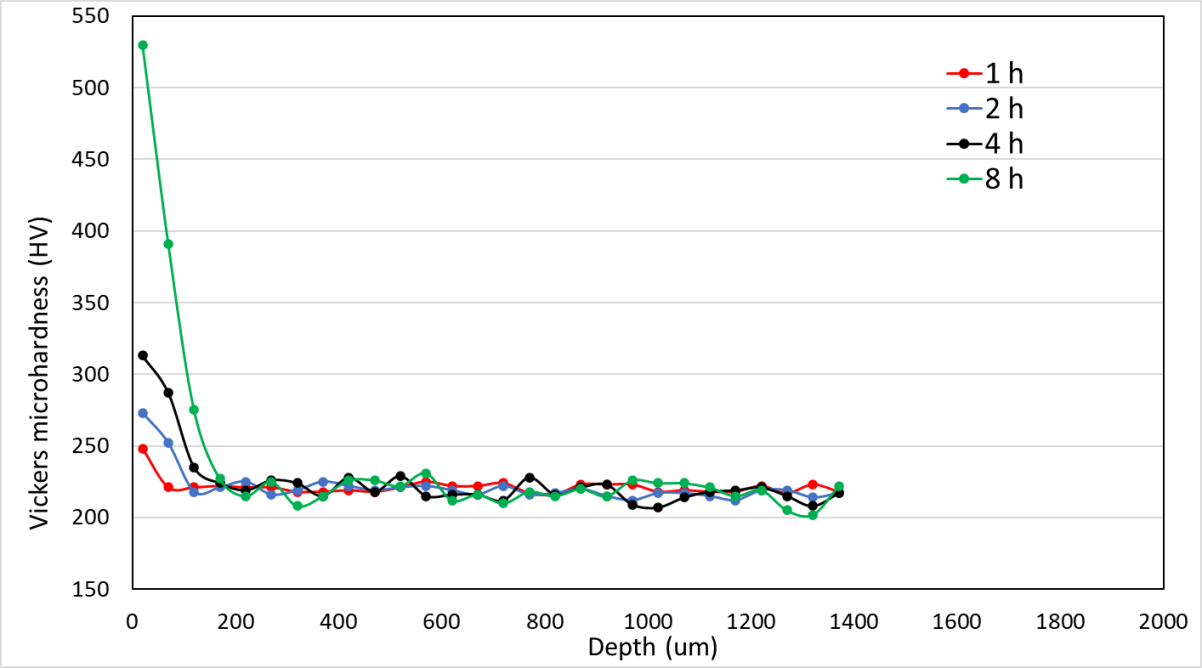

Figure 28 Microhardness profiles in the diffusion zone of cast iron samples processed with Kc=9 for various process durations

The nitrogen and carbon concentration profiles were measured using OES with a layer-by-layer method for both AISI 4140 and AISI 1018 samples. After removing the surface compound layer by grinding, the average nitrogen and carbon content on the current layer was measured, and then, a layer (typically 70 – 100 µm) was removed and the measurement was carried out again. After multiple measurements, the nitrogen and carbon concentration profiles in the diffusion zone were obtained.

Figure 29 and *Figure 30* show the nitrogen and carbon concentration profiles for AISI 4140 and AISI 1018 samples processed with Kc=9 for various durations. As we can see, both AISI 4140 and AISI 1018 samples have a region with increased nitrogen content near the surface, however, the carbon concentration in the diffusion zone was barely changed after FNC trials, except the slight decarburizing in the near surface region.

Figure 31 compares the nitrogen concentration profiles for the samples with the same carburizing potential but different durations. As shown, the local nitrogen content increases with longer process duration for both AISI 4140 and AISI 1018 samples. For the samples with the same process duration, the AISI 4140 sample has higher local nitrogen content while the AISI 1018 sample has higher case depth, which agrees with the microhardness profile results described above. More nitrogen and carbon concentration profiles for the samples with different carburizing potentials could be found in Appendix 2: Nitrogen and

carbon concentration profiles measured with OES, the tendency above remains similar when the carburizing potential was changed.

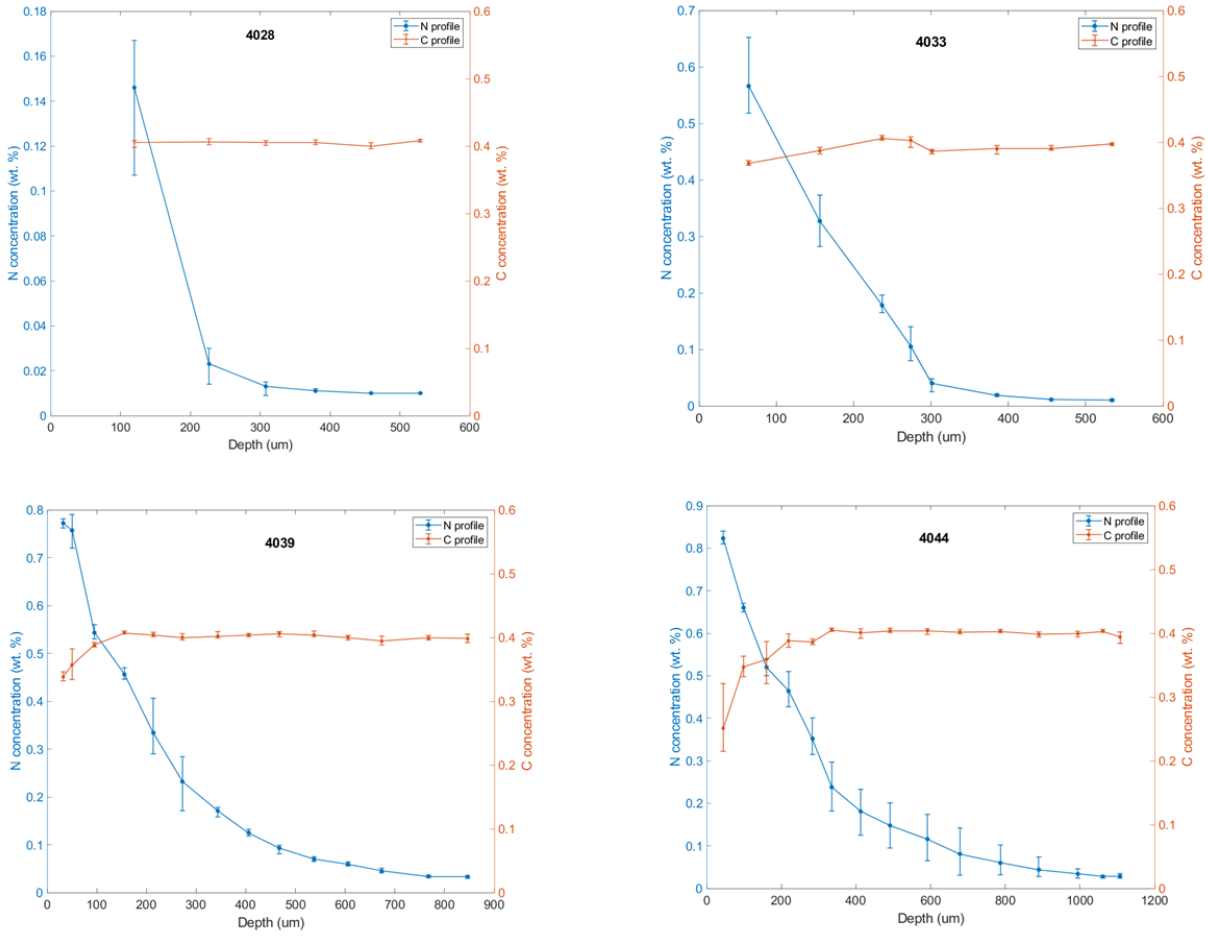

Figure 29 Nitrogen and carbon concentration profiles of AISI 4140 samples processed with Kc=9 (left to right, top to bottom: t= 1 hour, 2 hours, 4 hours, and 8 hours)

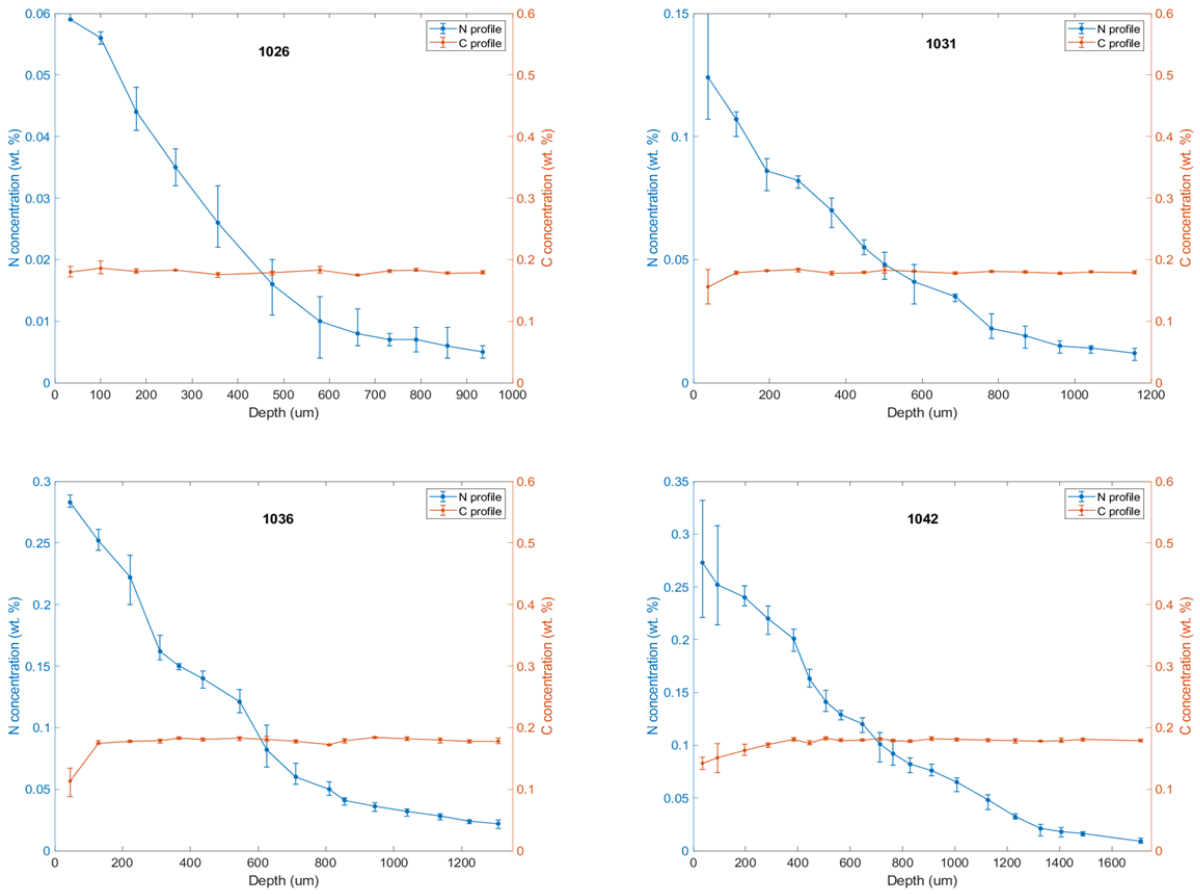

Figure 30 Nitrogen and carbon concentration profiles of AISI 1018 samples processed with Kc=9 (left to right, top to bottom: t= 1 hour, 2 hours, 4 hours, and 8 hours)

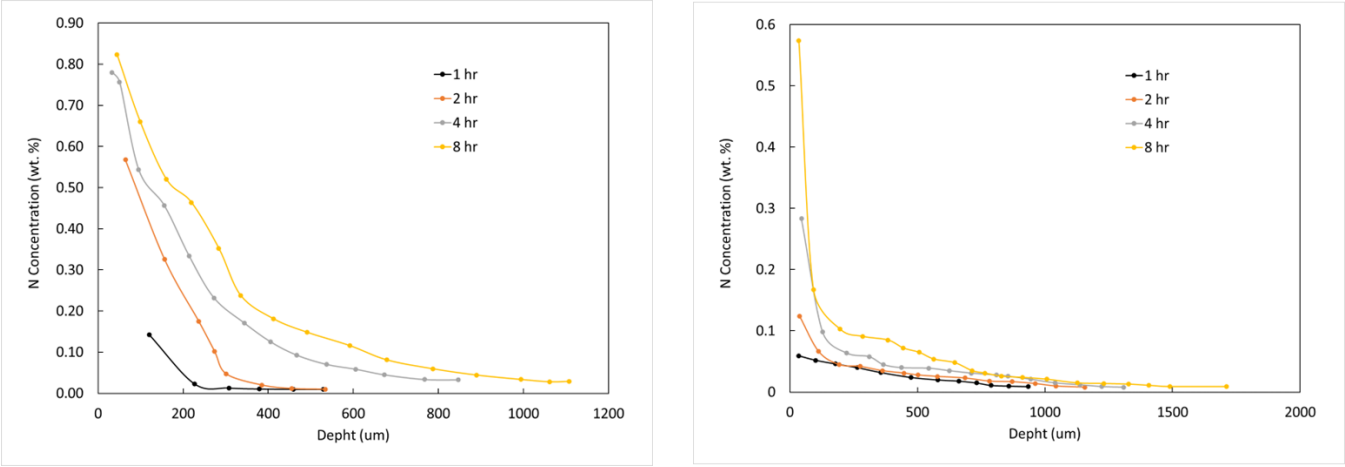

Figure 31 Comparison of nitrogen concentration profiles for samples processed with Kc=9 for various durations (left: AISI 4140 samples, right: AISI 1018 samples)

Diffusion of nitrogen and carbon in tempered martensite

During the nitriding or nitrocarburizing process, the nascent nitrogen and carbon diffuse into steel to form iron (carbon-)nitrides. In the current work, the effective nitrogen diffusion coefficients in different steels are estimated based on experimentally measured nitrogen concentration profiles. The diffusion process can be interpreted using a diffusion with chemical reaction process or a diffusion with trapping model (McNabb-Foster) [20].

As mentioned in the previous section, the nitrogen and carbon concentration profiles in the diffusion zone of nitrocarburized samples are measured by OES with a layer by layer method. Based on the measured nitrogen concentration profiles, the effective nitrogen diffusion coefficient was estimated for AISI 4140 and AISI 1018 samples. The nitrogen concentration in the diffusion zone can be fitted with error function:

$$C = N_0 \operatorname{erf}\left(\frac{x}{\sqrt{4Dt}}\right) \quad (2)$$

In which:

C – nitrogen concentration at depth x, wt. %

N_0 – nitrogen concentration at the 1st layer measurement, wt. %

x – depth from the surface, m

D – nitrogen diffusivity in the diffusion zone,m^2/s

t – process time, s

By adjusting the diffusivity value in the error function to make the function curve fit with experimentally measured nitrogen concentration profile, the effective nitrogen diffusivity can be estimated.

Figure 32 and *Figure 33* shows the fitting of error function curve together with experimentally measured nitrogen concentration profiles for AISI 4140 and AISI 1018 samples respectively. The estimation results for different AISI 4140 and AISI 1018 samples processed with various carburizing potentials and process durations are summarized in *Table 6*. As we can see, for certain material, the estimated diffusivity doesn't change with carburizing potential. Besides, the average nitrogen diffusivity in AISI 1018 is much higher

than it in AISI 4140 steel, which is contributed by much lower alloy content in AISI 1018 steel.

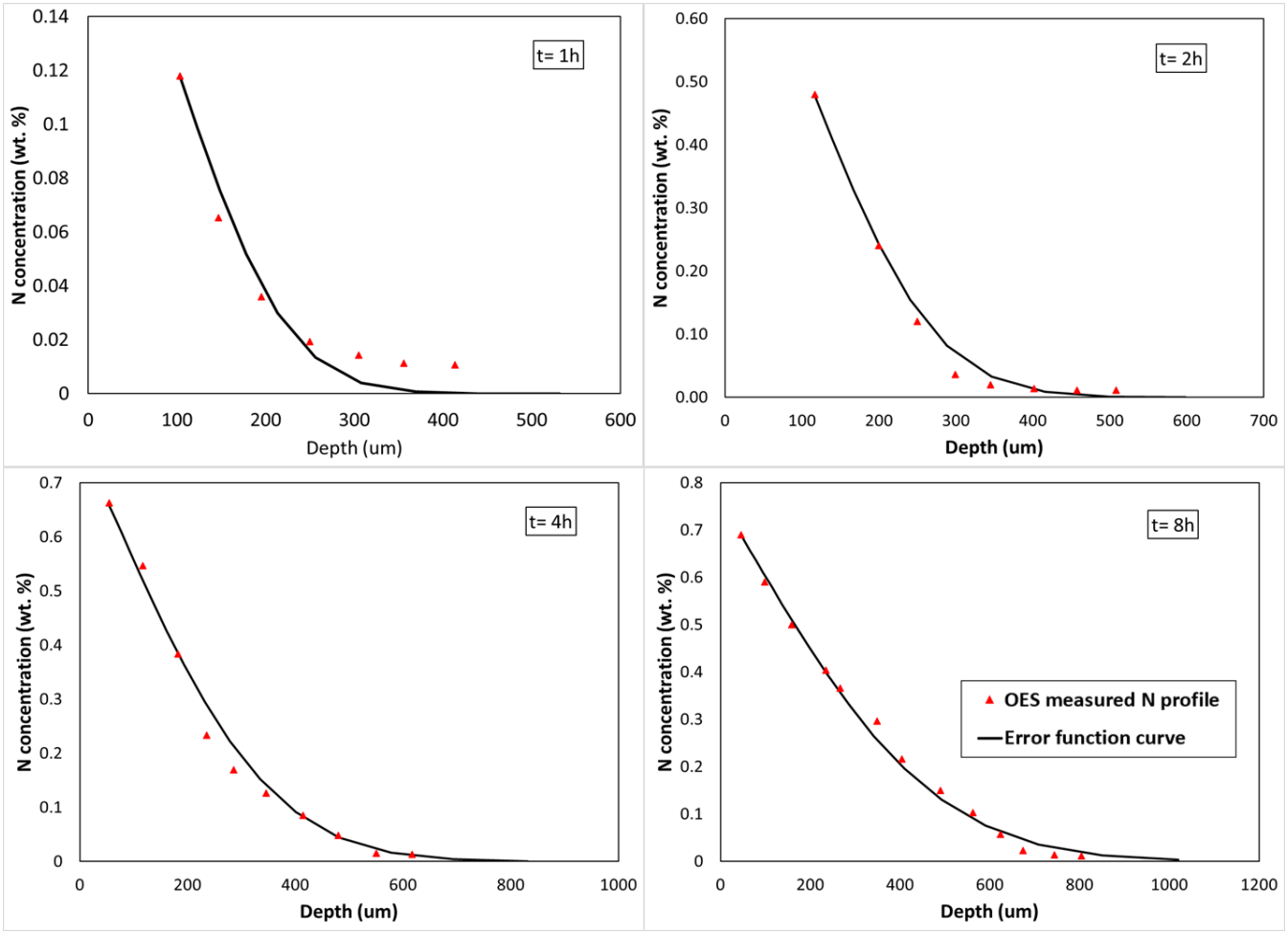

Figure 32 Experimentally measured nitrogen concentration profile fitting with error function curve for AISI 4140 samples processed with Kc=12, various process durations

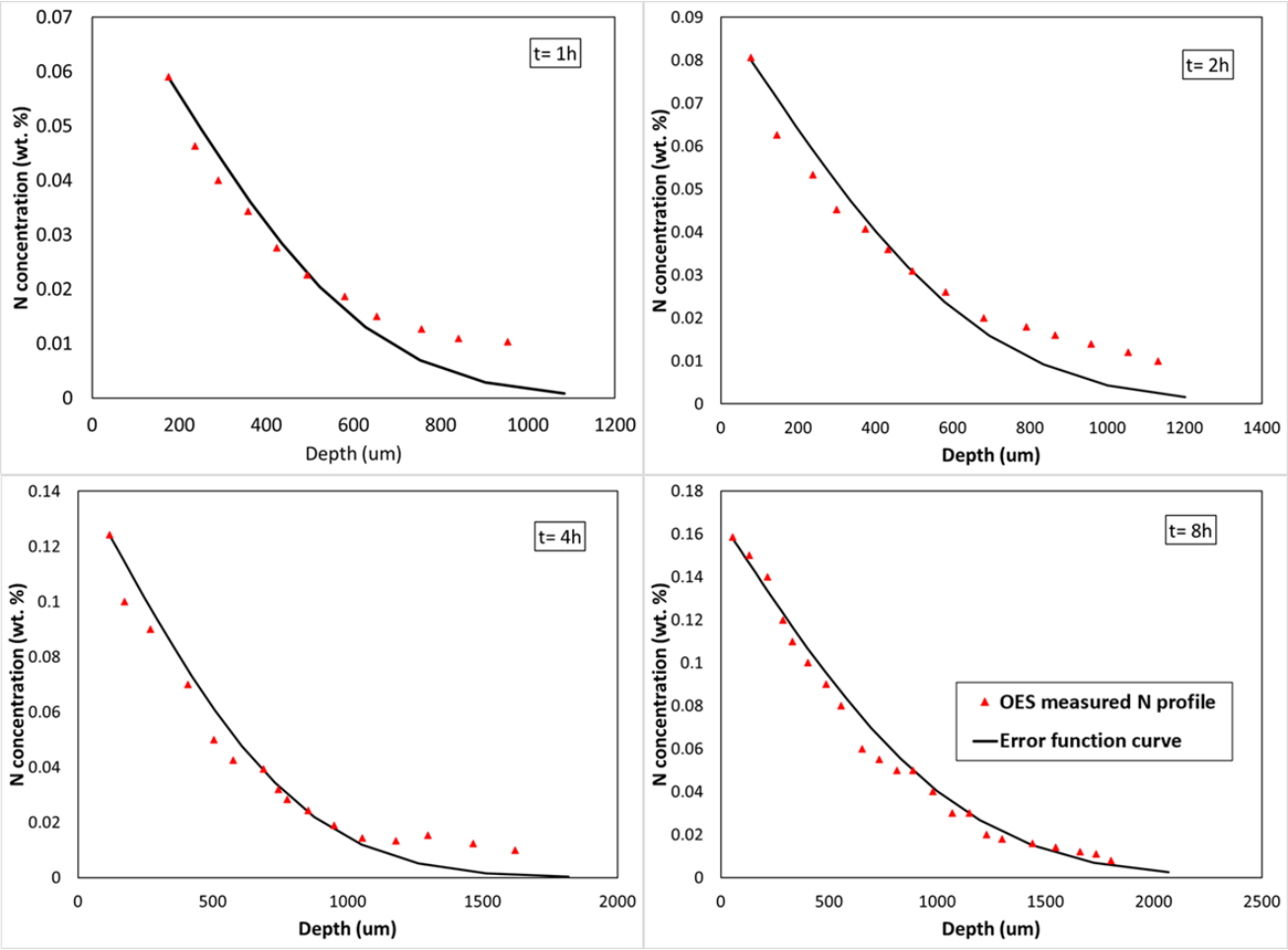

Figure 33 Experimentally measured nitrogen concentration profile fitting with error function curve for AISI 1018 samples processed with Kc=12, various process durations

Table 6 Estimated nitrogen diffusivity in different AISI 4140 and AISI 1018 samples

K_N= 4, T= 579 °C, diffusivity(m^2/s)					
		AISI 4140		**AISI 1018**	
Carburizing potential	Process time	Estimated diffusivity	Average diffusivity	Estimated diffusivity	Average diffusivity
KC=0	t=1h	1.5×10^{-12}	1.8×10^{-12}	2.2×10^{-11}	1.7×10^{-11}
	t=2h	1.8×10^{-12}		1.8×10^{-11}	
	t=4h	2.2×10^{-12}		1.5×10^{-11}	
	t=8h	1.5×10^{-12}		1.2×10^{-11}	
KC=9	t=1h	1.1×10^{-12}	1.7×10^{-12}	2.1×10^{-11}	1.7×10^{-11}
	t=2h	1.8×10^{-12}		2.2×10^{-11}	
	t=4h	2.2×10^{-12}		1.1×10^{-11}	
	t=8h	1.8×10^{-12}		1.2×10^{-11}	
KC=12	t=1h	1.3×10^{-12}	1.6×10^{-12}	1.9×10^{-11}	1.5×10^{-11}
	t=2h	1.1×10^{-12}		1.6×10^{-11}	
	t=4h	1.9×10^{-12}		1.1×10^{-11}	
	t=8h	2.1×10^{-12}		1.2×10^{-11}	

Table 7 Comparison of nitrogen diffusivity in different materials

Temperature		**Nitrogen diffusivity (m^2/s)**			
°C	K	AISI 4140	AISI 1018	Pure iron [21]	AISI 4140 [22]
500	773			3.8E-08	1.7E-13
579	852	1.7E-12	1.5E-11	1.1E-07	8.7E-13
600	873			1.4E-07	1.3E-12

Table 7 compares the nitrogen diffusivity in AISI 4140 and AISI 1018 steels estimated from current experimental results with the nitrogen diffusivity in the pure iron[21] and the nitrogen diffusivity in AISI 4140 obtained by Mei [22]with the same approach in a series of AISI 4140 nitriding trials [22]. The data were also plotted in *Figure 34*. As we can see, the nitrogen diffusivity in AISI 4140 from current work is very close to Mei's result. The diffusivity in AISI 1018 is higher than AISI 4140 and lower than pure iron.

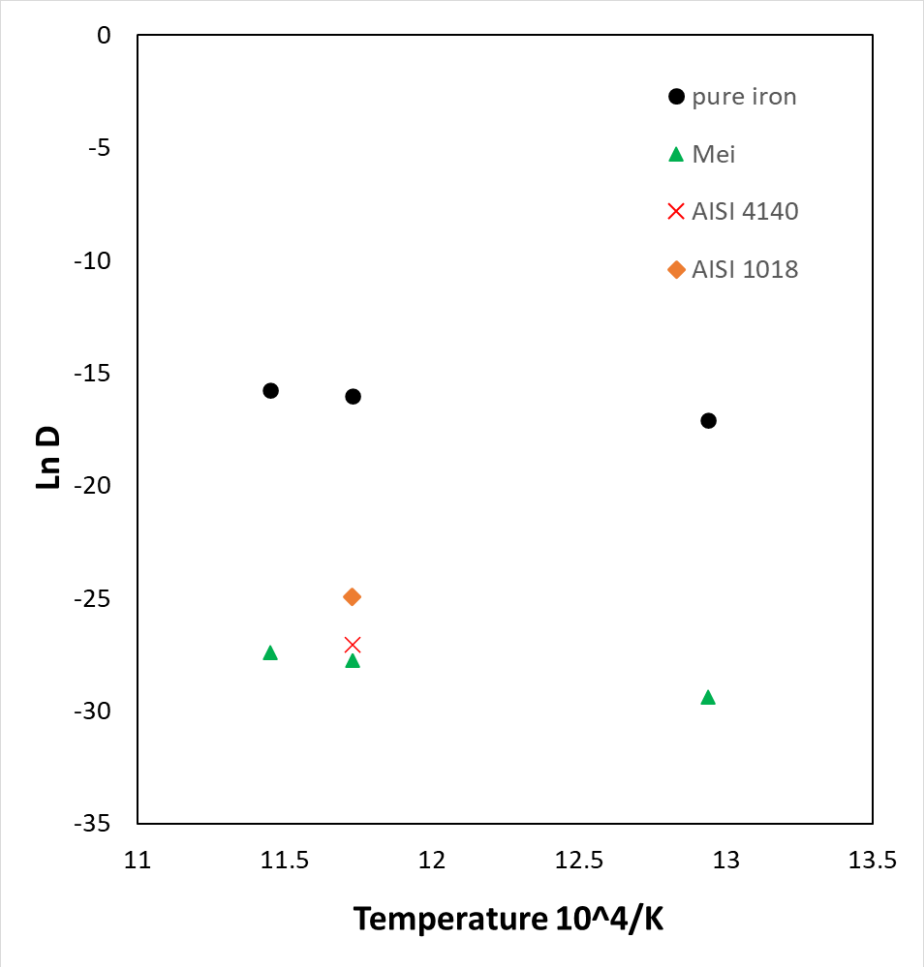

Figure 34 Comparison of nitrogen diffusivity in different materials

The nitrogen diffusion process in the steel can be interpreted with the diffusion with trapping model. The diffusion with trapping model was proposed by McNabb and Foster to describe the interstitial atoms such as hydrogen, nitrogen, and carbon diffusion process in the solid [20, 23].

With certain number of traps in the solid, the concentration of the interstitial atom is determined by the percentage of the traps that has been occupied, which is governed by the rate of atoms capturing and releasing of the traps:

$$\frac{\partial C}{\partial t} + N\frac{\partial n}{\partial t} = D\frac{\partial^2 C}{\partial x^2} \quad (3)$$

$$\frac{\partial n}{\partial t} = KC(1-n) - pn \quad (4)$$

N – total traps per unit volume

n – fraction of occupied traps

K – rate constant for capture of traps

p – rate constant of release of traps

If we consider the diffusion of the interstitial atoms through the traps and through the normal lattice separately [24]:

$$J_L = -D_L\frac{dC_L}{dx} \quad (5)$$

$$J = -D\frac{dC_T}{dx} \quad (6)$$

$$C_T = C_L + C_x \quad (7)$$

Then, the effective diffusivity can be derived as:

$$D = D_L\frac{dC_L}{dC_T} \quad (8)$$

And can be solved as:

$$D = \frac{1}{1 + \frac{C_x}{C_L}(1-n)} D_L \quad (9)$$

J_L – flux through normal lattice sites

D_L – diffusivity without traps

D – apparent diffusivity with traps

C_L – concentration in normal lattice sites

C_x – concentration in traps

C_T – total concentration

n – fraction of occupied traps

Applying the model to current nitrocarburizing of alloy steels case, the apparent diffusivity with traps 'D' is the effective nitrogen diffusivity in specific alloys. And the diffusivity without traps 'D_L' is the free lattice nitrogen diffusivity which is also the nitrogen diffusivity in the pure iron. If we define a trap coefficient as:

$$\alpha = 1 + \frac{C_x}{C_L}(1-n) \quad (10)$$

Then, the effective nitrogen diffusivity in different alloy steels could be determined with this trap coefficient which is a function of temperature and element content in the specific alloys as:

$$D = \frac{1}{\alpha} D_L$$

Based on the estimated nitrogen diffusivity from the current work, the trap coefficient for AISI 4140 and AISI 1018 steels are determined as shown in *Table 8*.

Table 8 Trap coefficient for AISI 4140 and AISI 1018 steels

Material	AISI 4140	AISI 1018	Pure iron [21]
N diffusivity (m^2/s)	1.7E-12	1.5E-11	1.1E-07
α	6.5E4	7.3E3	1

The phase evolution and diffusion path in the compound layer

For nitriding process, the Lehrer diagram, which provides the phase stability information with different nitriding potentials and temperatures, is typically utilized to provide the nitriding process control parameters [25].

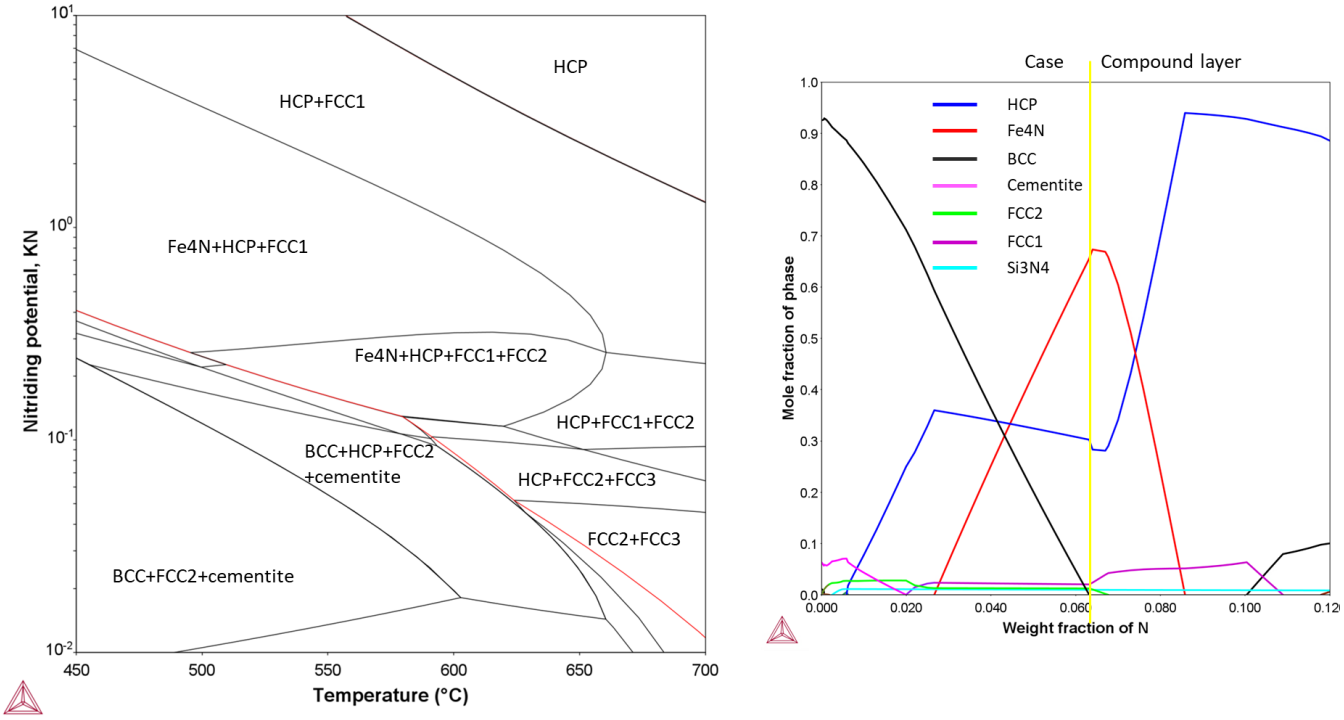

Figure 35 Alloy specific Lehrer diagram for AISI 4140 (left) and phase evolution as function of nitrogen content for AISI 4140 at 580 °C (right) [26]

Figure 35 shows the alloy specific Lehrer diagram for AISI 4140 steel and the derived phase evolution plot as function of nitrogen content. Combining these two diagrams, the phase evolution of the compound layer during nitriding of AISI 4140 steel process can be determined. When the nitrogen content is higher than 0.5 wt.%, the ε – $Fe_{2-3}(C,N)$ will form and become more stable until the nitrogen content increases to 2.1 wt.%. When the nitrogen content reaches 2.1 wt.% the γ' nitrides will form and become more stable until the nitrogen content increases to 6.4 wt.%, which should be located at the boundary of compound layer and the diffusion zone. When the nitrogen content is within the range between 6.4 wt.% -

8.7 wt.%. The ε and γ' nitrides coexist in the compound layer and the stability of γ' nitrides decrease. With the nitrogen content higher than 8.7 wt.%, the ε phase dominant in the compound layer.

For the nitrocarburizing process, the Fe-C-N ternary system should be investigated to determine the phase evolution during the process. Whoehrle carried out a series of nitrocarburizing trials for pure iron with various process durations and determined the nitrogen diffusion path based on the observation of compound layer phase evolution [18]. As shown in *Figure 36* (left), the diffusion path during the nitrocarburizing of pure iron process is plotted as the green line with arrows in the isothermal section of Fe-C-N ternary phase diagram. The phase evolution during the nitrocarburizing process can be illustrated as the following steps. At the initial stage of the process, since the carburizing reaction is faster than the nitriding reaction and carbon solubility in the ferrite is lower than nitrogen, a cementite layer will form at the surface. The ε phase will nucleate at the interface of cementite layer and the substrate. Then, the ε phase layer will grow by both growing towards the substrate and also converting the cementite layer. Finishing the growth of the ε phase layer, a single layer of ε phase will exist and the γ' nitrides will nucleate near the boundary of ε phase layer and the substrate. The γ' phase layer will keep growing and in the final stage of the process, a single γ' phase compound layer could be obtained. In current work, the pseudo ternary phase diagram for AISI 4140 steel at 580 °C is developed with Thermo-Calc as shown in *Figure 36* (right). The similar diffusion path as in pure iron system is indicated as the red line with arrows. The main difference for AISI 4140 case is the existence of the Cr rich iron nitrides in the compound layer (FCC_1- $Fe_{3.4}Cr_{2.3}N_4$ and FCC_2- $FeCr_{3.5}N_5$) and also the region of ε phase is expanded since the higher carbon content in AISI 4140 stabilize the ε phase.

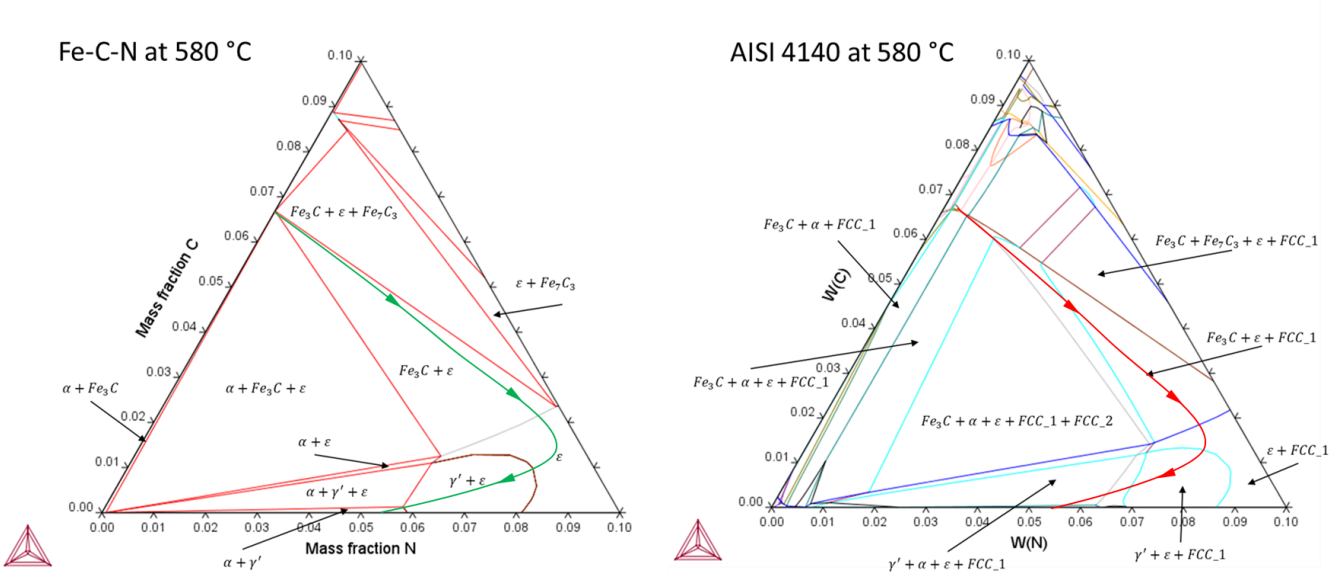

Figure 36 Isothermal section of Fe-C-N ternary phase diagram at 580 °C with diffusion path indicated (left) and isothermal section of pseudo ternary phase diagram of AISI 4140 at 580 °C (right)

For the purpose of process control during the nitrocarburizing of steel process, potential diagrams which provide phase stability information as function of nitriding potential and carburizing potential should be utilized. According to AMS 2759/12A standard, the carburizing potential for Boudouard reaction Kcb should be measured and controlled during the nitrocarburizing potential, the potential diagrams for pure iron, AISI 4140, AISI 1018, and cast iron (ASTM A536 80-55-06) are developed and shown in *Figure 37*.

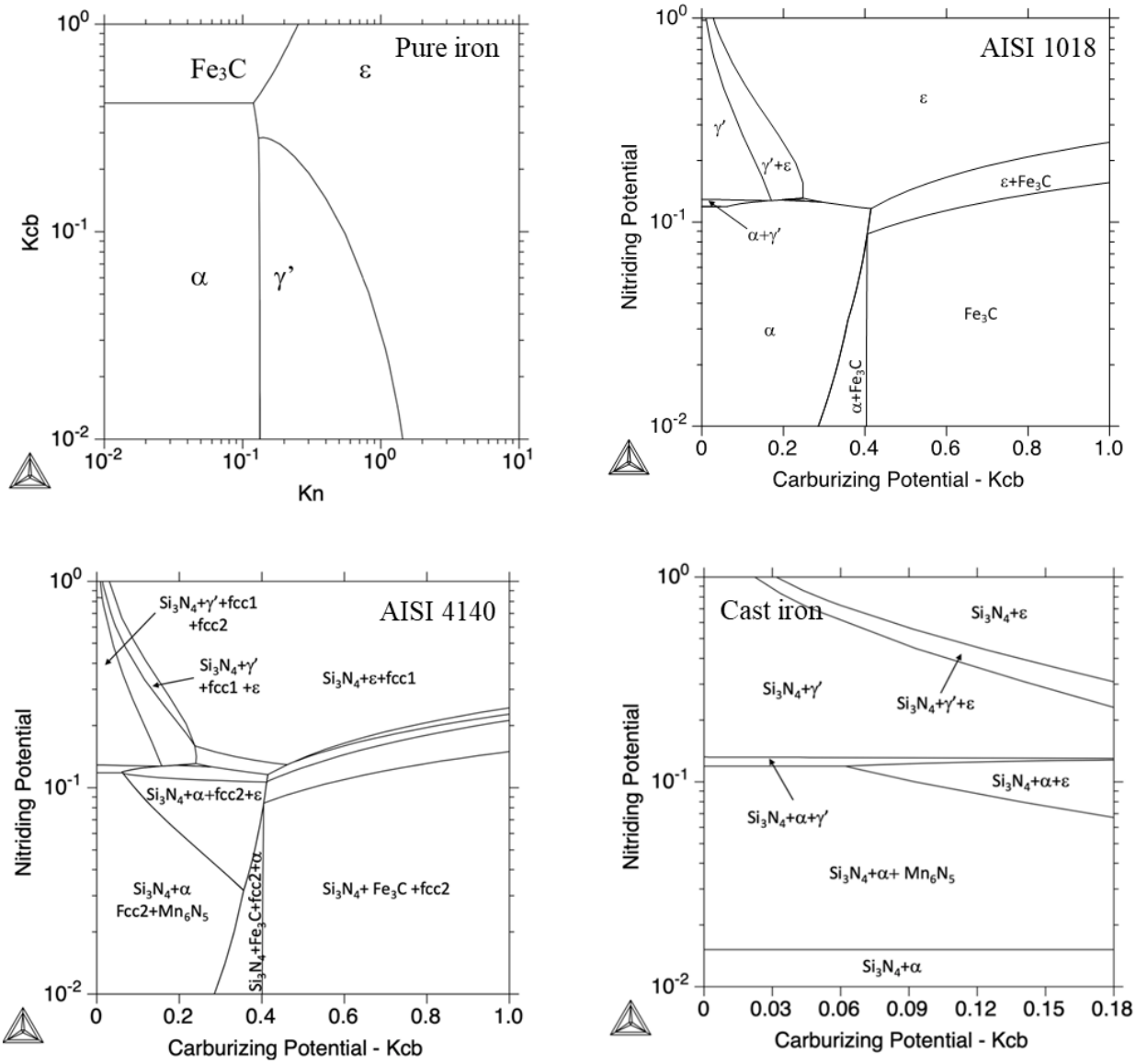

Figure 37 Potential diagrams for pure iron, AISI 1018, AISI 4140, and cast iron at 580 °C

Conclusions

In the present work, various FNC trials with different carburizing potentials and process durations were carried out on three different material samples, including AISI 4140 steel, AISI 1018 steel, and cast iron (ASTM A536 80-55-06). A compound layer composed of a top oxide layer, a porous layer and a dense layer was formed on both AISI 4140 and AISI 1018 samples. No compound layer was observed on cast iron samples, however, according to the microhardness profile, there is a hardened case near the surface on cast iron samples. The compound layer phase constitution on both AISI 4140 and AISI 1018 samples were identified as ε and γ'. The compound layer phase evolution and the diffusion path were determined for AISI 4140 samples based on the pseudo ternary phase diagrams. The formation of the compound layer starts with carbon rich phase and proceeds towards nitrogen rich phase.

Acknowledgement

The support of the Center of Heat Treating Excellence (CHTE) at Worcester Polytechnic Institute and the member companies is greatly appreciated. Special thanks to Bodycote for carrying out the pre-FNC heat treatment and the FNC trials. Great appreciation to Mei Yang for her assistance and guidance in developing the alloy specific potential diagrams.

References

1. Pye, D., *Practical nitriding and ferritic nitrocarburizing*. 2003: ASM international.
2. Dossett, J. and G. Totten, *Fundamentals of nitriding and nitrocarburizing.* ASM Handbook: Steel Heat Treating Fundamentals and Processes; ASM International: Materials Park, OH, USA, 2013: p. 619.
3. Mittemeijer, E.J. and M.A. Somers, *Thermochemical surface engineering of steels*. 2014: Woodhead Publishing Cambridge.
4. Machlet, A., *Treatment of Steel, Iron, etc*, in *U. S. Patent*. 1913.
5. Nam, N.D., et al., *Control gas nitriding process: A review.* J. Mech. Eng. Res. Dev, 2019. **42**: p. 17-25.
6. Yang, M., et al., *Modeling the gas nitriding process of low alloy steels.* Journal of Materials Engineering and Performance, 2013. **22**(7): p. 1892-1898.
7. Maldzinski, L., et al., *New possibilities for controlling gas nitriding process by simulation of growth kinetics of nitride layers.* Surface Engineering, 1999. **15**(5): p. 377-384.

8. Cavaliere, P., G. Zavarise, and M. Perillo, *Modeling of the carburizing and nitriding processes.* Computational Materials Science, 2009. **46**(1): p. 26-35.
9. Yang, M. and R. Sisson, *Alloy effects on the gas nitriding process.* Journal of materials engineering and performance, 2014. **23**(12): p. 4181-4186.
10. Afzaal, U., *Modeling of gas nitriding using artificial neural networks.* 2006.
11. Hosseini, S., F. Ashrafizadeh, and A. Kermanpur, *Calculation and experimentation of the compound layer thickness in gas and plasma nitriding of iron.* 2010.
12. Kogan, Y.D. and A. Bulgach, *Computer modeling of diffusion-saturation kinetics during gas nitriding.* Metal Science and Heat Treatment, 1984. **26**(1): p. 14-27.
13. Khalaf Mohanad, M., *Modeling of the case depth and surface hardness of steel during ion nitriding.* Eastern-European Journal of Enterprise Technologies, 2016. **2**(5): p. 80.
14. Winter, K.-M., *Gaseous nitriding: in theory and in real life.* Technical Paper of United Process Controls, Process-Electronic GmbH, Heiningen, Germany, 2009.
15. Somers, M.A. *Nitriding and nitrocarburizing: Status and future challenges*. in *Proceedings of heat treat & surface engineering conference & expo, Chennai, India*. 2013.
16. Slycke, J., L. Sproge, and J. Agren, *Nitrocarburizing and the Ternary Fe--N--C Phase Diagram.* Scand. J. Metall., 1988. **17**(3): p. 122-126.
17. Mittemeijer, E.J. and M.A. Somers, *Thermodynamics, kinetics, and process control of nitriding.* Surface Engineering, 1997. **13**(6): p. 483-497.
18. Woehrle, T., A. Leineweber, and E. Mittemeijer, *Microstructural and phase evolution of compound layers growing on α–iron during gaseous nitrocarburizing.* Metallurgical and Materials Transactions A, 2012. **43**(7): p. 2401-2413.
19. Du, H. and J. Ågren. *Kinetics of Compound-Layer Growth during Nitrocarburizing*. in *Materials science forum*. 1992. Trans Tech Publ.
20. McNabb, A. and P. Foster, *A new analysis of diffusion of hydrogen in iron and ferritic steels.* Transactions of the Metallurgical Society of AIME, 1963. **227**(3): p. 618-&.
21. Somers, M.A. and E.J. Mittemeijer, *Layer-growth kinetics on gaseous nitriding of pure iron: Evaluation of diffusion coefficients for nitrogen in iron nitrides.* Metallurgical and Materials Transactions A, 1995. **26**: p. 57-74.
22. Yang, M. and R. Sisson Jr, *Modeling the nitriding process of steels.* Advanced Materials & Processes, 2012. **170**(7): p. 33-37.
23. Oriani, R.A., *The diffusion and trapping of hydrogen in steel.* Acta metallurgica, 1970. **18**(1): p. 147-157.
24. Makhlouf, M.M., *Hydrogen uptake by AISI 4340 steel during cadmium electroplating.* 1990.
25. Lehrer, E., *Über das Eisen-Wasserstoff-Ammoniak-Gleichgewicht.* Zeitschrift für Elektrochemie und angewandte physikalische Chemie, 1930. **36**(6): p. 383-392.

26. Yang, M., et al., *Simulation of the ferritic nitriding process.* International Heat Treatment and Surface Engineering, 2011. **5**(3): p. 122-126.

Chapter 4: Effects of pre & post oxidation process on nitrocarburizing of tempered martensite

Haoxing You, Richard D. Sisson Jr.
Center for Heat Treating Excellence (CHTE)
Worcester Polytechnic Institute; 100 Institute Rd; Worcester, MA 01609, USA

Abstract

In the practical nitriding and ferritic nitrocarburizing(FNC) process, a pre and post FNC oxidation process is typically applied. The pre oxidation process is reported to be greatly helpful to enhance the iron (carbon-)nitrides and reduce the incubation time[1]. During the post oxidation process, the top of compound layer formed during the FNC process is converted into magnetite (Fe_3O_4), which helps to improve the corrosion resistance [2]. In the current project, the effects of pre and post oxidation process on nitrocarburizing of tempered martensite are investigated by comparing the gas nitrocarburized samples with/without pre and post oxidation process. AISI 4140 samples with tempered martensite microstructure were processed with different oxidation procedure, carburizing potentials, and durations. The total weight gain during the nitrocarburizing process is measured by recording the individual sample weight before and after the nitrocarburizing process. The compound layer morphology is observed with SEM and EDS mapping, the compound layer phase constitution is analyzed with XRD. An oxide layer characterized as Fe_3O_4 with 2-4 μm thickness is observed on the samples processed with pre and post oxidation procedure. The porosity in the compound layer is analyzed. The microhardness and nitrogen and carbon profiles in the diffusion zone are measured and compared.

Introduction

The gas nitriding and nitrocarburizing process are commonly used to improve the wear and corrosion resistance, as well as the fatigue endurance of steel parts such as shafts and gears. For practical gas nitriding and nitrocarburizing process, a pre oxidation process, which is typically carried out at 350-450 °C in air for 1-2 hours[3] will be performed. Then, the gas nitrocarburizing process will be carried out, during which a compound layer composed of ε – $Fe_{2-3}(C,N)$ and γ' – Fe_4N nitrides will form at the part surface and enhance the wear and corrosion resistance of the part. Underneath the compound layer, there will be a diffusion

zone with dispersed alloy (carbon-)nitrides improving the fatigue endurance [2, 4, 5]. Following the nitriding or nitrocarburizing process, a post oxidation process is typically carried out at a temperature well below the nitriding/nitrocarburizing temperature to further improve the corrosion resistance of the compound layer [2].

During the pre oxidation process, as reported by many researchers [1, 6-8], the iron oxide formed on steel surface can enhance the nucleation of iron nitrides, thus, reducing the incubation time during nitriding and nitrocarburizing process [9, 10]. A more uniform distribution of iron nitrides nucleation was obtained after pre oxidation and more uniform compound layer was observed after nitriding or nitrocarburizing process [1, 11, 12].

Typically, the compound layer formed during nitriding or nitrocarburizing process has a porous top layer structure that affects the corrosion resistance [13]. With the post oxidation process, the top of the compound layer is converted into iron oxide magnetite (Fe_3O_4). This thin iron oxide layer (typically 2-4 μm)[14] can effectively improve the corrosion resistance by 'sealing' the porous layer of the compound layer [15-17].

In the current work, one group of AISI 4140 samples were nitrocarburized with both pre and post oxidation process while another group was processed at the same condition but without any oxidation process. The compound layer morphology is observed, and the average compound layer thickness is measured and compared. The phase constitution of the compound layer is characterized with XRD and Rietveld refinement. The porosity in the compound layer is analyzed and compared. The microhardness and nitrogen and carbon concentration profiles in the diffusion zone are measured and compared. Based on the characterization results, the effects of pre and post oxidation process on nitrocarburizing of tempered martensite are discussed.

Experiments

AISI 4140 steel was selected for current gas nitrocarburizing trials. Prior to the nitrocarburizing process, the steel rods were hardened and tempered at 565 ℃ for 2 hours, machined into disks with 1.2" diameter and 0.5" thickness as shown in *Figure 38*. Each individual sample was engraved with its sample ID and all samples have the same surface finishing after machining. The samples were ultrasonically cleaned with ethanol and the weight of each sample was recorded before the nitrocarburizing trial to obtain the weight gain during the process.

There were two groups of trials, the first group of samples were pre-oxidized, nitrocarburized, and post-oxidized, while the second group was only nitrocarburized with the same nitrocarburizing condition as the first group. For both groups, there were three different carburizing potentials applied and for each carburizing potential, there were two different process durations which were 2 hours and 4 hours. The detailed process parameters are listed in *Table 9*.

The chemical composition of AISI 4140 sample used in the current work was measured as (in wt.%) 0.41C, 0.90 Cr, 0.88 Mn, 0.28 Si, 0.16 Mo, 0.01S, 0.01 P, and with Fe balance. The average surface hardness after tempering was measured as 36.2 HRC. The microstructure of AISI 4140 sample after hardening and tempering was characterized as tempered martensite as shown in the micrograph in *Figure 38*.

Table 9 Process parameters for FNC trials

Nitriding potential ($atm^{-1/2}$)	**Temperature (°C)**	**Oxidation process**	**Carburizing potential**	**Time (hrs)**
4	579	Pre-oxidation at 360 °C in air for 1 hour. Post-oxidation at 496 °C in air for 1 hour	0	2
				4
			9	2
				4
			12	2
				4
		Without oxidation process	0	2
				4
			9	2
				4
			12	2
				4

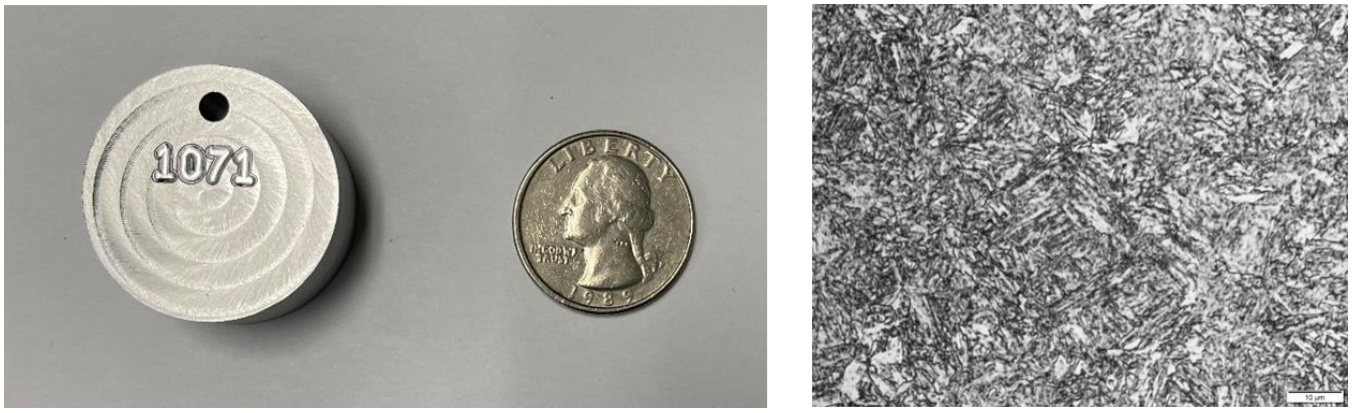

Figure 38 Machined disk AISI 4140 sample (left), microstructure of tempered AISI 4140 sample (right)

Results and Discussion

The sample characterization after nitrocarburizing trials includes the total weight gain and average flux measurement by recording the weight before and after the FNC process, the compound layer morphology observation with Nikon EPIPHOT optical microscopy, JEOL JSM-7000F SEM, and EDS. Besides, the compound layer phase constitution was analyzed with PANalytical x-ray diffractometer using Cr-Kα radiation at 30 kV voltage and 55 mA current. In the diffusion zone, the microhardness profiles were measured with Wilson VH 3300 Hardness Tester with 0.5 kgf. The nitrogen and carbon concentration profiles were measured with SPECTROLSB arc spark OES. The characterization results are compared for the samples with/without pre & post oxidation process from the following aspects.

Weight gain and average flux measurement

After nitrocarburizing trials, the weight of each sample was recorded and the compared with the weight before the nitrocarburizing trials to obtain the weight gain of each sample. The weight gain and average flux during the corresponding process duration were calculated (average value of 5 samples from each trial) and compared for different trial groups as listed in *Table 4*. The results indicates that in low carburizing potential situation (Kc=0, Kc=9), the samples without pre & post oxidation process usually have higher weight gain and average flux than the samples without oxidation process. At high carburizing potential condition, the samples that have been pre & post oxidized have higher weight gain during the nitrocarburizing process.

Table 10 Total weight gain and average flux data comparison for AISI 4140 samples

Process parameters	Average weight gain (g)		Average flux (g/m^2*hr)	
	With oxidation	Without oxidation	With oxidation	Without oxidation
Kn=4, Kc=0, t= 2 hr	0.0300	0.0401	5.6007	7.4710
Kn=4, Kc=0, t= 4 hr	0.0574	0.0616	5.3507	5.7403
Kn=4, Kc=9, t= 2 hr	0.0398	0.0438	7.4216	8.1760
Kn=4, Kc=9, t= 4 hr	0.0629	0.0609	5.8657	5.6807
Kn=4, Kc=12, t= 2 hr	0.0446	0.0429	8.3284	8.0045
Kn=4, Kc=12, t= 4 hr	0.0658	0.0615	6.1343	5.7385

Compound layer morphology and phase constitution

In the present work, a compound layer was formed on each sample after the nitrocarburizing process. The compound layer morphology was observed with optical microscopy and SEM. EDS mapping was also applied to identify the oxide layer formed on the samples with pre & post oxidation process. *Figure 39* compares the compound layer micrographs together with the EDS mapping patterns (oxygen and nitrogen) of the samples processed with Kc=9 for 2 hours and 4 hours. As we see, the compound is thicker with longer process duration. The samples with oxidation process have usually have a 2-4 μm thick oxide layer at the top surface, while there is no continues oxide layer on the samples without oxidation process. Furthermore, the compound layer formed on the samples with oxidation process is more uniform compared with it on the samples without oxidation process.

Regarding to the compound layer thickness, the average compound layer thickness was measured from the micrographs for each trial and compared in

Table 11. The compound layer thickness of the samples with oxidation process excludes the thickness of the oxide layer, which is typically 2-4 μm. The compound layer thickness of the samples without oxidation process is close to the total thickness of the oxide layer and compound layer of the samples with oxidation process.

Table 11 Average compound layer thickness for different trials

Process parameters	**Average compound layer thickness (µm)**	
	With oxidation	Without oxidation
Kn=4, Kc=0, t= 2 hr	11.11	13.52
Kn=4, Kc=0, t= 4 hr	16.86	22.43
Kn=4, Kc=9, t= 2 hr	10.93	14.62
Kn=4, Kc=9, t= 4 hr	20.41	23.56
Kn=4, Kc=12, t= 2 hr	11.69	15.49
Kn=4, Kc=12, t= 4 hr	20.47	23.72

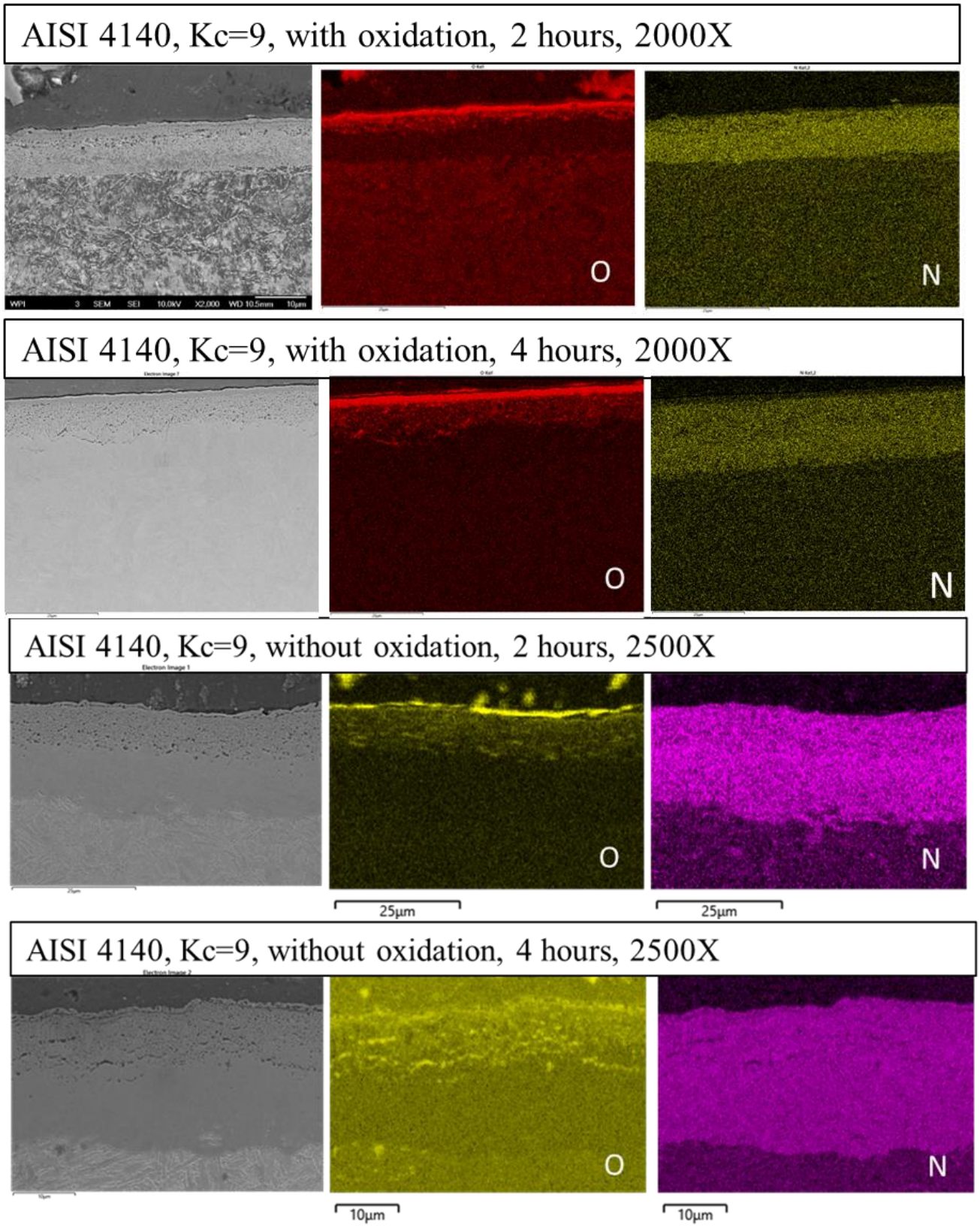

Figure 39 SEM micrographs with corresponding EDS mapping pattern (oxygen and nitrogen) for the samples with/without oxidation process

The phase constitution of the compound layer was analyzed by applying X-ray diffraction on the original surface of the nitrocarburized sample. With penetration depth around 10 µm, the phase constitution of 10 µm thick compound layer was identified by Rietveld refinement.

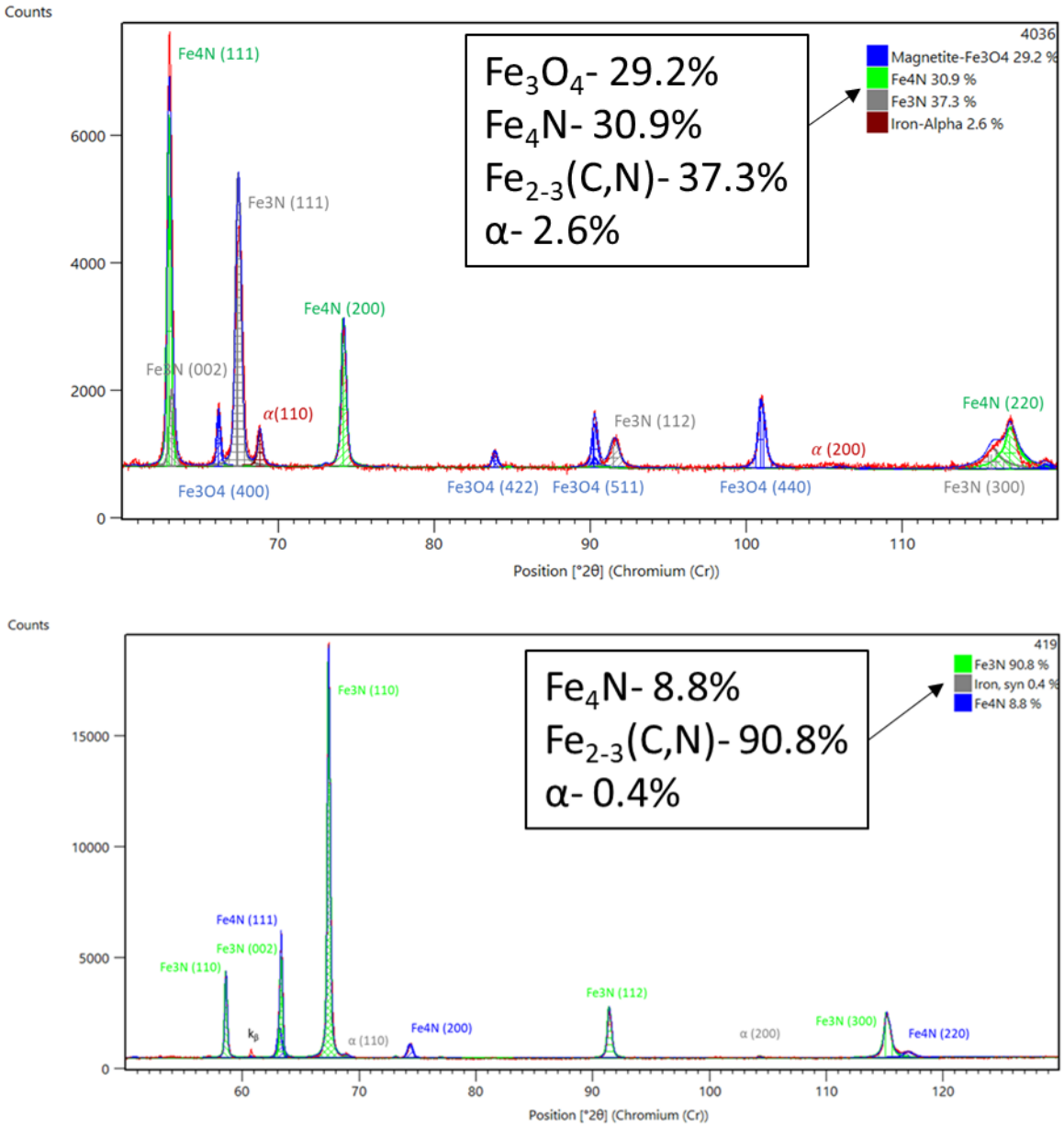

Figure 40 compares the XRD pattern and refinement results of the samples (Kc=9, 4 hours) with/without pre & post oxidation process. The oxide formed on the samples with oxidation process was identified as magnetite. For all the samples, the compound layer is dominantly composed of ε – $Fe_{2-3}(C,N)$ and γ' – Fe_4N nitrides. The detailed compound layer phase constitution for different trial samples is summarized and compared in *Table 12*.

Table 12 Compound layer phase constitution from Rietveld refinement reuslts

	With pre & post oxidation process				
Kc	Time (hr)	α-iron	ε-$Fe_{(2-3)}$(C,N)	γ'-Fe_4N	Fe_3O_4
Kc=0	2 hr	81.9%	0	0	18.1%
	4 hr	5.0%	13.8%	53.3%	27.9%
Kc=9	2 hr	10.4%	12.8%	62.1%	14.6%
	4 hr	2.6%	37.3%	30.9%	29.2%
Kc=12	2 hr	6.9%	17.3%	38.8%	37.0%
	4 hr	1.2%	12.8%	52.1%	33.9%
	Without pre & post oxidation process				
	Time (hr)	α-iron	ε-$Fe_{(2-3)}$(C,N)	γ'-Fe_4N	
Kc=0	2 hr	3.8%	50.1%	46%	
	4 hr	0	59.2%	40.8%	
Kc=9	2 hr	1.4%	80.0%	18.6%	
	4 hr	0.4%	90.8%	8.8%	
Kc=12	2 hr	2.0%	81.9%	16.1%	
	4 hr	0.3%	91.9%	7.8%	

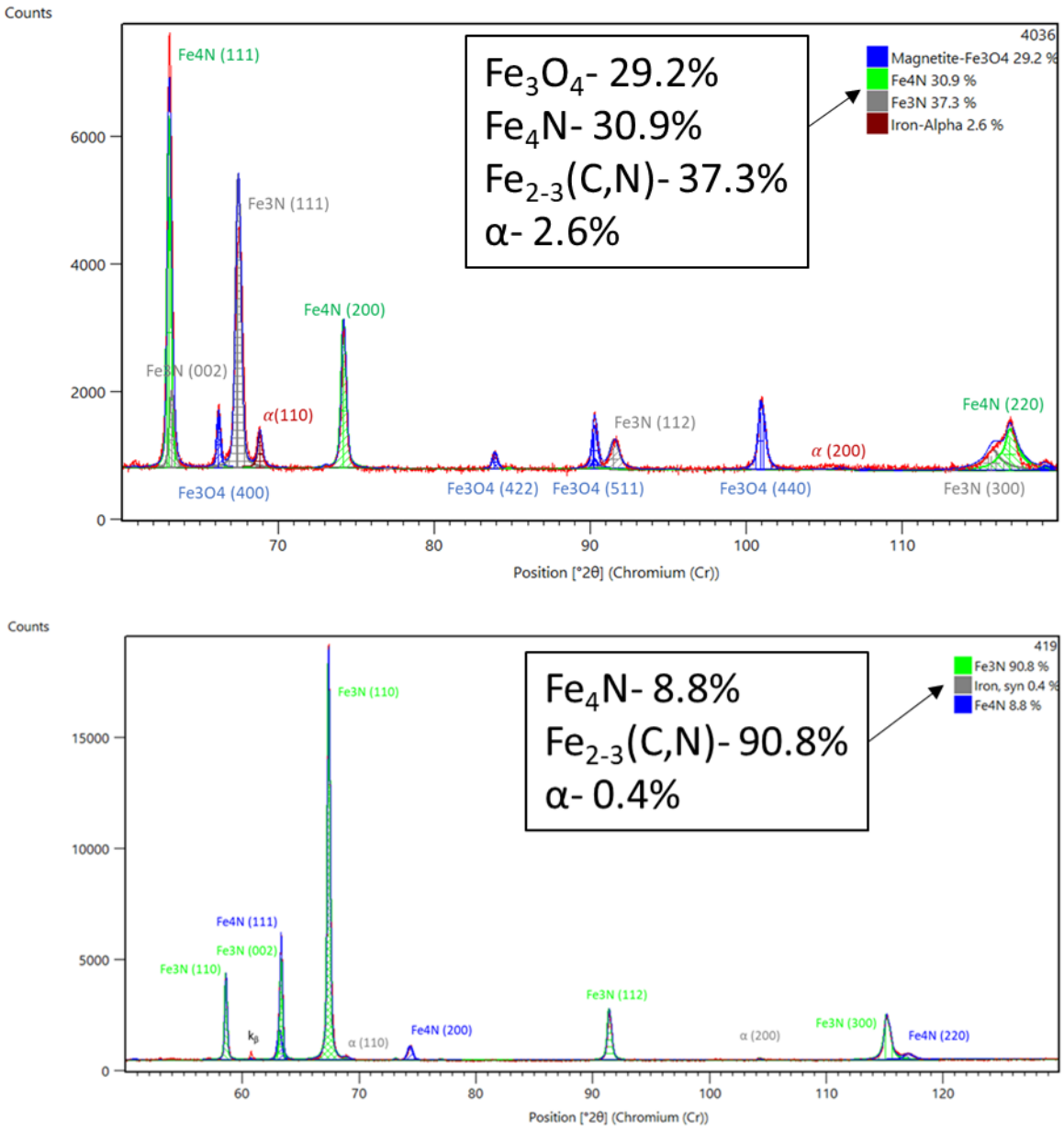

Figure 40 XRD pattern and refinement results for the samples processed with Kc=9 for 4 hours (top: sample with oxidation, bottom: sample without oxidation)

The typical compound layer formed on the current samples have porous top layer and a dense layer underneath. The porosity of the compound layer was investigated by processing micrographs with ImageJ software. For each sample, three micrographs were taken at different locations to analyze the average pore size and the total pore area, and the average value was taken for each trial. The average value of average pore size and pore area percentage in the porous layer are compared for different trials in *Table 13*. Obviously, with longer process duration, the average pore size gets larger, and the total pore area gets higher.

Without oxidation, Kc=12, t=2 hours

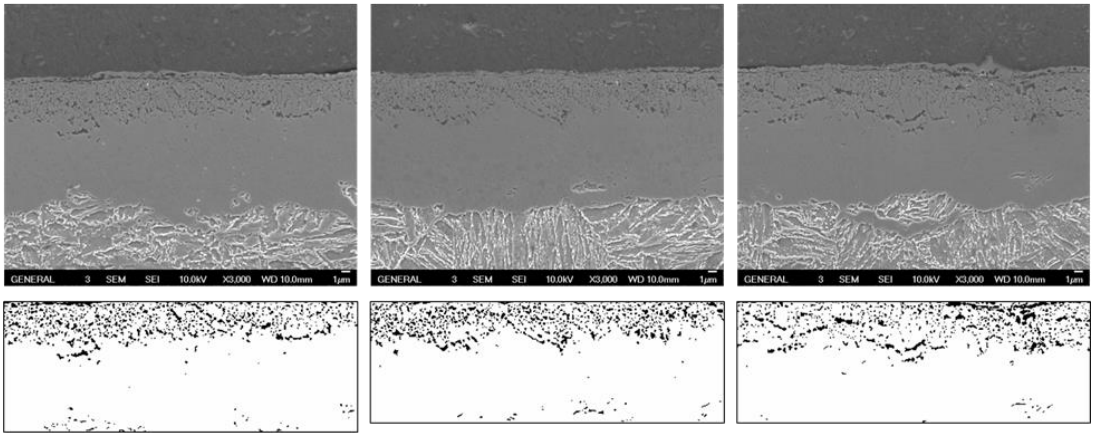

Without oxidation, Kc=12, t=4 hours

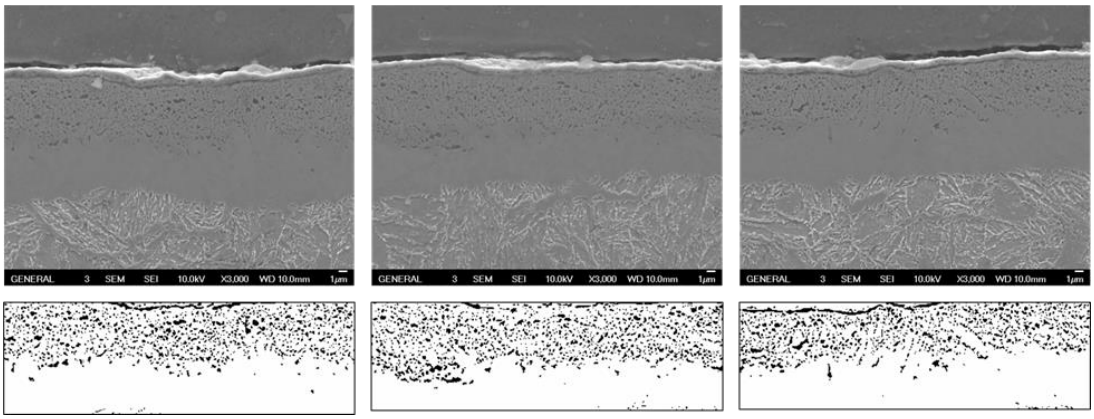

Figure 41 Porosity analysis on the samples processed with Kc=12, without oxidation

Table 13 Porosity analysis results comparison

Kc	Process time (hour)	Average Pore size (um^2)		% Area in porous layer	
		With oxidation	Without oxidation	With oxidation	Without oxidation
Kc=0	2 hours		0.014		34.99
	4 hours	0.016	0.021	32.34	39.84
Kc=9	2 hours	0.012	0.023	36.28	37.96
	4 hours	0.014	0.035	48.71	42.42
Kc=12	2 hours	0.015	0.020	22.65	29.11
	4 hours	0.022	0.032	42.53	59.01

Diffusion zone microhardness profile and N & C concentration profile

The influence of the pre & post oxidation process on the diffusion zone was also assessed by measuring and comparing the microhardness profile and N & C concentration profiles in the diffusion zone.

The microhardness profile in the diffusion zone was measured by line scans from sample surface to the core. *Figure 42* compares the microhardness profiles for the samples processed for the sample durations (left plot: samples processed for 2 hours, right plot: samples processed for 4 hours), as we can see, after the same process duration, the samples with the same oxidation condition but different carburizing potentials have close microhardness profiles. Typically, the oxidized samples have slightly higher local hardness compared to the ones without oxidation process.

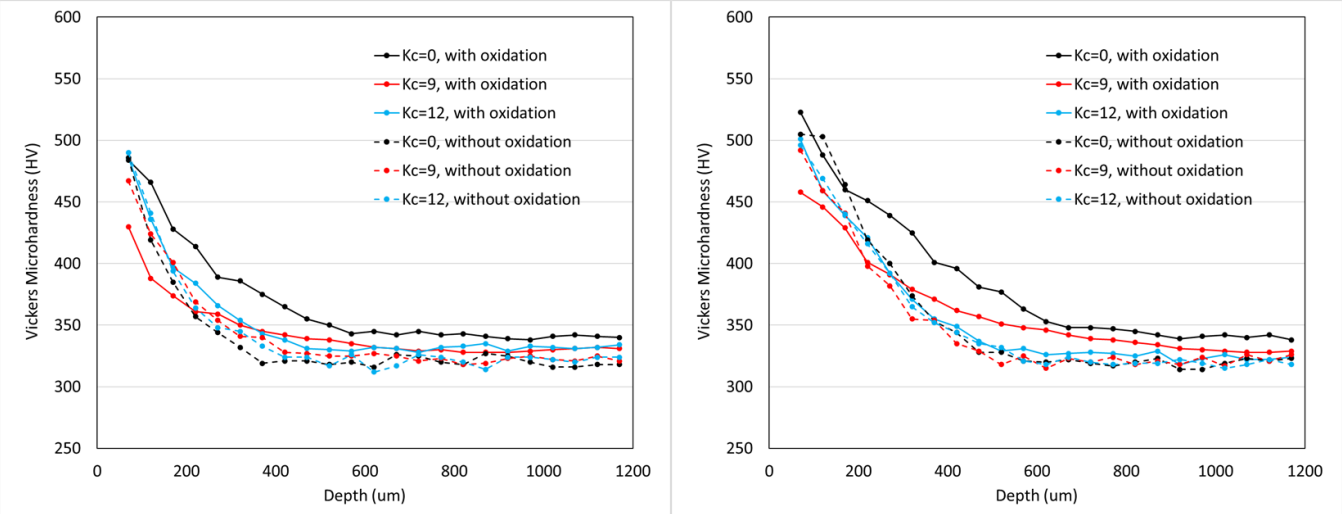

Figure 42 Diffusion zone microhardness profile comparison (left: samples processed for 2 hours, right: samples processed for 4 hours)

The nitrogen and carbon concentration profiles were measured layer by layer with OES. The compound layer on the sample surface was removed by grinding prior to the measurement. After each measurement, a layer (around 50-70 μm) was removed to carry out the next measurement. The nitrogen and carbon concentration profiles for the nitrocarburized samples with/without oxidation process were measured and compared.

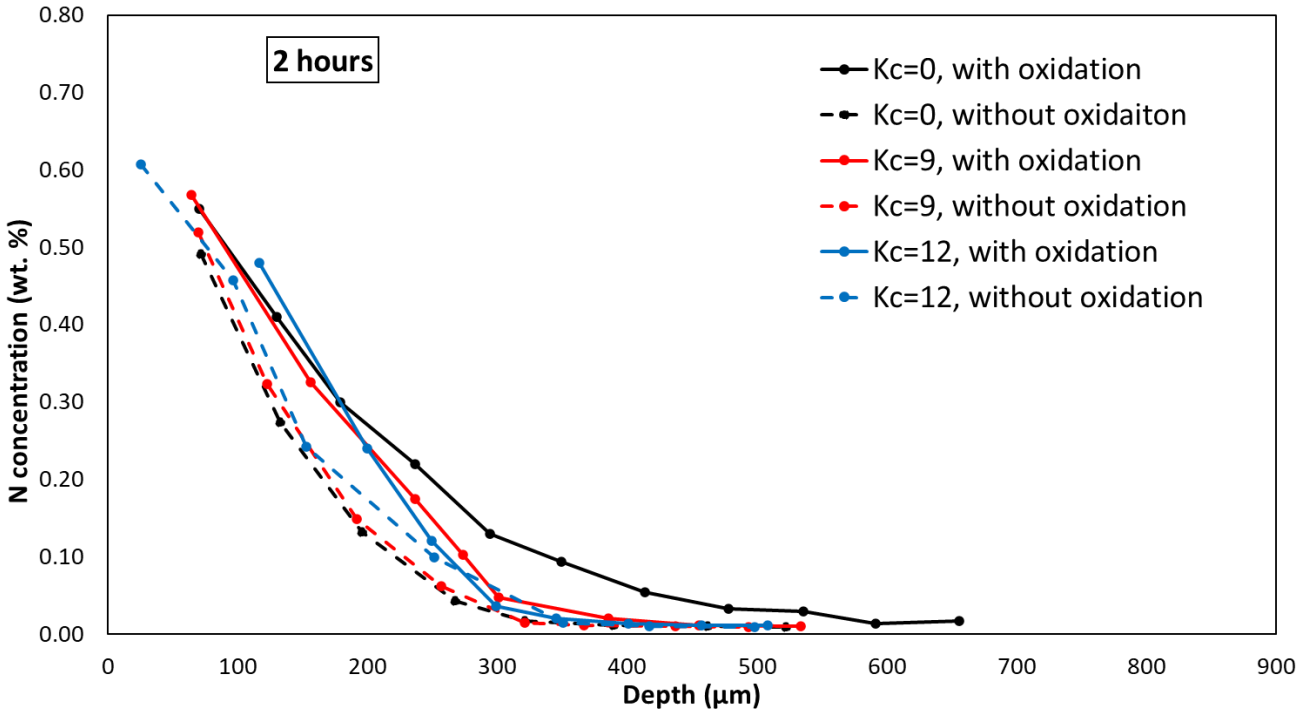

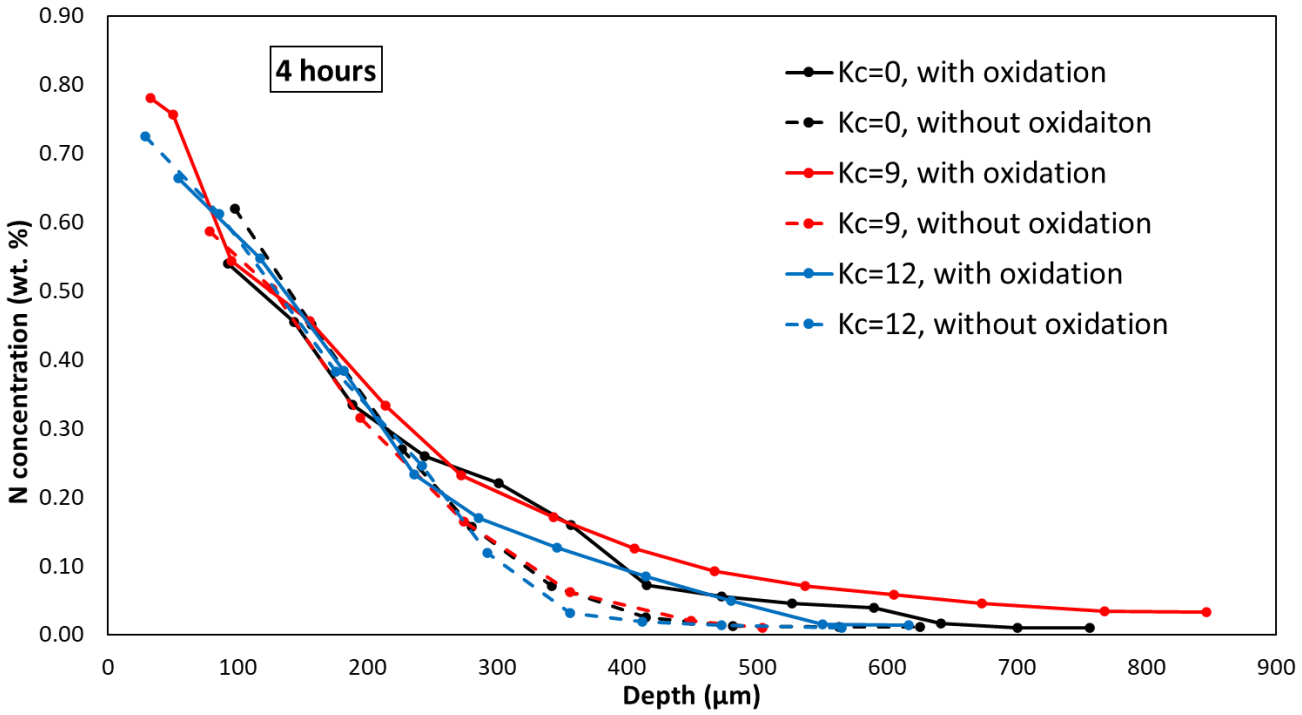

Figure 43 Nitrogen concentration profiles comparison for the samples with/without oxidation process

Figure 43 compares the measured nitrogen concentration profiles for the nitrocarburized samples with/without oxidation process. In the first plot, the samples processed for 2 hours at different carburizing potential conditions were compared. The solid lines indicate the samples with pre & post oxidation process, while the dashed lines indicate the samples

without any oxidation process. For the same oxidation condition, the samples processed with different carburizing potential have overlapped nitrogen concentration profiles. However, a slightly higher local nitrogen content was observed for the samples with pre & post oxidation process, which agrees with the tendency in the microhardness profile test results. After 4 hours, as shown in the second plot, the local nitrogen content difference between the samples with oxidation and the samples without oxidation was eliminated. For the carbon concentration in the diffusion zone, the measured results show that there is no change of carbon content in the diffusion zone during the nitrocarburizing process. Only slight decarburizing phenomenon near the surface is observed in the samples with 2 hours process duration.

Conclusions

AISI 4140 steel samples with tempered martensite microstructure were nitrocarburized with/without pre and post oxidation process. The total weight gain was measured by recording the individual sample weight before and after the nitrocarburizing process. The results indicate that at the same carburizing potential and process duration condition, samples without oxidation process usually have higher weight gain. The compound layer morphology is observed with SEM and the average compound layer thickness is measured from micrographs. The results show that the compound layer thickness of the samples without oxidation process is close to the total thickness of the oxide layer (2-4 μm) and the compound layer underneath. From the EDS mapping patterns, the compound layer formed on the oxidized samples have better uniformity than the samples without oxidation. With XRD and Rietveld refinement, the compound layer phase constitution is analyzed, the oxidized sample has Fe_3O_4, ε – $Fe_{2-3}(C,N)$ and γ' – Fe_4N nitrides in the compound layer while the samples without oxidation only have ε – $Fe_{2-3}(C,N)$ and γ' – Fe_4N nitrides. Regarding to the diffusion zone, the local microhardness and local nitrogen content in the oxidized sample is slightly higher than the sample without oxidation process after 2 hours process time, but this difference is eliminated after longer process time.

Acknowledgement

The support of the Center of Heat Treating Excellence (CHTE) at Worcester Polytechnic Institute and the member companies is greatly appreciated. Special thanks to Bodycote for carrying out the pre-FNC heat treatment and the FNC trials

References

1. Friehling, P.B., F.W. Poulsen, and M.A. Somers, *Nucleation of iron nitrides during gaseous nitriding of iron; effect of a preoxidation treatment.* International Journal of Materials Research, 2022. **92**(6): p. 589-595.
2. Mittemeijer, E.J. and M.A. Somers, *Thermochemical surface engineering of steels*. 2014: Woodhead Publishing Cambridge.
3. Dossett, J. and G. Totten, *Fundamentals of nitriding and nitrocarburizing.* ASM Handbook: Steel Heat Treating Fundamentals and Processes; ASM International: Materials Park, OH, USA, 2013: p. 619.
4. Pye, D., *Practical nitriding and ferritic nitrocarburizing*. 2003: ASM international.
5. Winter, K.-M., *Gaseous nitriding: in theory and in real life.* Technical Paper of United Process Controls, Process-Electronic GmbH, Heiningen, Germany, 2009.
6. Ogale, S., et al., *Synthesis of Iron Oxynitride by Nitrogen Ion Implantation of Iron Oxide.* MRS Online Proceedings Library (OPL), 1988. **100**: p. 261.
7. Strydom, I.l.R., A. Wells, and N. Ferreira, *Surface layers on fe formed during plasma nitriding studied by XPS and reflection EELS.* Surface and interface analysis, 1988. **12**(3): p. 211-217.
8. Inia, D., et al., *Nitrogen uptake and rate-limiting step in low-temperature nitriding of iron.* Journal of applied physics, 1999. **86**(2): p. 810-816.
9. Schreiner, A., *The Influence of Passivating Layers on the Thermo-Chemical Diffusion.* Hart.-Tech. Mitt., 1986. **41**(6): p. 399-410.
10. Spies, H.-J. and F. Vogt, *Gasoxinitrieren hochlegierter stähle.* HTM Journal of Heat Treatment and Materials, 1997. **52**(6): p. 342-349.
11. Baranowska, J. and M. Wysiecki, *Influence of surface pretreatment on case formation during gaseous nitriding.* Surface and Coatings Technology, 2000. **125**(1-3): p. 30-34.
12. Friehling, P.B. and M.A. Somers, *On the effect of preoxidation on nitriding kinetics.* Surface Engineering, 2000. **16**(2): p. 103-106.
13. Alsaran, A., et al., *Effect of post-oxidizing on tribological and corrosion behaviour of plasma nitrided AISI 5140 steel.* Surface and Coatings Technology, 2004. **176**(3): p. 344-348.
14. Wännman, S., *Influence of Nitrocarburization on Thermo-Mechanical Fatigue Properties*. 2018, License Thesis), Retrieved from http://www. divaportal. se/smash/get/diva2.
15. Sola, R., et al., *Development of post-oxidation treatments to improve wear and corrosion resistance.* la metallurgia italiana, 2008.

16. Yilmaz, U., et al., *Effect of nitrocarburizing and post-oxidation processes on the microstructure and surface properties of AISI 4140 steel.* JOURNAL OF POLYTECHNIC-POLITEKNIK DERGISI, 2022.
17. Sola, R., et al., *Improvement of wear and corrosion resistance of ferrous alloys by post-nitrocarburizing treatments.* Metallurgical Science and Tecnology, 2011. **29**(2).

Chapter 5: Flux analysis of nitrogen and carbon during nitriding and FNC heat treating

Haoxing You, Richard D. Sisson Jr.
Center for Heat Treating Excellence (CHTE)
Worcester Polytechnic Institute; 100 Institute Rd; Worcester, MA 01609, USA

Abstract

As part of a project to develop simulation software for the gaseous FNC process, an experimental investigation of the total fluxes of nitrogen and carbon was conducted. The total mass increase of each test sample was measured and converted to total flux and flux as a function of time. The nitrogen and carbon concentration profiles were measured in the hardened case. The weight gain due to compound layer growth and the weight gain in the case were analyzed. The results are presented as a function of K_N and K_C in the gas atmosphere.

Introduction

As an important surface treatment method, ferritic nitrocarburizing (FNC) is widely used to improve the wear, corrosion resistance and fatigue endurance of the steels [1]. During typical ferritic nitrocarburizing of steels, atomic nitrogen and carbon are introduced into the steel surface. A compound layer (up to 20 μm) composed of ε-$Fe_{2\text{-}3}$(C,N) and γ'-Fe_4N phase will form at the surface, which can significantly improve the wear and corrosion resistance. Underneath the compound layer, the diffusion zone (case) with dispersed alloy (carbon-)nitrides can improve the fatigue endurance of the steel [2-4].

Gaseous ferritic nitrocarburizing is widely used in industry since the process is easy to control by controlling the gas composition and gas flow rate during the process [5]. the mechanical properties of the steel after FNC process are determined by the thickness and microstructure of the compound layer and diffusion zone, which are controlled by several critical process parameters such as temperature, process time, nitriding potential, and carburizing potential [6]. Traditionally, the industry use try and error method to determine specific process parameters[7]. To improve the performance reliability, the current project aims to establish a computational model capable of predicting the compound layer

composition and growth kinetics, as well as case depth with given process parameters for specific alloys.

As part of the project, gaseous FNC trials with different carburizing potentials and different process times were conducted. The weight gain and total flux of nitrogen and carbon during the process was investigated. The weight gain from the compound layer growth was determined based on the phase composition data. The weight gain in the diffusion zone was estimated based on the nitrogen and carbon concentration profiles in the case. The estimated weight gain in the compound layer and diffusion zone has good agreement with the experimentally measured results.

Experiment

In the current project, AISI 4140 was chosen as the material for the trial. The steel was quenched and furnace tempered at 565 ℃ for 2 hours. After pre-FNC heat treatment, the microstructure of the steel was characterized as tempered martensite, with hardness measured as 34 HRC. The samples were machined into cylinder disks with a diameter of 1.25 inches and a thickness of 1 cm, maintaining the same surface finish after machining. Each sample was drilled with a small hole for hanging in the furnace and engraved with a unique sample ID (Figure 44). Subsequently, the samples were ultra-sonically cleaned with acetone and dried immediately. Then, the weight of each sample was recorded before the FNC trial.

Figure 44 FNC sample after machining and cleaning

The FNC trials were carried out at Bodycote, with two different carburizing potentials (zero and medium) and two different process durations (2 hours and 4 hours) for various trials. The detailed process parameters for each trial are listed in

Table 14. Each trial group consisted of 5 samples for characterization purposes. After the FNC trials, the samples were characterized for flux analysis. The weight of each sample was measured to determine the total weight gain and total flux during the FNC process.

Table 14 Process parameters for FNC trials

Trial ID	Material	Nitriding potential (K_N), $atm^{-1/2}$	Temperature (℃)	Carburizing potential (K_C)	Process time (hours)
Trial 1	AISI 4140	4	579 ℃	Zero	2
Trial 2					4
Trial 3				Medium	2
Trial 4					4

X-ray diffraction (XRD) analysis was performed on the original surface of the samples using a PANalytical X-ray diffractometer with Cr-Kα radiation at 30 kV voltage and 55 mA current, which provided information about the phase composition within approximately 10 μm of the compound layer. Rietveld Refinement was applied to the XRD patterns to quantify the phase fractions in the compound layer. In addition, cross-sections of the samples were observed using Nikon EPIPHOT optical microscopy and JSM 700F scanning electron microscopy (SEM). The average thickness of the compound layer was measured based on cross-sectional optical micrographs with ImageJ software. Microhardness profiles in the diffusion zone were measured by Wilson VH 3300 Hardness Tester with a 0.5 kgf load. Furthermore, the nitrogen and carbon concentration profiles in the diffusion zone were determined by optical emission spectrometer (OES) with a layer-by-layer method.

Results and Discussion

Total weight gain and flux

The weight gain of each sample and the average weight gain for each trial group were determined by weighing the samples before and after the FNC trial. The results are detailed in Table 15. The total flux of each sample during the FNC process was calculated with Equation 1. The average total flux for each trial group was also determined and listed in Table 15.

$$J_{total} = \frac{m_A - m_B}{At} \quad (1)$$

J_{total} – total flux, g/m^2*h

m_A – weight after FNC trial, g

m_B – weight before FNC trial, g

A – surface area of the sample, m^2

t – process time, h

Flux analysis as a function of time was also conducted for different carburizing potential conditions. The average flux within specific time durations (0~2 hours and 2~4 hours) was calculated as shown in Equation 2. The results of flux analysis as a function of time for different carburizing potentials are presented in Figure 45. During the 0~2 hour duration, the average flux for medium carburizing potential was higher than that for zero carburizing potential. However, during the 2-4 hour duration, the average flux for zero carburizing potential was higher.

$$J_{1\sim2} = \frac{\Delta m_2 - \Delta m_1}{A\Delta t} \quad (2)$$

$J_{1\sim2}$ – average flux between time 1 and time 2, g/m^2*h

Δm_1 – weight gain at time 1, g

Δm_2 – weight gain at time 2, g

Δt – time duration between time 1 and time 2, h

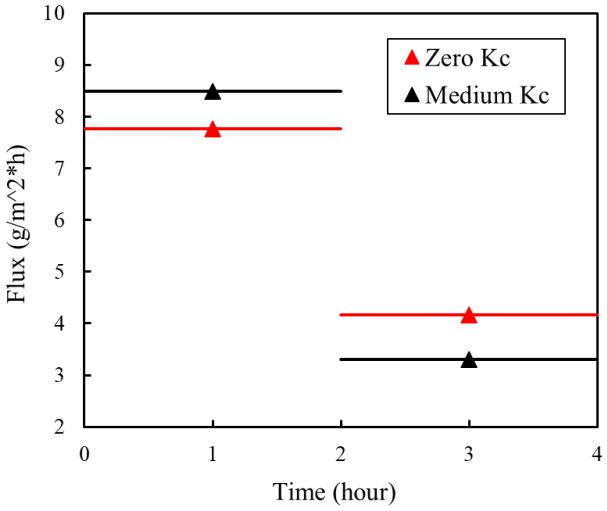

Figure 45 Flux calculated as function of time for different carburizing potentials

Weight gain in the compound layer

To measure the thickness of the compound layers formed in different trial groups, the samples were cut, metallurgically mounted, and ground and polished to 0.5 um diamond suspension, and then etched in 2% Nital. The cross-section of each sample was observed under optical microscopy and SEM. The micrographs of the samples from different trial groups are shown in Figure 46.

The compound layer, indicated by the region between the two red solid lines in the optical micrographs, typically consists of a porous top layer (between the first solid line and the dashed line) and a dense layer beneath it. The thickness of the compound layer was measured at different locations, and an average value was obtained for each sample.

To measure the microhardness profiles and case depth of the diffusion zone, a line scan from the sample surface to the core was performed on each as-polished sample. 23 indents were measured on each line scan at intervals of 50 μm. The microhardness profiles measured for various samples are shown in Figure 47. Based on the microhardness profiles, the case depth for each sample was determined at the depth where the microhardness was 50 HV higher than the average core hardness (322 HV). The results of average compound layer thickness and case depth measurements for all trial groups are summarized in Table 16.

Figure 48 displays the XRD patterns with the Rietveld Refinement results for various samples. The information of compound layer phase fractions is detailed in Table 17.

By combining the compound layer thickness and phase fraction information, the total weight of the compound layer can be estimated using Equation 3. The results are summarized in Table 18. Subsequently, the weight gains due to nitrogen absorption in the ε and γ' phase in the compound layer can be estimated using Equation5 and Equation 6 and the results are detailed in Table 18.

$$m_{CL} = A \times T_{CL} \times \rho_{CL} \quad (3)$$

$$\rho_{CL} = \rho_{\varepsilon} \times \varepsilon\% + \rho_{\gamma'} \times \gamma'\% \quad (4)$$

$$m_{N,\varepsilon} = m_{CL} \times \varepsilon\% \times \%N_{\varepsilon} \quad (5)$$

$$m_{N,\gamma'} = m_{CL} \times \gamma'\% \times \%N_{\gamma'} \quad (6)$$

$$m_{N,CL} = m_{N,\varepsilon} + m_{N,\gamma'} \quad (7)$$

m_{CL} – total weight of the compound layer, g

A – sample surface area, cm^2

T_{CL} – compound layer thickness, cm

$\rho_{\varepsilon}/\rho_{\gamma'}$ – density of ε/γ' phase, g/cm^3 [8, 9]

$\varepsilon\%/\gamma'\%$ – fraction of ε/γ' phase in the compound layer

$m_{N,\varepsilon}/m_{N,\gamma'}$ – weight of nitrogen in the ε/γ' phase in the compound layer, g

$\%N_{\varepsilon}/\%N_{\gamma'}$ – weight fraction of nitrogen in ε/γ' phase

$m_{N,CL}$ – total nitrogen weight gain in the compound layer, g

Table 15 Total weight gain and total flux for each sample and average value for each trial group

Trial ID	Sample ID	Weight before FNC, g	Weight after FNC, g	Total weight gain, g	Average total weight gain, g	Total flux, g/m^2*h	Average total flux, g/m^2*h
Trial 1	401	77.3991	77.4381	0.0390	0.0401	7.5552	7.7606
	402	78.8391	78.8788	0.0397		7.6908	
	403	78.1279	78.1687	0.0408		7.9039	
	404	80.2298	80.2709	0.0411		7.9620	
	405	77.8831	77.9228	0.0397		7.6908	
Trial 2	406	79.3933	79.4552	0.0619	0.0616	5.9957	5.9628
	407	78.2471	78.3091	0.0620		6.0054	
	408	78.1192	78.1803	0.0611		5.9182	
	409	77.1375	77.1982	0.0607		5.8795	
	410	80.6445	80.7066	0.0621		6.0151	
Trial 3	411	79.7068	79.7511	0.0443	0.0438	8.5819	8.4928
	412	78.1951	78.2386	0.0435		8.4270	
	413	77.6487	77.6925	0.0438		8.4851	
	414	77.1049	77.1488	0.0439		8.5045	
	415	78.6016	78.6453	0.0437		8.4657	
Trial 4	416	81.5831	81.6522	0.0691	0.0609	6.6931	5.9008
	417	79.4165	79.4751	0.0586		5.6761	
	418	76.5101	76.5689	0.0588		5.6955	
	419	77.1051	77.1652	0.0601		5.8214	
	420	74.8141	74.8721	0.0580		5.6180	

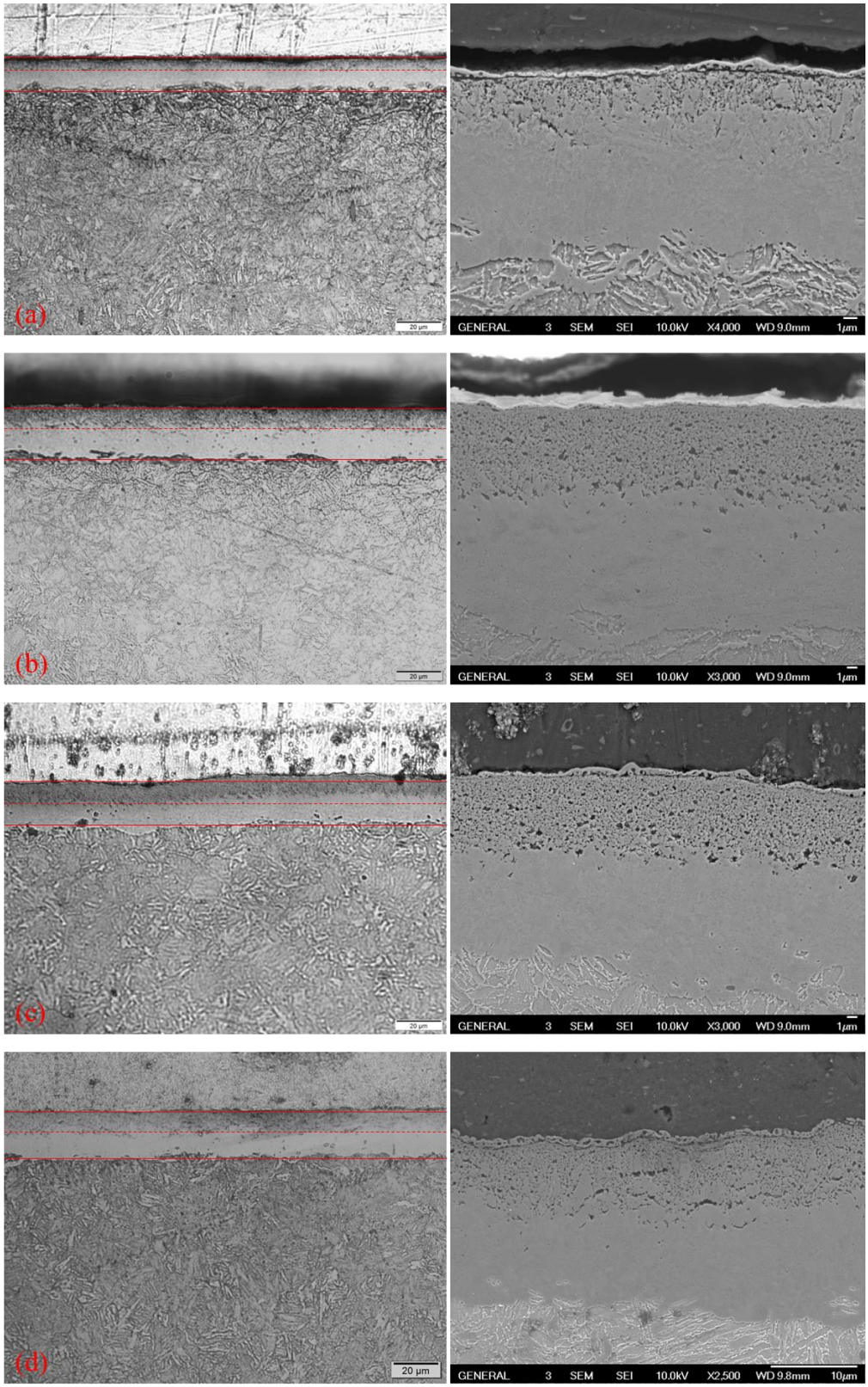

Figure 46 Optical micrographs at 500X magnification (left) and SEM micrographs (right) for samples (a) zero Kc, 2 hours; (b) zero Kc, 4 hour; (c) medium Kc, 2 hours; (d) medium Kc, 4 hours

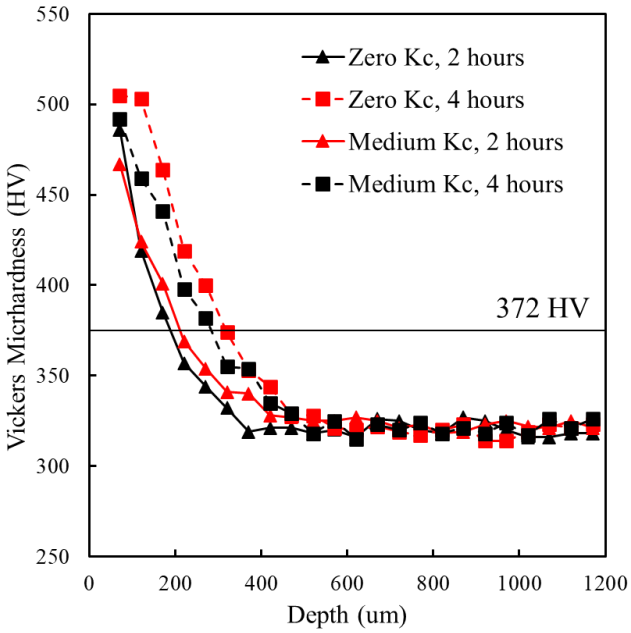

Figure 47 Microhardness profiles for various samples

Table 16 Average compound layer thickness and case depth measured for each trial group

Trial ID	Carburizing potential	Time (hour)	Compound layer thickness (um)	Case depth (um)
Trial 1	Zero	2	13.52	198
Trial 2		4	22.43	318
Trial 3	Medium	2	16.73	225
Trial 4		4	23.56	285

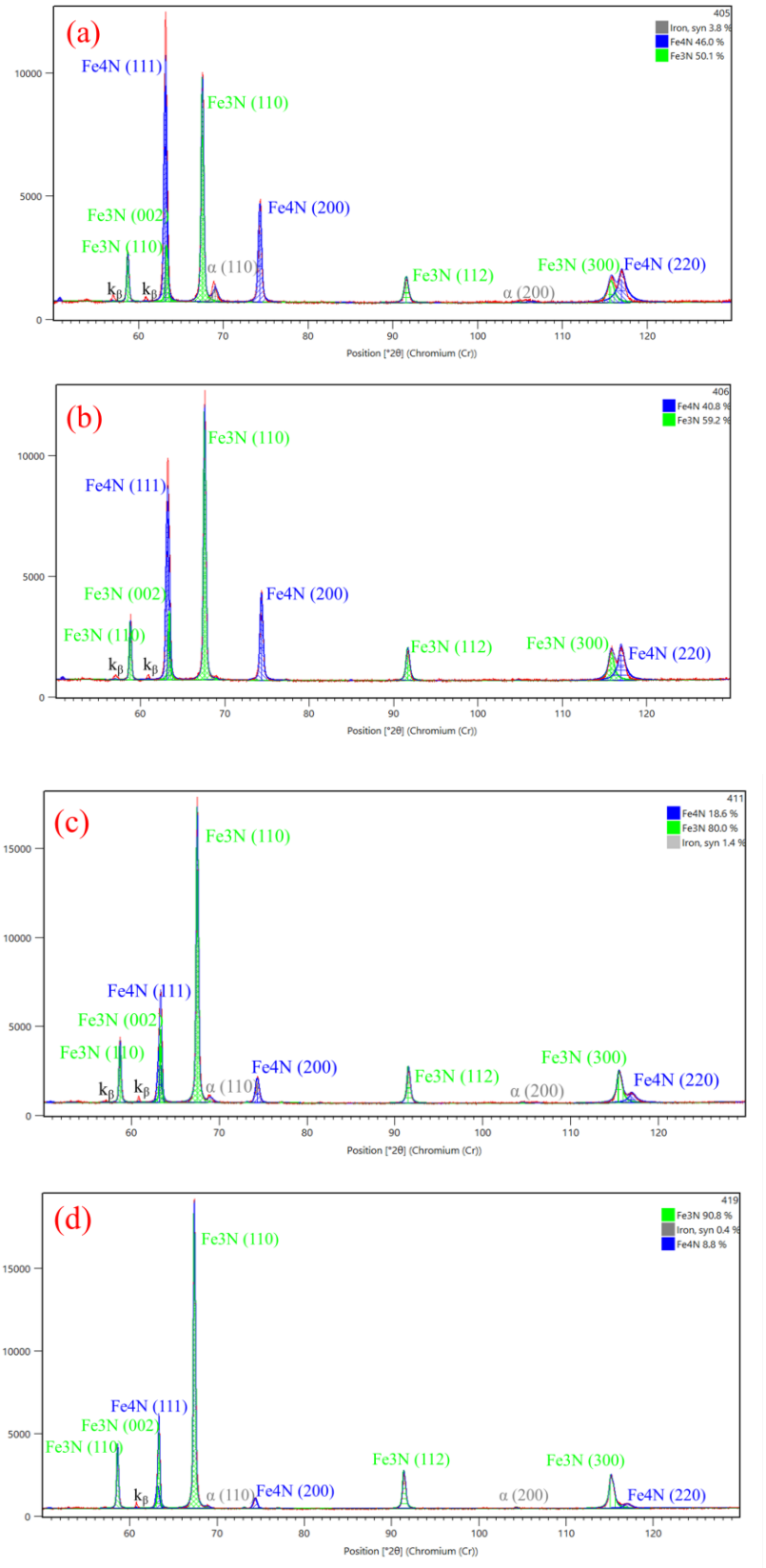

Figure 48 XRD patterns and Rietveld Refinement results

Table 17 Phase fraction in the compound layer from Rietveld Refinement

Trial ID	Carburizing potential	Time (hour)	α-iron	ε-Fe_3N	γ'-Fe_4N
Trial 1	Zero	2 hr	3.8%	50.1%	46%
Trial 2		4 hr	0	59.2%	40.8%
Trial 3	Medium	2 hr	1.4%	80.0%	18.6%
Trial 4		4 hr	0.4%	90.8%	8.8%

Weight gain in the case

To estimate the weight gain in the diffusion zone, nitrogen and carbon concentration profiles were measured using OES with a layer-by-layer method. Three tests were performed at different locations on each layer, and the average values of nitrogen and carbon contents were obtained. Before the first layer measurement, the original surface of the sample was ground, and a 30~50 μm thick layer was removed. After each layer measurement, a 50-100 μm thick layer was removed. The results of nitrogen and carbon concentration profiles in the diffusion zone are shown in Figure 49. The experimentally measured nitrogen and carbon concentration profiles are indicated by the black and red dashed lines, respectively. The nitrogen concentration profiles can be fitted with the Error Function as Equation 8 by setting an appropriate nitrogen diffusivity value. The nitrogen concentration profiles fitted with the Error Function are plotted as solid black lines in Figure 49. The carbon concentration was close to the original value and uniform within the diffusion zone as shown in Figure 49.

$$C = N_0 \operatorname{erf}\left(\frac{x}{\sqrt{4Dt}}\right) \quad (8)$$

C – nitrogen concentration at depth x, wt. %

N_0 – nitrogen concentration at the 1st layer measurement, wt. %

x – depth from the surface, m

D – nitrogen diffusivity in the diffusion zone,m^2/s

t – process time, s

The weight of nitrogen in the diffusion zone can be calculated by integrating the Error Function in the diffusion zone, then, multiplied by the sample surface area and material density, as indicated in Equation 9. The integral of the Error Function was numerically solved by applying the trapezoidal rule with MATLAB (code appended). The calculated weight of nitrogen in the diffusion zone is listed in Table 18.

$$m_{N,case} = \int_a^b N_0 \operatorname{erf}\left(\frac{x}{\sqrt{4Dt}}\right) dx * A * \rho \qquad (9)$$

As observed, the calculated weight gain due to nitrogen absorption is close to the experimentally measured total weight gain. The slight difference between the experimentally measured weight gain and the estimated total weight of nitrogen could be the carbon absorbed into the compound layer. Additionally, with zero carburizing potential, the weight of nitrogen in the compound layer was lower than that in the diffusion zone, whereas it was higher with medium carburizing potential.

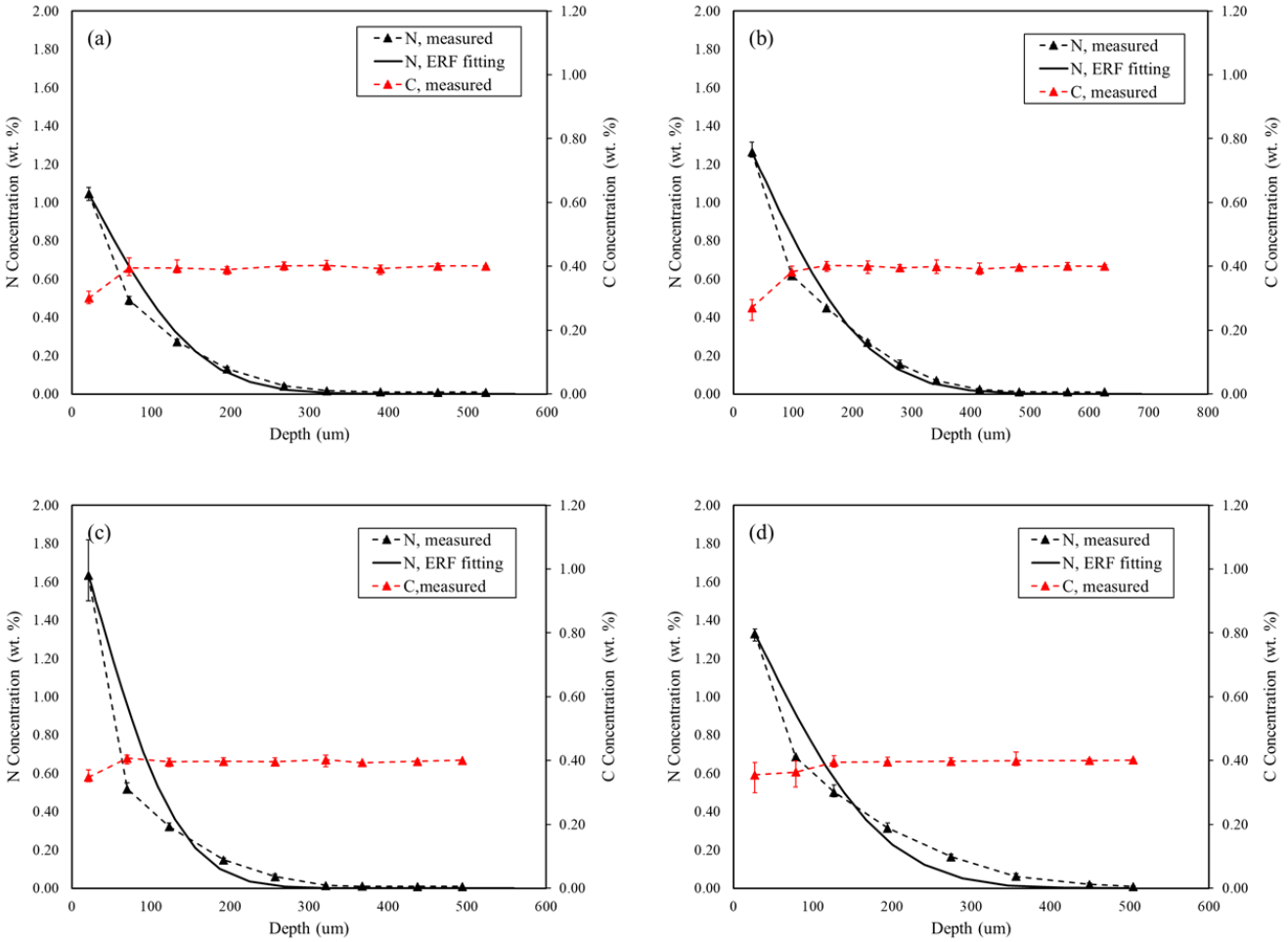

Figure 49 N and C concentration profiles measured by OES and Error Function fitted N concentration profiles

Table 18 Summarized calculation results of weight gain in the compound layer and diffusion zone

Trial ID	K_C	Weight of CL (m_{CL}), g	Weight of N in ε phase ($m_{N,\varepsilon}$), g	Weight of N in γ' phase ($m_{N,\gamma'}$), g	Total weight of N in CL ($m_{N,CL}$), g	Weight of N in case ($m_{N,case}$), g	Experimentally measured total weight gain, g	Calculated total weight gain, g	$m_{N,CL}/m_{N,case}$
Trial 1	Zero	0.2389	0.0092	0.0065	0.0157	0.0240	0.0401	0.0397	0.6548
Trial 2		0.4119	0.0188	0.0099	0.0287	0.0314	0.0616	0.0601	0.9153
Trial 3	Medium	0.3019	0.0186	0.0033	0.0220	0.0206	0.0438	0.0426	1.0659
Trial 4		0.4288	0.0301	0.0022	0.0323	0.0274	0.0609	0.0597	1.1778

Conclusions

In the present study, FNC trials with different carburizing potentials and different process times were carried out and the samples were characterized. The total weight gain and flux during the FNC process were determined by recording the weight of each sample before and after the FNC trial. The weight gain due to nitrogen absorption in the compound layer was determined based on the compound layer thickness and compound layer phase fraction information. The weight gain in the diffusion zone was calculated by integrating the Error Function fitted nitrogen concentration profiles. The estimated weight gain shows good agreement with the experimentally measured results.

Acknowledgements

The support of the Center Heat Treating Excellence (CHTE) at Worcester Polytechnic Institute and the member companies is gratefully acknowledged. Special thanks to Bodycote for carrying out the pre-FNC heat treatment and FNC trials in the present work.

References

1. Pye, D., *Practical nitriding and ferritic nitrocarburizing*. 2003: ASM international.
2. Winter, K.-M., *Gaseous nitriding: in theory and in real life.* Technical Paper of United Process Controls, Process-Electronic GmbH, Heiningen, Germany, 2009.
3. Dossett, J. and G. Totten, *Fundamentals of nitriding and nitrocarburizing.* ASM handbook: steel heat treating fundamentals and processes. Materials Park (OH): ASM International, 2013: p. 619.
4. Somers, M.A., *Thermodynamics, kinetics and microstructural evolution of the compound layer; A comparison of the states of knowledge of nitriding and nitrocarburising.* HEAT TREATMENT OF METALS-BIRMINGHAM-, 2000. **27**(4): p. 92-101.
5. Mittemeijer, E.J. and M.A. Somers, *Thermochemical surface engineering of steels*. 2014: Woodhead Publishing Cambridge.
6. Leineweber, A., T. Gressmann, and E. Mittemeijer, *Simultaneous control of the nitrogen and carbon activities during nitrocarburising of iron.* Surface and Coatings Technology, 2012. **206**(11-12): p. 2780-2791.
7. Mittemeijer, E.J. and M.A. Somers, *Thermodynamics, kinetics, and process control of nitriding.* Surface Engineering, 1997. **13**(6): p. 483-497.
8. Jacobs, H., D. Rechenbach, and U. Zachwieja, *Structure determination of γ'-Fe4N and ϵ-Fe3N.* Journal of Alloys and Compounds, 1995. **227**(1): p. 10-17.

9. Yang, J., et al., *Effects of nitrogen in the (Fe1− xNix) 4N compounds (0≤ x≤ 0.6).* physica status solidi (a), 1996. **153**(2): p. 307-312.

Publications and presentations

Publications:

1. You, Haoxing, Mei Yang, Yishu Zhang, and Richard D. Sisson Jr. "Austempering and Bainitic Transformation Kinetics of AISI 52100." In HT2021, pp. 203-211. ASM International, 2021. Accepted by Journal of Materials Engineering and Performance.
2. You, Haoxing, and Richard D. Sisson Jr. “Flux Analysis of Nitrogen and Carbon During Nitriding and FNC Heat Treating.” In HT2023, 2023 HTS/Bodycote Best Paper in Heat Treating Awards.
3. Yang, Mei, Yishu Zhang, Haoxing You, Richard Smith, and Richard D. Sisson. "Hardening of Selective Laser Melted M2 Steel." Journal of Materials Engineering and Performance (2024): 1-9. (10.1007/s11665-024-09199-8).
4. Yang, Mei, Haoxing You, and Richard D. Sisson. "Nitriding and Ferritic Nitrocarburizing of Quenched and Tempered Steels." Proceedings of the HT (2021): 110-116.
5. Sisson, Richard D., Mei Yang, and Haoxing You. "CHTE INTRODUCES SIMULATION SOFTWARE FOR GAS NITRIDING OF STEELS: NitrideTool software simulates the gas nitriding of steels to understand nitriding potential, temperature, time, and surface condition." Advanced Materials & Processes 178, no. 8 (2020): 64-67.

Presentations:

6. You, Haoxing, and Richard D. Sisson Jr. “Phase distributions in the compound layer of Ferritic Nitrocarburized (FNC) 4140 steel using alloy specific Kunze diagrams as a function of KN and KC in the heat treat gas atmosphere.” In HT 2023 (Detroit, MI)
7. You, Haoxing, and Richard D. Sisson Jr. “Flux analysis of nitrogen and carbon during nitriding and FNC Heat Treating.” In HT 2023 (Detroit, MI)
8. You, Haoxing, and Richard D. Sisson Jr. “Diffusion of nitrogen and carbon in tempered martensite.” In IMAT 2023 (Detroit, MI)
9. You, Haoxing, and Richard D. Sisson Jr. “Modelling of Ferritic Nitrocarburizing of Steels.” In 15th Furnaces North America conference, 2022 (Indianapolis, IN)
10. You, Haoxing, and Richard D. Sisson Jr. “Nitriding and Ferritic Nitrocarburizing of Quenched and Tempered Martensitic steels.” In IMAT 2022 (New Orleans, LA)

Appendix 1: Compound layer morphology of FNC samples

1st FNC trial with pre & post oxidation

Section 1: Kc=0 trials

AISI 4140

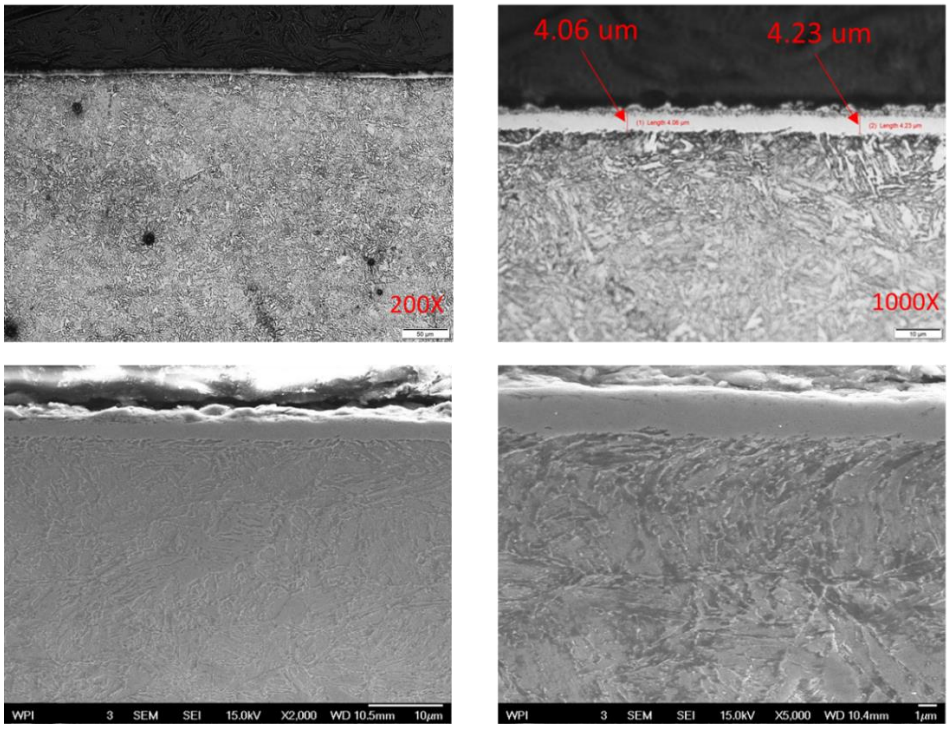

Figure 50 Compound layer of AISI 4140 sample (KN=4 atm^(-1/2), KC=0, t=1 hr)

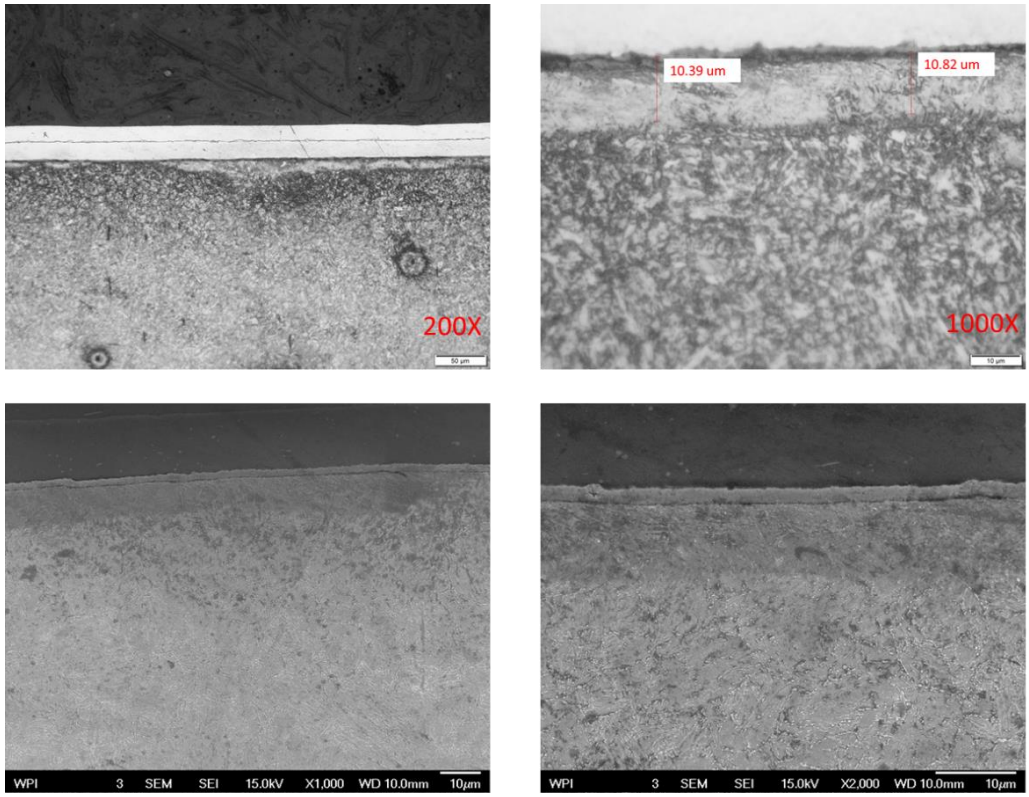

Figure 51 Compound layer of AISI 4140 sample (KN=4 atm^(-1/2), KC=0, t=2 hr)

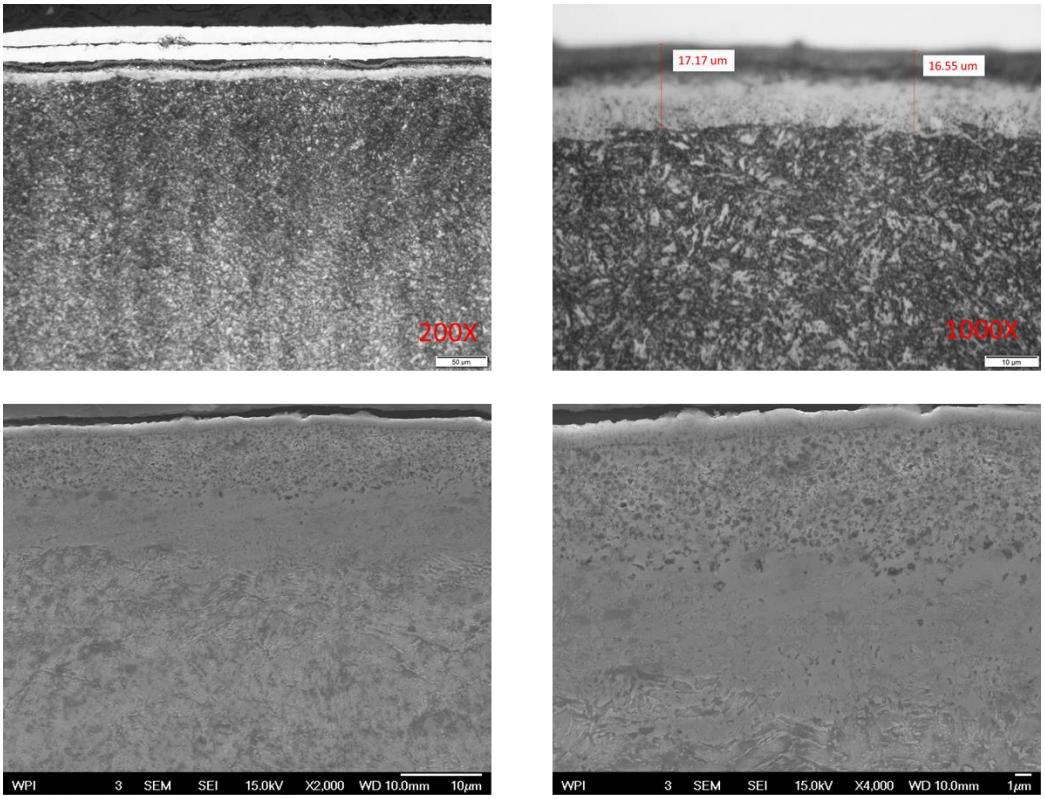

Figure 52 Compound layer of AISI 4140 sample (KN=4 atm^(-1/2), KC=0, t=4 hr)

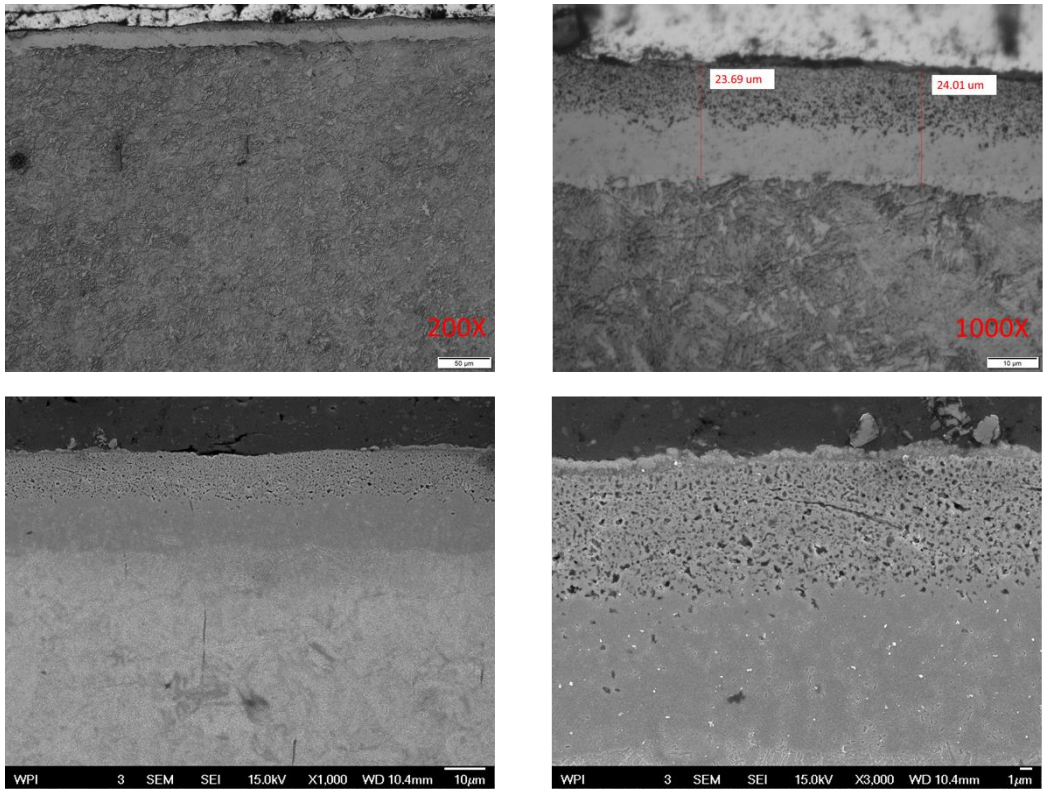

Figure 53 Compound layer of AISI 4140 sample (KN=4 atm^(-1/2), KC=0, t=4 hr)

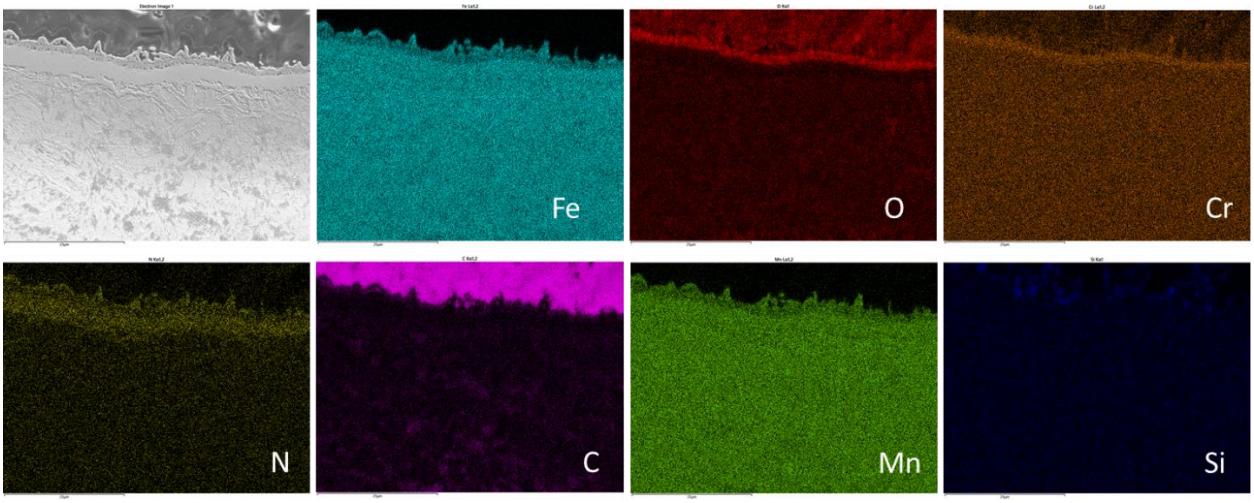

Figure 54 EDS mapping of AISI 4140 sample (KN=4 atm^(-1/2), KC=0, t=1 hr)

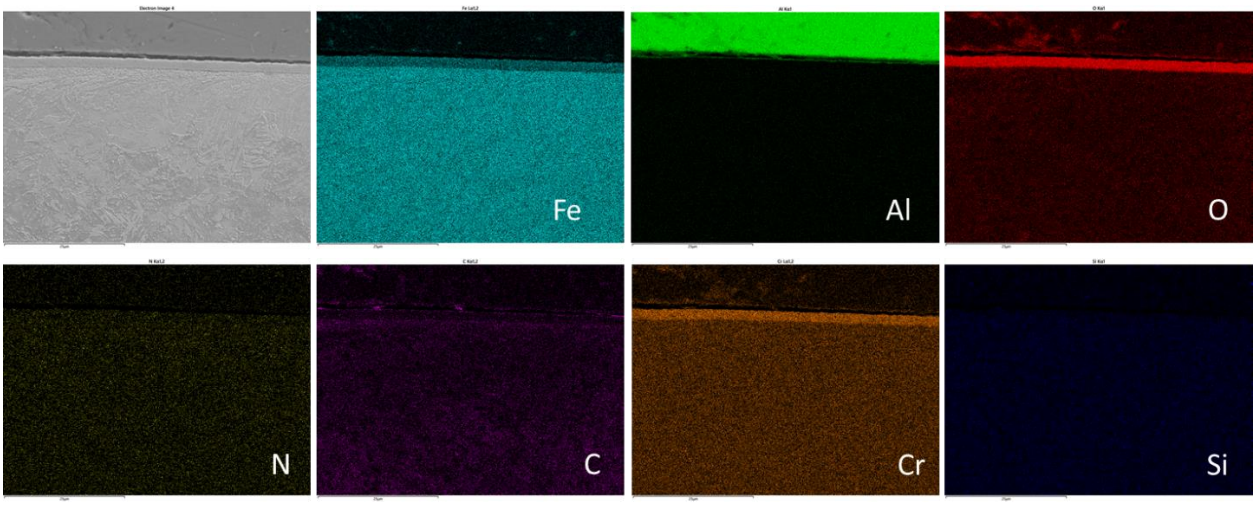

Figure 55 EDS mapping of AISI 4140 sample (KN=4 atm^(-1/2), KC=0, t=2 hr)

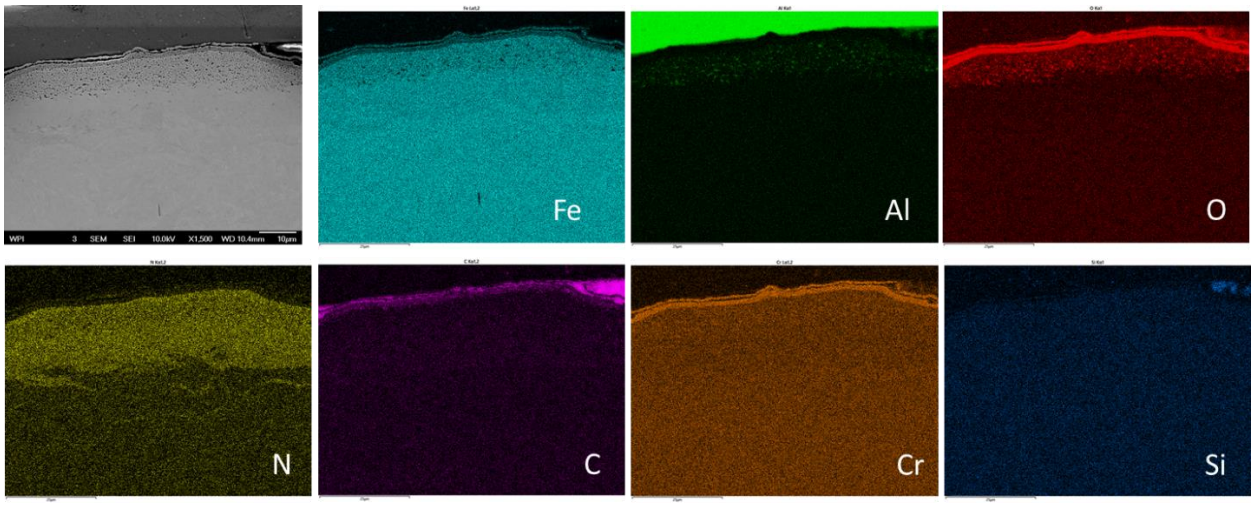

Figure 56 EDS mapping of AISI 4140 sample (KN=4 atm^(-1/2), KC=0, t=4 hr)

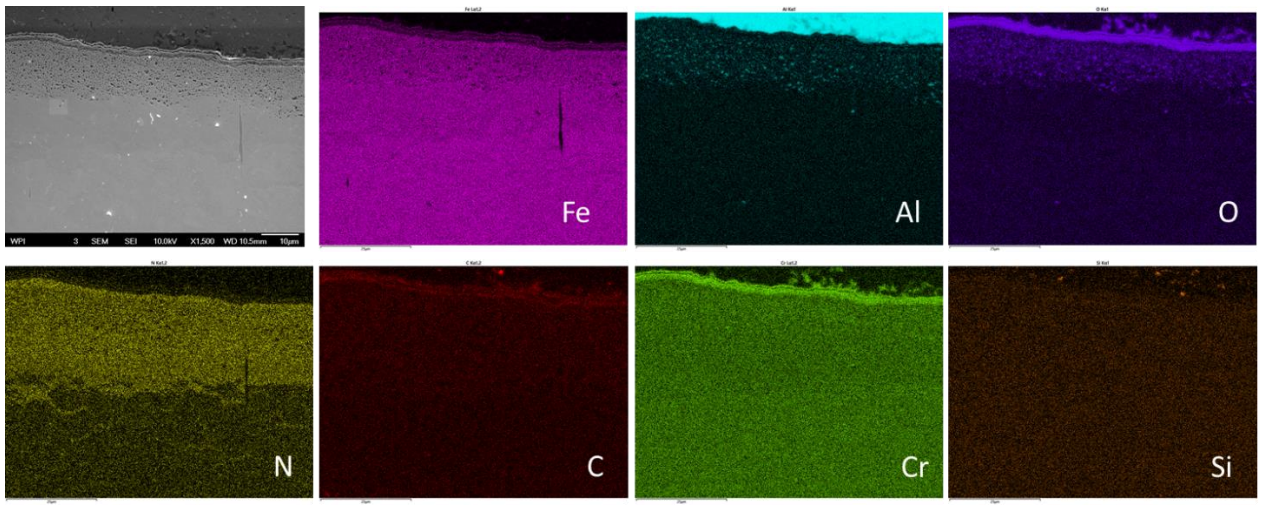

Figure 57 EDS mapping of AISI 4140 sample (KN=4 atm^(-1/2), KC=0, t=8 hr)

AISI 1018

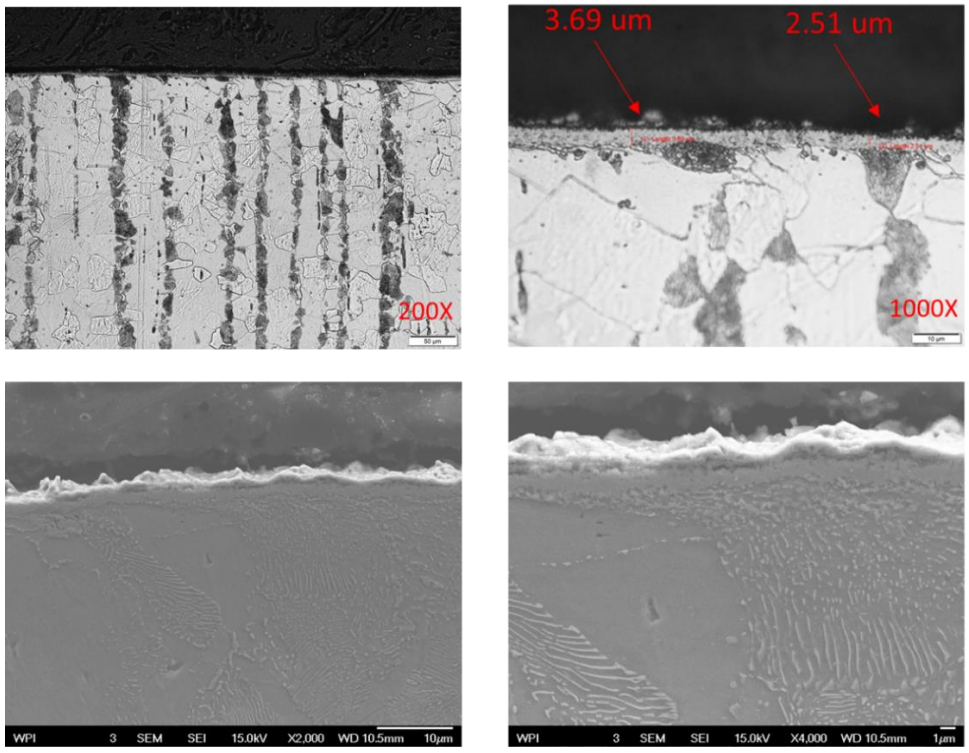

Figure 58 Compound layer of AISI 1018 sample (KN=4 atm^(-1/2), KC=0, t=1 hr)

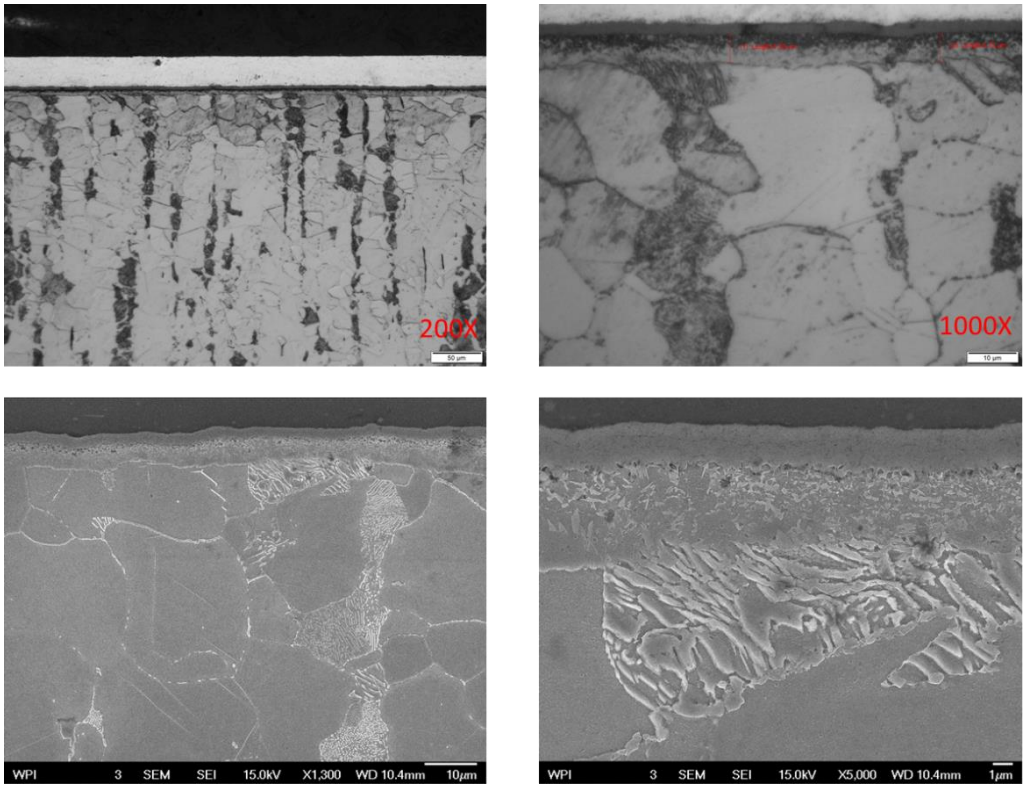

Figure 59 Compound layer of AISI 1018 sample (KN=4 atm^(-1/2), KC=0, t=2 hr)

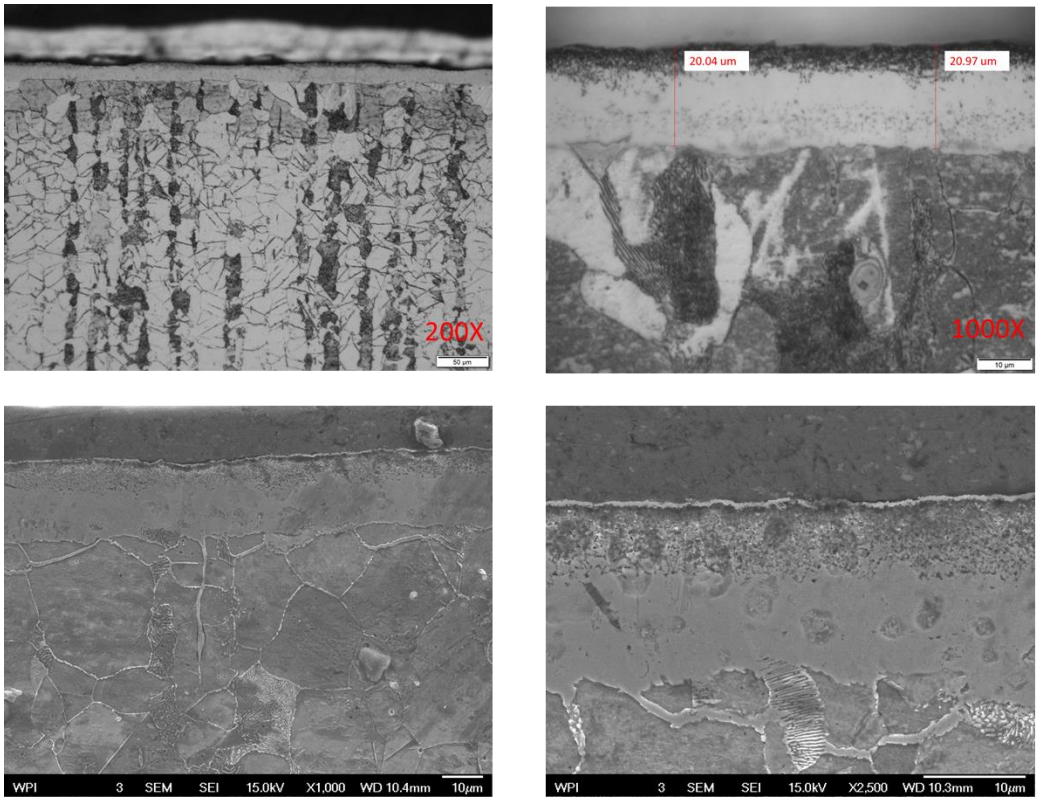

Figure 60 Compound layer of AISI 1018 sample (KN=4 atm^(-1/2), KC=0, t=4 hr)

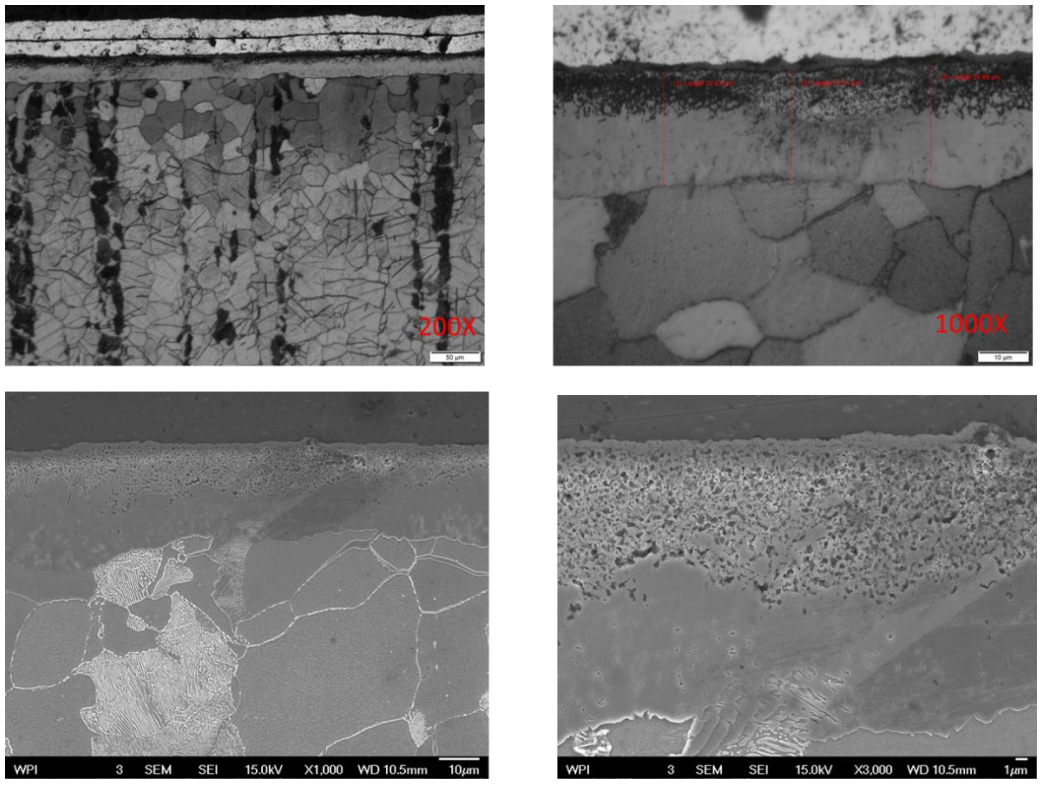

Figure 61 Compound layer of AISI 1018 sample (KN=4 atm^(-1/2), KC=0, t=8 hr)

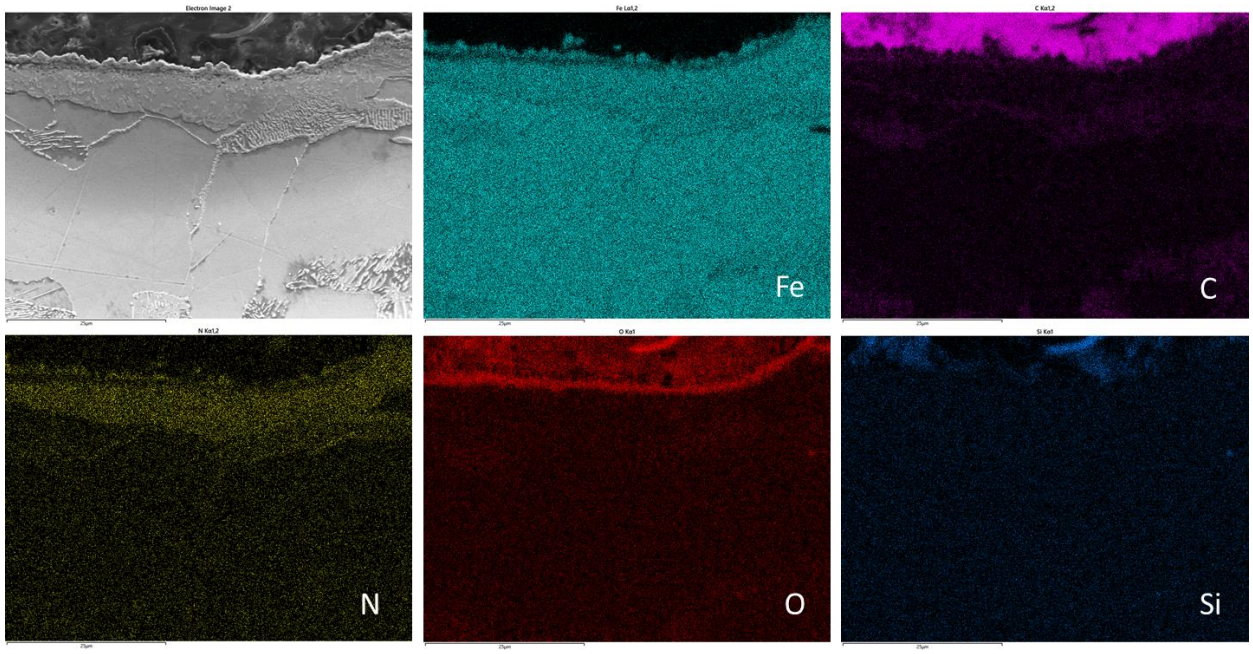

Figure 62 EDS mapping of AISI 1018 sample (KN=4 atm^(-1/2), KC=0, t=1 hr)

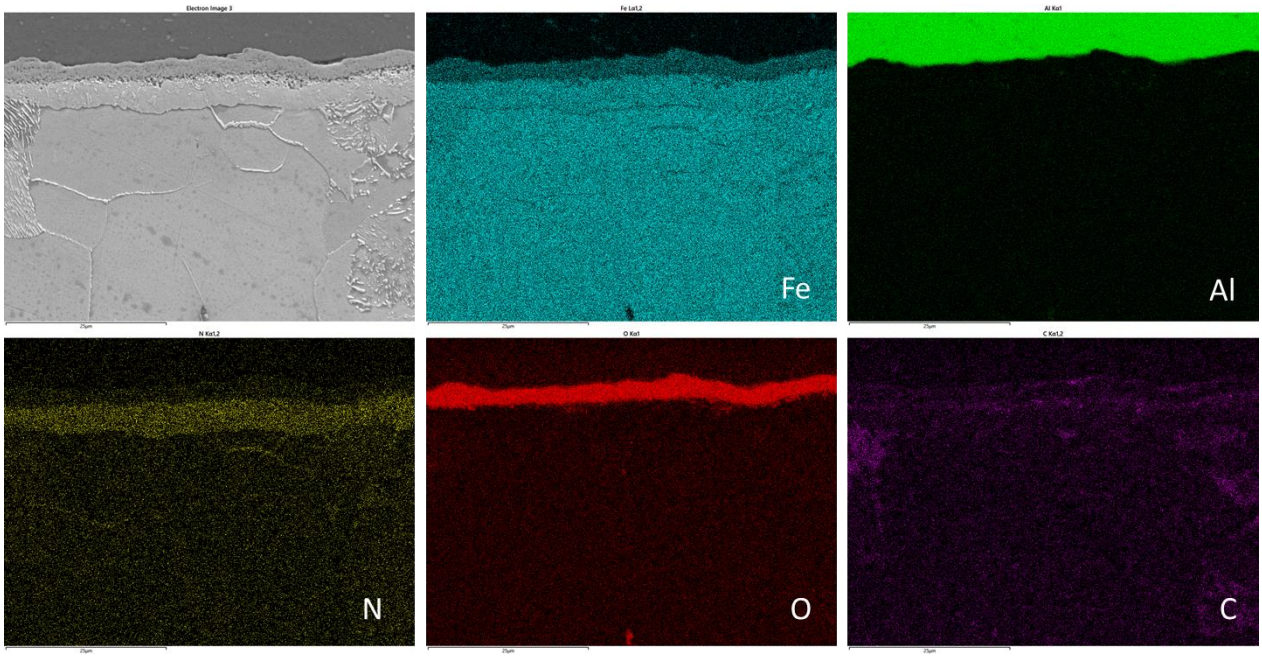

Figure 63 EDS mapping of AISI 1018 sample (KN=4 atm^(-1/2), KC=0, t=2 hr)

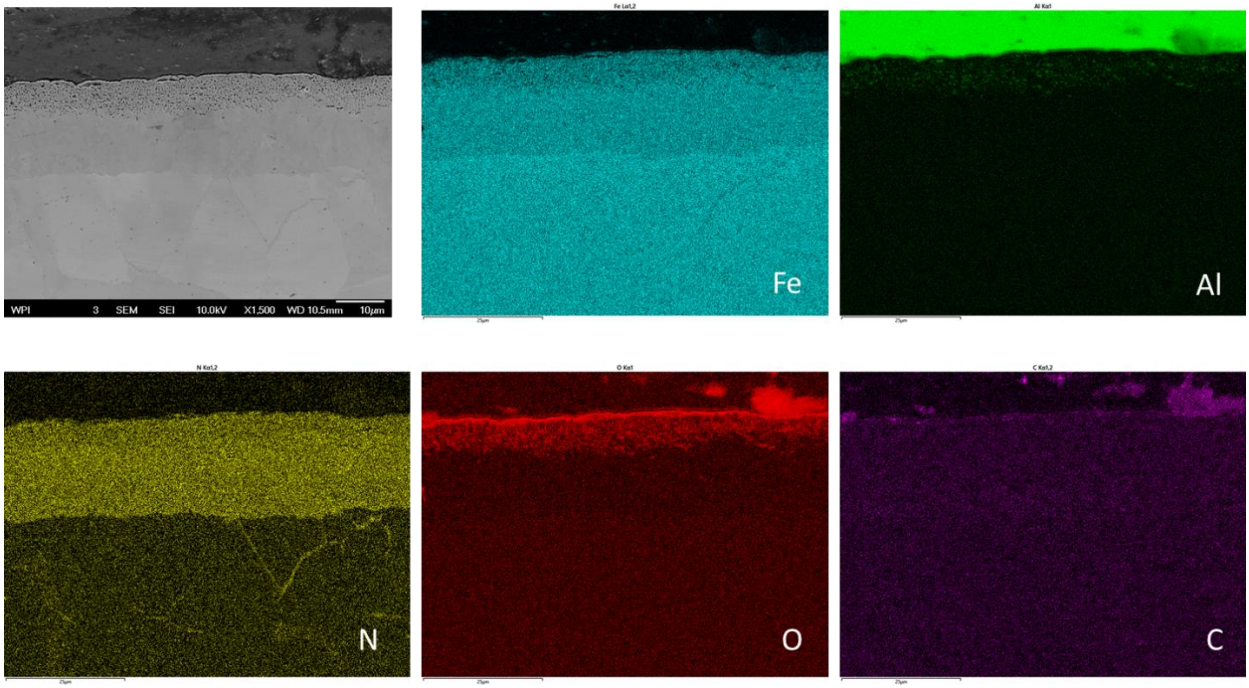

Figure 64 EDS mapping of AISI 1018 sample (KN=4 atm^(-1/2), KC=0, t=4 hr)

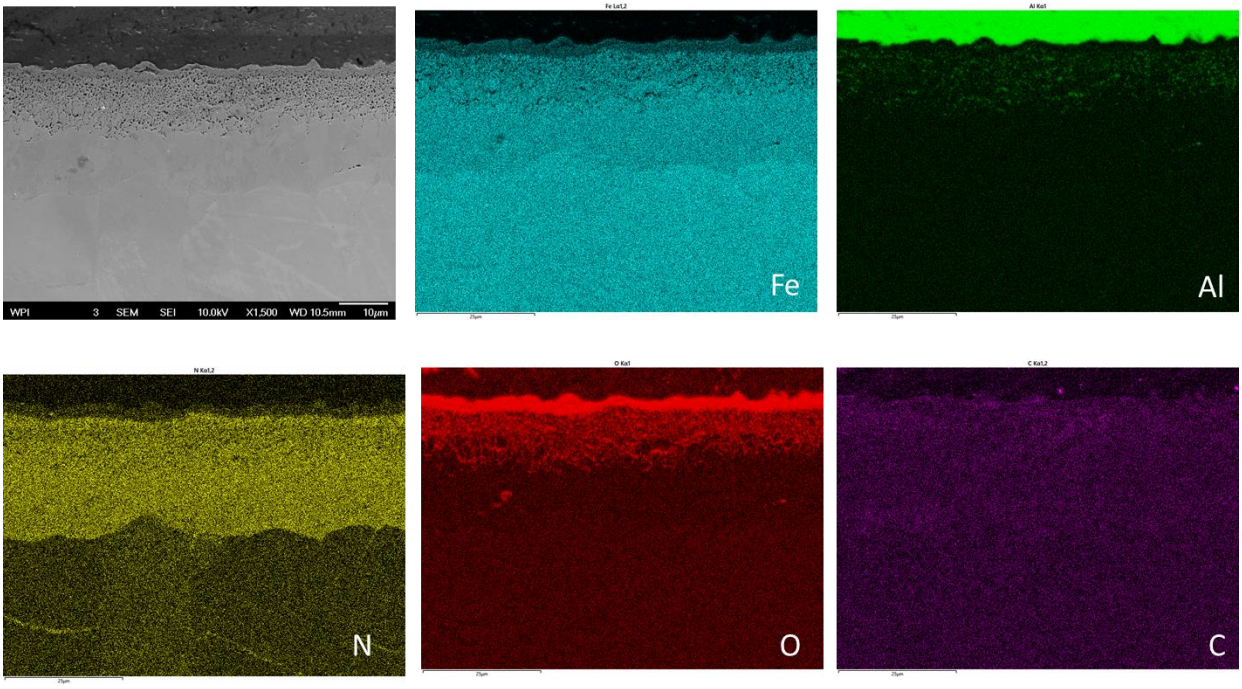

Figure 65 EDS mapping of AISI 1018 sample (KN=4 atm^(-1/2), KC=0, t=8 hr)

Cast iron (ASTM A536 80-55-06)

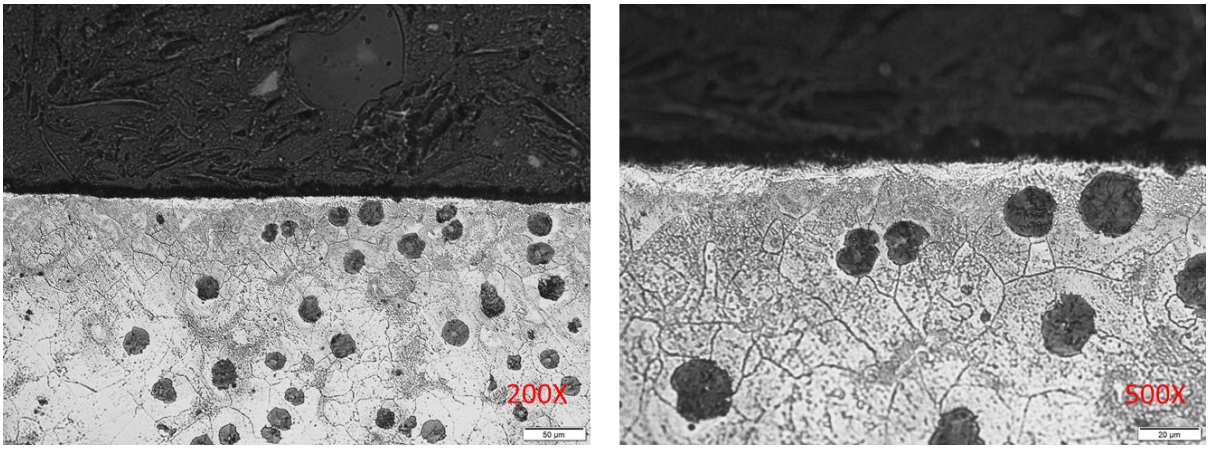

Figure 66 Optical micrographs of cast iron sample (KN=4 atm^(-1/2), KC=0, t=1 hr)

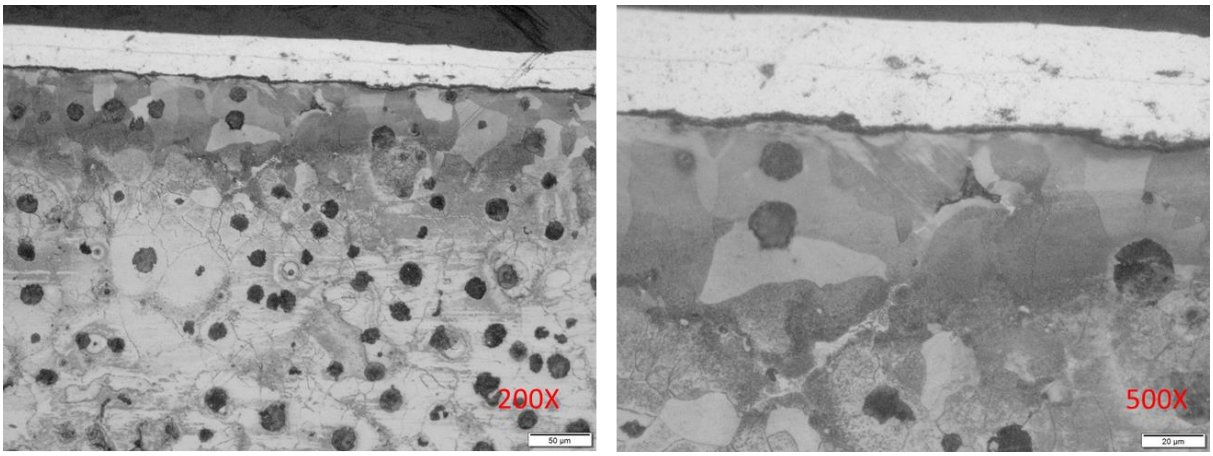

Figure 67 Optical micrographs of cast iron sample (KN=4 atm^(-1/2), KC=0, t=2 hr)

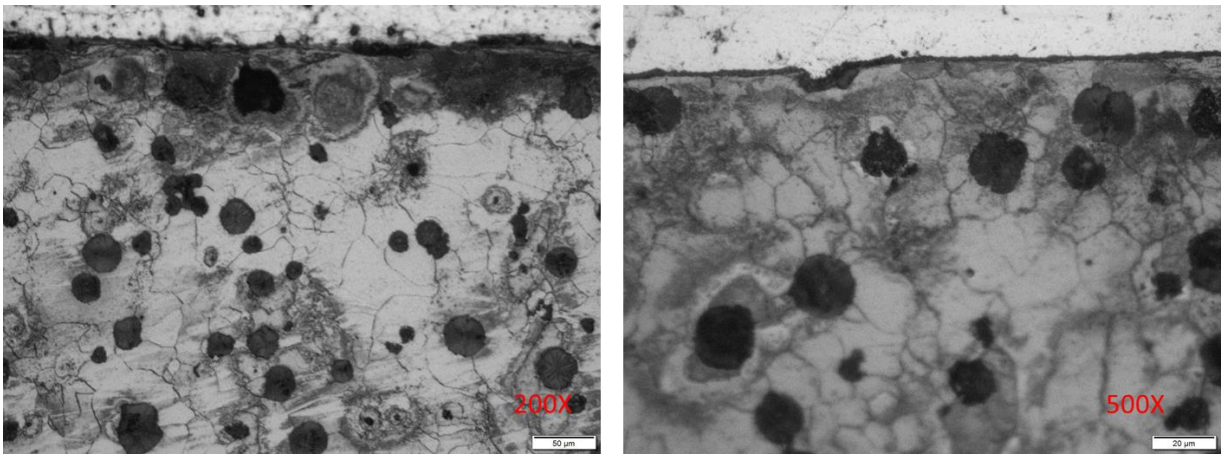

Figure 68 Optical micrographs of cast iron sample (KN=4 atm^(-1/2), KC=0, t=4 hr)

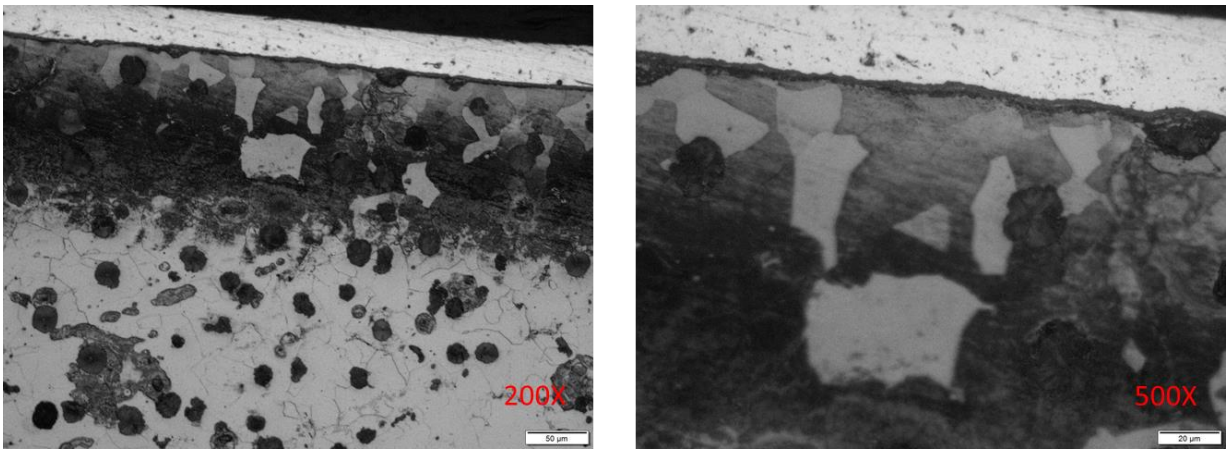

Figure 69 Optical micrographs of cast iron sample (KN=4 atm^(-1/2), KC=0, t=8 hr)

Section 2: Kc=9 trials

AISI 4140

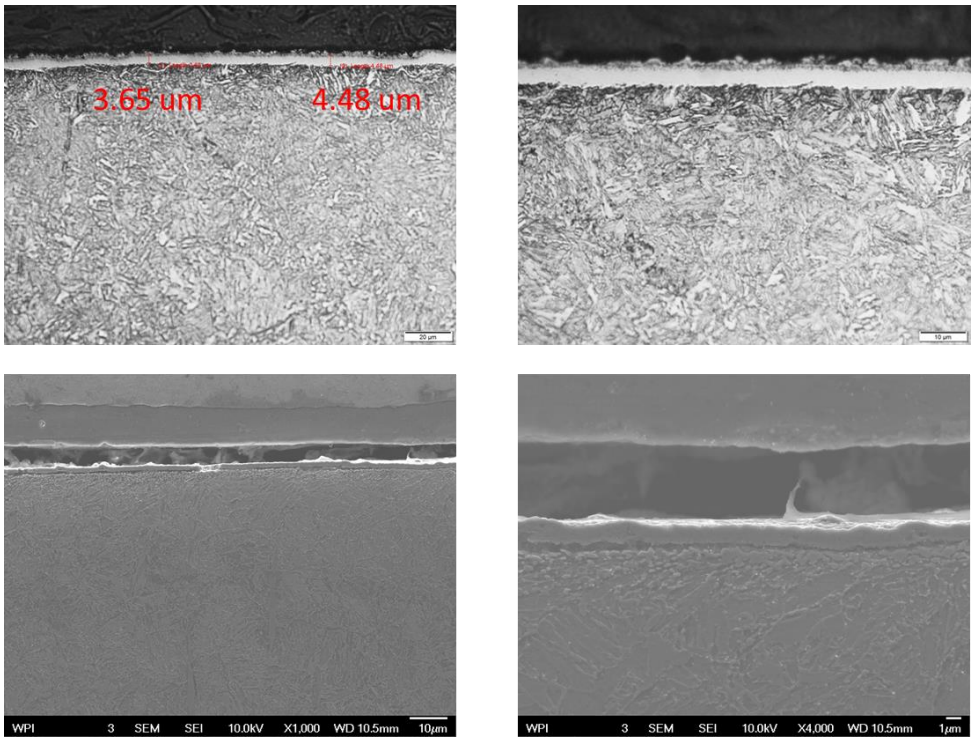

Figure 70 Compound layer of AISI 4140 sample (KN=4 atm^(-1/2), KC=9, t=1 hr)

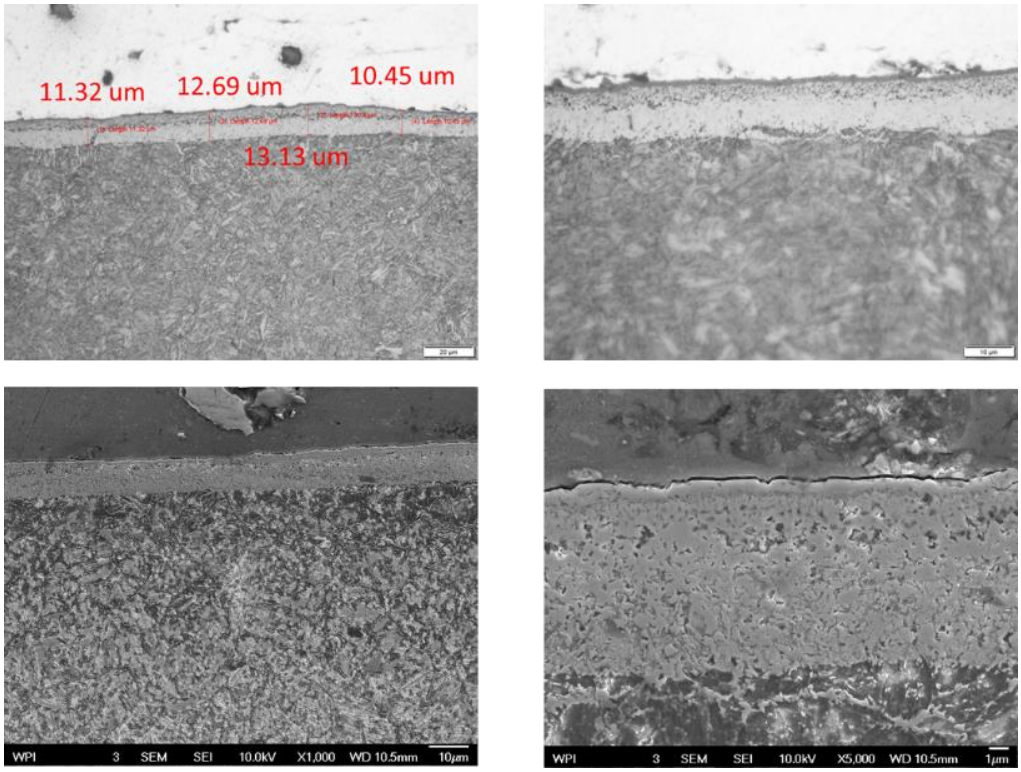

Figure 71 Compound layer of AISI 4140 sample (KN=4 atm^(-1/2), KC=9, t=2 hr)

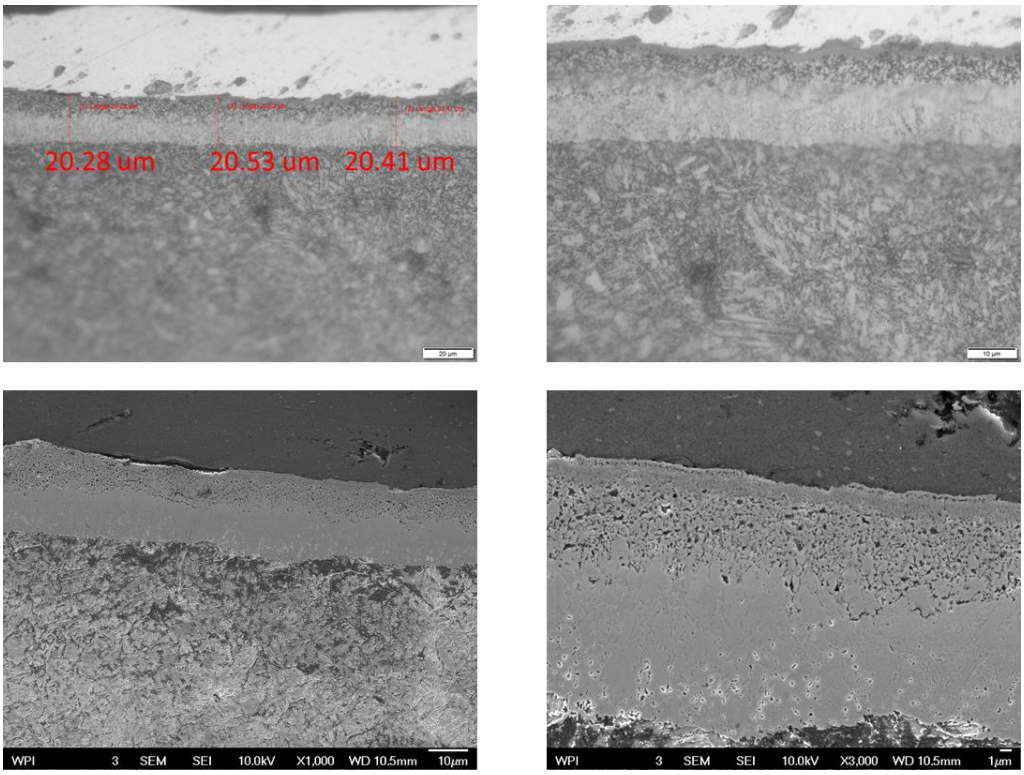

Figure 72 Compound layer of AISI 4140 sample (KN=4 atm^(-1/2), KC=9, t=4 hr)

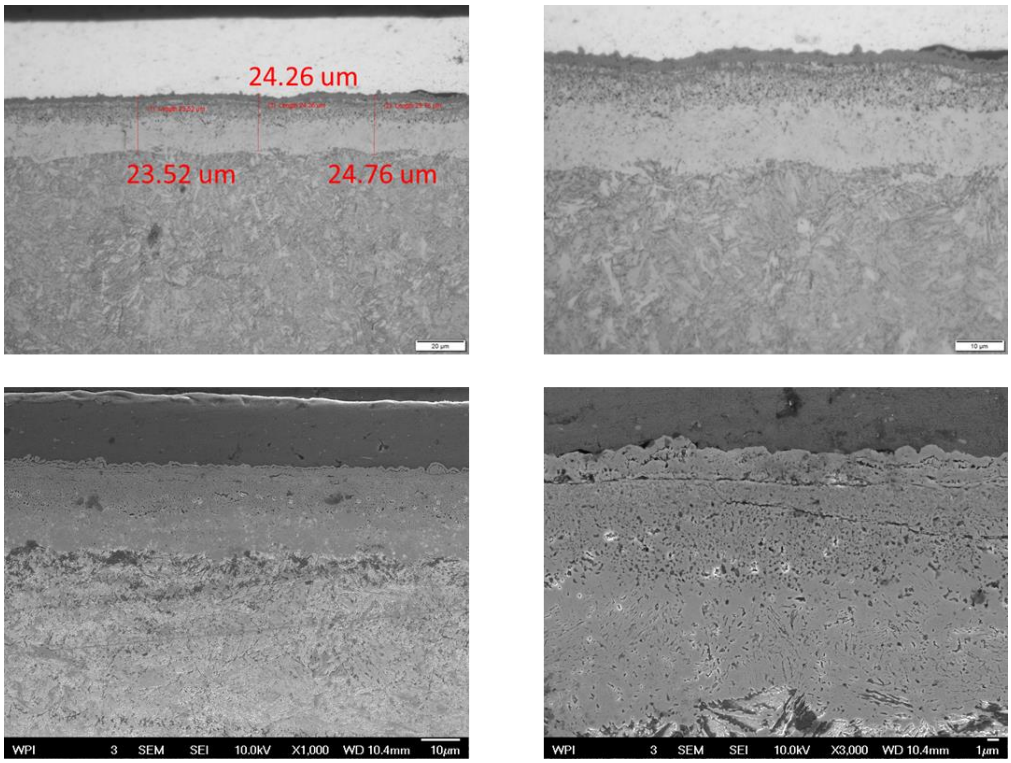

Figure 73 Compound layer of AISI 4140 sample (KN=4 atm^(-1/2), KC=9, t=8 hr)

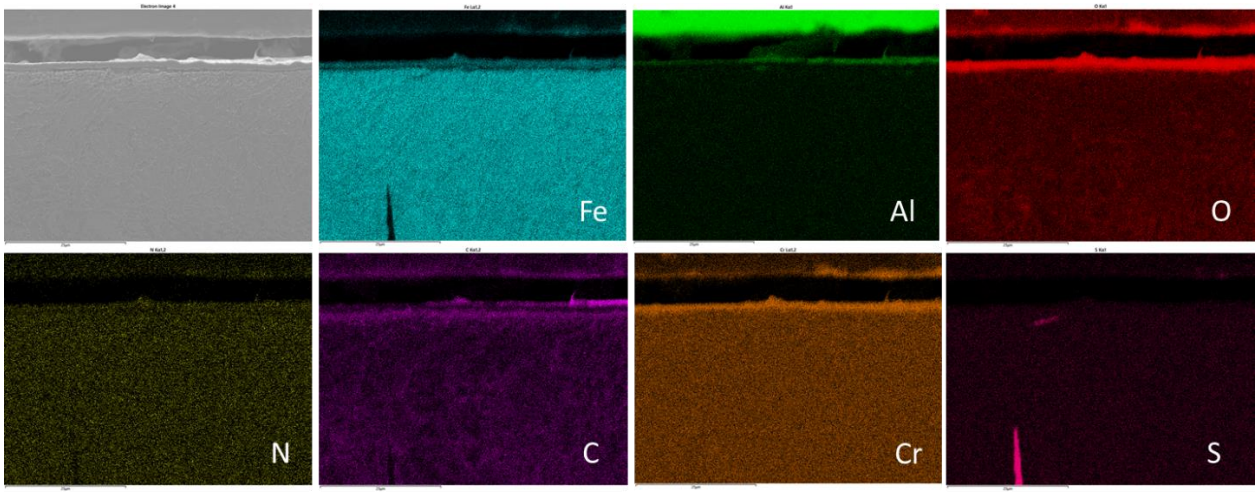

Figure 74 EDS mapping of AISI 4140 sample (KN=4 atm^(-1/2), KC=9, t=1 hr)

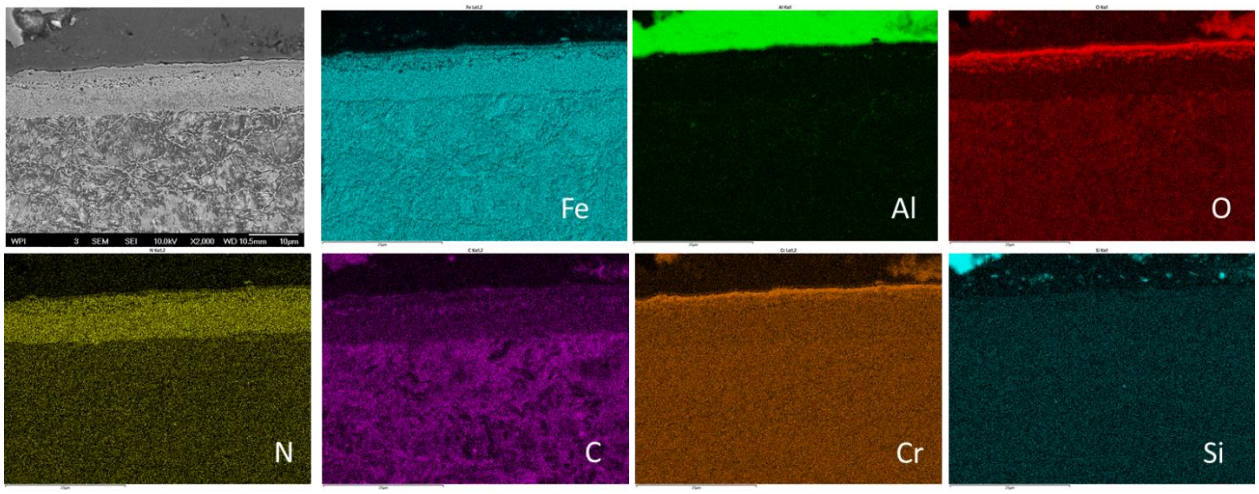

Figure 75 EDS mapping of AISI 4140 sample (KN=4 atm^(-1/2), KC=9, t=2 hr)

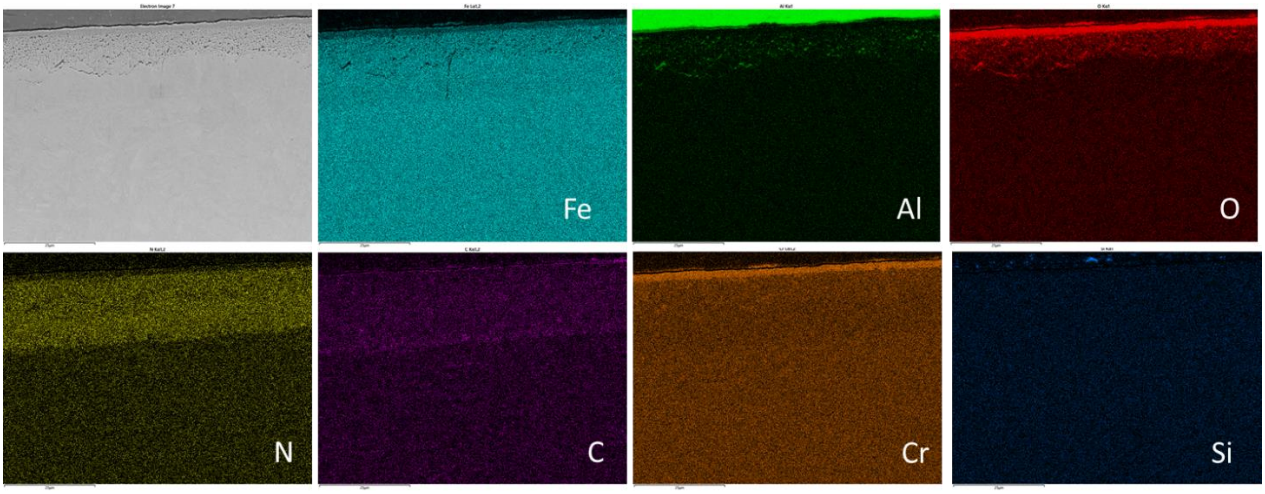

Figure 76 EDS mapping of AISI 4140 sample (KN=4 atm^(-1/2), KC=9, t=4 hr)

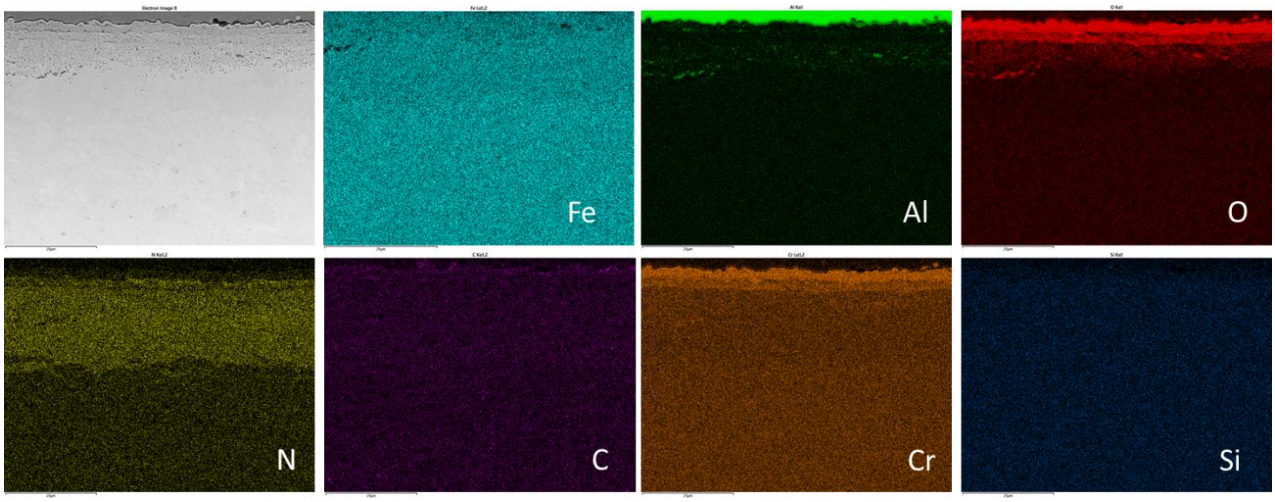

Figure 77 EDS mapping of AISI 4140 sample (KN=4 atm^(-1/2), KC=9, t=8 hr)

AISI 1018

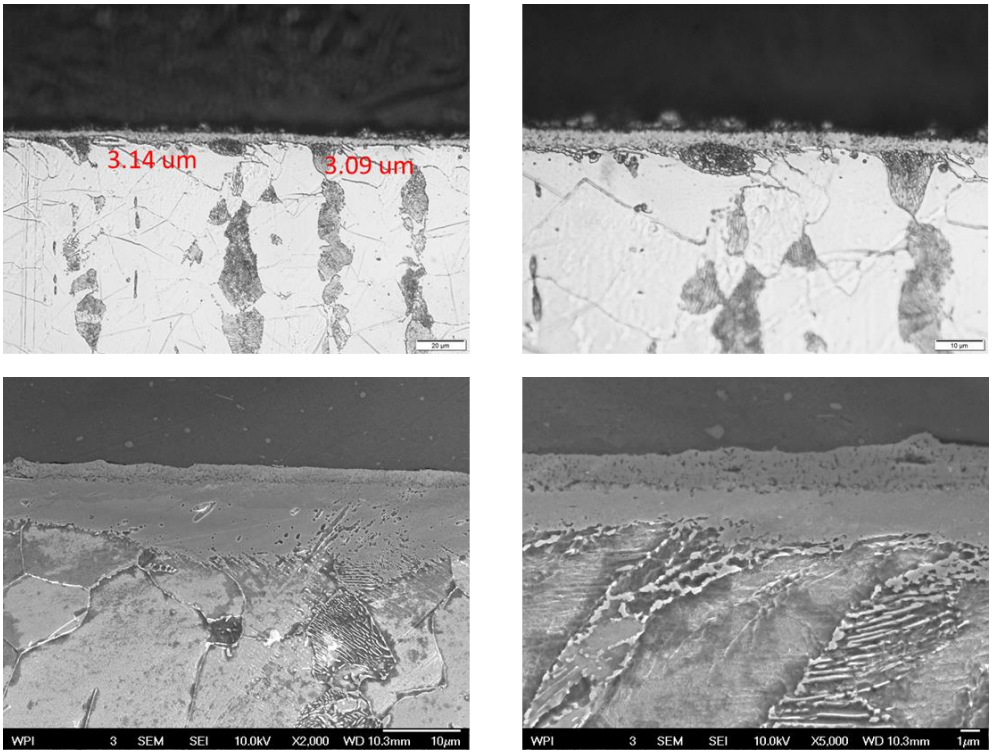

Figure 78 Compound layer of AISI 1018 sample (KN=4 atm^(-1/2), KC=9, t=1 hr)

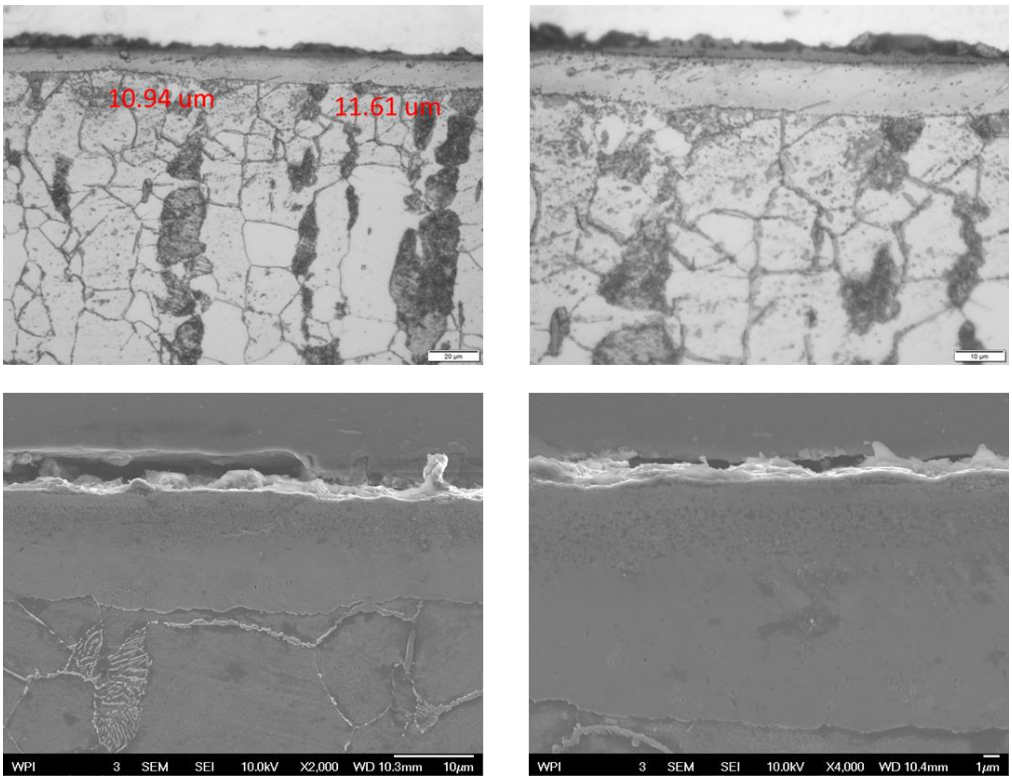

Figure 79 Compound layer of AISI 1018 sample (KN=4 atm^(-1/2), KC=9, t=2 hr)

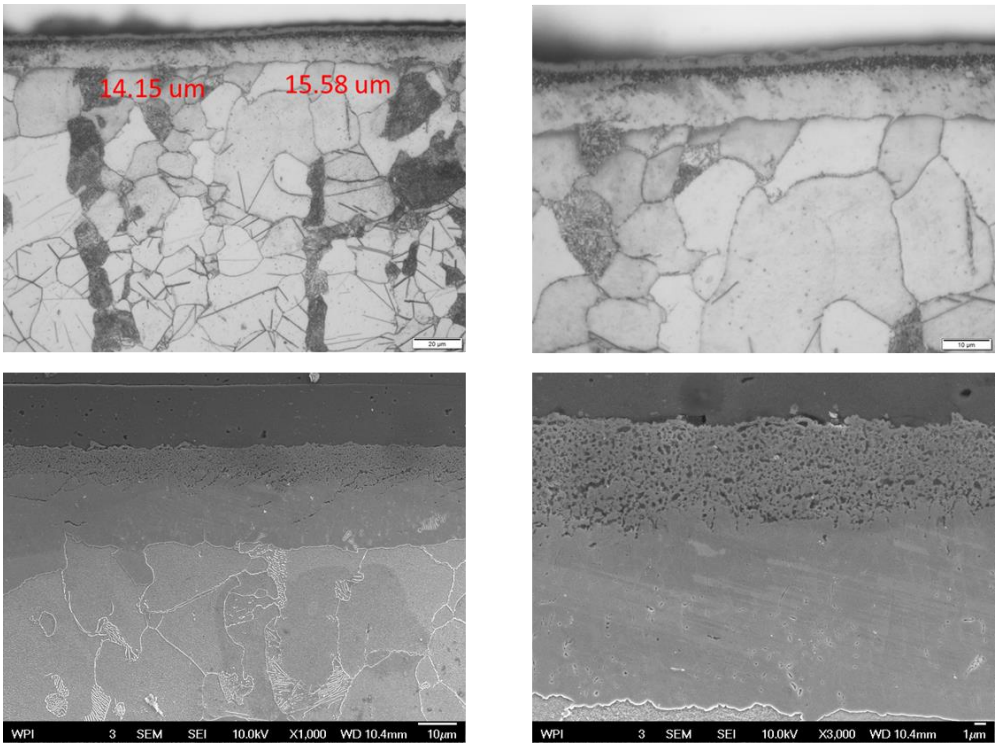

Figure 80 Compound layer of AISI 1018 sample (KN=4 atm^(-1/2), KC=9, t=4 hr)

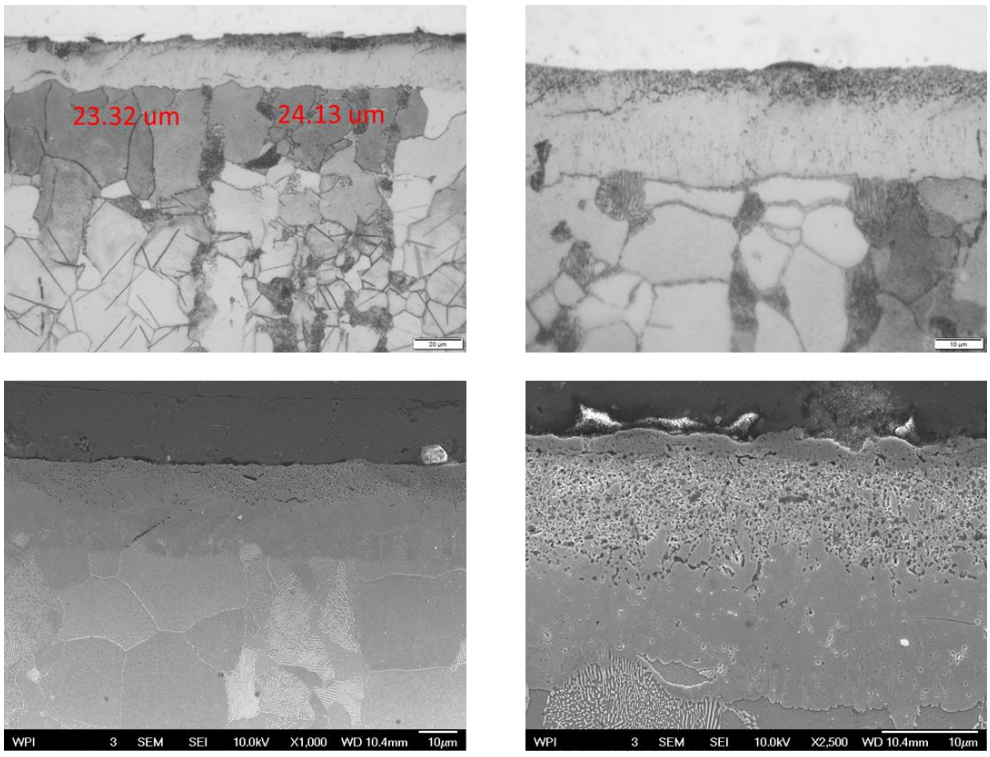

Figure 81 Compound layer of AISI 1018 sample (KN=4 atm^(-1/2), KC=9, t=8 hr)

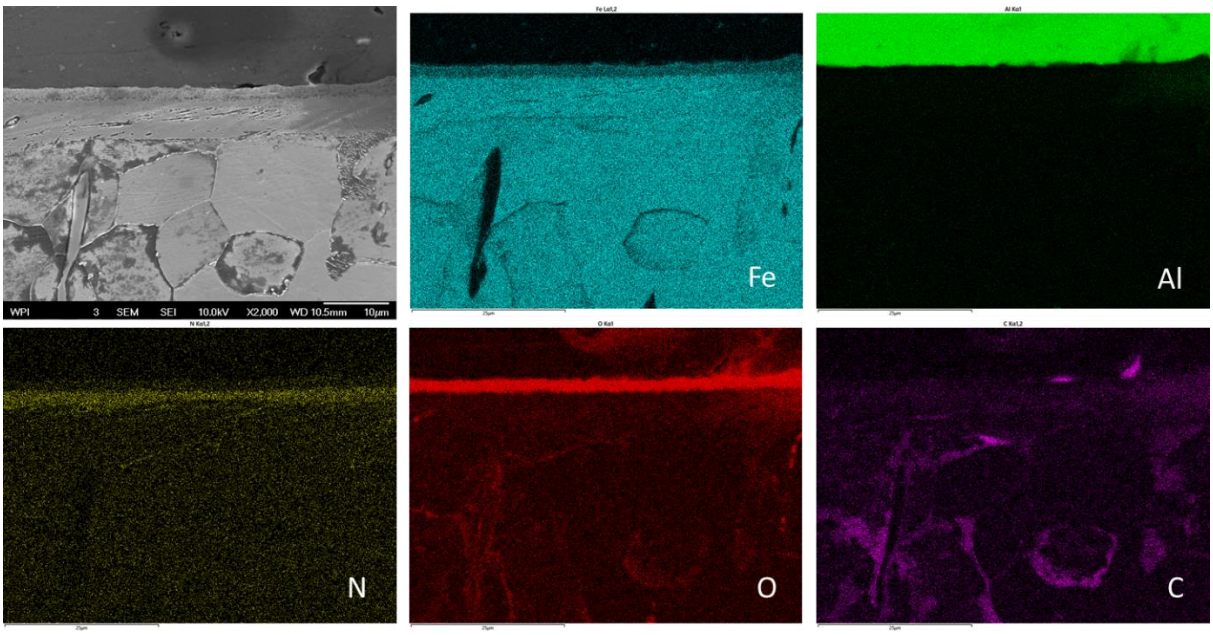

Figure 82 EDS mapping of AISI 1018 sample (KN=4 atm^(-1/2), KC=9, t=1 hr)

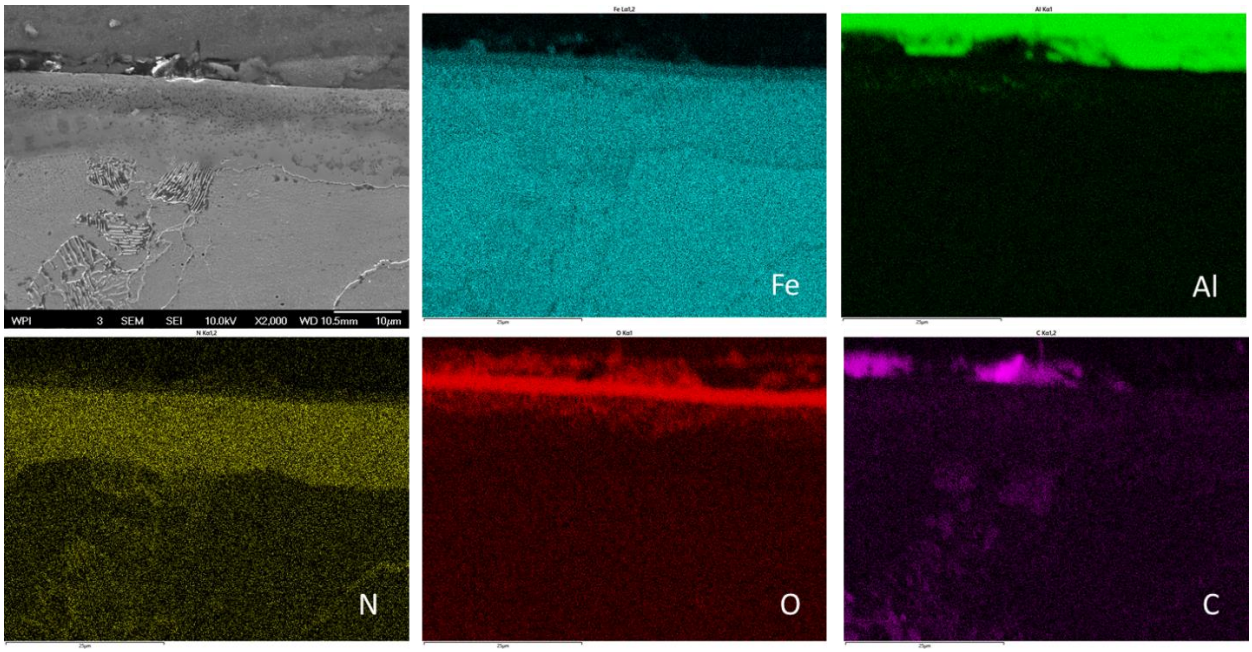

Figure 83 EDS mapping of AISI 1018 sample (KN=4 atm^(-1/2), KC=9, t=2 hr)

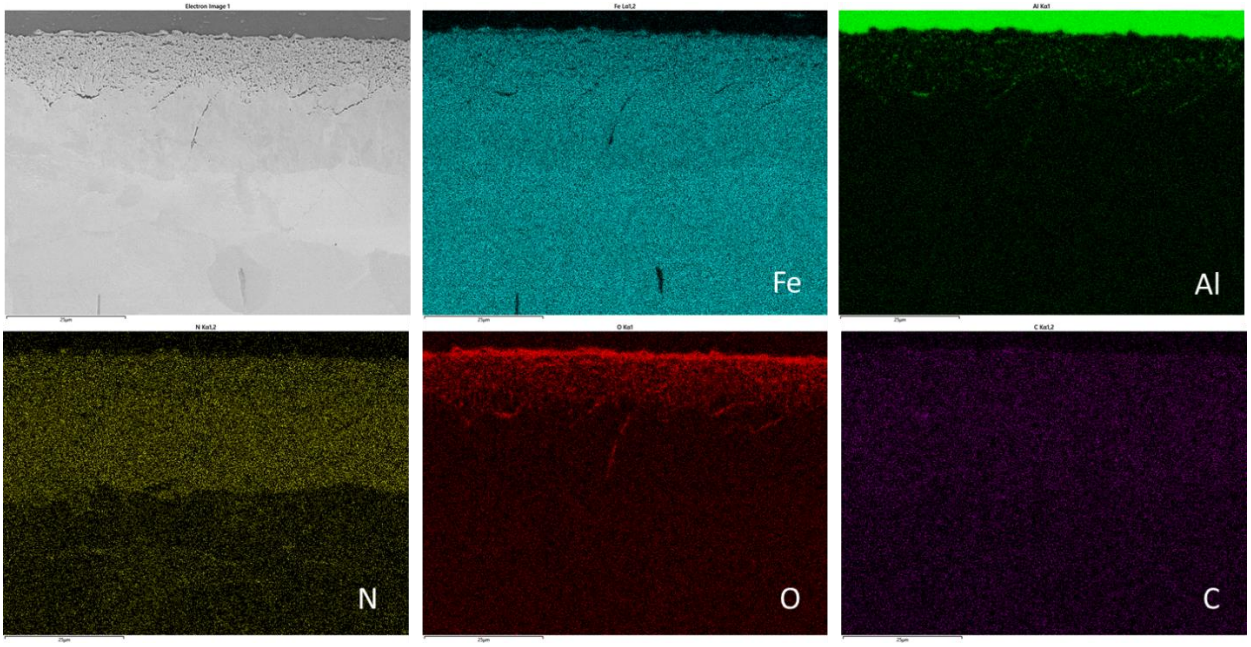

Figure 84 EDS mapping of AISI 1018 sample (KN=4 atm^(-1/2), KC=9, t=4 hr)

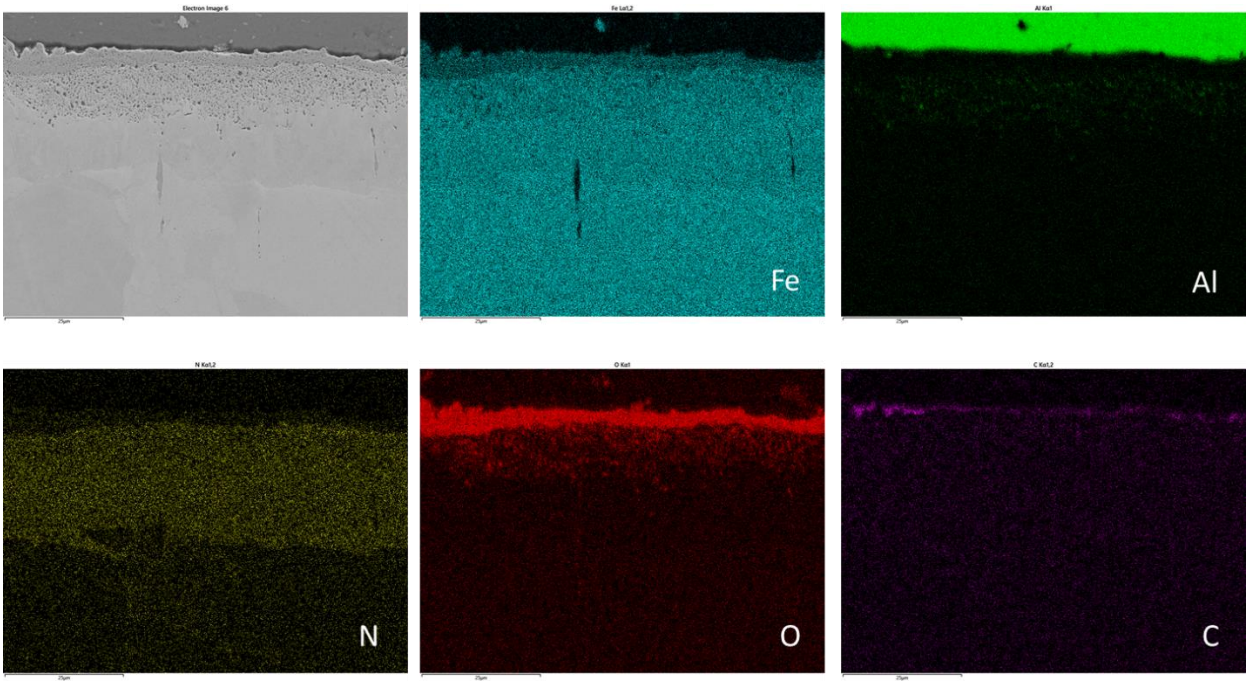

Figure 85 EDS mapping of AISI 1018 sample (KN=4 atm^(-1/2), KC=9, t=8 hr)

Cast iron (ASTM A536 80-55-06)

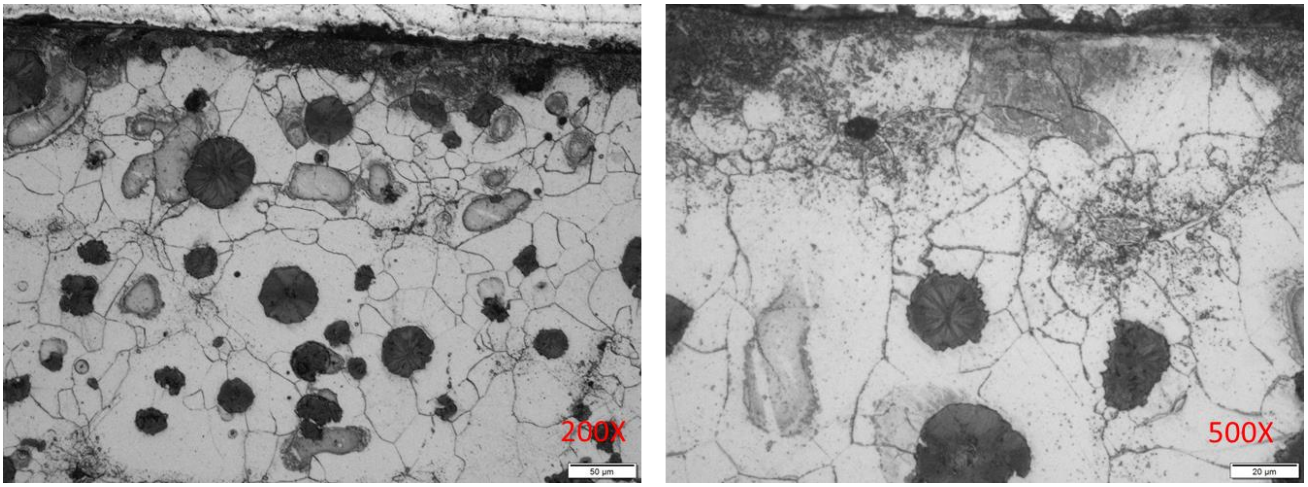

Figure 86 Optical micrographs of cast iron sample (KN=4 atm^(-1/2), KC=9, t=1 hr)

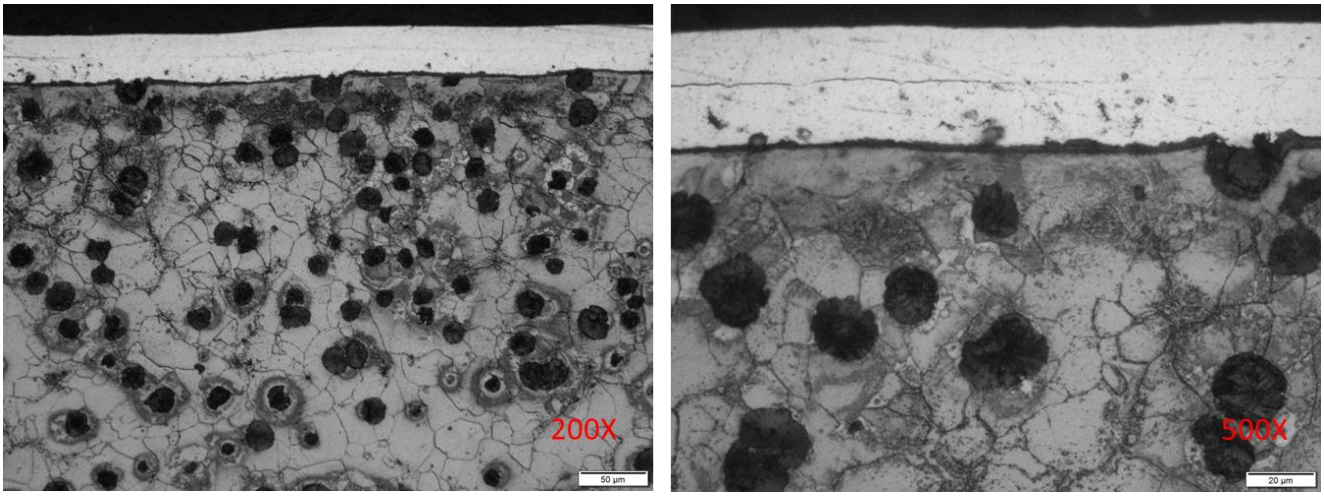

Figure 87 Optical micrographs of cast iron sample (KN=4 atm^(-1/2), KC=9, t=2 hr)

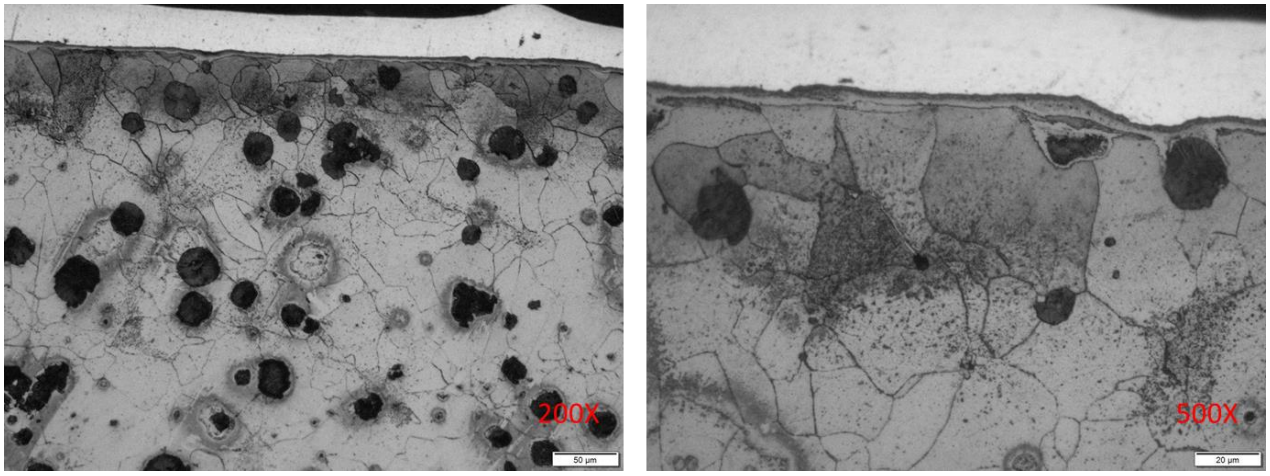

Figure 88 Optical micrographs of cast iron sample (KN=4 atm^(-1/2), KC=9, t=4 hr)

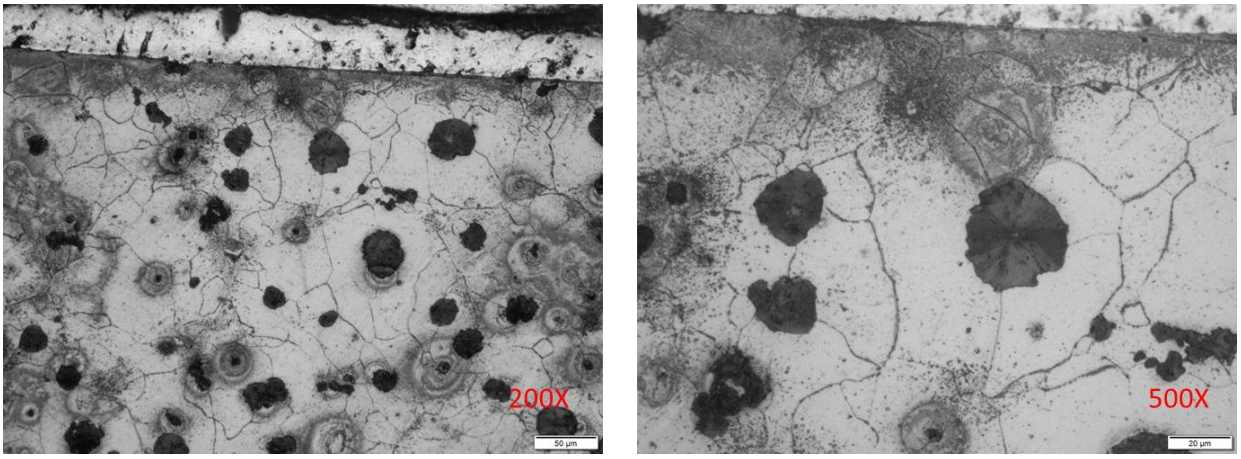

Figure 89 Optical micrographs of cast iron sample (KN=4 atm^(-1/2), KC=9, t=8 hr)

Section 3: Kc=12 trials

AISI 4140

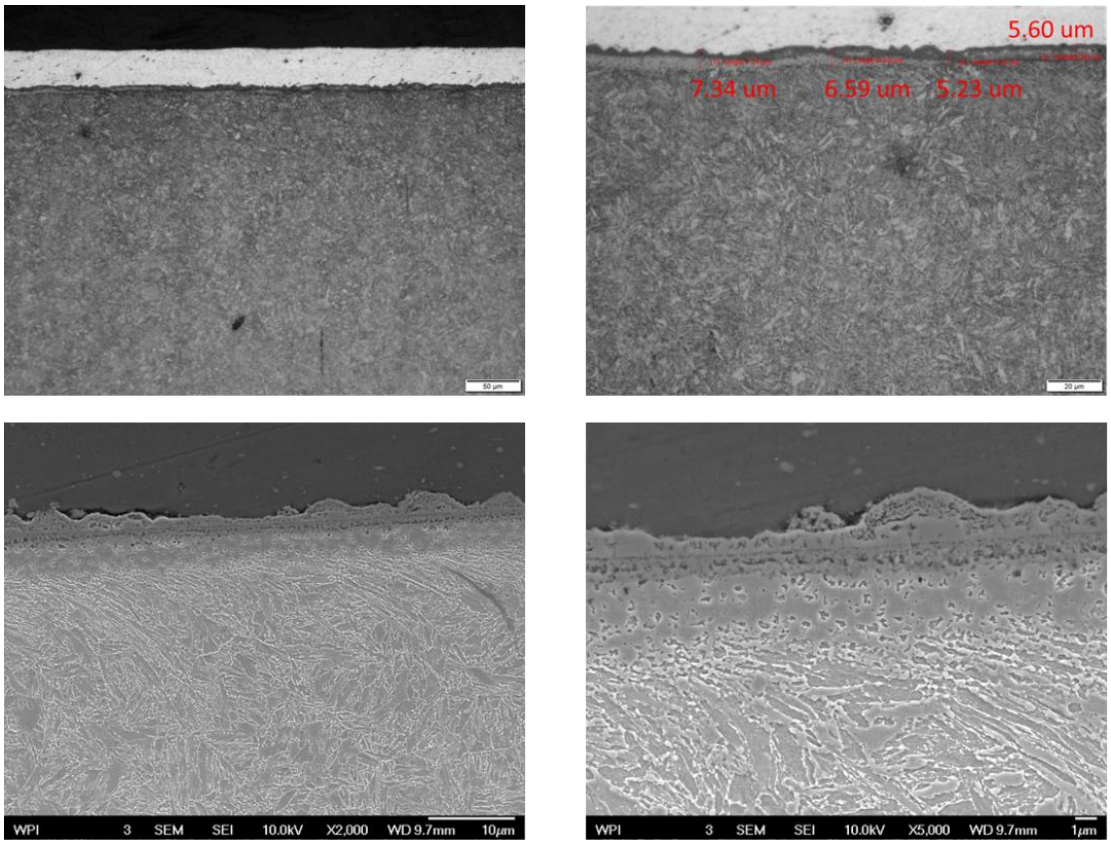

Figure 90 Compound layer of AISI 4140 sample (KN=4 atm^(-1/2), KC=12, t=1 hr)

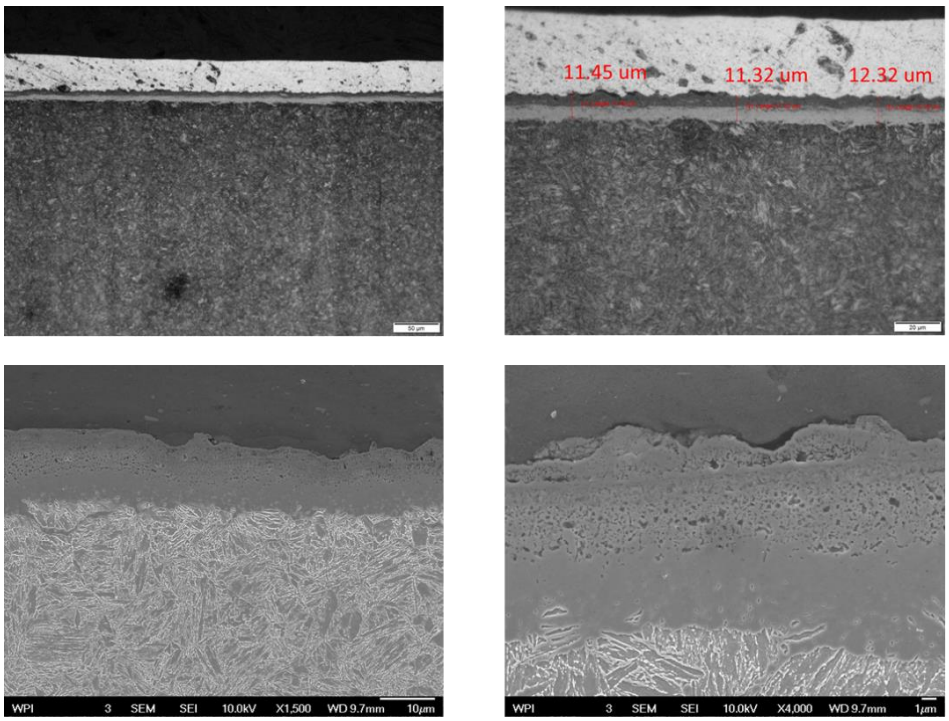

Figure 91 Compound layer of AISI 4140 sample (KN=4 atm^(-1/2), KC=12, t=2 hr)

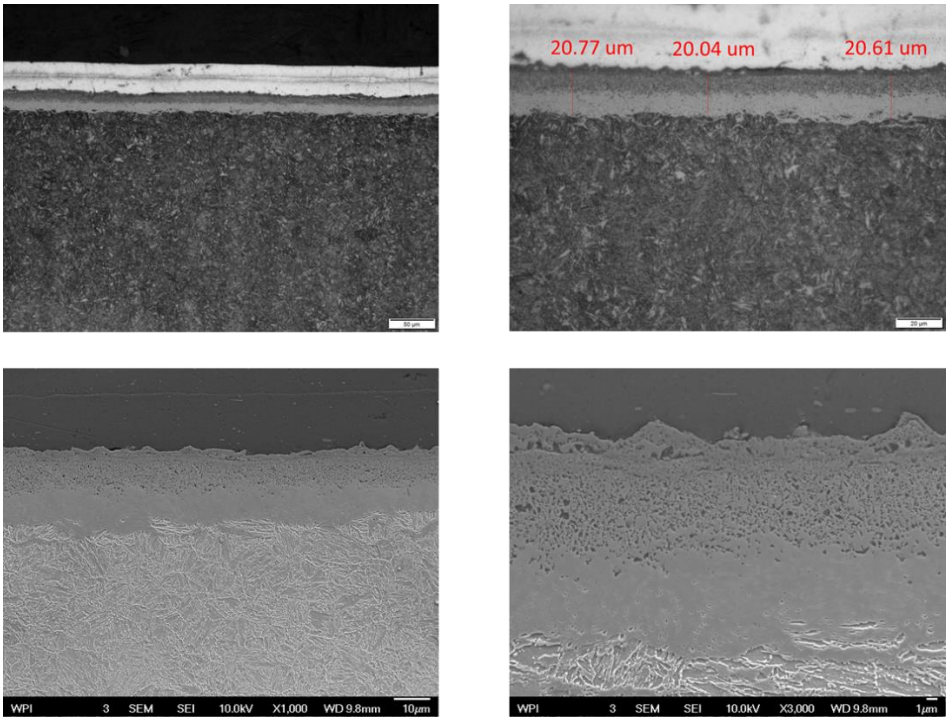

Figure 92 Compound layer of AISI 4140 sample (KN=4 atm^(-1/2), KC=12, t=4 hr)

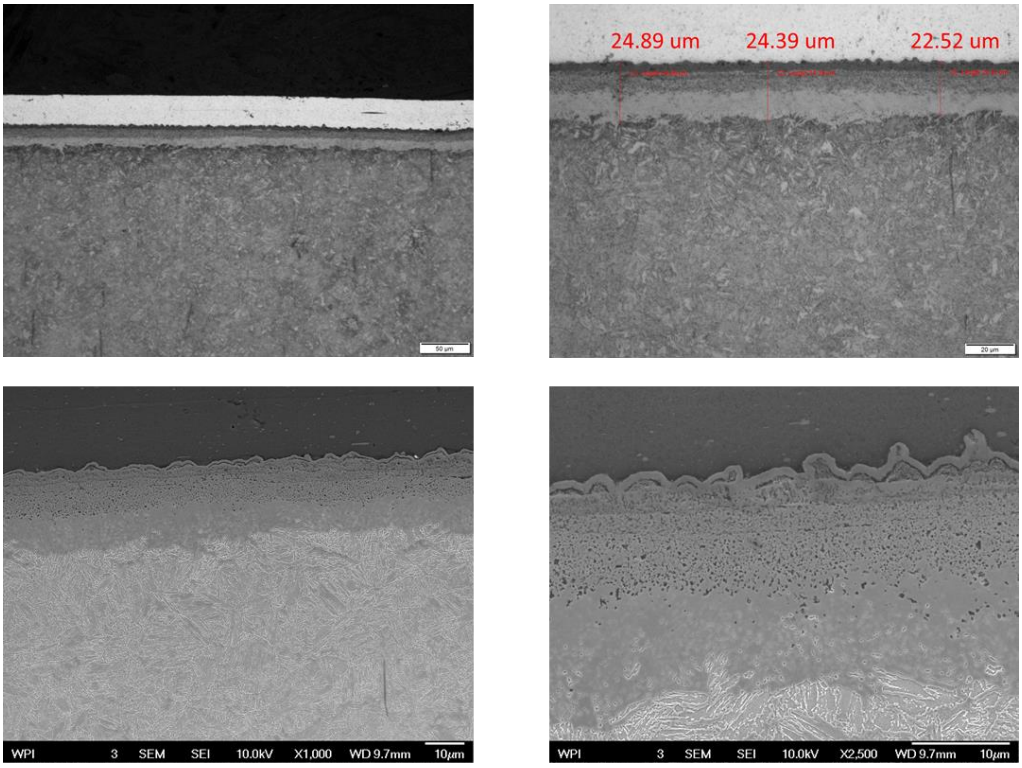

Figure 93 Compound layer of AISI 4140 sample (KN=4 atm^(-1/2), KC=12, t=1 hr)

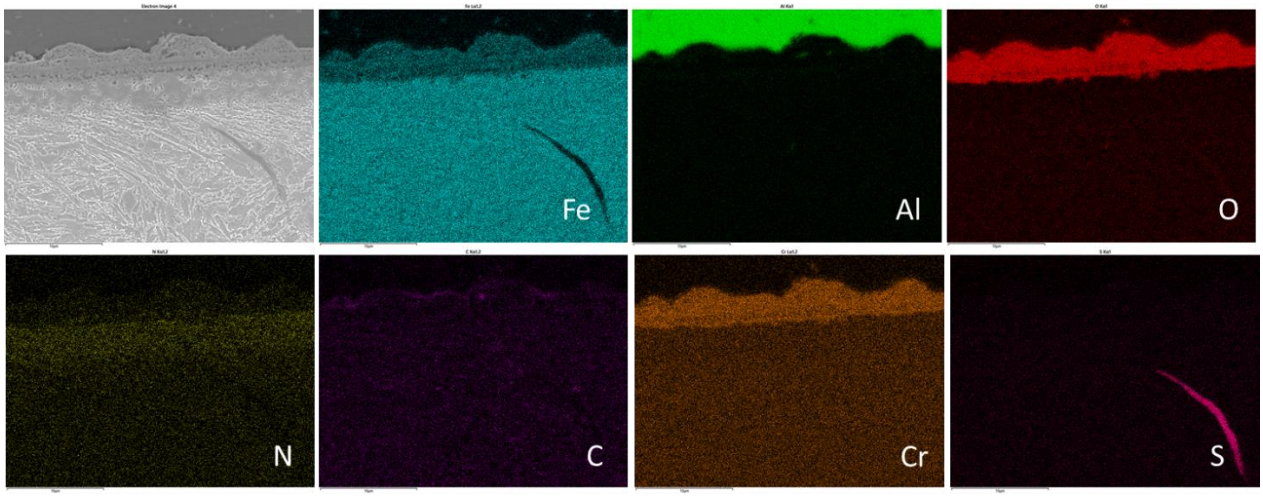

Figure 94 EDS mapping of AISI 4140 sample (KN=4 atm^(-1/2), KC=12, t=1 hr)

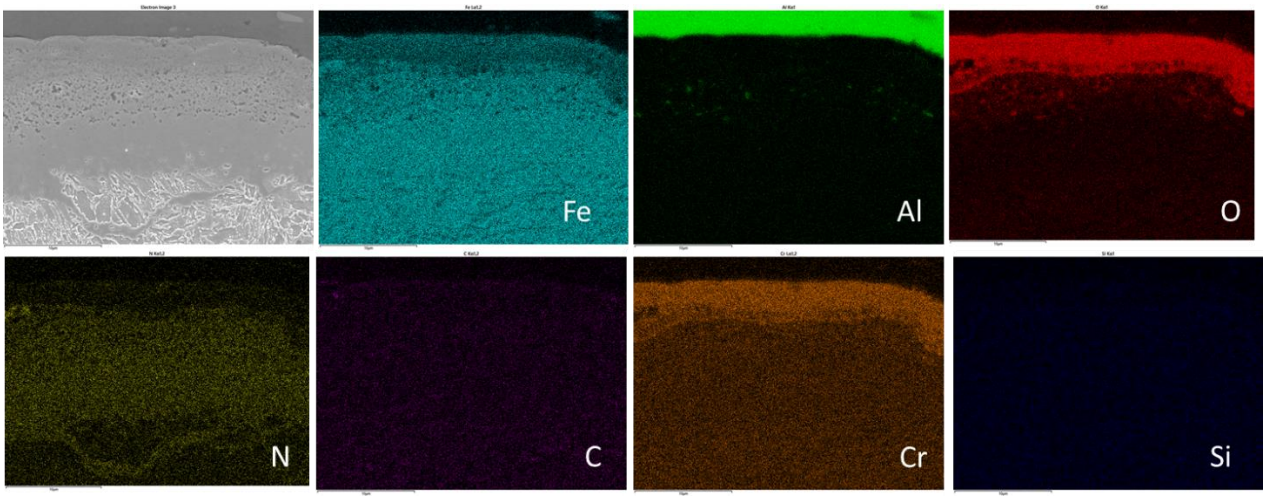

Figure 95 EDS mapping of AISI 4140 sample (KN=4 atm^(-1/2), KC=12, t=2 hr)

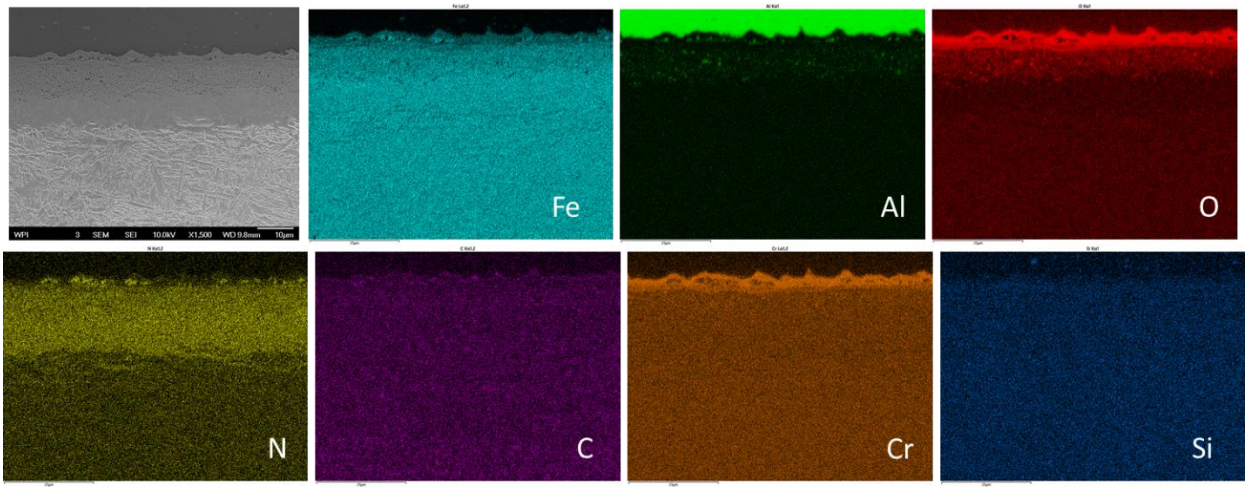

Figure 96 EDS mapping of AISI 4140 sample (KN=4 atm^(-1/2), KC=12, t=4 hr)

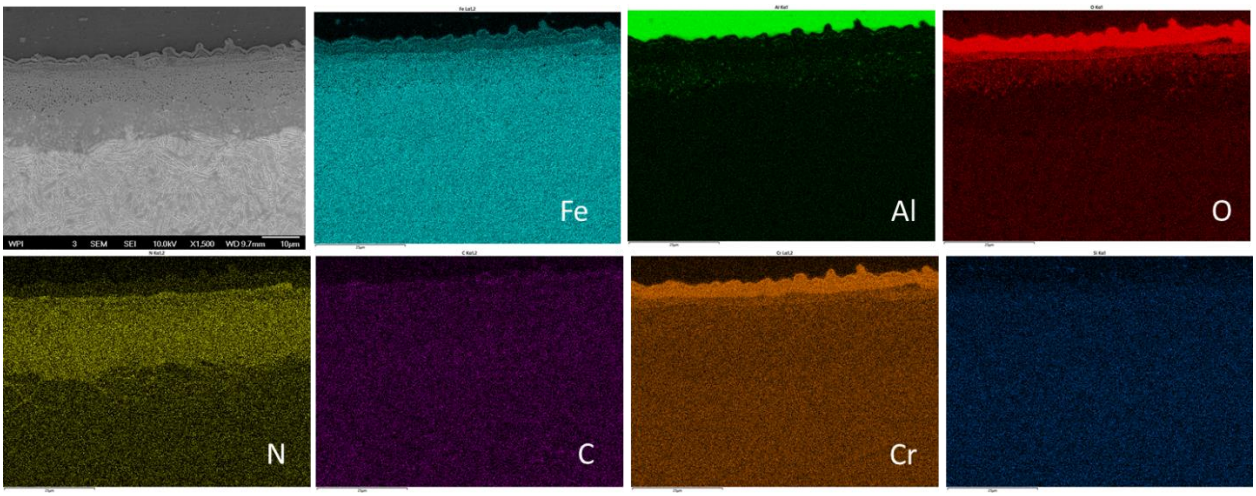

Figure 97 EDS mapping of AISI 4140 sample (KN=4 atm^(-1/2), KC=12, t=8 hr)

AISI 1018

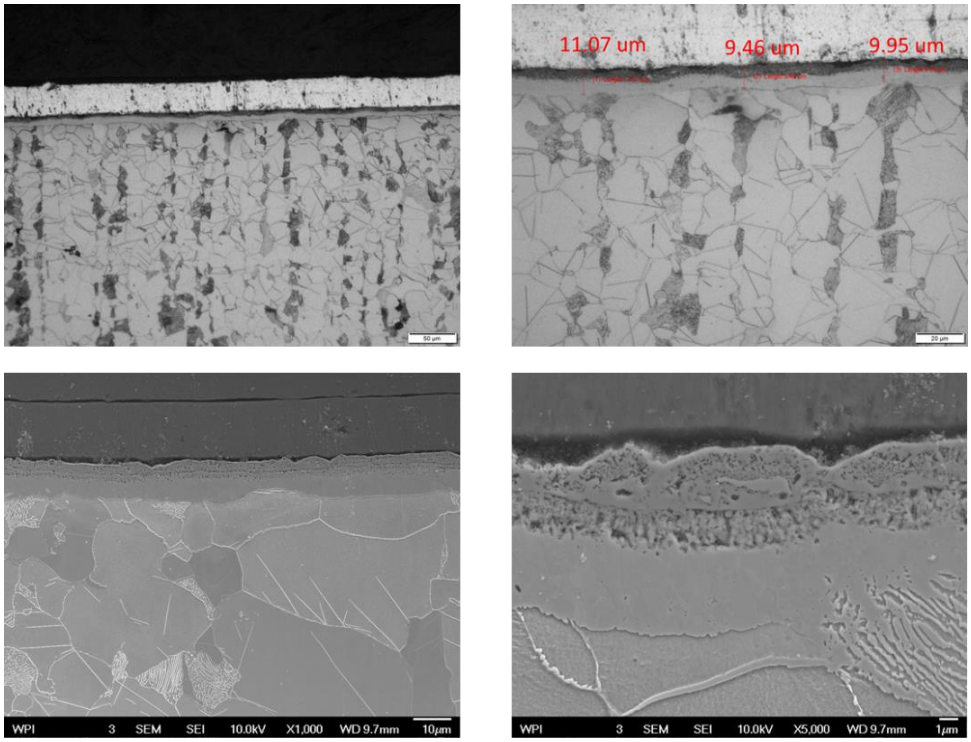

Figure 98 Compound layer of AISI 1018 sample (KN=4 atm^(-1/2), KC=12, t=1 hr)

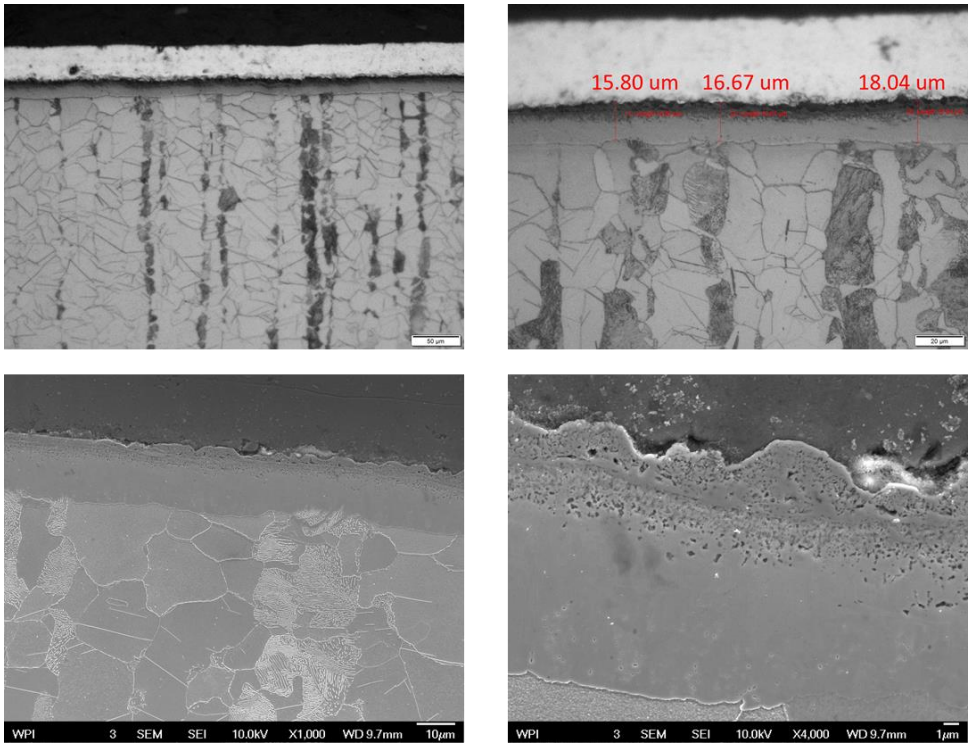

Figure 99 Compound layer of AISI 1018 sample (KN=4 atm^(-1/2), KC=12, t=2 hr)

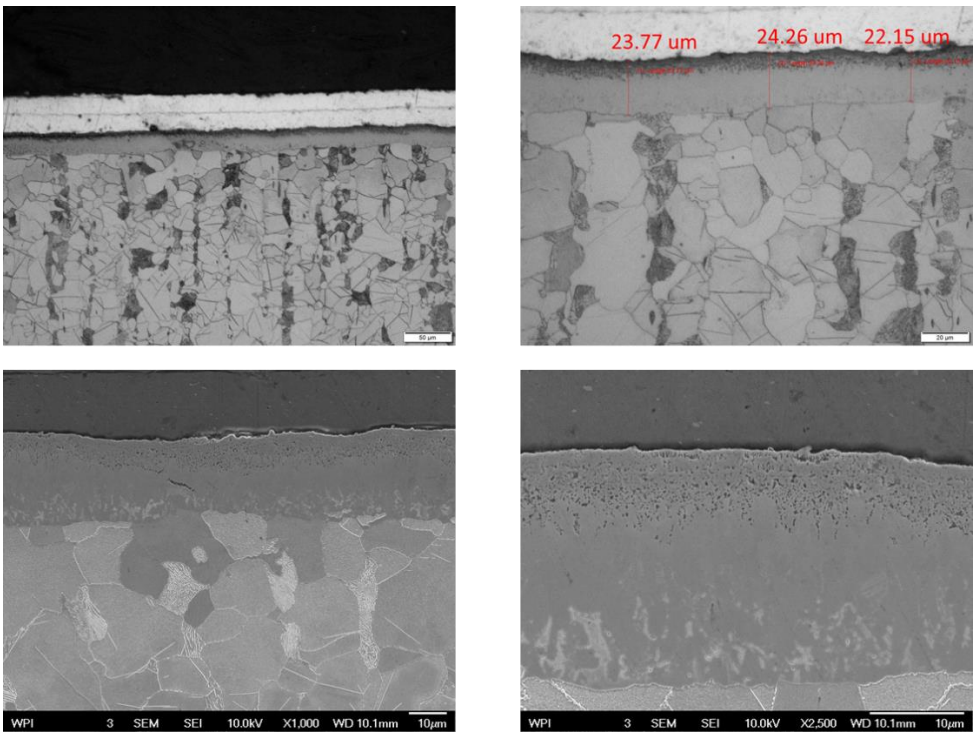

Figure 100 Compound layer of AISI 1018 sample (KN=4 atm^(-1/2), KC=12, t=4 hr)

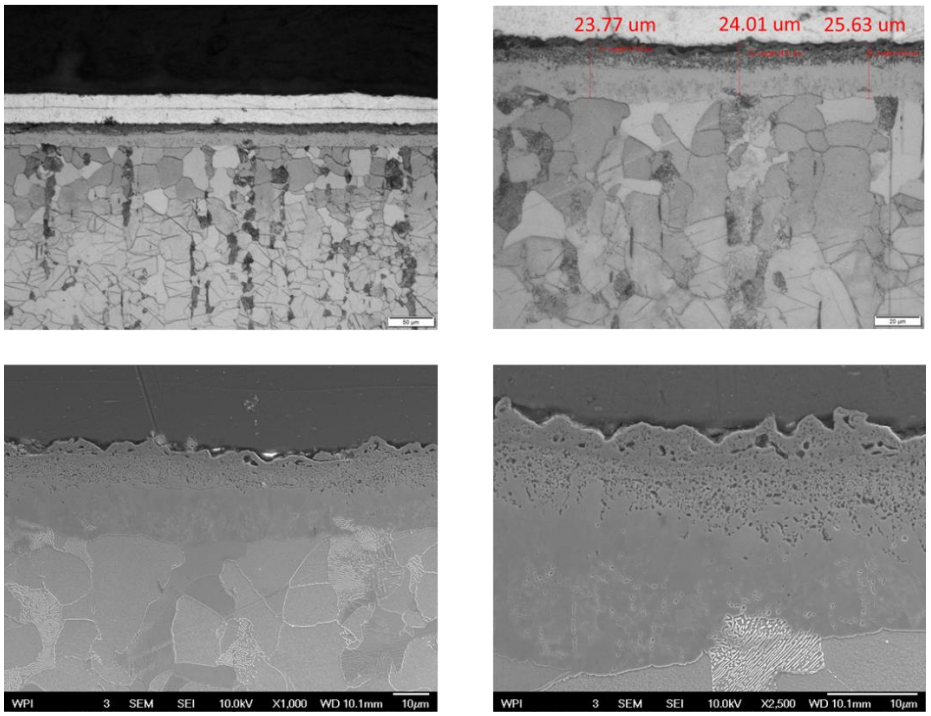

Figure 101 Compound layer of AISI 1018 sample (KN=4 atm^(-1/2), KC=12, t=8 hr)

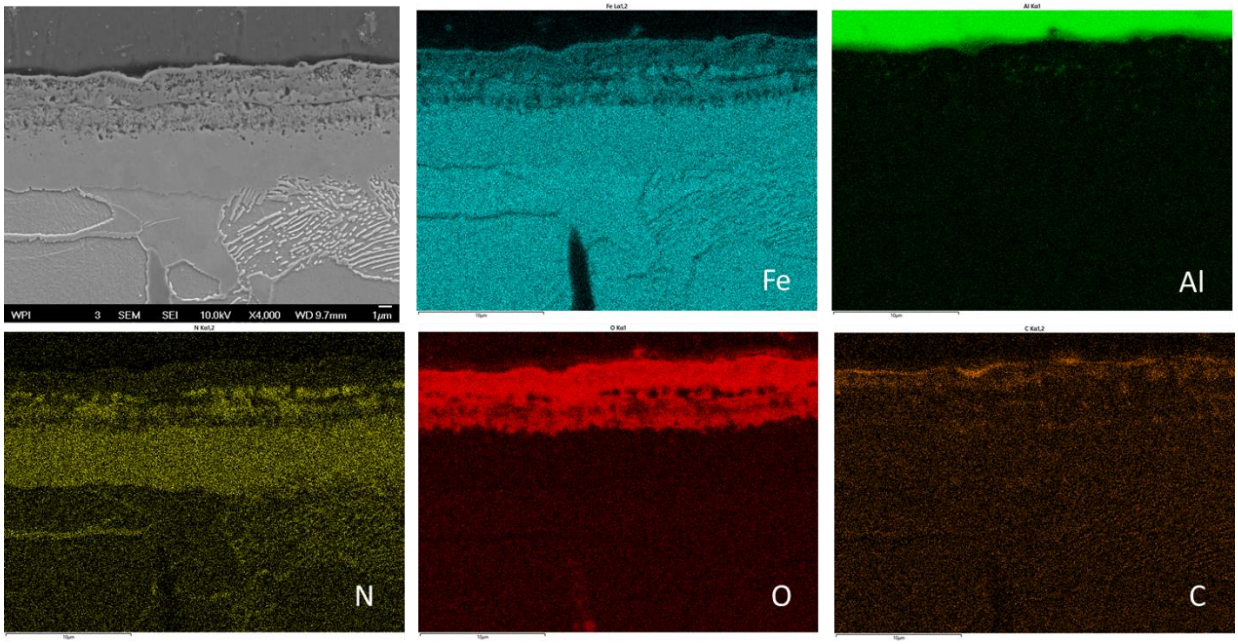

Figure 102 EDS mapping of AISI 1018 sample (KN=4 atm^(-1/2), KC=12, t=1 hr)

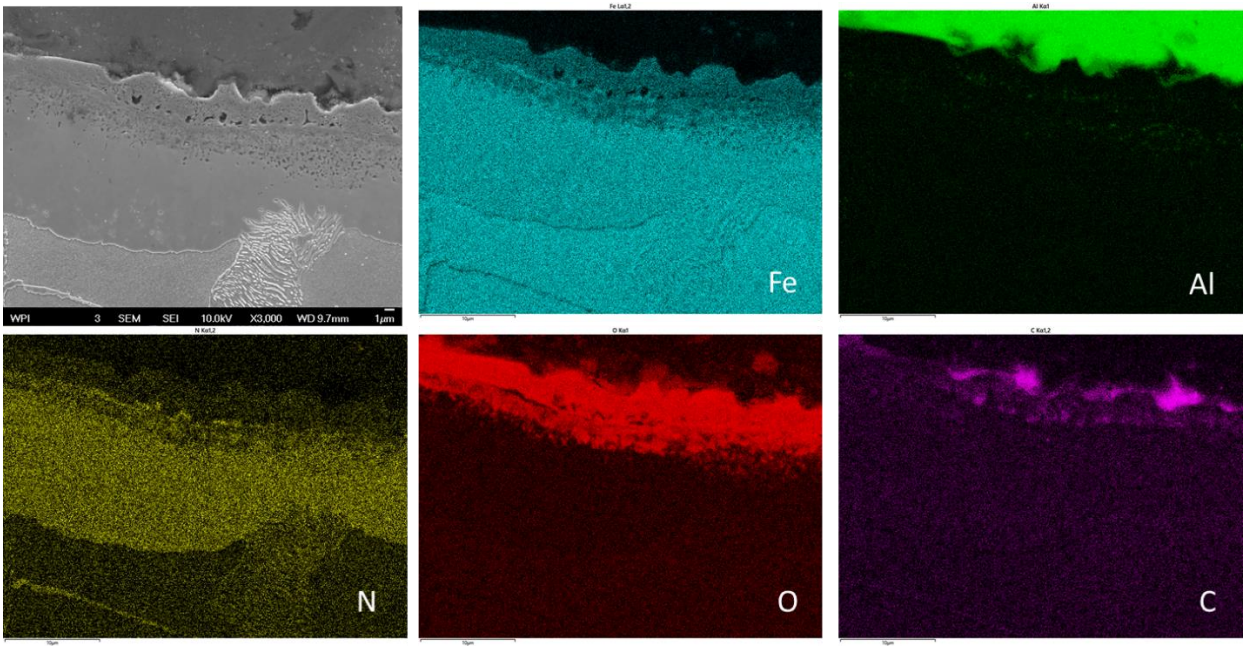

Figure 103 EDS mapping of AISI 1018 sample (KN=4 atm^(-1/2), KC=12, t=2 hr)

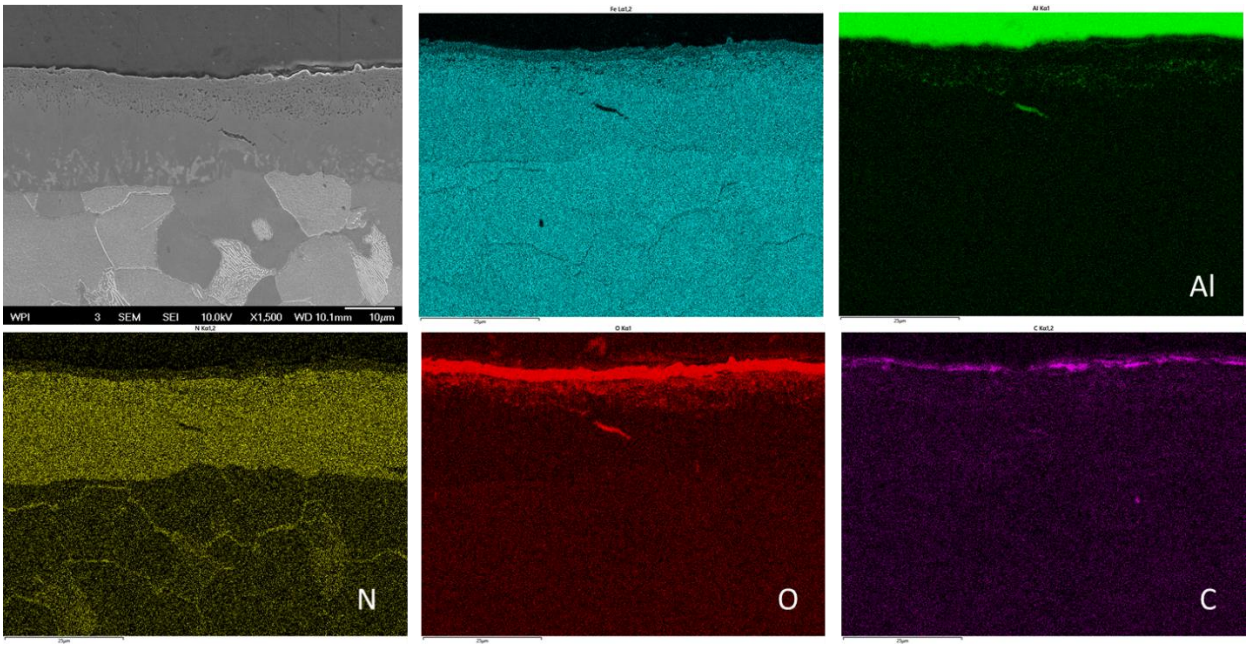

Figure 104 EDS mapping of AISI 1018 sample (KN=4 atm^(-1/2), KC=12, t=4 hr)

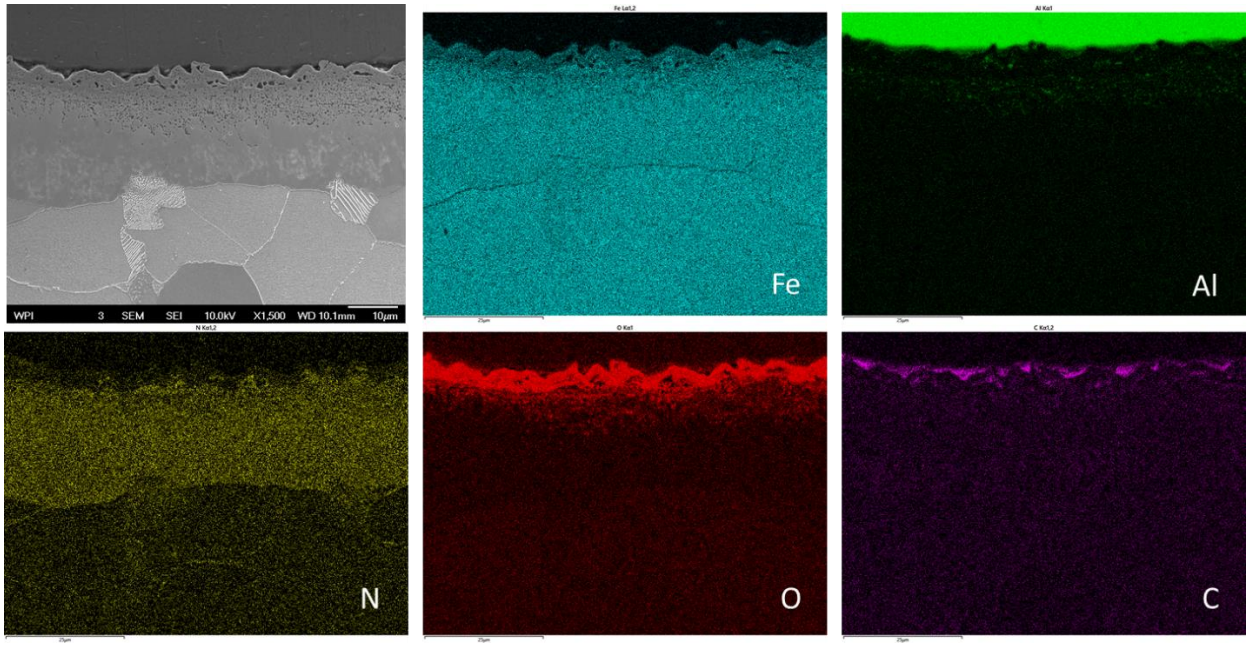

Figure 105 EDS mapping of AISI 1018 sample (KN=4 atm^(-1/2), KC=12, t=8 hr)

Cast iron (ASTM A536 80-55-06)

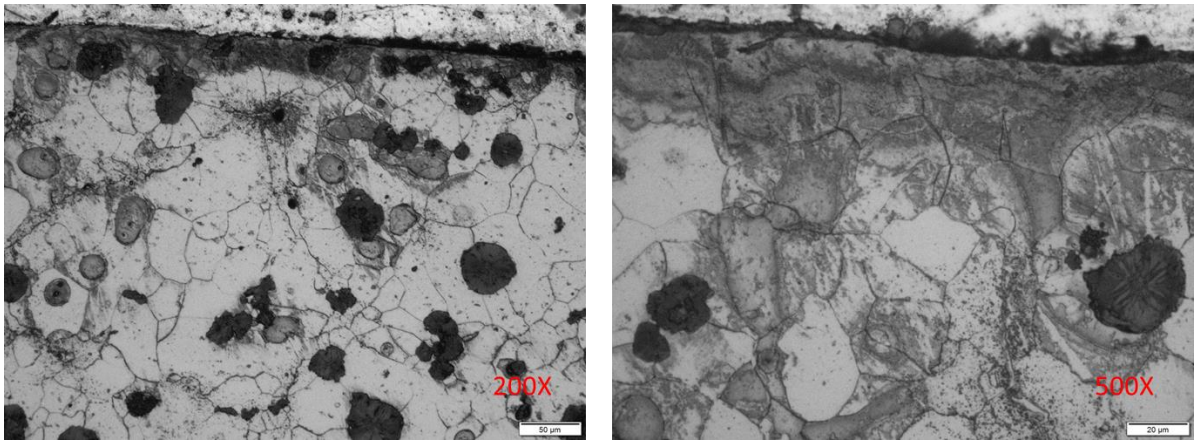

Figure 106 Optical micrographs of cast iron sample (KN=4 atm^(-1/2), KC=12, t=1 hr)

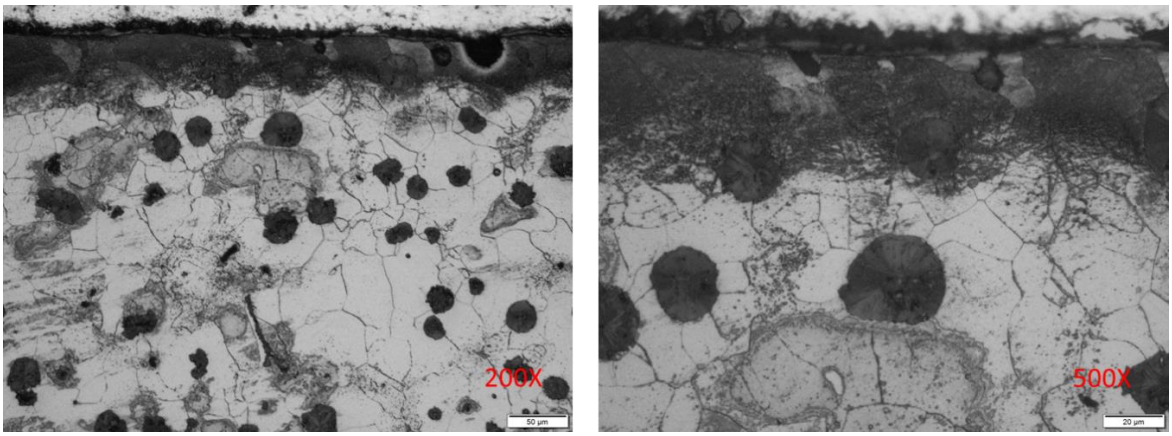

Figure 107 Optical micrographs of cast iron sample (KN=4 atm^(-1/2), KC=12, t=2 hr)

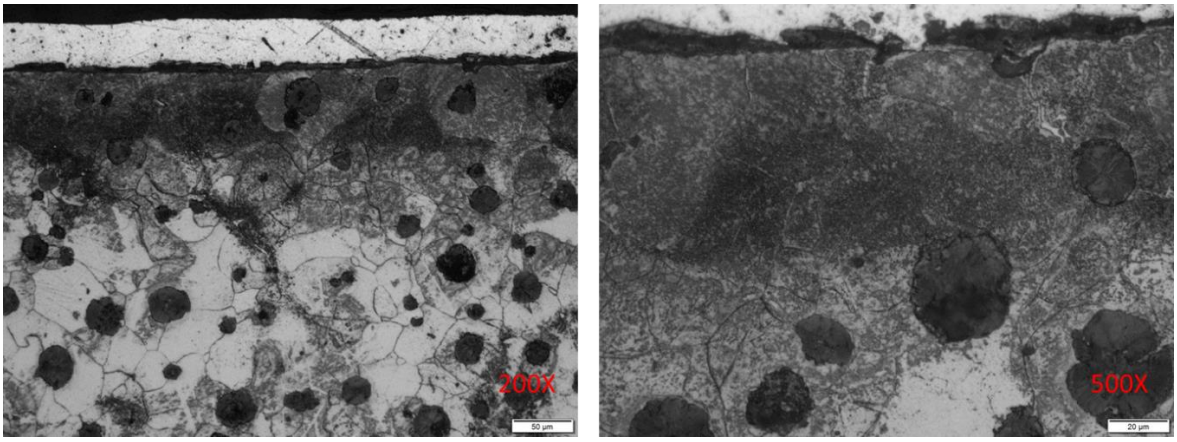

Figure 108 Optical micrographs of cast iron sample (KN=4 atm^(-1/2), KC=12, t=4 hr)

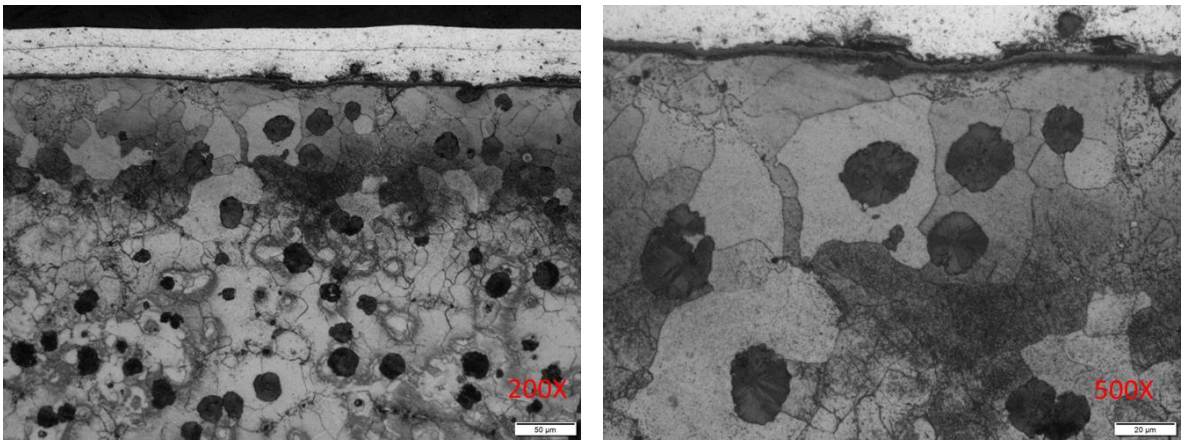

Figure 109 Optical micrographs of cast iron sample (KN=4 atm^(-1/2), KC=12, t=8 hr)

2nd FNC trial without oxidation

Section 1: Kc=0 trials

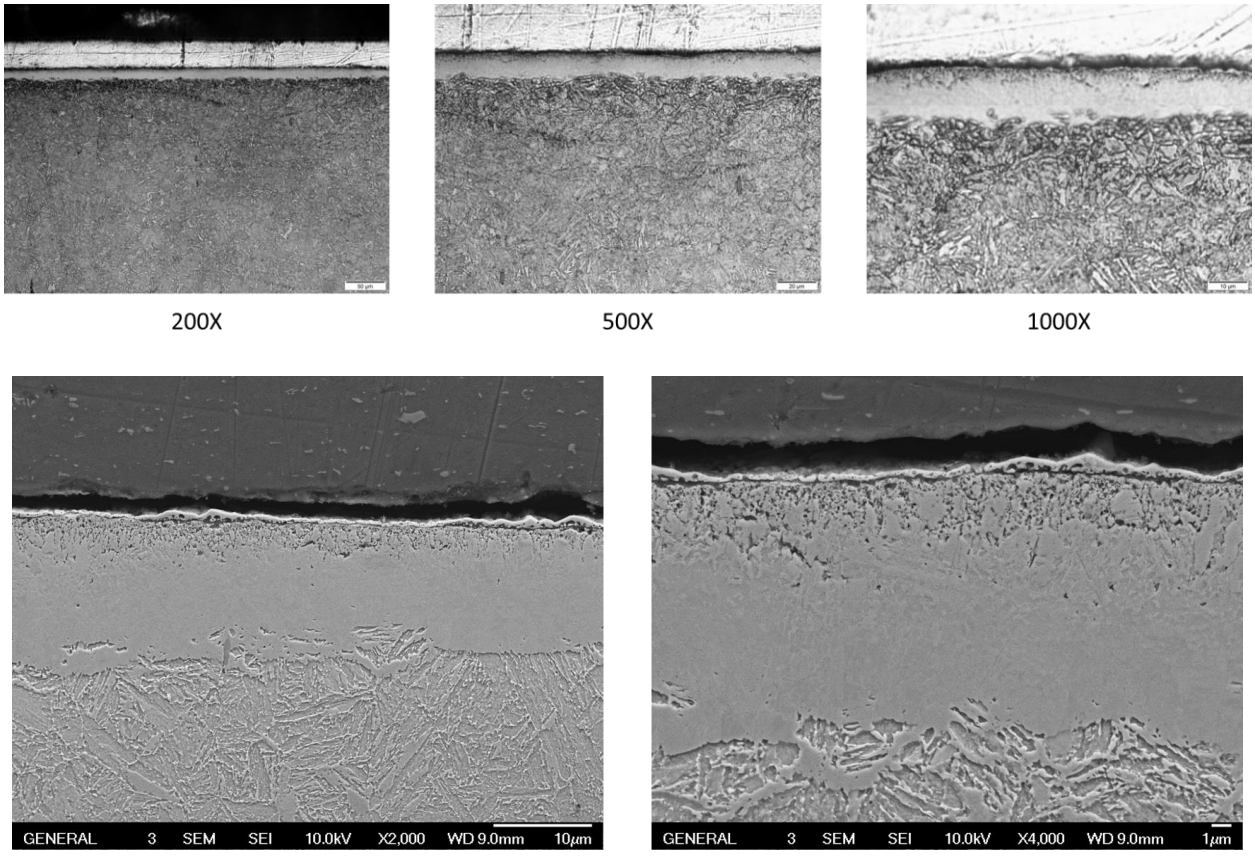

Figure 110 Compound layer of AISI 4140 sample (KN=4 atm^(-1/2), KC=0, t=2 hr)

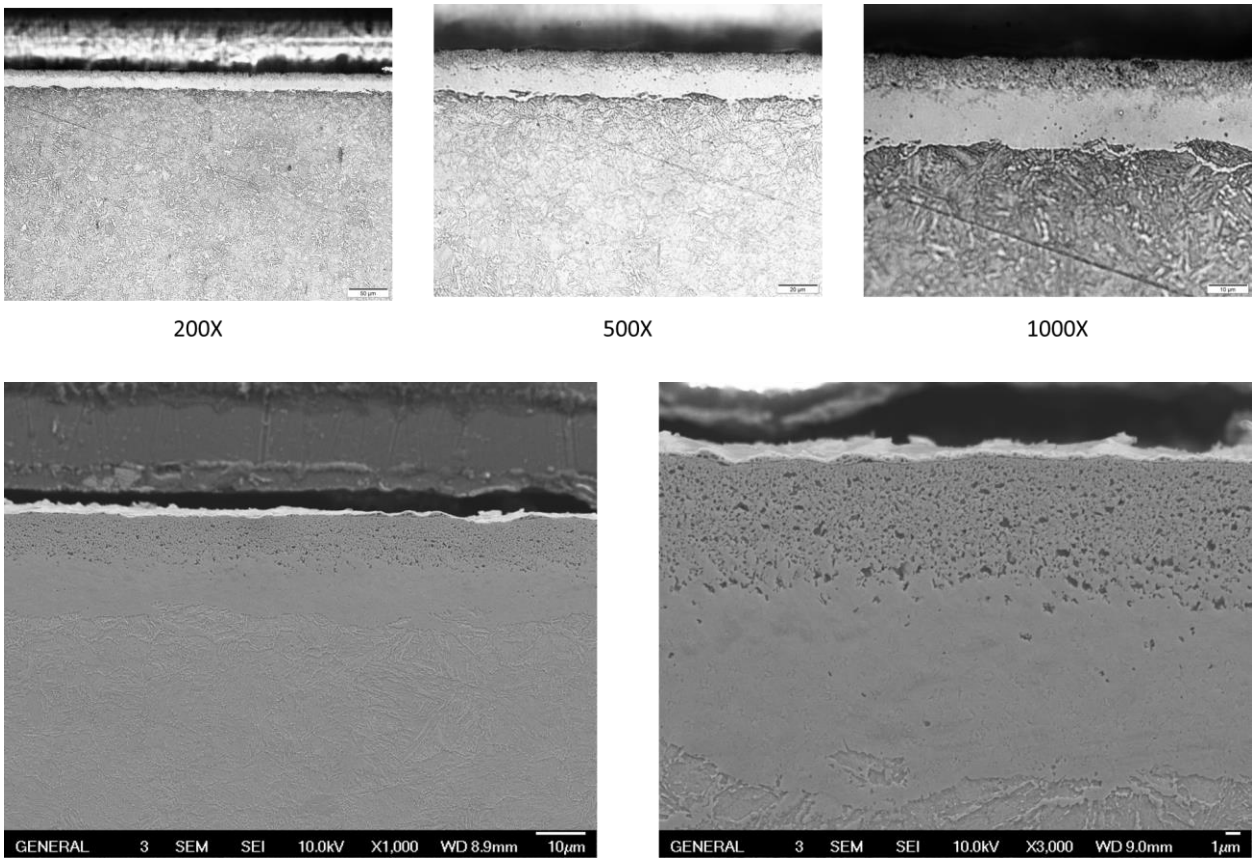

Figure 111 Compound layer of AISI 4140 sample (KN=4 atm^(-1/2), KC=0, t=4 hr)

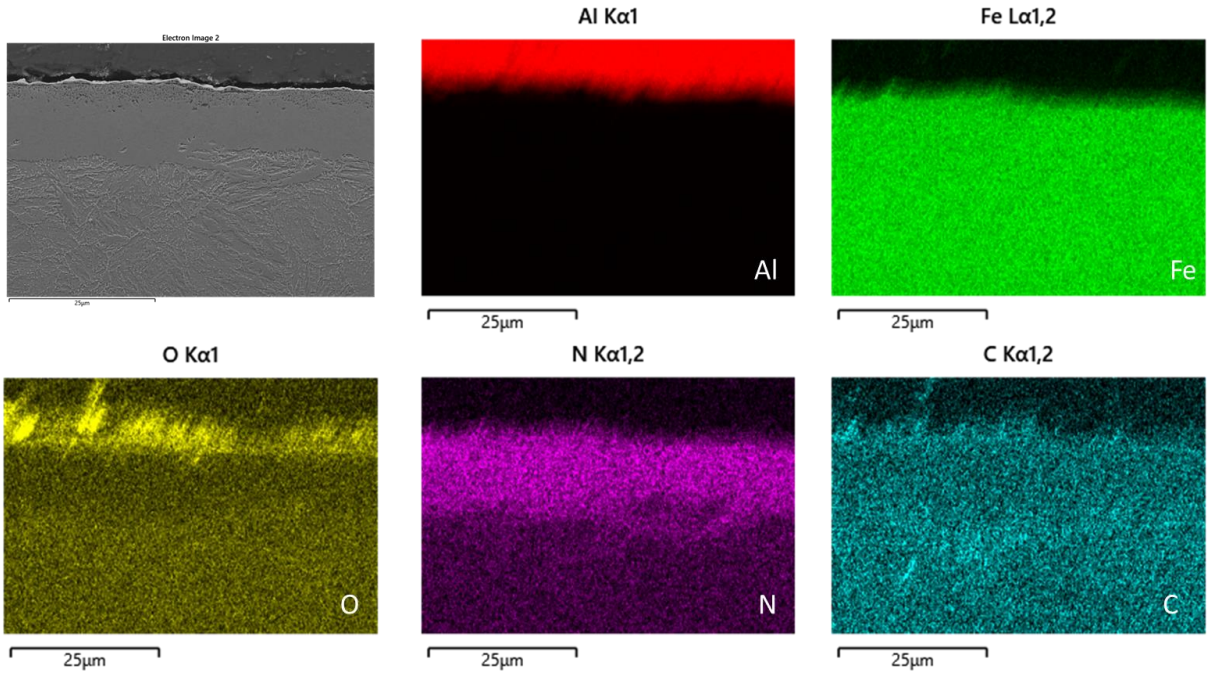

Figure 112 EDS mapping of AISI 4140 sample (KN=4 atm^(-1/2), KC=0, t=2 hr)

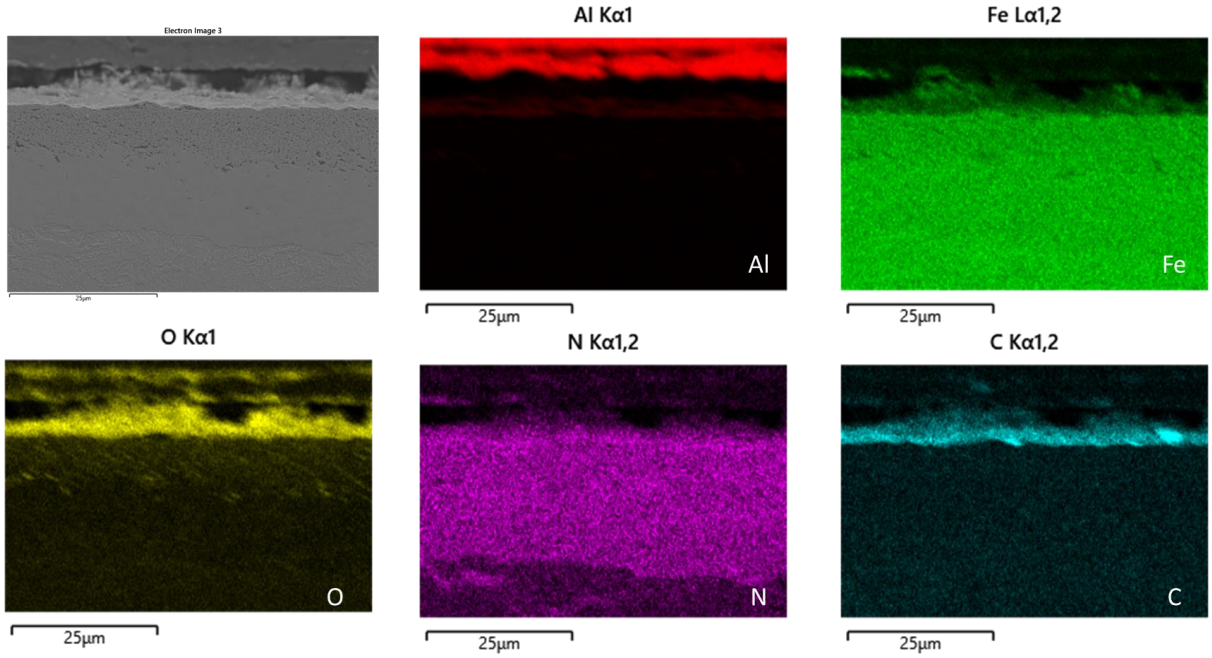

Figure 113 EDS mapping of AISI 4140 sample (KN=4 atm^(-1/2), KC=0, t=4 hr)

Section 2: Kc=9 trials

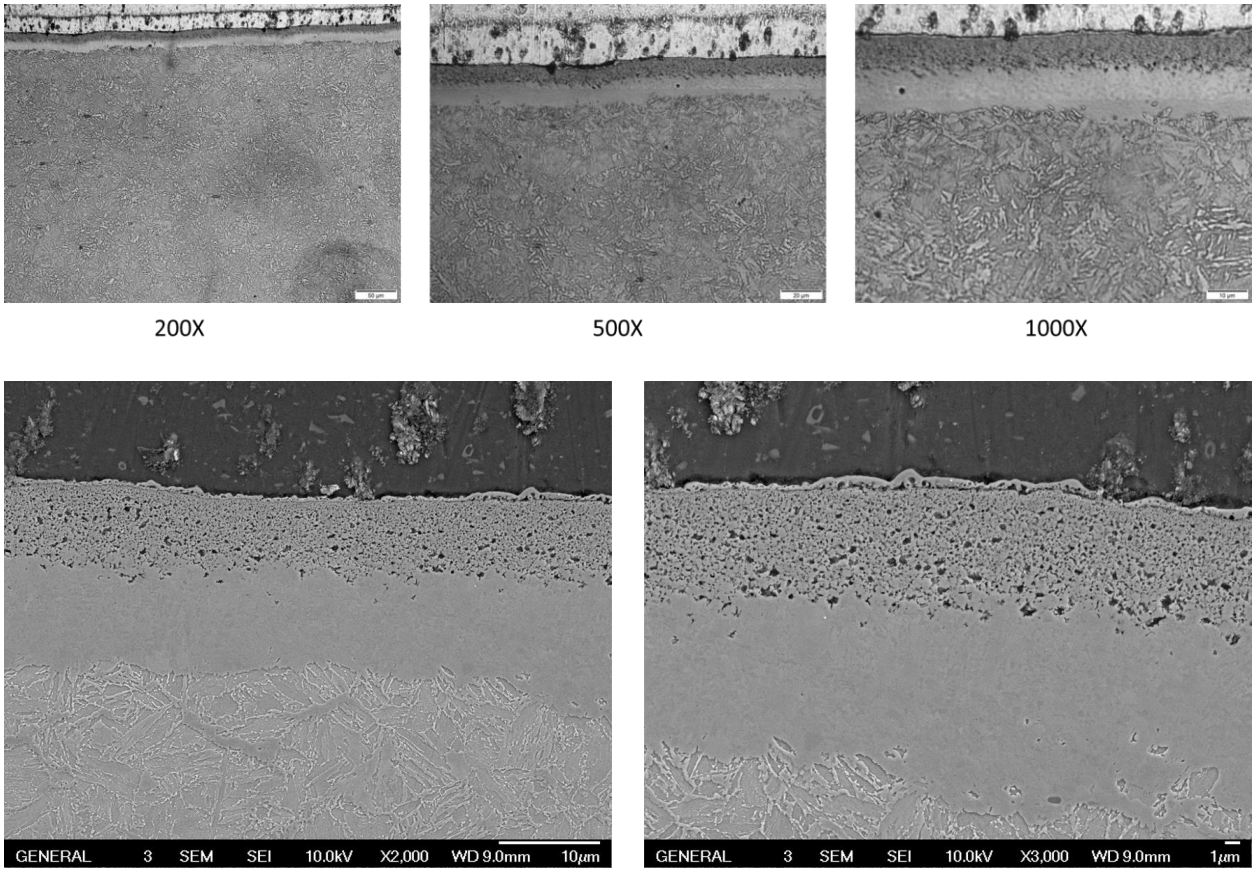

Figure 114 Compound layer of AISI 4140 sample (KN=4 atm^(-1/2), KC=9, t=2 hr)

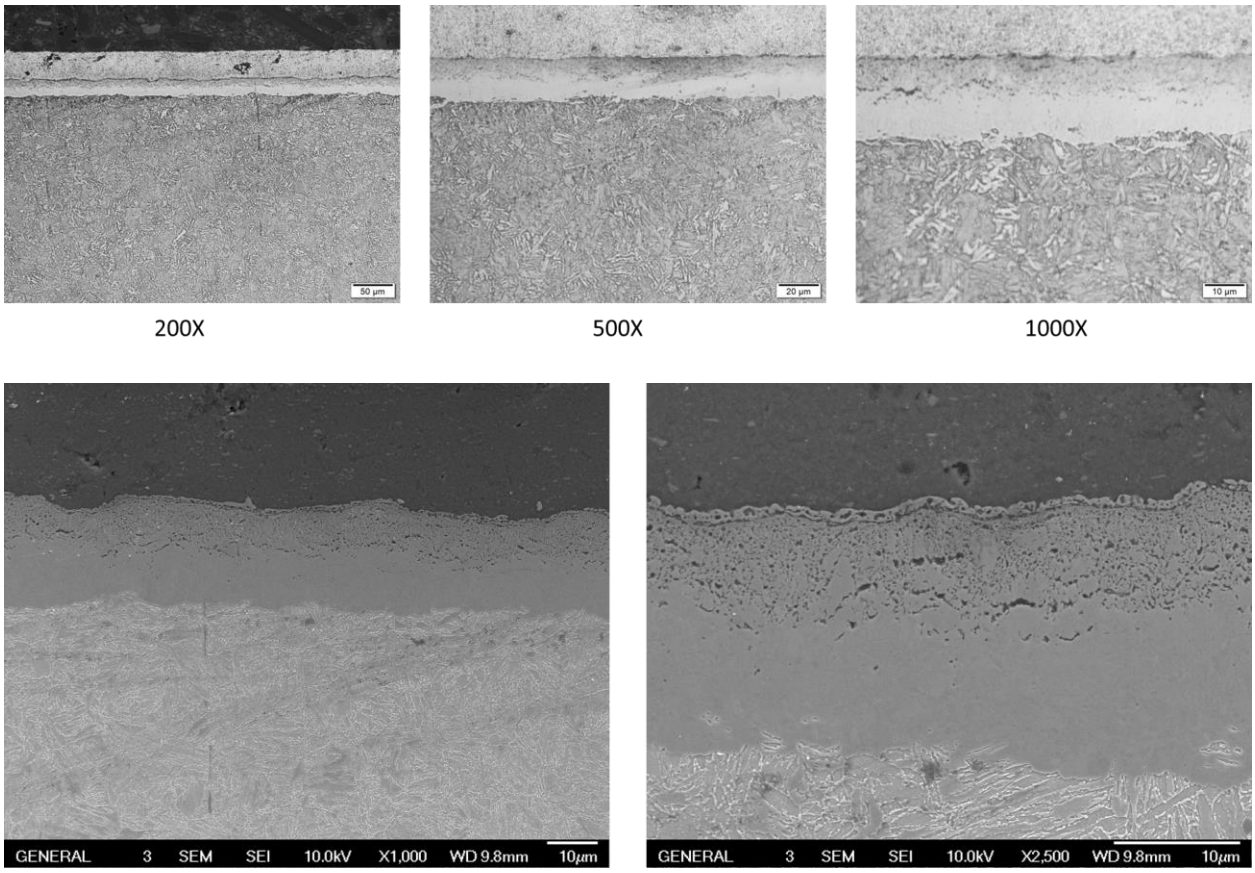

Figure 115 Compound layer of AISI 4140 sample (KN=4 atm^(-1/2), KC=9, t=4 hr)

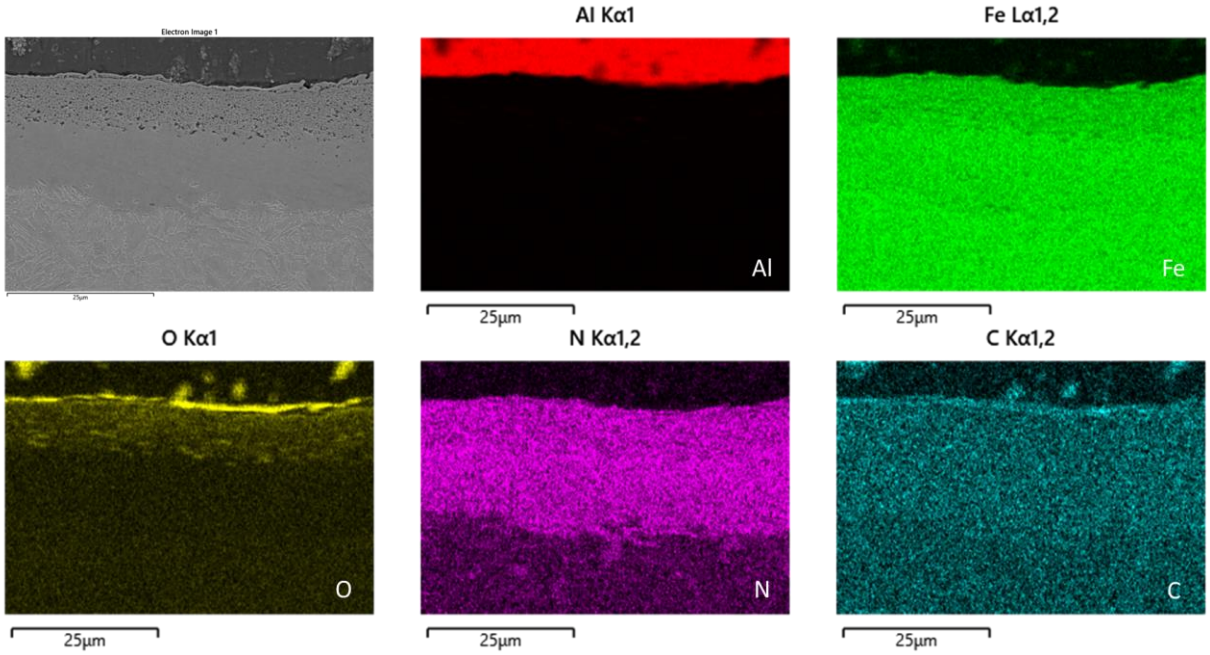

Figure 116 EDS mapping of AISI 4140 sample (KN=4 atm^(-1/2), KC=9, t=2 hr)

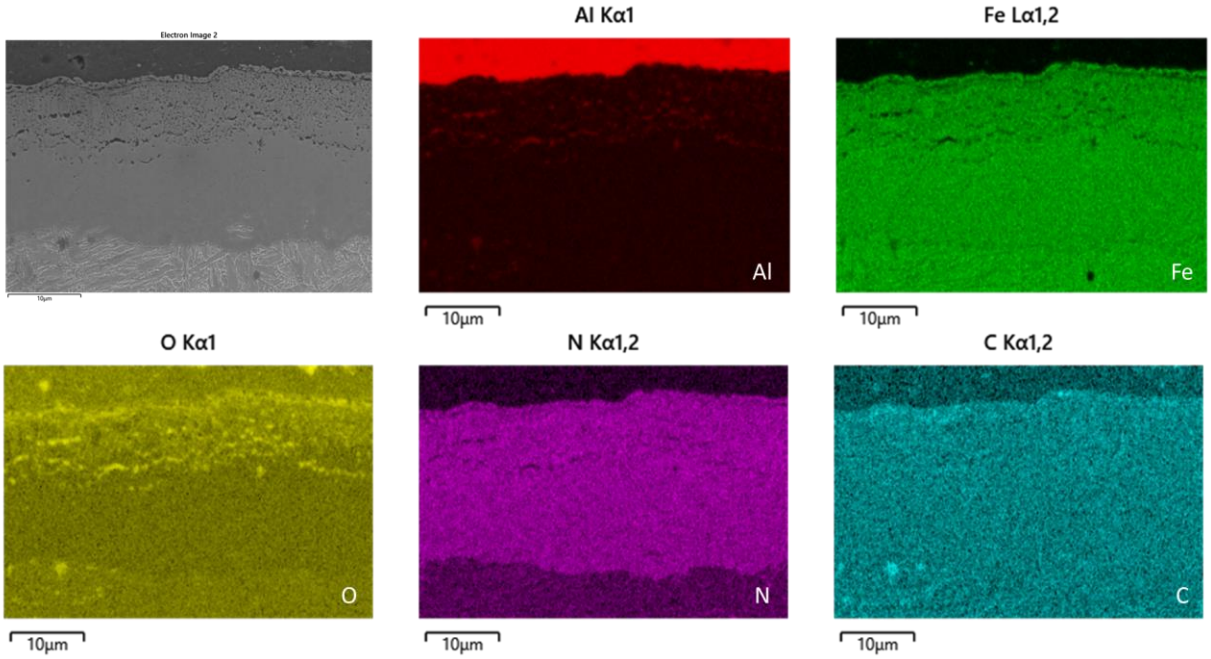

Figure 117 EDS mapping of AISI 4140 sample (KN=4 atm^(-1/2), KC=9, t=4 hr)

Section 3: Kc=12 trials

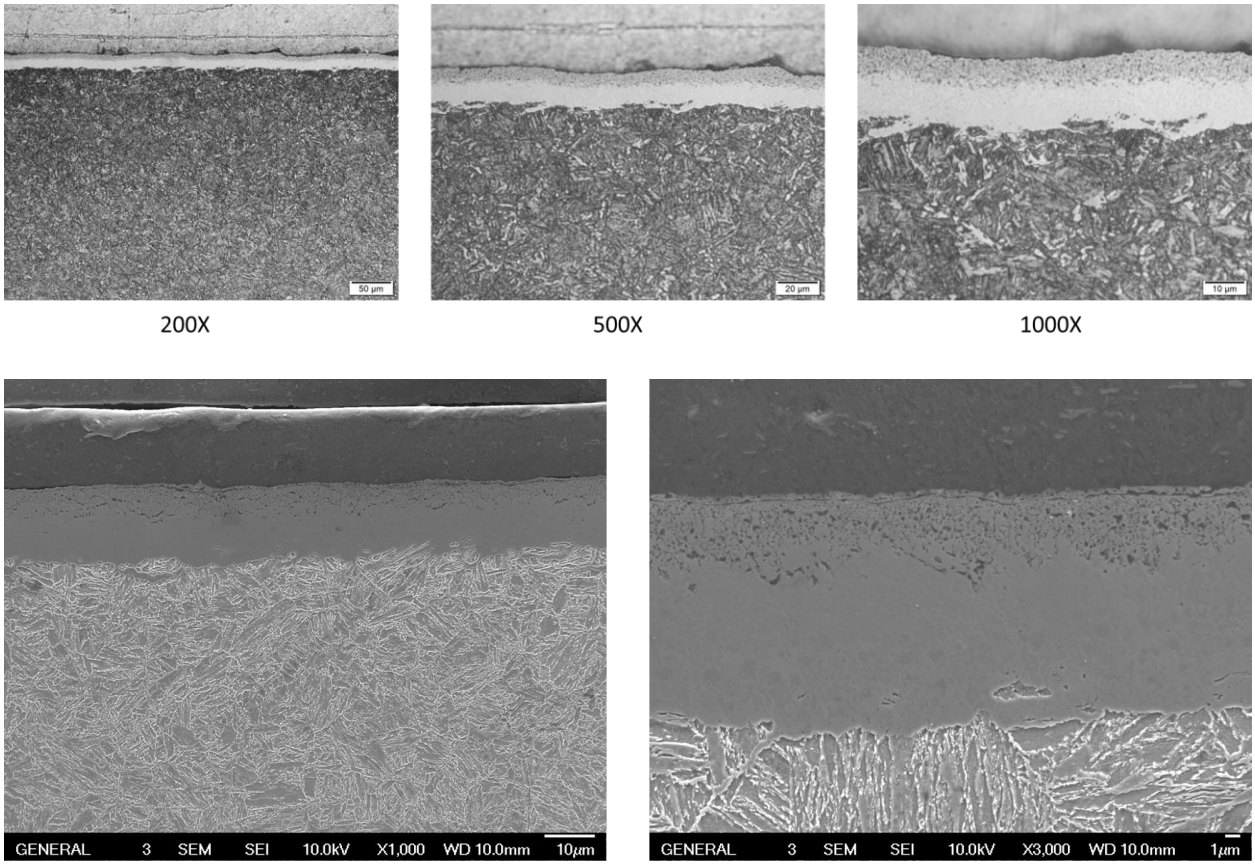

Figure 118 Compound layer of AISI 4140 sample (KN=4 atm^(-1/2), KC=12, t=2 hr)

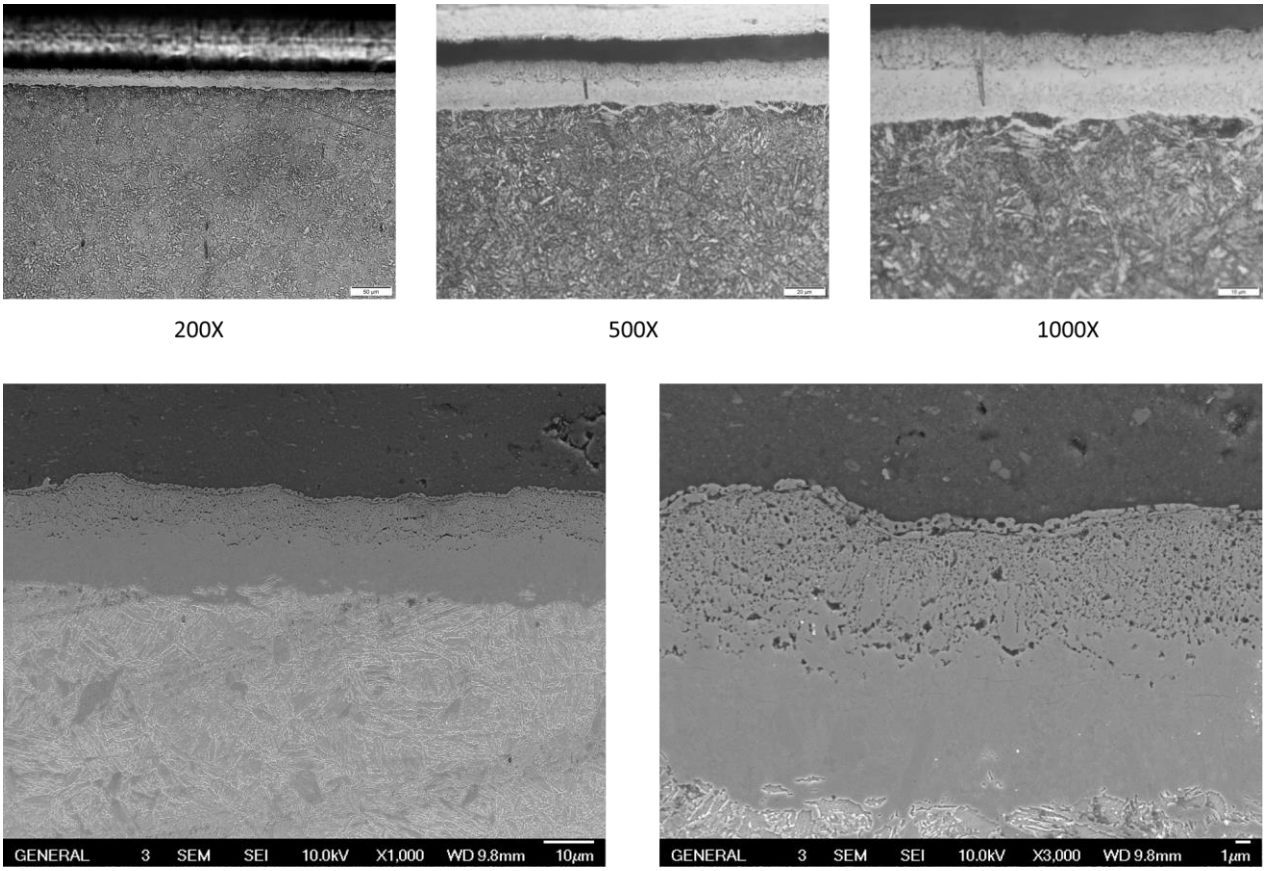

Figure 119 Compound layer of AISI 4140 sample (KN=4 atm^(-1/2), KC=12, t=4 hr)

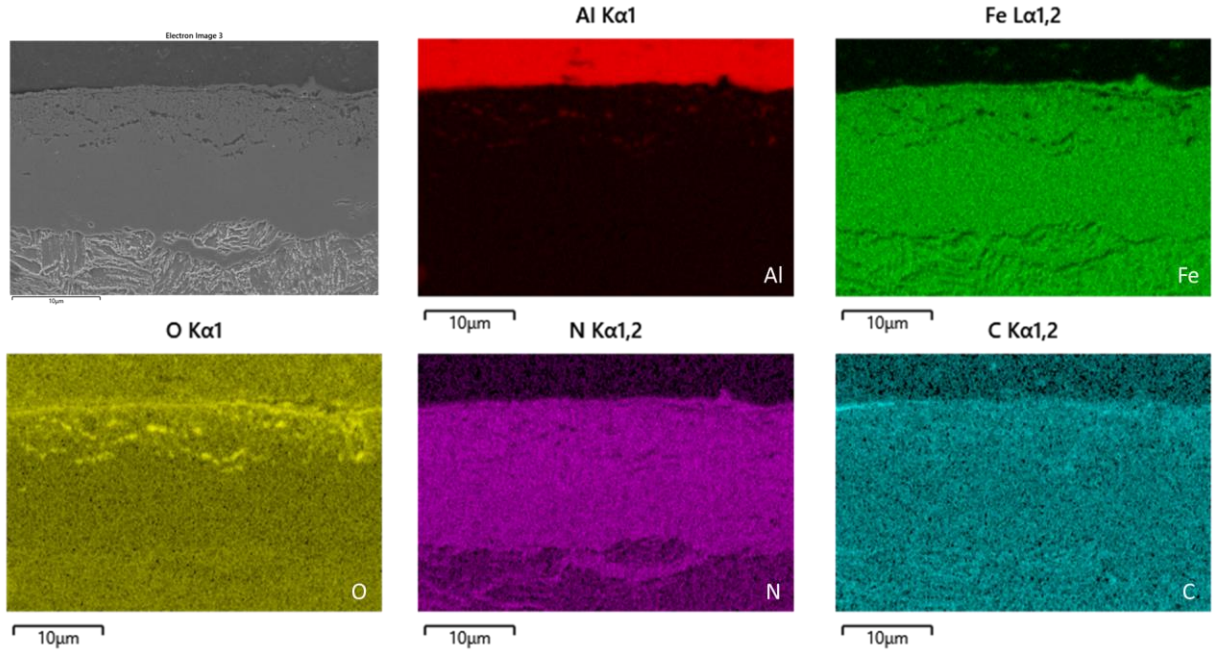

Figure 120 EDS mapping of AISI 4140 sample (KN=4 atm^(-1/2), KC=12, t=2 hr)

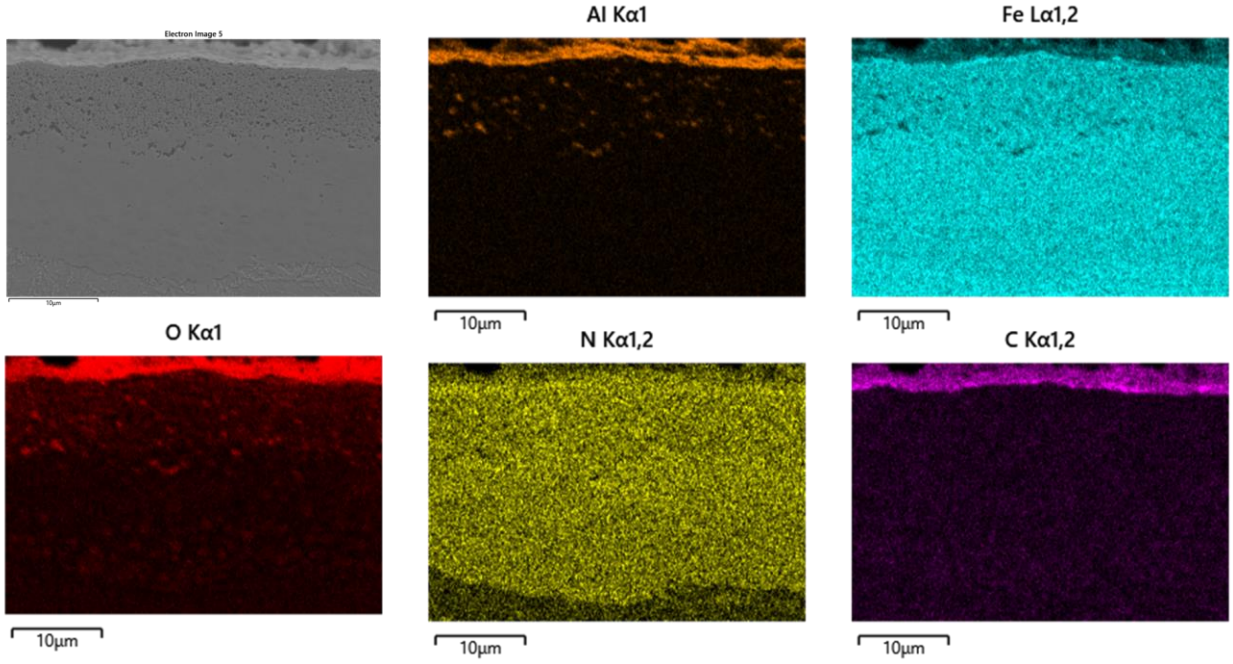

Figure 121 EDS mapping of AISI 4140 sample (KN=4 atm^(-1/2), KC=12, t=4 hr)

Appendix 2: Nitrogen and carbon concentration profiles measured with OES

1st FNC trial with pre & post oxidation

Section 1: Kc=0 trials

AISI 4140

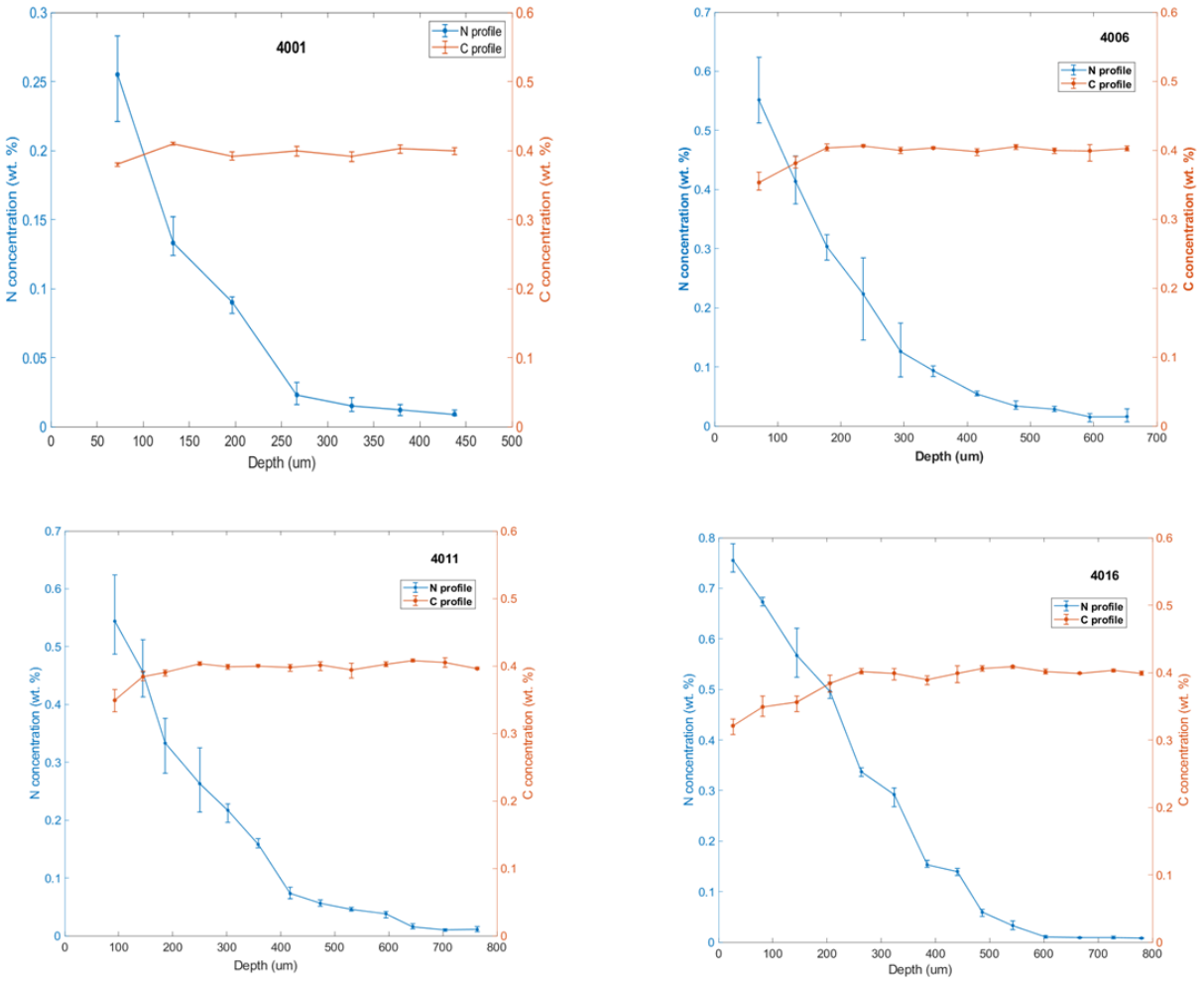

Figure 122 Nitrogen and carbon concentration profiles of the first group samples (AISI 4140, KC=0, t=1h, 2h,4h, and 8h)

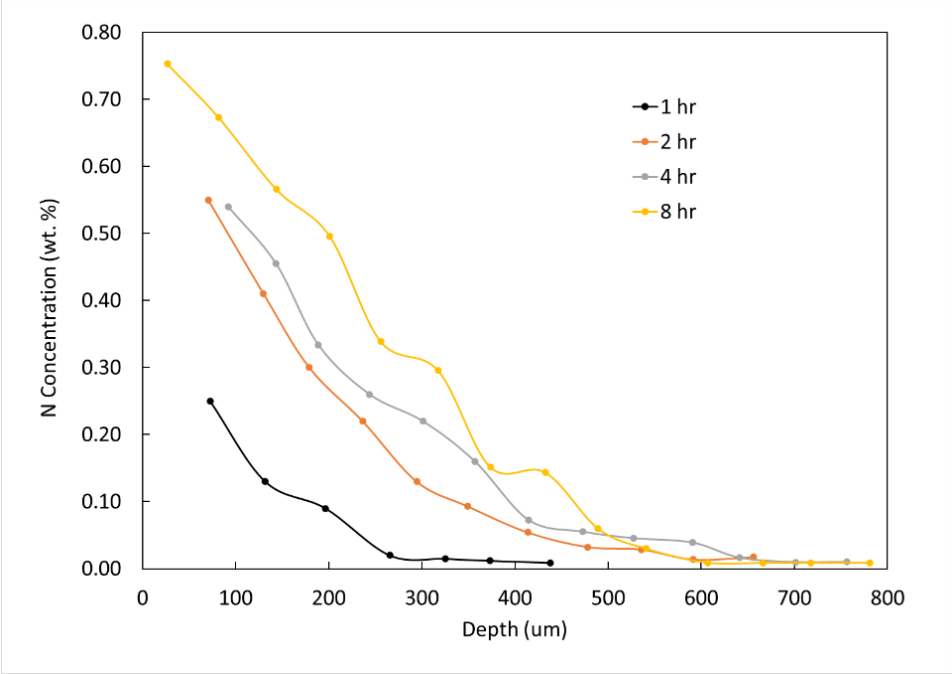

Figure 123 Comparison of nitrogen concentration profiles of the first group samples (AISI 4140, KC=0, t= 1h, 2h. 4h. and 8h)

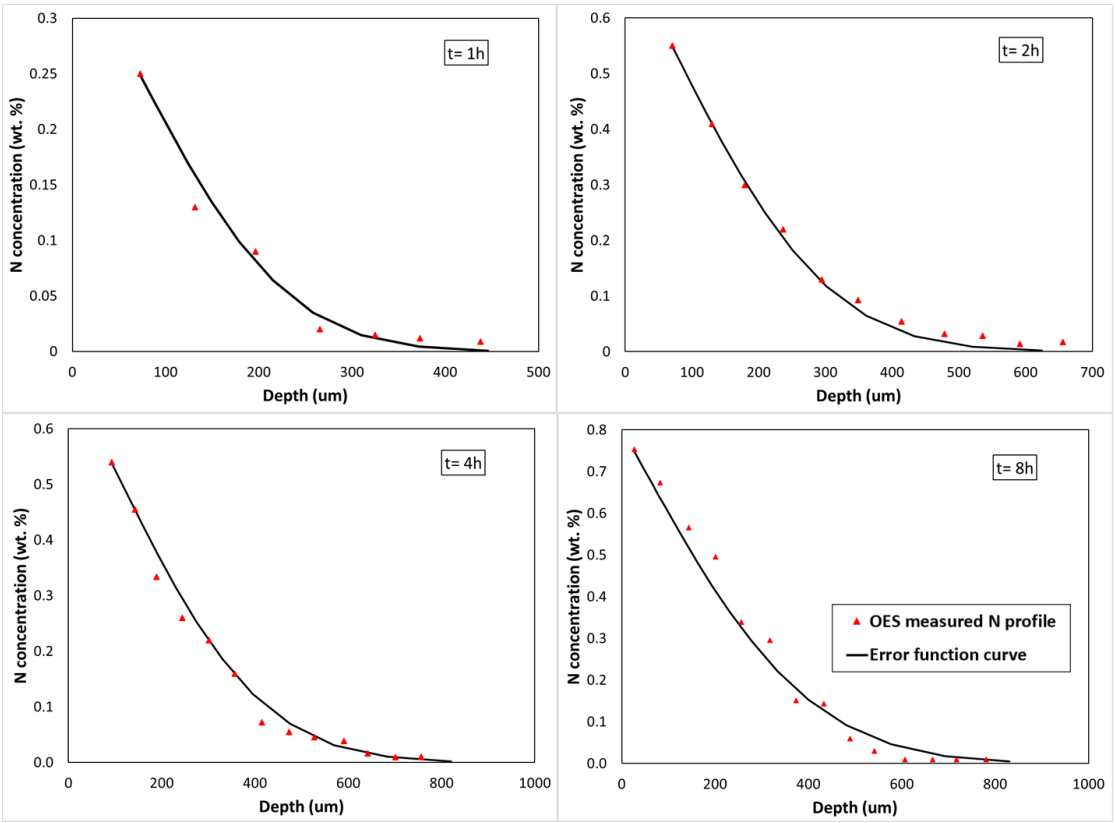

Figure 124 Measured nitrogen concentration profile and fitted Error function curve of the first group AISI 4140 samples (KC=0)

AISI 1018

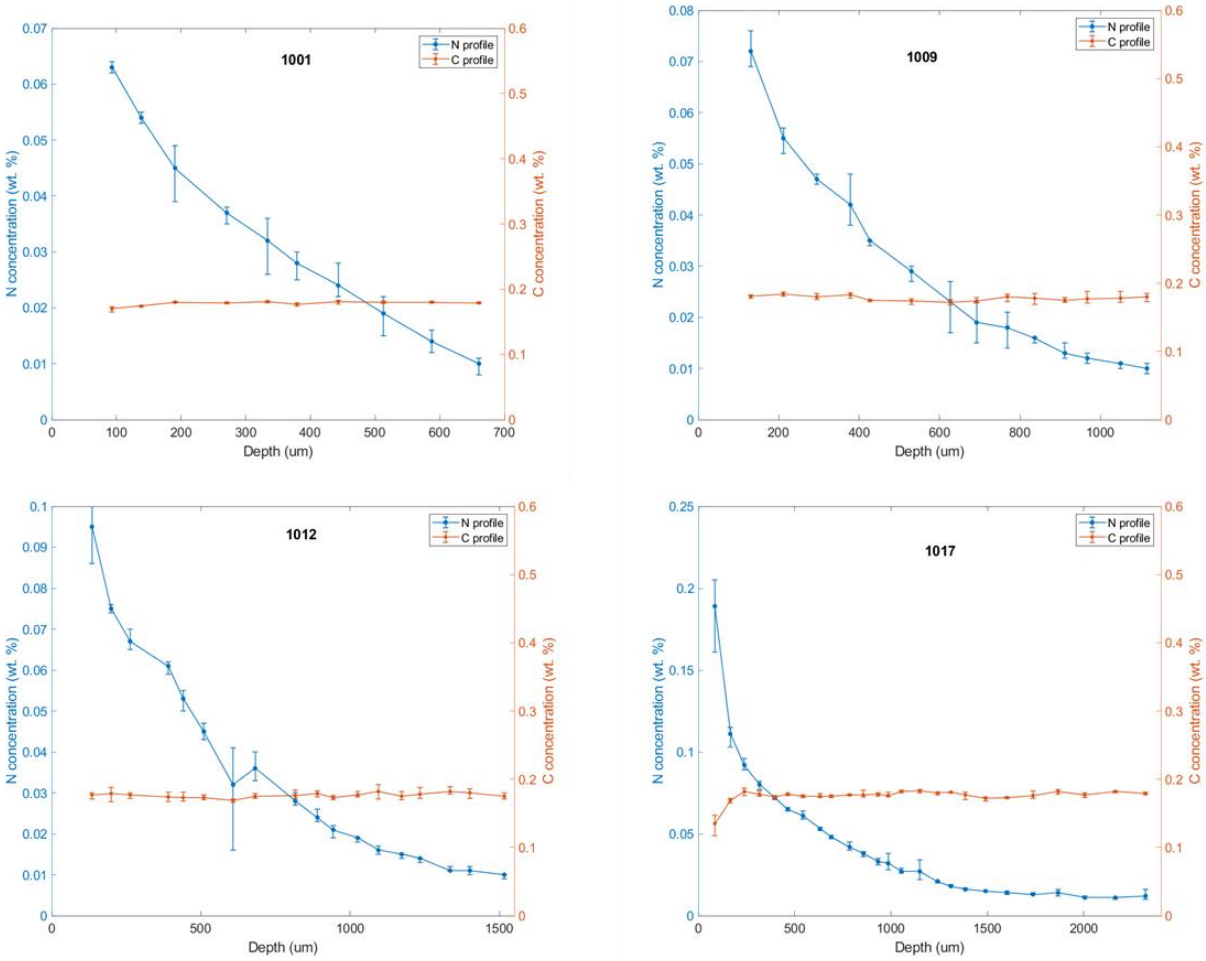

Figure 125 Nitrogen and carbon concentration profiles of the first group samples (AISI 1018, KC=0, t=1h, 2h,4h, and 8h)

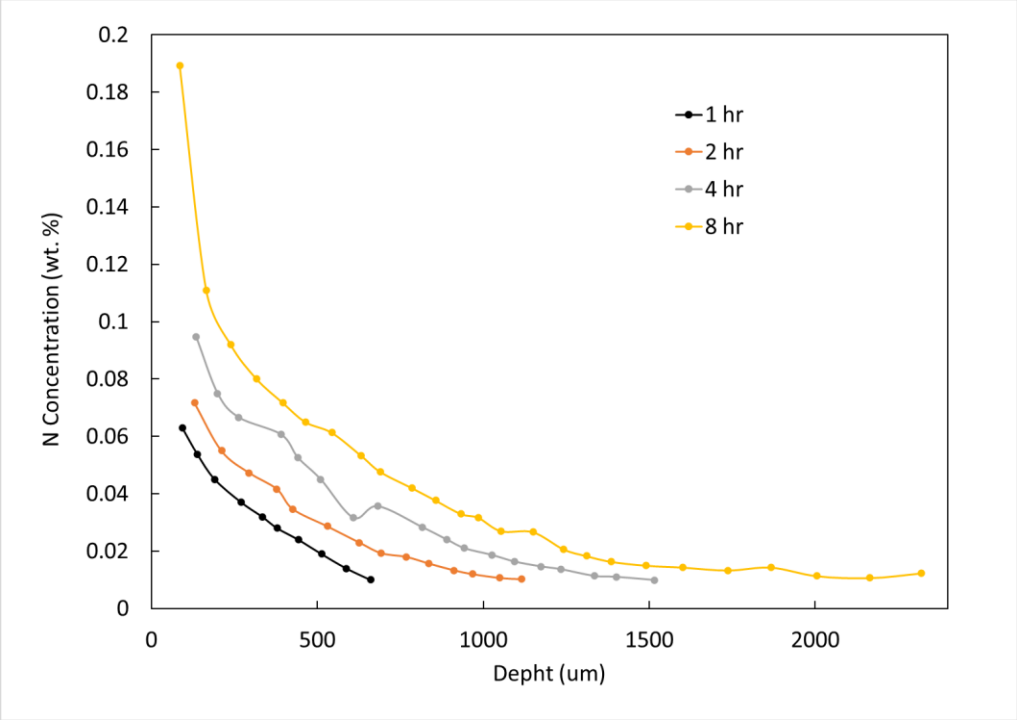

Figure 126 Comparison of nitrogen concentration profiles of the first group samples (AISI 1018, KC=0, t= 1h, 2h. 4h. and 8h)

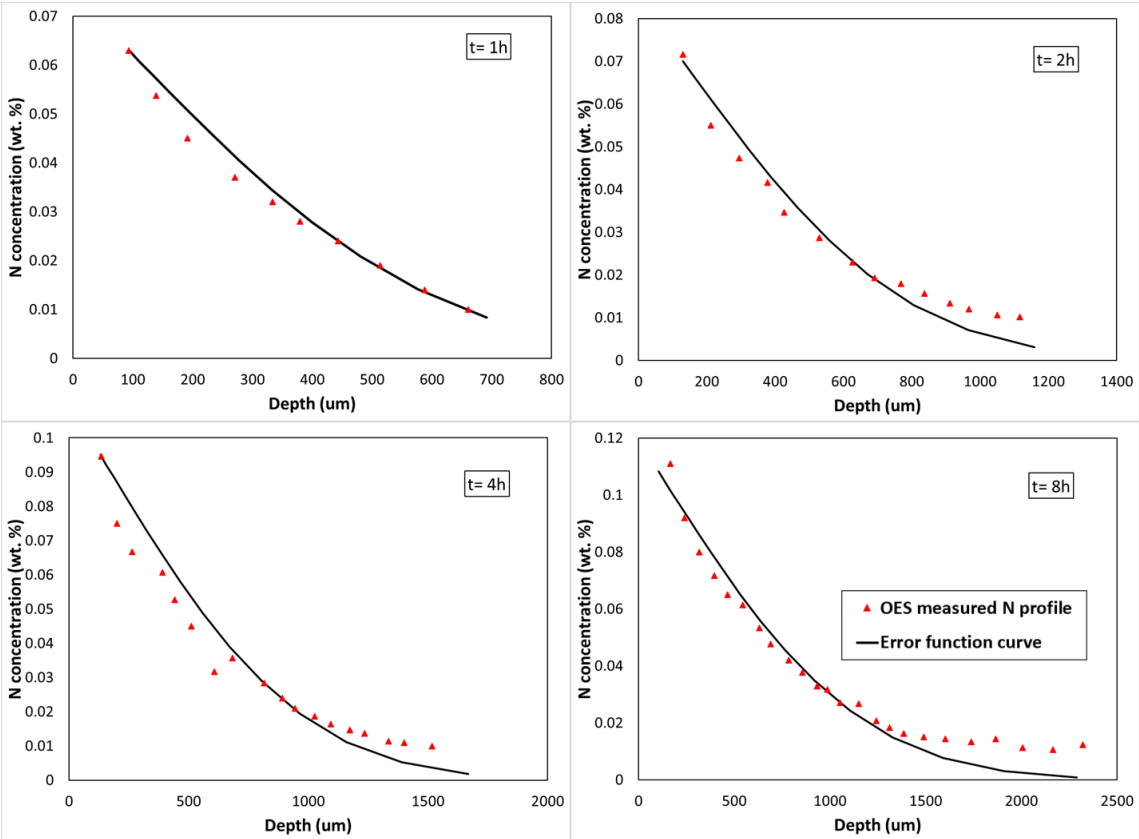

Figure 127 Measured nitrogen concentration profile and fitted Error function curve of the first group AISI 1018 samples (KC=0)

Section 2: Kc=9 trials

AISI 4140

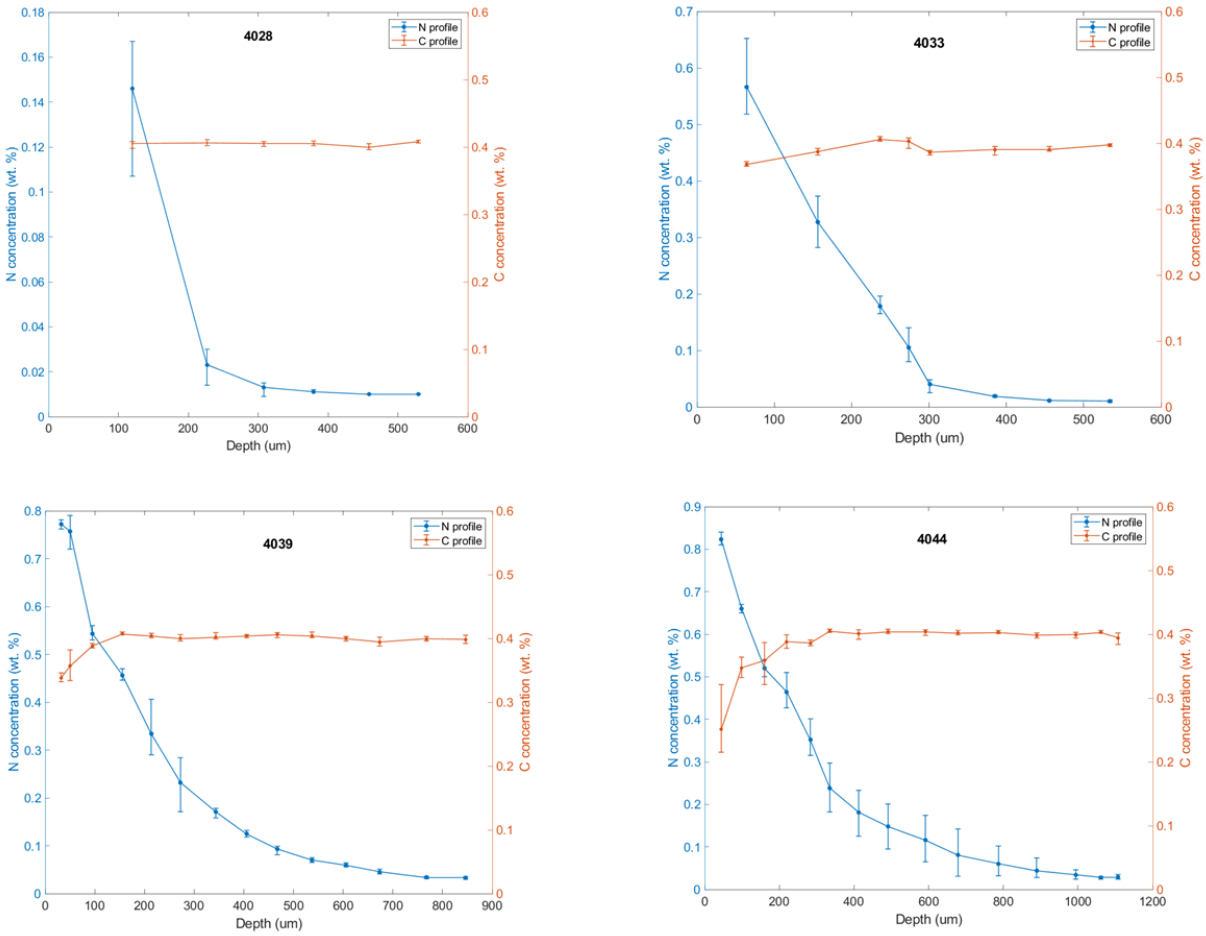

Figure 128 Nitrogen and carbon concentration profiles of the second group samples (AISI 4140, KC=9, t=1h, 2h,4h, and 8h)

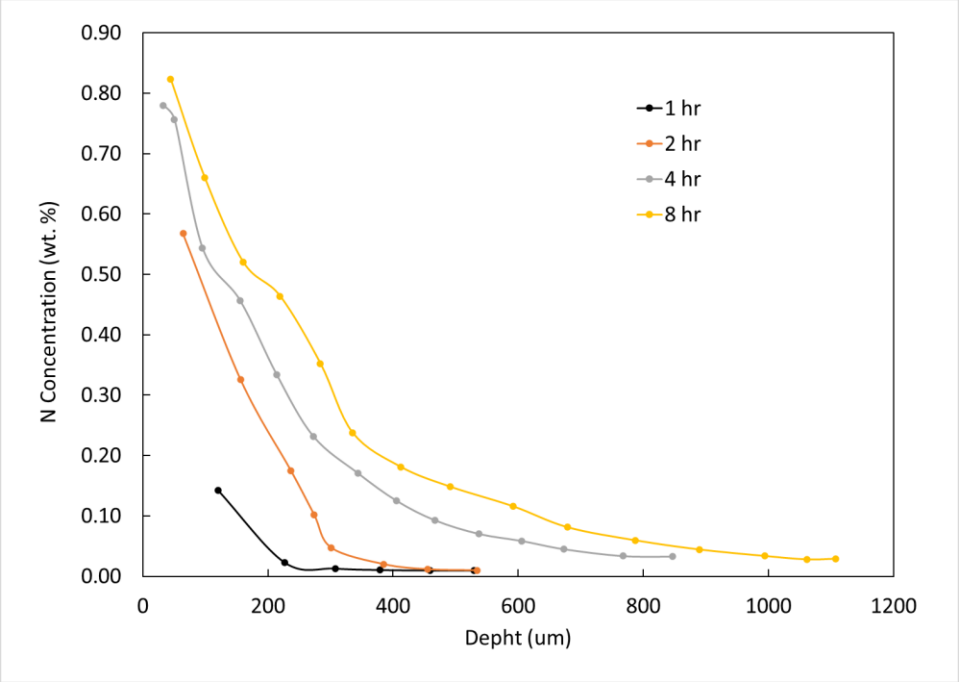

Figure 129 Comparison of nitrogen concentration profiles of the second group samples (AISI 4140, KC=9, t= 1h, 2h. 4h. and 8h)

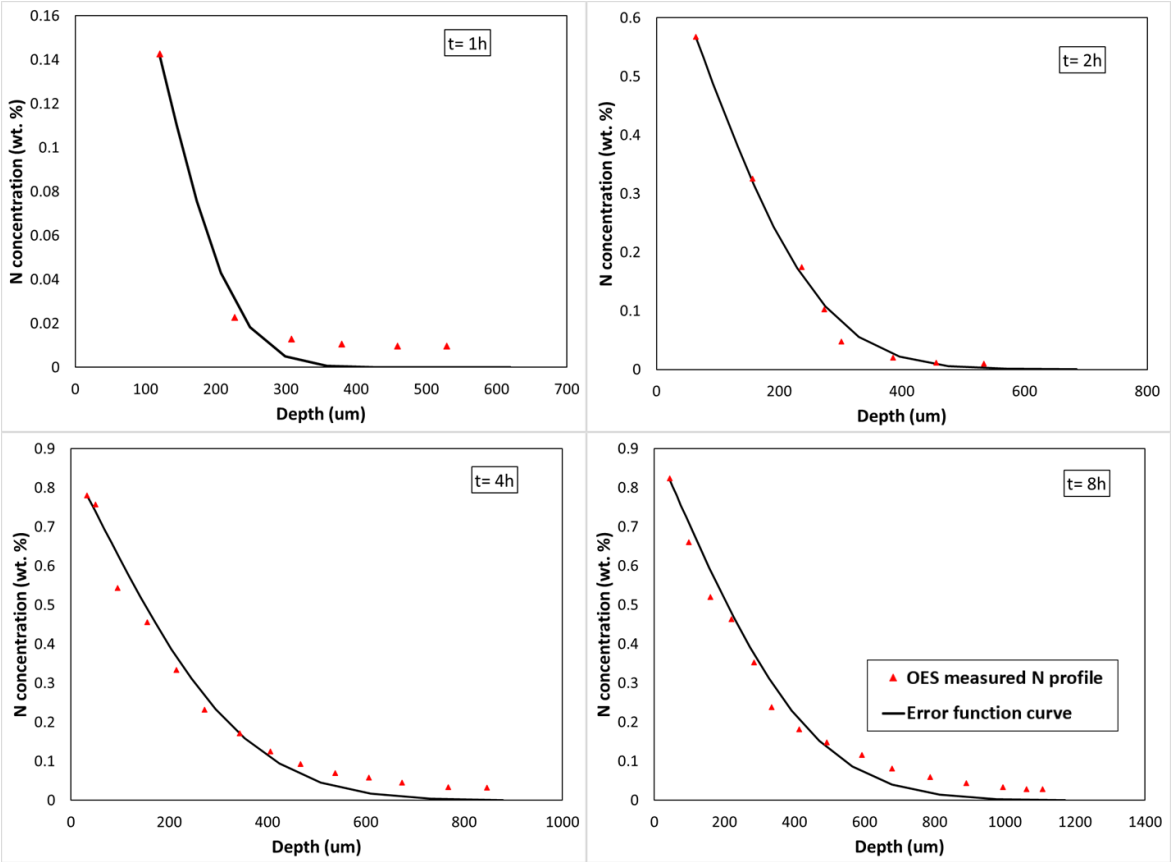

Figure 130 Measured nitrogen concentration profile and fitted Error function curve of the second group AISI 4140 samples (KC=9)

AISI 1018

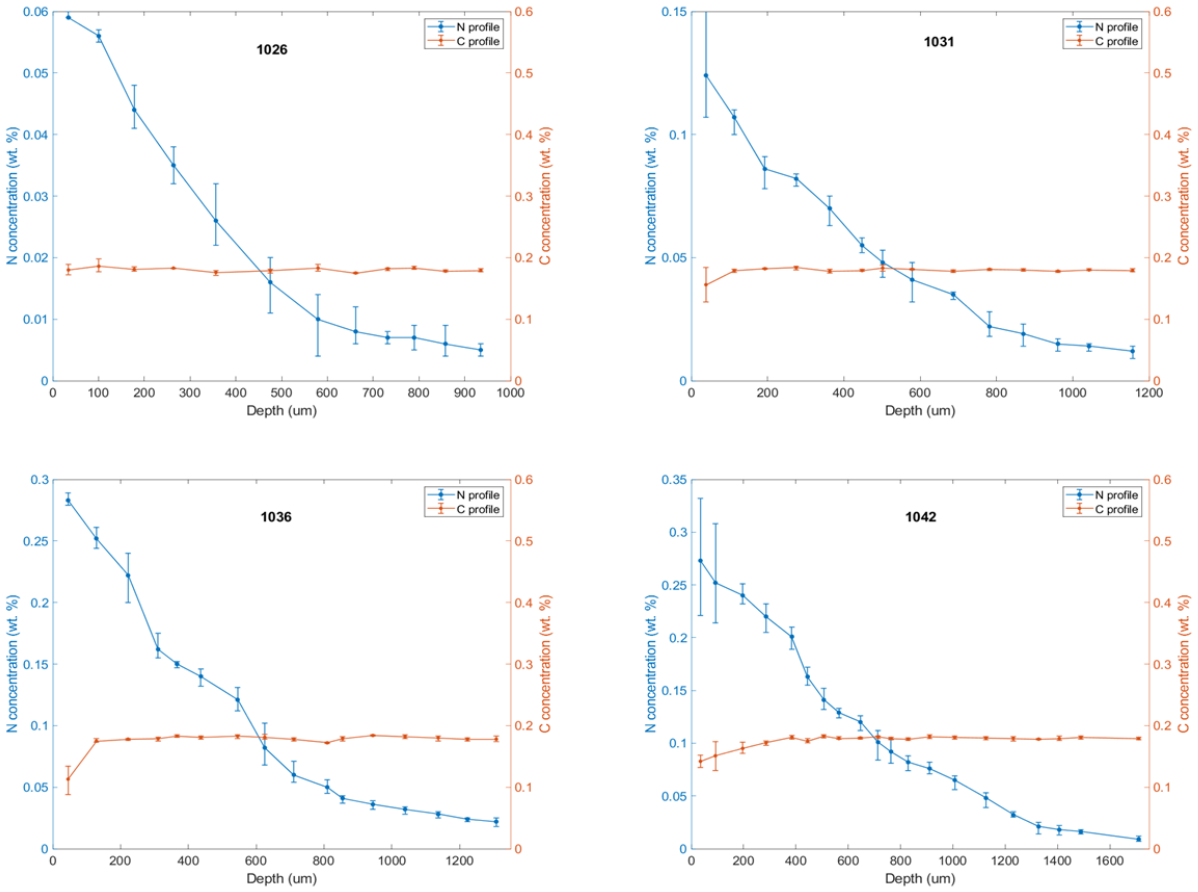

Figure 131 Nitrogen and carbon concentration profiles of the second group samples (AISI 1018, KC=9, t=1h, 2h,4h, and 8h)

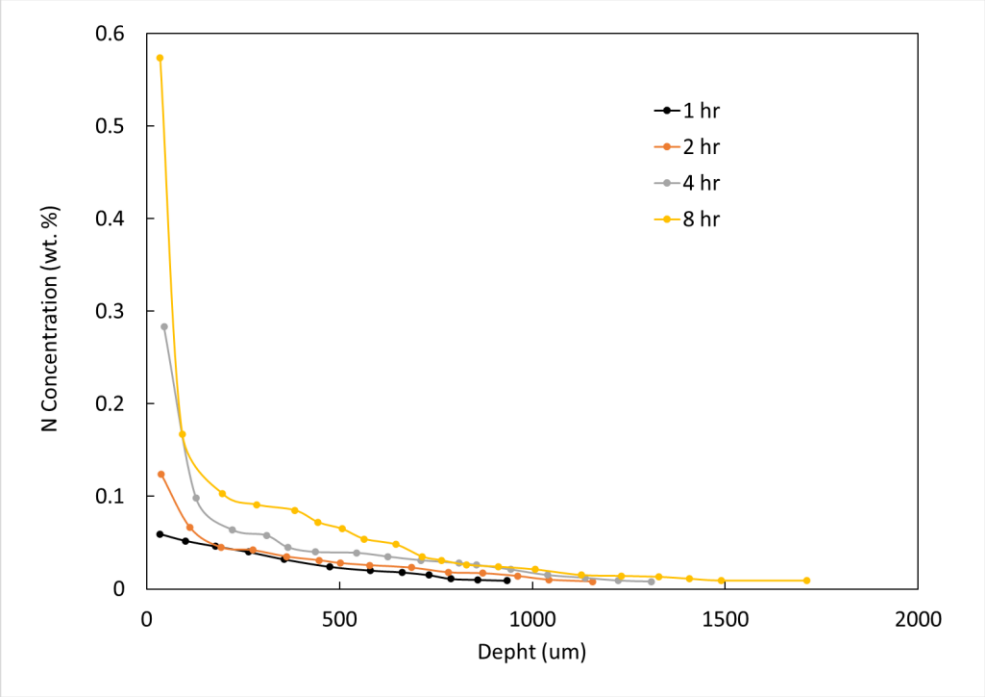

Figure 132 Comparison of nitrogen concentration profiles of the second group samples (AISI 1018, KC=9, t= 1h, 2h. 4h. and 8h)

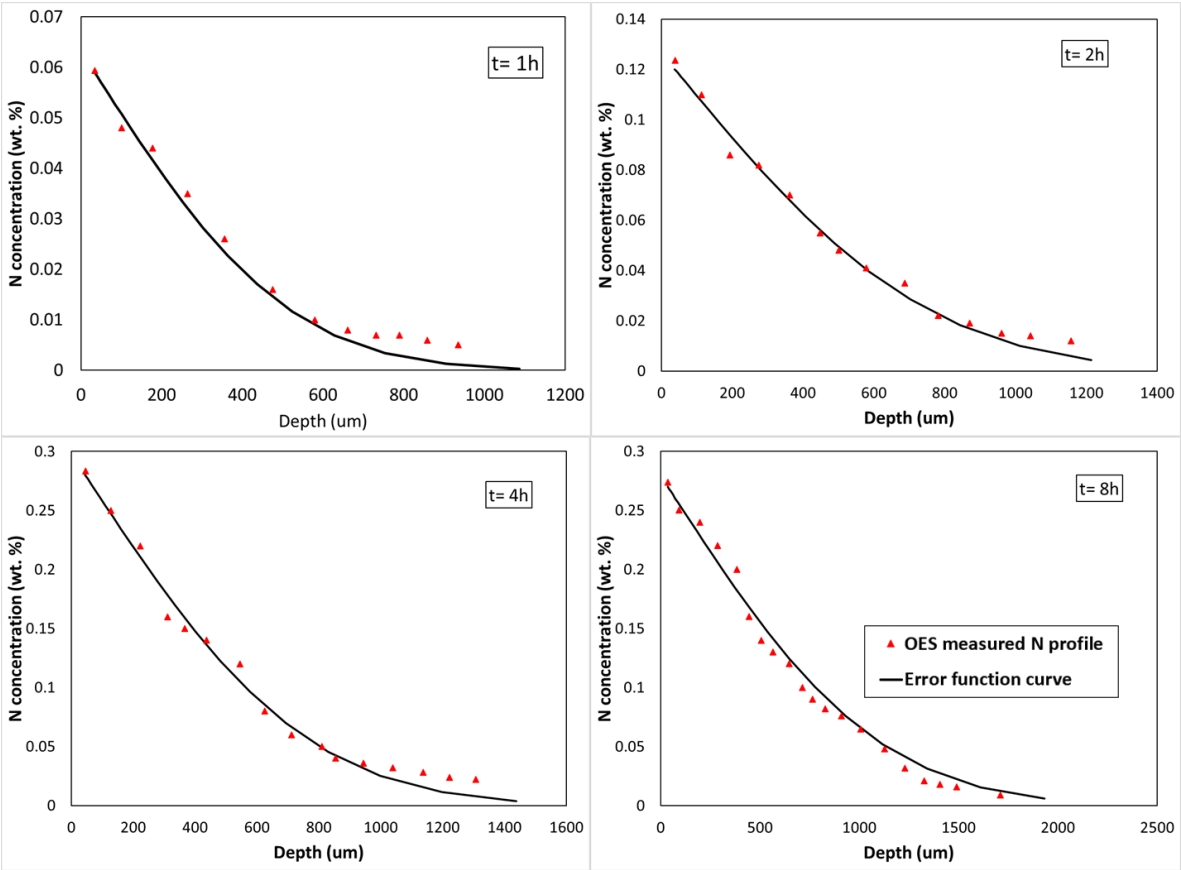

Figure 133 Measured nitrogen concentration profile and fitted Error function curve of the second group AISI 1018 samples (KC=9)

Section 3: Kc=12 trials

AISI 4140

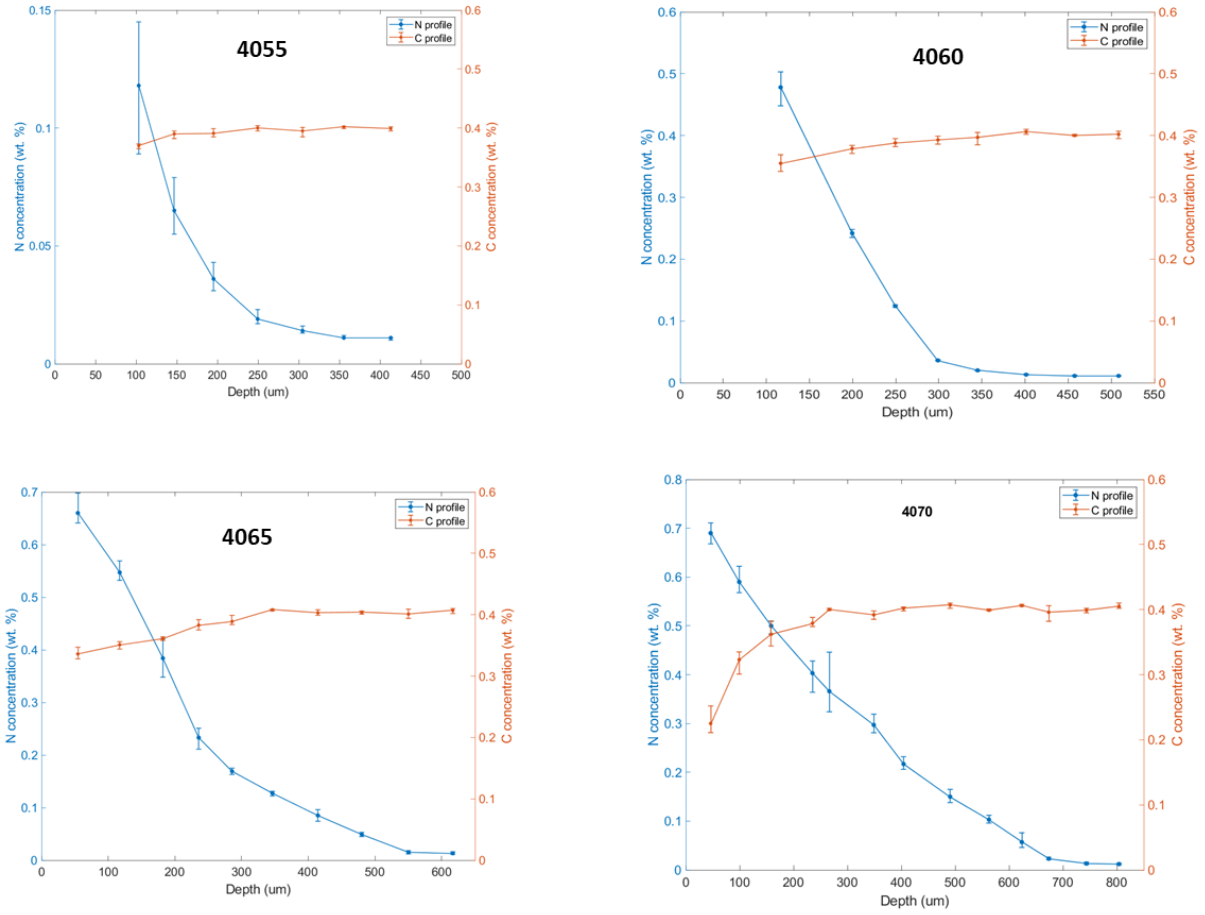

Figure 134 Nitrogen and carbon concentration profiles of the third group samples (AISI 4140, KC=12, t=1h, 2h,4h, and 8h)

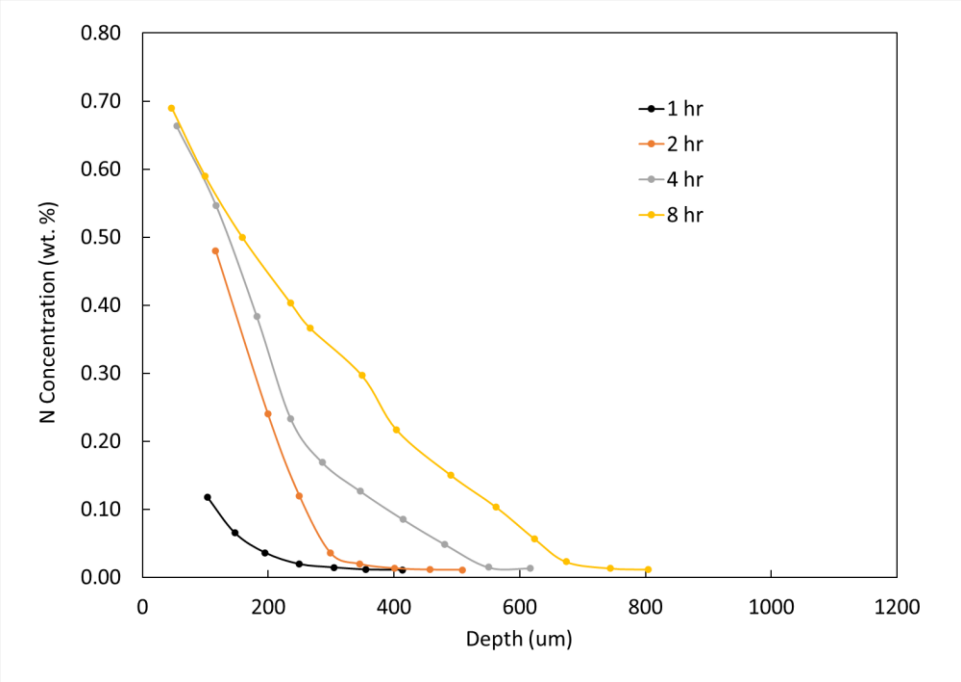

Figure 135 Comparison of nitrogen concentration profiles of the third group samples (AISI 4140, KC=12, t= 1h, 2h. 4h. and 8h)

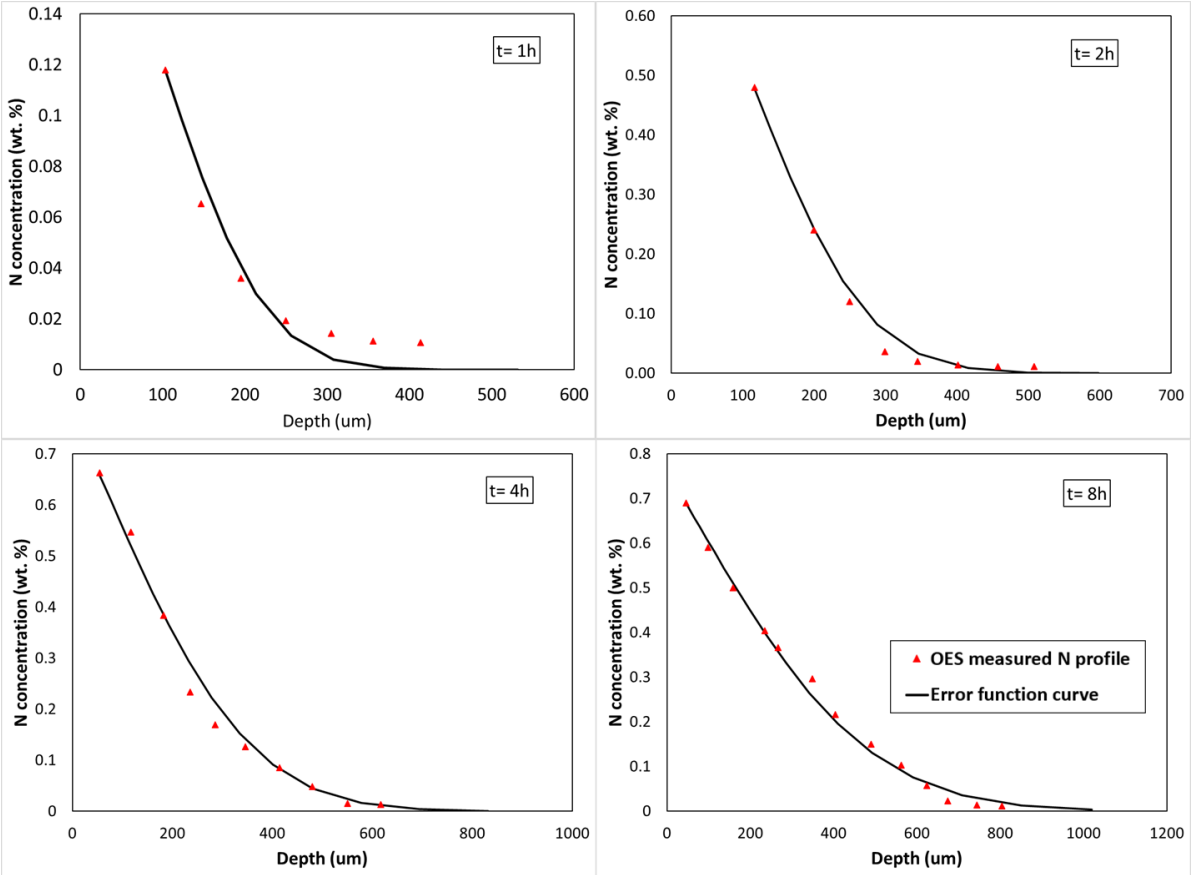

Figure 136 Measured nitrogen concentration profile and fitted Error function curve of the third group AISI 4140 samples (KC=12)

AISI 1018

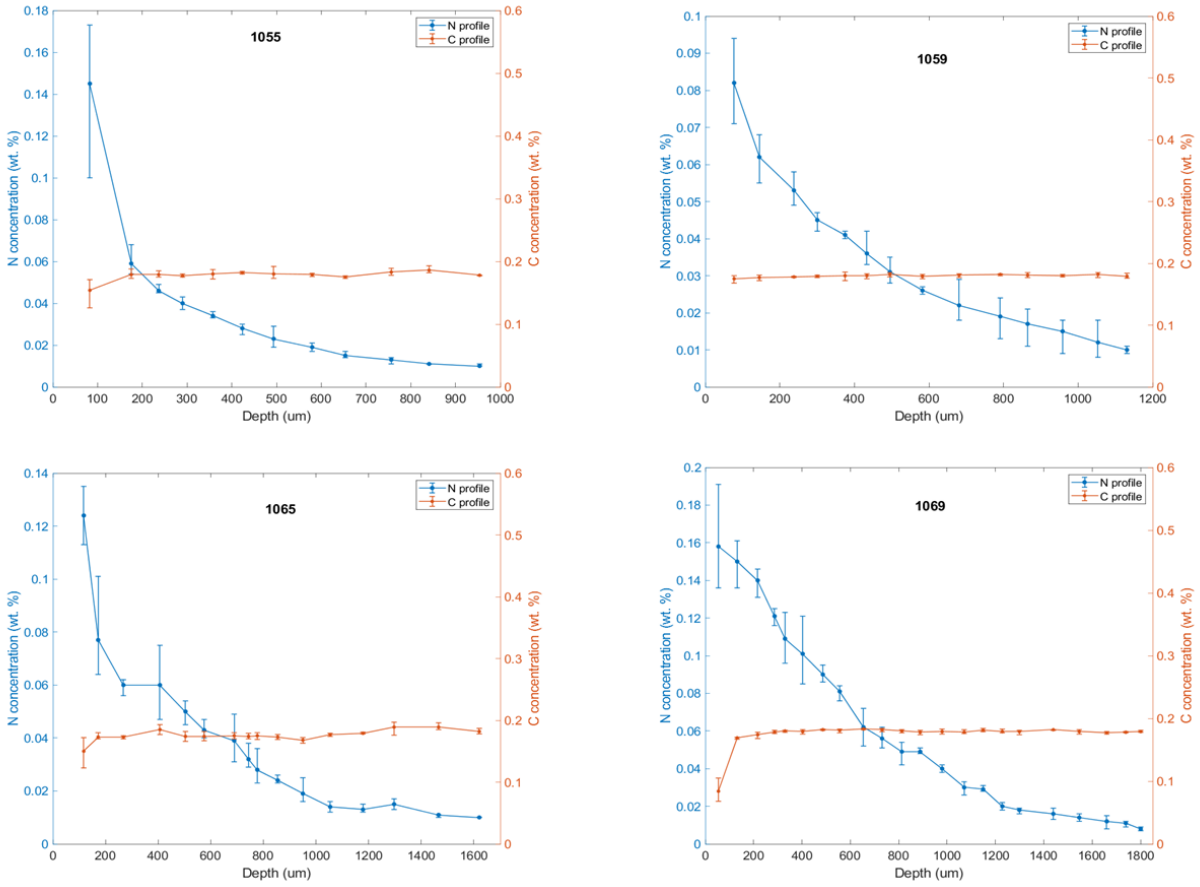

Figure 137 Nitrogen and carbon concentration profiles of the third group samples (AISI 1018, KC=12, t=1h, 2h,4h, and 8h)

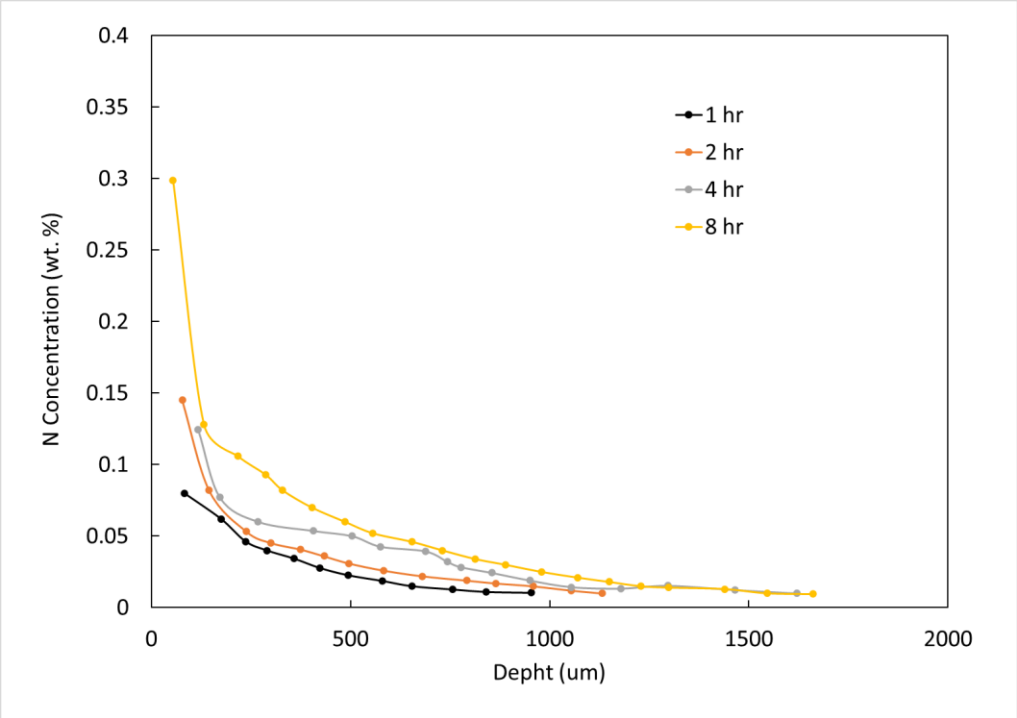

Figure 138 Comparison of nitrogen concentration profiles of the third group samples (AISI 1018, KC=12, t= 1h, 2h. 4h. and 8h)

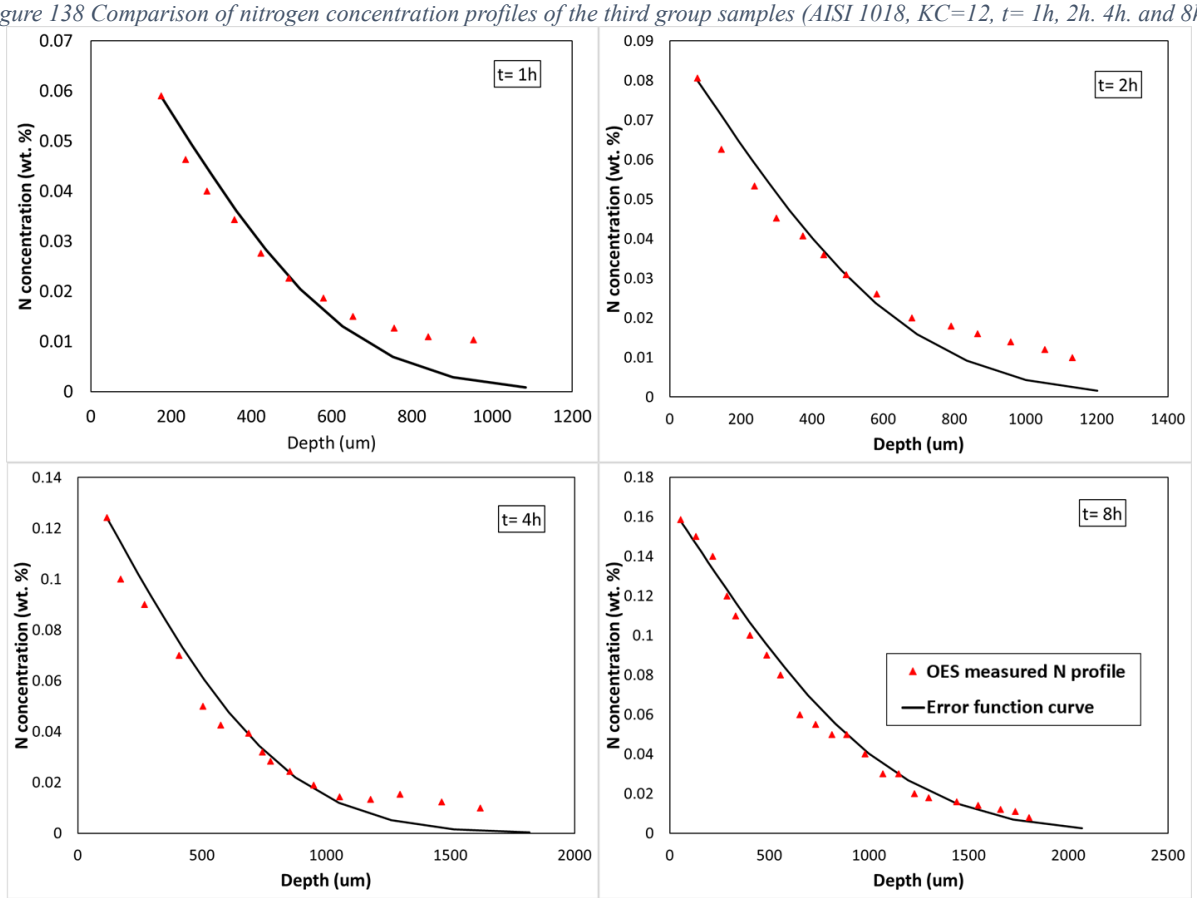

Figure 139 Measured nitrogen concentration profile and fitted Error function curve of the third group AISI 1018 samples (KC=12)

2nd FNC trial without oxidation

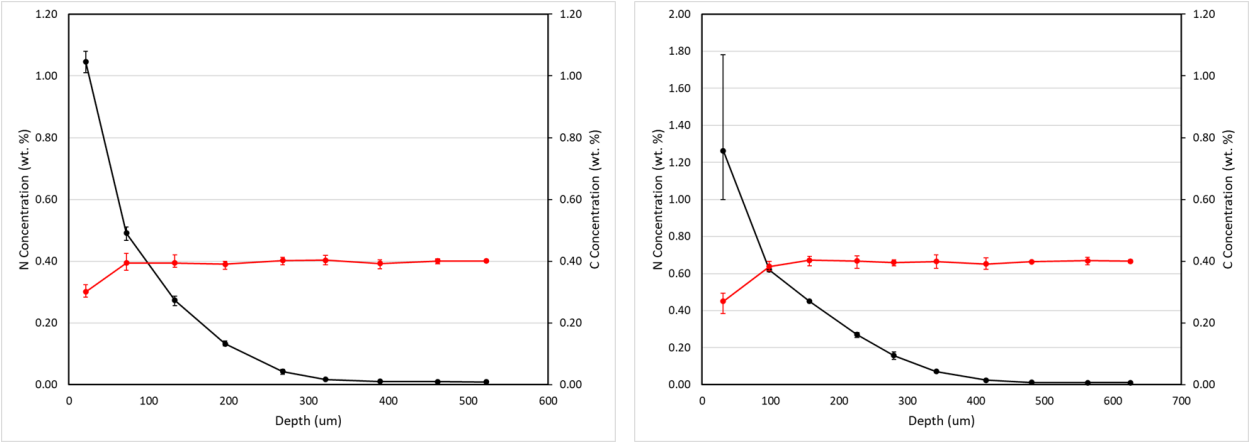

Figure 140 N & C concentration profiles of Kc=0 samples (left: t=2 hr, right: t=4 hr)

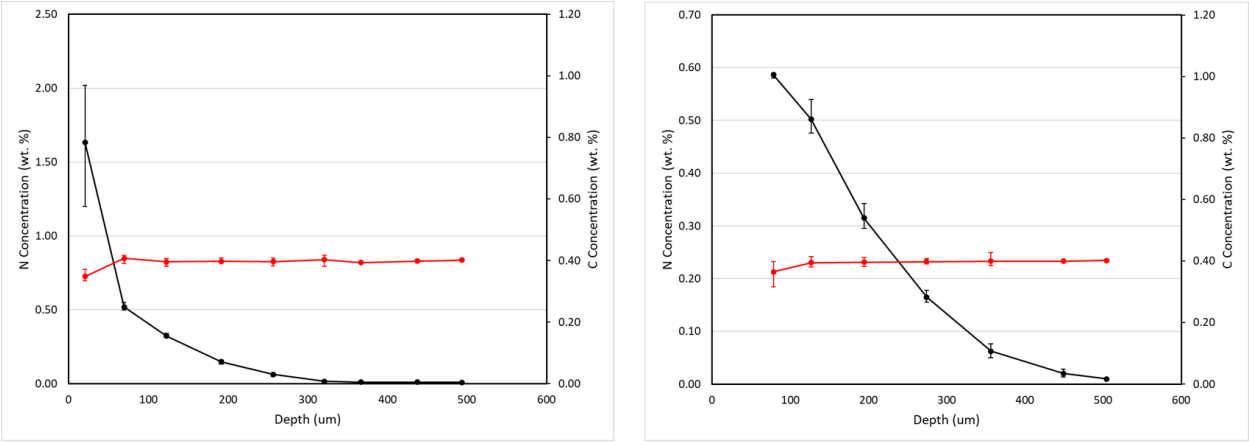

Figure 141 N & C concentration profiles of Kc=9 samples (left: t=2 hr, right: t=4 hr)

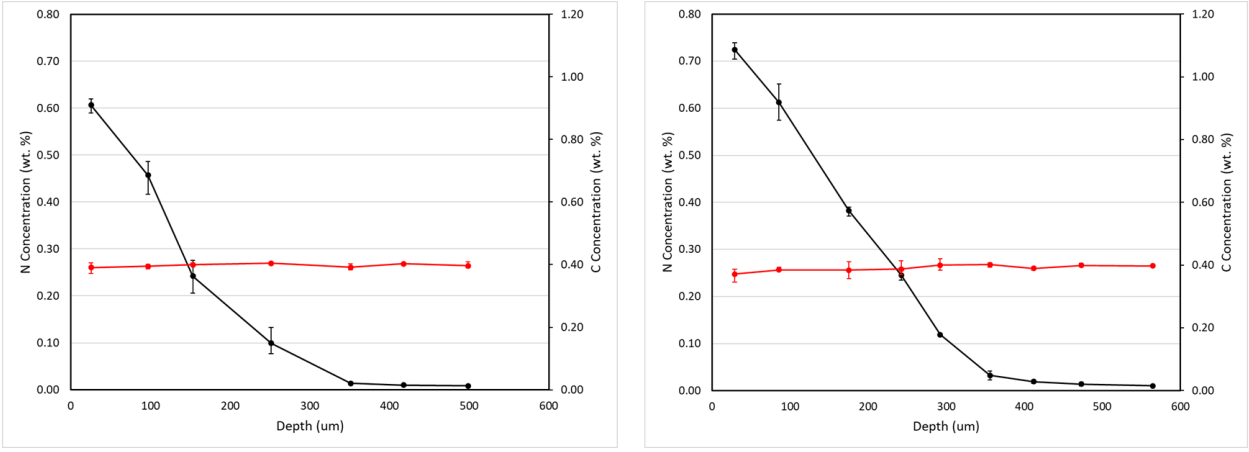

Figure 142 N & C concentration profiles of Kc=12 samples (left: t=2 hr, right: t=4 hr)

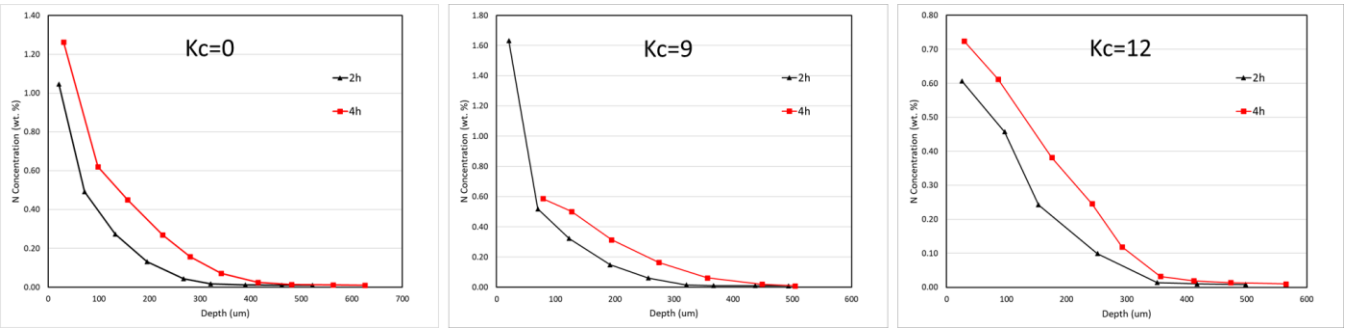

Figure 143 Comparison of N concentration profiles with the same carburizing potential but different process time

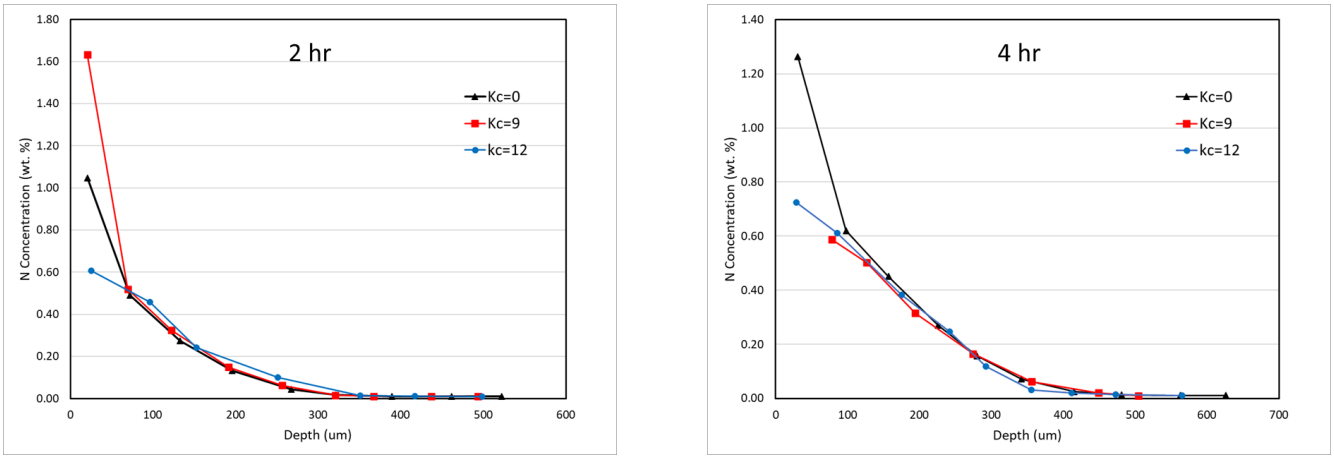

Figure 144 Comparison of N concentration profiles with the same process time but different carburizing potential.

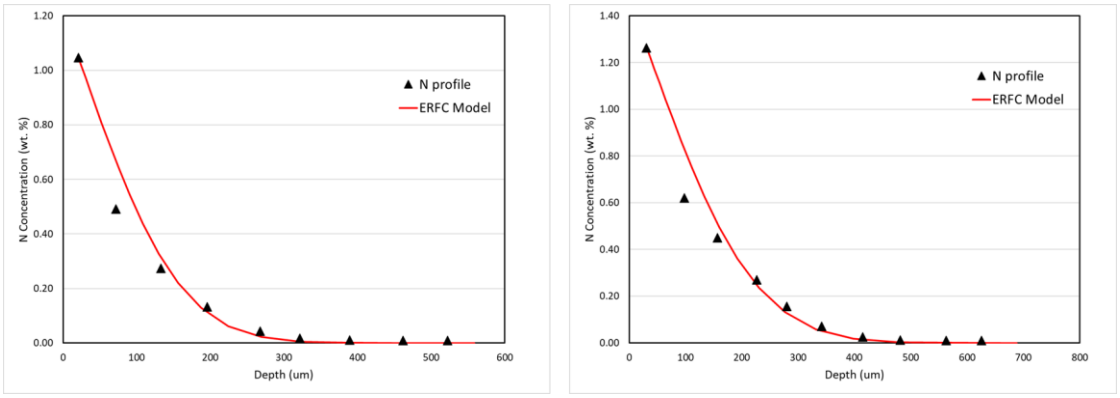

Figure 145 Error function model curve fitting with measured N concentration profile (Kc=0, left: t=2 hr, right: t=4 hr)

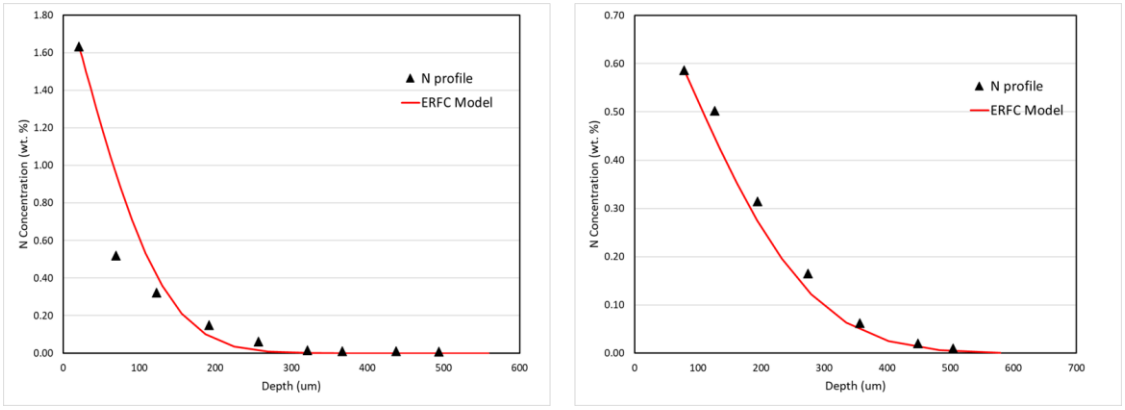

Figure 146 Error function model curve fitting with measured N concentration profile (Kc=9, left: t=2 hr, right: t=4 hr)

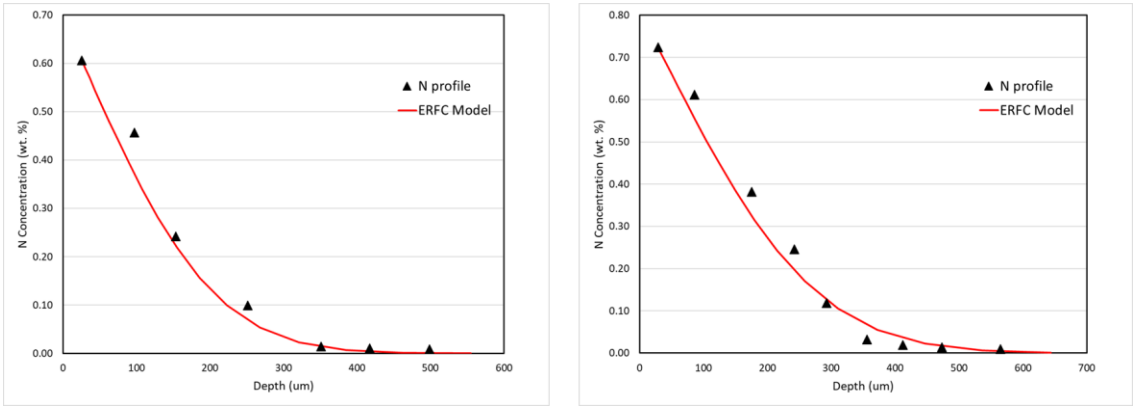

Figure 147 Error function model curve fitting with measured N concentration profile (Kc=12, left: t=2 hr, right: t=4 hr)

Appendix 3: MATLAB script code for numerical approximation of Error Function integral

```
% Input values of N0, D, t, a, and b
N0 = input("Enter the value of N0: ");
D = input("Enter the value of D: ");
t = input("Enter the value of t: ");
a = input("Enter the value of a: ");
b = input("Enter the value of b: ");

% Define the number of subintervals
n = 100;

% Calculate the width of each subinterval
h = (b - a) / n;

% Calculate the function at the endpoints of each subinterval
x = a:h:b;
f = N0 * erf(x ./ sqrt(4 * D * t));

% Apply the trapezoidal rule
integral = (h / 2) * (f(1) + 2 * sum(f(2:end-1)) + f(end));

% Display the result
disp(integral);
```